



HAL
open science

Experimental characterization and modeling non-Fickian dispersion in aquifers

Filip Gjetvaj

► **To cite this version:**

Filip Gjetvaj. Experimental characterization and modeling non-Fickian dispersion in aquifers. Earth Sciences. Université Montpellier, 2015. English. NNT : 2015MONT204 . tel-02049304

HAL Id: tel-02049304

<https://theses.hal.science/tel-02049304>

Submitted on 26 Feb 2019

HAL is a multi-disciplinary open access archive for the deposit and dissemination of scientific research documents, whether they are published or not. The documents may come from teaching and research institutions in France or abroad, or from public or private research centers.

L'archive ouverte pluridisciplinaire **HAL**, est destinée au dépôt et à la diffusion de documents scientifiques de niveau recherche, publiés ou non, émanant des établissements d'enseignement et de recherche français ou étrangers, des laboratoires publics ou privés.

THÈSE

Pour obtenir le grade de
Docteur

Délivré par Université de Montpellier

**Préparée au sein de l'école doctorale Sibaghe
Et de l'unité de recherche Géosciences Montpellier**

Spécialité : Science de la Terre et de l'Univers

Présentée par Filip GJETVAJ

**EXPERIMENTAL CHARACTERIZATION
AND MODELING NON-FICKIAN
DISPERSION IN AQUIFERS**

Soutenue le 12 novembre 2015 devant le jury composé de

Philippe GOUZE, DR, CNRS – Montpellier
Anna RUSSIAN, Post-doc, Université de Montpellier
Branko BIJELJIC, Senior Research Fellow, Imperial College
Michel QUINTARD, DR, CNRS – Toulouse
Alberto GUADAGNINI, Professeur, POLIMI - Milan
Séverin PISTRE, Professeur, Université de Montpellier
Marco DENTZ, Research Professor, CSIC – Barcelona

Directeur de thèse
Co-encadrant
Rapporteur
Rapporteur
Examineur
Examineur
Invite



Acknowledgement

There is a lot of people that I would like to thank for a support during this thesis. First of all this thesis would not be possible without prof. Sonja Zlatović and prof. Jolanta Lewandowska, their friendship provided me an opportunity to enroll doctoral study in Montpellier. There I was welcomed by prof. Philippe Gouze who was my mentor for three years. To Philippe I have to thank really a lot, he was not just my advisor who guided me through studies he also helped me a lot in my private life. Without him I wouldn't be able to rent a flat, solve numerous administrative problems, visit Barcelona, Gottingen, Padova, learn to wakeboard and actually he made this three years in Montpellier much nicer. Since, I started to talk about administrative problem I would like to express my gratitude to Bernadette Marie and Dominique Arnau who helped me overcome all administrative obstacles (and there is a lot of them in French administration).

I would also like to thank all the team (Richard, Gerard and Olivier (the big one)) in MSE that was really kind to me, and our conversations during the coffee breaks helped me to progress in French, beside helping me with technical parts of my manipulations or computers. Charlotte Garing was the most dedicated teacher trying to teach me French, I don't know why but she especially focused that J'ai and Je are not pronounced in a same way :D. At that time I was mostly hanging out with Ousman. He is a really great guy and big tnx to him for introducing me to all his friends, taking me out and for sure we had a great year in Montpellier. This chapter would not be complete without second (the small one) Olivier. This guy showed me the best hikes, MTB trails and other spots around Montpellier and also really helped me with programming, tnx big guy.

During my first year in Mtp a new post-doc (Anna Russian) came from Barcelona and during the thesis she become one of my advisors and biggest support in critical points of the thesis. So thank you Anna because without you this thesis would never been finished. Discussions with Anna, Marco Dentz and Philippe were really important part of the thesis so all three of them deserve to be acknowledged.

I would like to acknowledge both reviewers and all jury members for agreeing to participate in the process of thesis defense and evaluating my work. Also I would like to tnx Alessito Claude Cristianito, Maria and Francesca who helped my mother in preparation of pot de these.

Last, but surely not the least I would like to thank my parents, sister and girlfriend for all the support during the thesis. I know that I can be really pain in the a** so bravo for withstanding that and I believe that Marta will be really happy not to receive any more so much emoji not that I am not away any more (but for sure I will send her some govnic, dogs, cows, ghosts not to forget the feeling).

Table of contents

Acknowledgement	iii
Chapter 1 Introduction	13
Chapter 2 Transport in porous media.....	19
2.1 Diffusion	19
2.2 Advective transport.....	21
2.3 Asymptotic Fickian hydrodynamic dispersion	22
2.4 Characterization of dispersion regime.....	26
2.5 Alternative Approaches	28
2.5.1 Multi-Rate Mass Transfer Model (MRMT).....	29
2.5.2 Continuous Time Random Walk (CTRW)	31
Chapter 3 Tracer experiments	33
3.1 Introduction and objectives	33
3.2 Experiment setup	33
3.2.1 Pumps.....	34
3.2.2 Experimental materials and procedures.....	35
3.2.3 Tracer injection point.....	38
3.2.4 Fluorescein	38
3.2.5 The TELog sensor	39
3.2.6 TELog calibration and data readings	40
3.3 Results and discussion	44
3.3.1 Glass beads flow-through experiments	44
3.3.2 Glass beads push-pull experiments	47
3.3.3 Berea sandstone flow-through experiments	51
3.4 Summary and conclusion	54
Chapter 4 Pore-scale numerical simulations of the flow field.....	55
4.1 Introduction and framework.....	55
4.2 Rock structure imaging	55
4.2.1 X-ray microtomography (XRMT)	55
4.2.2 Segmentation.....	56

4.2.3	Percolation clusters.....	60
4.2.4	Characteristic length	61
4.3	Obtaining flow field.....	62
4.3.1	Representative elementary volume.....	62
4.3.2	Mesh generator.....	64
4.3.3	Solving flow	68
	Convergence criterion.....	70
	Parallelization performance.....	71
4.4	Results and discussion	71
4.4.1	Mesh comparison.....	72
4.5	Summary and conclusion	86
Chapter 5	Pore-scale modeling of anomalous transport.....	87
5.1	Introduction	87
5.2	Immobile region properties	87
5.2.1	Percolation threshold of microporosity.....	87
5.2.2	Tortuosity.....	89
5.2.3	Effective diffusion in the microporosity.....	90
5.3	Article 1 – Dual control of flow field heterogeneity and immobile porosity on non-Fickian transport in Berea sandstone	91
5.4	Summary and conclusion	113
Chapter 6	Simulations of flow in both the macroporosity and the microporosity: the Darcy-Brinkman approach.....	115
6.1	Introduction	115
6.2	Article 2 – Effect of microporosity on pore-scale simulation of flow using X-ray microtomography images.....	115
6.3	Results – comparison with Navier-Stokes equation	136
6.4	Summary and conclusion	136
Chapter 7	General conclusions and prospective	139
	Bibliography	142
	Résumé substantiel	151

Table of figures

Figure 1.1 BTC of fluorescein tracer from laboratory experiment on Berea sandstone core (blue line) compared with the solution of ADE (red line). Experimental setup: flow-through experiment, flow rate $10 \text{ cm}^3/\text{h}$; Berea sandstone, core diameter 18mm, core length 15 cm; pulse injection, concentration 50 ppm, tracer volume $50 \mu\text{L}$	14
Figure 1.2 Concentration of solute in the porous medium consisting of glass beads. Different permeability zones were created by inserting circular regions filled with glass beads with significantly smaller radius than the surrounding medium. Three experiments are presented; they differ in permeability of low permeability zones. Concentration is represented as fraction of initial concentration, scale is at the bottom of image – reprinted from Zinn et al. [2004]	16
Figure 2.1 Spreading of a solute pulse with time (t), transport only due to diffusion. Solute pulse was injected into the aquifer at time t_0 with an initial concentration C_0 – reprinted from Fetter [1999] .	19
Figure 2.2 Illustration of diffusion a) free in space and b) in the pore space	20
Figure 2.3 Illustration of advective transport in the porous medium with time. Solute pulse was injected at $x=0$ and at the time t_0	22
Figure 2.4 Illustration of different trajectories taken by solute traveling through the porous medium	22
Figure 2.5 Illustration of the mechanical dispersion in the porous medium. On the illustration at the top, blue line denotes flow-path with lower velocity while red line denotes flow-path with faster flowing fluid. On the bottom image there is an illustration of two different paths taken by the solute, both paths have same starting and finishing points but the path length is significantly different. Magnified is example of the parabolic velocity distribution in one pore that causes Taylor dispersion.....	23
Figure 2.6 Illustration of the transport and spreading of the solute pulse in the porous medium with time, according to advection-dispersion theory. Solute pulse was injected at $x=0+a$ and at the time t_0 . Transported and spreading is due to advection and dispersion – reprinted from Fetter [1999].....	24
Figure 2.7 Illustration of dead-end pores in the natural porous medium	25
Figure 2.8 Experimental results showing relation between the longitudinal dispersion coefficient (DL) and Peclet number (Pe). Dashed lines indicate limits between five different transport regimes – reprinted from Sahimi [1993]	26
Figure 2.9 a) Illustration of “natural” heterogeneous porous medium with solute exchange between different phases indicated by arrows. Left image presents mass transfer between zones with different permeability (slow and fast flowing zones) and right presents mass exchange on the pore scale between porosity with different flow regimes (i.e. diffusion between stagnant and flowing zones), microporosity (e.g. clay pockets) and surface sorption. b) Illustration of different mass exchange processes incorporated in one multi-rate mass transfer model designed to simulate different mass exchange principles that happen in nature. – reprinted from Haggerty and Gorelick[1995]	30

Figure 3.1 Schematic diagram of the experimental test-bench circuit layout with arrows indicating flow direction. Blue arrows – permanent flow direction; green arrows – flow direction for flow-through experiment and pull phase of push-pull experiment; red arrows – flow direction during push phase of push-pull experiment.....	34
Figure 3.2 Different stages of glass bead column preparation for the experiments. a) microscopic image of glass beads; b) sorting machine at the Geosciences Montpellier laboratory and one of the sieves; c)underwater column filling with sorted glass beads; d)experiment on the transparent column with high fluorescein content in the tracer to visual check for side flow and other anomalies	36
Figure 3.3 Cross section through experimental cell for laboratory tracer experiment (a) and different stages of preparing core samples; b) Berea sandstone block from which core is extracted; c) coring machine at Geosciences Montpellier laboratory and d) on the left Berea sandstone core and on the rights same core coated with thermo-plastic coating.....	37
Figure 3.4 Schematic cross-section of injection part at the top of the cell with labeled essential parts	38
Figure 3.5 Fluorescein in various forms, on the right is disodium salt which is also known as “uranin” and on the left is dissolution in the water with typical bright green color.	39
Figure 3.6 Schematic representation of the TELog measurement head displaying optical path - reprinted form Gouze et al. [2009].....	40
Figure 3.7 Schematic illustration of master concentration and its diluted products with list of all solutes concentrations.....	42
Figure 3.8 TELog calibration results. Symbols present measured tension output for given concentration at different gains (photomultiplier sensitivity), lines present functions used to transform voltage to fluorescein concentration for different gains (line color matches symbol color for same gain), two dashed red lines present limit of function application in standalone mode for all gains except gain 8.	43
Figure 3.9 Experimental breakthrough curve data of tracer concentration at the outlet of the column packed glass beads (L=20cm \varnothing =18mm), flow-through experiment, flow rate 50cm ³ /h. Comparison between different solution concentration of injected tracer ranging from 1 ppm to 1000 ppm.	45
Figure 3.10 Experimental breakthrough curve data of tracer concentration at the outlet of the column packed glass beads (L=20cm \varnothing =18mm), flow-through experiment, flow rate 50cm ³ /h. Displaying different tail behavior due to density effect in experiments with injection concentration 500ppm and tracer volume 2 μ L.	46
Figure 3.11 Experimental breakthrough curve data of tracer concentration at the outlet of the column packed glass beads (L=20cm \varnothing =18mm), flow-through experiment, flow rate 50cm ³ /h. Displaying behavior for injected tracer with concentration of 50ppm, with two different tracer volumes 2 μ L (blue line) and 10 μ L (red line).	47

- Figure 3.12 Experimental breakthrough curve data of tracer concentration at the outlet of the column packed glass beads ($L=20\text{cm}$ $\varnothing=18\text{mm}$), push-pull experiment, flow rate $50\text{cm}^3/\text{h}$, duration of push phase is 22 minutes, injected tracer volume $10\ \mu\text{L}$. Comparison between different concentrations of the injected solutions; 50 ppm (green line) and 1 ppm (red line)..... 48
- Figure 3.13 Experimental breakthrough curve data of tracer concentration at the outlet of the column packed glass beads ($L=20\text{cm}$ $\varnothing=18\text{mm}$), push-pull experiment, flow rate $50\text{cm}^3/\text{h}$, injected tracer concentration 50 ppm, injected tracer volume $10\ \mu\text{L}$. Differences between BTC's are in duration of push and resting period. Red curve – push duration 900s, resting duration 300s; green curve – push duration 1320s, resting period 0s; blue curve– push duration 1320s, resting period 300s. Times noted in legend are in minutes, SW stands for duration of push and ST for resting period. 49
- Figure 3.14 Experimental breakthrough curve data of tracer concentration at the outlet of the column packed glass beads ($L=20\text{cm}$ $\varnothing=18\text{mm}$), push-pull experiment, flow rate $50\text{cm}^3/\text{h}$, injected concentration solution 50 ppm, push duration 22min. Magenta curve – fast injection, Green curve – slow injection 50
- Figure 3.15 Experimental breakthrough curve data of tracer concentration at the outlet of the column packed glass beads ($L=20\text{cm}$ $\varnothing=18\text{mm}$), push-pull experiment, flow rate $50\ \text{cm}^3/\text{h}$, injected concentration solution 50 ppm, injected volume $10\ \mu\text{L}$, duration of push phase 22 min. 51
- Figure 3.16 Experimental breakthrough curve data of tracer concentration at the outlet of the Berea sandstone core ($L=15\text{cm}$ $\varnothing=18\text{mm}$), flow-through experiment, injected concentration solution 50 ppm, injected volume $50\ \mu\text{L}$. Comparison between two different flow rates $10\ \text{cm}^3/\text{h}$ (red line) and $2\ \text{cm}^3/\text{h}$ (blue line). Black line denotes power-law function that fits late time behavior of the experiment with higher flow rate. 52
- Figure 3.17 Scaled BTC according to the estimated tracer volume that is injected (a); red line $10\ \text{cm}^3/\text{h}$, blue line $2\ \text{cm}^3/\text{h}$. Compared with results of transport simulations performed on XRMT images of the same rock (b) at $Pe = 1000$ (purple symbols) and $Pe = 100$ (green symbols). Black rectangular limits resolution that can be observed in the experiments. Unconnected symbols denotes simulations in which mass transfer to microporosity is neglected, while connected symbols represents simulations that account for mass transfer into the microporosity – original figure is in section 5.3, Figure 11 53
- Figure 4.1 Image acquisition from X-ray microtomography to the final 3D model of heterogeneous media – reprinted from Fernandes et al. 2012..... 56
- Figure 4.2 Mercury Intrusion Porosimetry test results for Berea sandstone (black line). Dashed red line denotes XRMT image resolution ($3.16\ \mu\text{m}$), delimitating microporosity and macroporosity, blue line marks average pore size ($11.71\ \mu\text{m}$)..... 57
- Figure 4.3 Gray scale level distribution for Berea sandstone (black line), dashed lines marks threshold values used for segmentation. Blue lines are for void-micoporosity interface and red lines are for solid-micoporosity interface 59
- Figure 4.4 3-dimensional visualization of pore-space network (blue) and connected microporosity (yellow) 60

Figure 4.5 Cross section through segmented Berea sandstone displaying pore-space structure of connected clusters (i.e. all unconnected porosity is eliminated). Black filled areas denote the solid phase, white colored areas denote connected macroporosity, orange colored areas indicate the microporous phase and blue areas denote macroporosity that is connected with percolation cluster only through microporous phase	61
Figure 4.6 Rock structure variogram for Berea sandstone	62
Figure 4.7 Definition of the representative elementary volume as a function of porosity – reprinted from Bear [1972].....	63
Figure 4.8 Normalized porosity in function of the normalized sample volume	63
Figure 4.9 Normalized permeability in function of normalized sample volume	64
Figure 4.10 Graphical illustration of differences between two mesh generation approaches. Left image (a) presents mesh generated from *.stl file (green line) with snappyHexMesh and right image (b) is presenting mesh made by developed mesh generator. Black – solid phase; white – void phase; green – surface from *.stl file; blue – internal mesh boundaries; red – external mesh boundaries.....	65
Figure 4.11 Velocity distribution in the pore throat with diameter equal to the XRMT image resolution a) parabolic velocity profile in real conditions; b) velocity distribution when mesh resolution is equal to image resolution; c) velocity distribution when mesh resolution is three times smaller than image resolution	66
Figure 4.12 Mesh generated in pore space of Berea sandstone used for flow simulations, including manifolds on inlet and outlet boundaries	68
Figure 4.13 Flow field obtained from OpenFOAM, blue color denotes areas with low velocities while red denotes areas with high velocities	69
Figure 4.14 Normalized permeability in function of initial residual, red dashed line denotes initial residual level chosen as convergence criterion of all OpenFOAM simulations.....	70
Figure 4.15 Results of OpenFOAM parallelization performance investigation, times are printed as relative speed-up compared to the simulation time of non-parallelized simulation.....	71
Figure 4.16 Cross-plot of calculated permeability from pore-scale flow simulations in function of the porosity for different sub-volumes extracted from Berea sandstone segmented image.	72
Figure 4.17 SubV1. Comparison of a) average, b) maximal and c) minimal velocity per cross-section profiles perpendicular to the flow direction for coarse (orange line) and fine mesh (blue line) with corresponding local porosity (black dashed line).	74
Figure 4.18 SubV2. Comparison of a) average, b) maximal and c) minimal velocity per cross-section profiles perpendicular to the flow direction for coarse (orange line) and fine mesh (blue line) with corresponding local porosity (black dashed line).	75

Figure 4.19 SubV3. Comparison of a) average, b) maximal and c) minimal velocity per cross-section profiles perpendicular to the flow direction for coarse (orange line) and fine mesh (blue line) with corresponding local porosity (black dashed line).	76
Figure 4.20 SubV4. Comparison of a) average, b) maximal and c) minimal velocity per cross-section profiles perpendicular to the flow direction for coarse (orange line) and fine mesh (blue line) with corresponding local porosity (black dashed line).	77
Figure 4.21 SubV5. Comparison of a) average, b) maximal and c) minimal velocity per cross-section profiles perpendicular to the flow direction for coarse (orange line) and fine mesh (blue line) with corresponding local porosity (black dashed line).	78
Figure 4.22 SubV6. Comparison of a) average, b) maximal and c) minimal velocity per cross-section profiles perpendicular to the flow direction for coarse (orange line) and fine mesh (blue line) with corresponding local porosity (black dashed line).	79
Figure 4.23 Artificial 3d symmetric structure, designed to investigate flow-through smallest possible throat (1 pixel)	80
Figure 4.24 Results of flow simulations on the artificial structure presented as a) pressure and b) velocity fields. Mesh resolution is the same as image resolution	82
Figure 4.25 Results of flow simulations on the artificial structure presented as a) pressure and b) velocity fields. Mesh resolution two times finer than image resolution (1 image pixels is represented with 4 mesh cells).	83
Figure 4.26 Results of flow simulations on the artificial structure presented as a) pressure and b) velocity fields. Mesh resolution three times finer than image resolution (1 image pixels is represented with 27 mesh cells).	84
Figure 4.27 Results of flow simulations on the artificial structure presented as a) pressure and b) velocity fields. Mesh resolution seven times finer than image resolution (1 image pixels is represented with 343 mesh cells).	85
Figure 5.1 Illustration of evolution of percolation threshold in microporous phase. Blue color denotes mobile domain from which solute diffuses in microporosity, microporous phase is represented with gray pixels where gray level represents intrinsic porosity (darker gray lower intrinsic porosity and vice versa) and yellow color denotes areas with intrinsic porosity lower than percolation threshold; a) no percolation threshold applied, b) low percolation threshold level, c) medium percolation threshold level and d) high percolation threshold	88
Figure 5.2 Illustration of tortuosity definition by Carman (1937). Effective average path (l_e) in the porous media (green line) and shortest possible distance measured along transport direction (l) (blue line)	89
Figure 5.3 Illustration of intrinsic porosity distribution as the function of exponent n	91

Chapter 1

Introduction

Porous media are all around us and our everyday life is imbued with the interaction with them. All solid or semisolid materials with exception of metals, some very dense rocks and plastics are in fact porous media and moreover often permeable. Therefore, understanding the hydrodynamic processes occurring in porous media is in the scientific focus since a long time.

One of the vital processes in the permeable media is the transport of dissolved substances (i.e. solute transport). It plays an important role in a whole range of natural processes, many of which are in everyday engineering or scientific scope, such as:

- transport of nutrients, oxygen, medicines and/or poisons through human/animal tissues in biological and medical sciences
- accessibility of nutrients and spreading of the pesticides in the agriculture
- enhanced oil recovery in petroleum engineering
- CO₂ underground storages and nuclear waste disposal areas in geology and environmental engineering
- pollutant transport and remediation in hydrogeology

Transport in porous media is driven by diffusion and advection, causing spreading of solute plume. First mathematical description of diffusion has been given by German physician and psychologist Adolf Eugen Fick [1855]. He observed movement of solute due to differences in the concentration. Development of advection transport theory began in the 1911 with simplest case of capillary flow [Griffiths, 1911], however it was Taylor [1953] who gave a mathematical description of the phenomenon.

Traditional theory of dispersion in porous media has been developed through the work of several authors [e.g., Scheidegger, 1961; Saffman, 1959; 1960; Bear and Bachmat, 1967]. This theory describes dispersion of a conservative (ideal) tracer in the fully saturated porous medium and with flow condition within the limits where Darcy's law is applicable by the advection-dispersion equation (ADE):

$$\phi \frac{\partial c}{\partial t} + \nabla \cdot (Uc) - \nabla \cdot (\mathbf{D}\nabla c) = 0, \quad (1.1)$$

where c denotes the concentration, t is the time, U is the Darcy velocity and \mathbf{D} is the dispersion tensor. The solution of the ADE is diffusion-like (Fickian) for the scale of the Representative Elementary Volume (REV) at which full mixing of the solute is assumed.

In order to capture true behavior of the dispersion there have been many field experiments of the nonreactive transport in the porous media in the aquifers with different properties around the world. Ranging from relatively homogeneous aquifers (e.g., sand aquifer at Borden [Mackay et al., 1986]; and sand-gravel at Cape Code [LeBlanc et al., 1991]); over more heterogeneous ones such as Macrodispersion Experimental (MADE) Site at Columbus [Adams and Gelhar, 1992], Ses Sitjoloes at Mallorca island in Spain [Gouze et al., 2008a], to fractured aquifers such as ones in New Mexico [Meigs and Beauheim, 2001] and at Grafton County [Becker and Shapiro, 2000]. Observations from all this

experiments indicate that the transport in real systems differs from Fickian assumption made by ADE. Moreover laboratory tracer experiments in bead column/packs [Kandhai et al., 2002; Moroni et al., 2006; Bijeljic et al., 2011a], natural rocks [Scheven et al., 2005; Gouze et al., 2009] and uniformly [Cortis et al., 2004] and randomly packed sands [Silliman and Simpson, 1987; Levy and Berkowitz, 2002] prove that anomalous (non-Fickian) transport is rather omnipresent than exceptional.

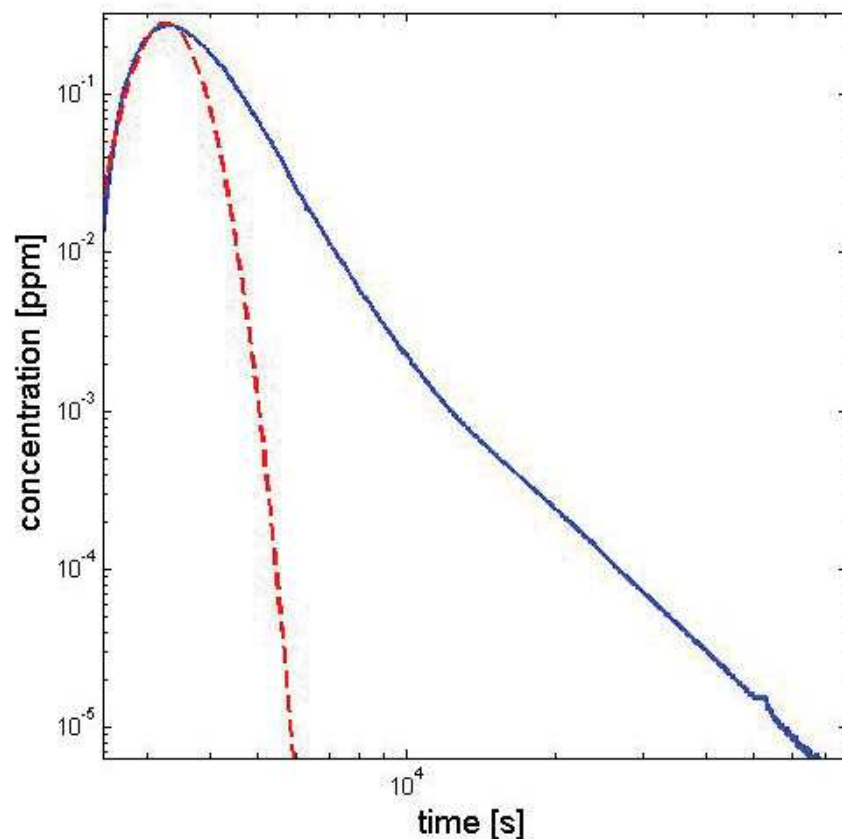


Figure 1.1 BTC of fluorescein tracer from laboratory experiment on Berea sandstone core (blue line) compared with the solution of ADE (red line). Experimental setup: flow-through experiment, flow rate $10 \text{ cm}^3/\text{h}$; Berea sandstone, core diameter 18mm, core length 15 cm; pulse injection, concentration 50 ppm, tracer volume $50 \mu\text{L}$

Breakthrough curves (BTC) from all these experiments are highly asymmetric, with signatures of anomalous transport such as early breakthrough, long tailing (concentration usually decreases as a power-law of time) and anomalous scaling of the mean square displacement. In Figure 1.1 one can see a comparison between the BTC obtained by the laboratory experiment and the best-fitted solution of the ADE. This BTC is obtained as the result of a flow-through experiment on a Berea sandstone core within experimental part of our work; details of the experiments are presented in the Chapter 3.

ADE fails to predict the transport behavior for the most homogeneous natural aquifers [Freyberg, 1986; Garabedian et al., 1991]. The constant dispersion coefficients used in ADE fail to capture the real dispersivity occurring in the porous medium that is dependent on the time and/or the observed scale. The spatial difference in the local dispersivity coefficients is usually explained by the flow field

heterogeneity that exists even in the macroscopically completely homogeneous media [Datta et al., 2013]. Accordingly, non-Fickian dispersion is a pre-asymptotic regime; dispersion becomes Fickian at long times if the scale of the heterogeneity is finite, i.e. when the tracer has visited the heterogeneity at all scales. Yet, in natural media displaying heterogeneity at virtually all scales, the effective dispersion regime is in general non-Fickian.

The non-Fickian dispersion properties, their origin and their relation to the geological heterogeneity are still debated. During the last several decades many authors have more or less successfully developed different models to simulate and predict anomalous transport. Many of these models heavily rely on the ADE formulation and try to fit experimental results by spatial variations of dispersivity. Major drawbacks of these models are that parameters that are strictly connected with the properties of the porous medium (e.g. dispersivity) are often used as fitting parameters and that transport is not necessarily Fickian even over very small domains [Cortis et al., 2004]. Two major groups of these models are based on the volume averaging and the stochastic approach.

Volume averaging models are based on solving ADE at smaller scale, usually smallest possible REV and then use these solutions to obtain results on larger scale. In these approaches one of the biggest challenges is the choice of the volume average operator to move from one scale to another [Berkowitz et al., 2006]. For an example Cushman [1984] and Quintard and Whitaker [1994] propose expressing the volume average operator in terms of convolution products of the spatial distribution functions. Most prominent representatives of the volume averaging models are the homogenization models and the models base on the renormalization techniques.

A stochastic approach is in the basis of many similar models that rely on the ADE [Dagan, 1989]. Stochasticity is introduced by spatial and temporal variations of the medium properties, such as hydraulic conductivity, porosity, etc. The resulting transport is the ensemble average of the transports in all the different realizations.

There are some alternative methods to model non-Fickian transport, such as multi-rate mass transfer (MRMT) and continuous time domain random walk (CTRW) models. It is worth noticing here that Dentz and Berkowitz [2003] have proven that there is equivalence between these models for special cases, and also included mobile-immobile mass transfer into the CTRW framework. These models aims at describing the anomalous behavior based on the assumption that non-Fickian dispersion comes from a broad distribution of the transition times that solute particles encounter in the porous medium. The transition time distribution is obviously related to the heterogeneity of the medium that triggers a broad range of possible flow paths for the tracer while diffusion tends to smooth the apparent differential tracer velocities. It follows that, a priori, the asymptotic Fickian dispersion regime should be recovered fast in highly diffusive systems [Liu and Kitanidis, 2012].

The MRMT models [Haggerty and Gorelick, 1995; Carrera et al., 1998; Haggerty et al., 2000] assume existence of two domains with completely different properties, relying on the idea of dual-porosity models [Barenblatt et al., 1960]. The mobile domain where the transport is governed by advection is modeled by classical ADE with the constant average velocity and the dispersion coefficient, while the diffusive transport is dominant in the immobile domain. Anomalous transport arises from the mobile-immobile mass exchange since tracer “particles” that enter the immobile domain on average experience

significantly larger transient times than ones passing only through the mobile domain. Heterogeneity in this models in introduced by size and spatial disposition of the mobile and immobile domains and their mutual interfaces. Modeling of the MRMT is usually done by adding a source-sink term in the ADE to account matrix diffusion [e.g., Carrera et al., 1998] or by CTRW as stated earlier. A major weakness of the MRMT approach is that it does not account for the effect of the velocity field heterogeneity in the mobile domain that may participate together with the immobile domain to control the observed non-Fickian dispersion. Moreover, the memory function is often used as a fitting parameter without any connections to measurable properties of the porous medium, although there were some attempts to connect the memory function with the tortuosity and properties of the microporous phase from X-ray microtomography images [e.g., Gouze et al., 2008b].

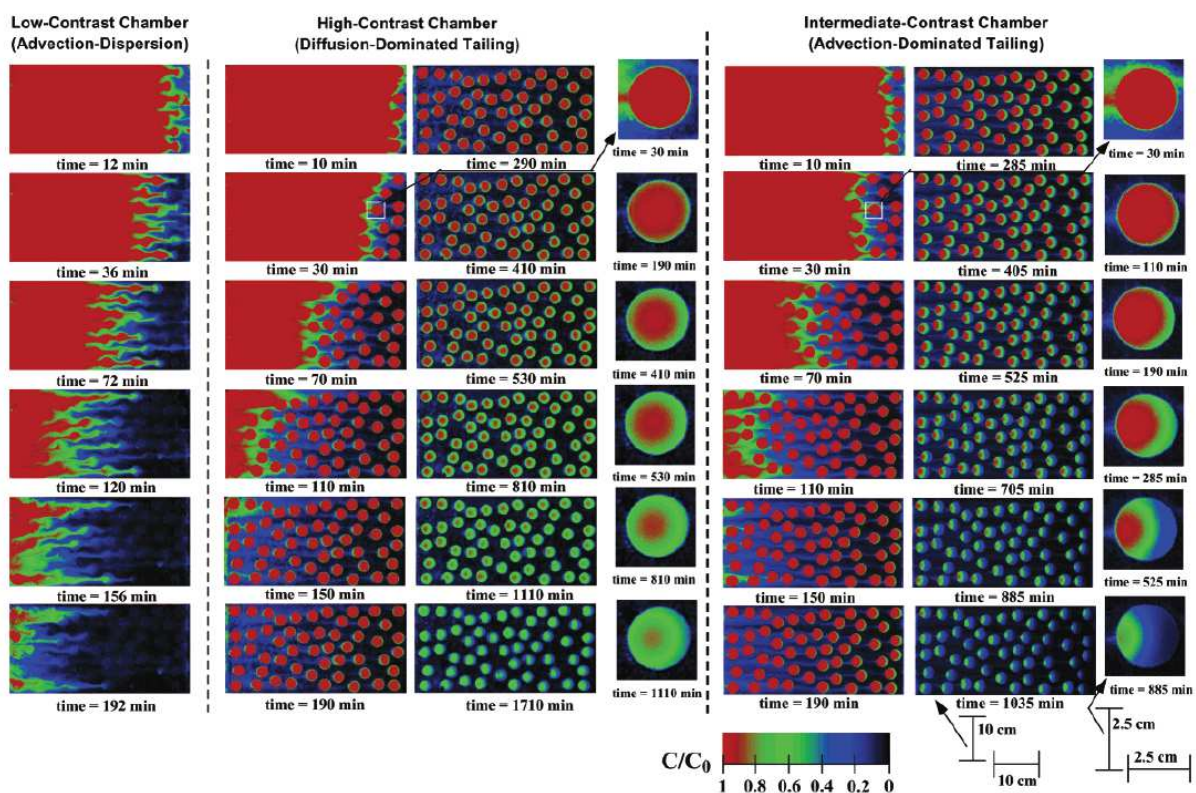


Figure 1.2 Concentration of solute in the porous medium consisting of glass beads. Different permeability zones were created by inserting circular regions filled with glass beads with significantly smaller radius than the surrounding medium. Three experiments are presented; they differ in permeability of low permeability zones. Concentration is represented as fraction of initial concentration, scale is at the bottom of image – reprinted from Zinn et al. [2004]

CTRW is a flexible framework that has proven capabilities to provide a convincing modeling of non-Fickian transport in the porous medium [Berkowitz et al., 2000; Cortis and Berkowitz, 2004; Le Borgne and Gouze, 2008; Cortis and Birkholzer, 2008]. In general CTRW is used to provide 1D upscaled model where the macroscopic behavior is reproduced only (i.e. all the details linked to the pore-scale mechanisms that act as producing fluctuation around the macroscopic behavior are not included). It is based on the basic mass transfer equations given by Scher and Lax [1973], who generalized Montroll-Weiss continuous time random walk [Montroll and Weiss, 1965] on a lattice. The main input parameter

in the CTRW is a probabilistic density function (pdf) of transition times, containing all the important properties of the porous medium influencing the macroscopic behavior of tracer transport. Accordingly, the macroscopic transport behavior in CTRW framework is determined by the shape of the transition time pdf, therefore it is essential to find pertinent correlation between the pdf shape and measurable physical parameters, but to the best of our knowledge this point has poorly been investigated so far. One of the most interesting CTRW models which appeared in recent years is the correlated CTRW. Le Borgne et al. [2011] have shown that anomalous transport in the simple 2D structures can be simulated by CTRW from correlated Lagrangian velocities along the streamlines. This approach was later successfully applied on Berea sandstone [Kang et al., 2014]. This approach sound interesting for relating the effective dispersion to the properties of the velocities along the flow paths that can be computed from solving pore-scale flow. It is also promising for introducing the distinction between mixing and spreading; or in other words the distinction between reversible and irreversible mechanisms of dispersion, such as measurable comparing push-pull and flow-through tracer tests [Gouze et al., 2008b].

The synthetic presentation of the actual dispersion models above indicates that they are based on the assumptions that anomalous transport arises from different transit times that the solute tracer experiences when travelling through the pore-space. The recent developments in computing resources gave us the opportunity of investigating mechanisms that control transport on the pore-scale. For instance, reliable techniques for the three-dimensional imaging of pore-space structures and flow showed rapid developments. Nuclear magnetic resonance (NMR) [e.g., Scheven, 2013] and X-ray microtomography (XRMT) [e.g., Fourar and Radilla, 2009; Klise et al., 2008] have been used to directly visualize transport effects in the natural and artificial porous media. Among other results, many of these investigations showed wide distributions of velocities [e.g., Seymour and Callaghan, 1997]. However, these methods have limitations in terms of the resolution, both of the solute and velocity distribution, because of the necessity of performing fast acquisition in order to tackle the dynamics of the transport processes. Although it is important to note that the (ubiquitous) diffusion mechanisms cannot be tackled accurately at small scale. For example, at a resolution of 5 microns, the characteristic time of diffusion through a pixel is smaller than 0.1 second which is far smaller than the actual imaging capabilities for X-ray tomography. The contribution of these methods for characterizing multiscale dispersion mechanisms is more qualitative than quantitative, similar to other imaging techniques developed for investigation of dispersion in transparent porous media. Nevertheless these methods are unmatched for characterizing the average macroscopic behavior and test models. An example of dispersion investigation performed by the visible light transmission technique on a glass bead pack (transparent porous media) can be seen on Figure 1.2. Zinn et al. [2004] created porous media of uniformly sized glass beads, and then inserted circular regions filled with uniformly sized glass beads but with significantly smaller diameter to obtain less permeable regions. Figure 1.2 clearly shows that heterogeneity in region permeability leads to different rates of the transport in different regimes, as well as shows different transport mechanisms occurring due to differences in the permeability.

Conversely, a detailed investigation of the transport processes is now possible by solving it numerically directly on the pore structure. Standard approach starts with the acquisition of high resolution XRMT images of the pore-structure. For reservoir rocks the optimal resolution (voxel size) is in the order of few micrometers. These raw images of the X-ray absorption in the sample are then

processed (segmentation) to distinguish different phases (usually rock and void). Processed images are then used to mesh the pore space for flow and transport calculations using computed fluid dynamic codes [Ovaysi and Piri, 2011; Blunt et al., 2013]. Many recent studies have been investigating spreading of solute in the relation of the velocity distribution in the flow field in different porous media ranging from simple structures [e.g., Le Borgne et al., 2011] and glass beads packs [e.g., Maier et al., 2008], to natural rocks with different level of complexity such as, sandstones [e.g., Kang et al., 2014] and carbonates [e.g., Bijeljic et al., 2013]. This approach gives useful insight into the processes happening at the pore-scale and its main limitations are related to the quality and resolution of XRMT images and to the computational limitations for solving flow on large domains. Also, results are very sensitive to the accurate segmentation of XRMT images [Schlüter et al., 2014], accuracy of the computational simulations and on the representativeness of the observed medium [Arns et al., 2005; Guibert et al., 2015; Siena et al., 2015].

The work presented in this manuscript focuses on the investigation of passive (i.e. non-reactive) tracer transport through reservoir rocks. We mainly used Berea sandstone samples. Berea sandstone is a relatively homogeneous rock that is used as a proxy to poorly altered sandstone reservoirs by the petroleum industry. Therefore it has been thoroughly investigated and its properties were well documented by several authors [e.g., Curcher et al., 1991; Øren and Bakke, 2003].

Theoretical background of the processes that control flow and transport in the porous media is presented in Chapter 2. Chapter 3 is dedicated to the experiments, starting from the experimental setup and with an explanation of all procedures and assumptions applied during the design of the experiment. At the end of the chapter results are presented and discussed on the base of the analysis of the breakthrough curves (BTC). The numerical modeling methodology is presented in Chapter 4 with detailed analysis of the flow field properties focusing on the mesh resolution importance. Developed approach is incorporated in the transport simulations Chapter 5 and as well as a base for the development of the Darcy-Brinkman solver presented in Chapter 6. General conclusion with a prospective of future work is given at the end.

Chapter 2

Transport in porous media

To understand solute transport on the large scale first one has to understand the transport mechanisms at the pore-scale. Two basic modes of solute displacement in porous media are miscible and immiscible displacement. Miscible transport is characterized by only one fluid phase present in the porous medium, but its properties or composition can vary in space and time. On the other hand, in the immiscible displacement there are two or more different fluid phases and between these phases there is a distinct fluid-fluid interface.

In this work we are only interested in the miscible transport. It may be a case of two miscible liquids (e.g., fresh water and salt water) or a substance completely dissolved in a liquid. Mechanisms of solute spreading through completely saturated porous medium are described in the following section.

2.1 Diffusion

The molecular diffusion is an ubiquitous transport mechanism occurring in the porous medium as soon as the solute concentration varies spatially. It occurs regardless of fluid motion and it is driven exclusively due to differences in the concentration. Substance moves from a region of high concentration to a region of low concentration. A concentration distribution change caused by diffusive transport without any influence of flow movement is illustrated in Figure 2.1. One can see that as time passes, concentration at the place of injection decreases and the plume is spreading in the space, with a diminution of relative differences in the concentration in the space. The solute concentration spatial distribution is normal (Gaussian).

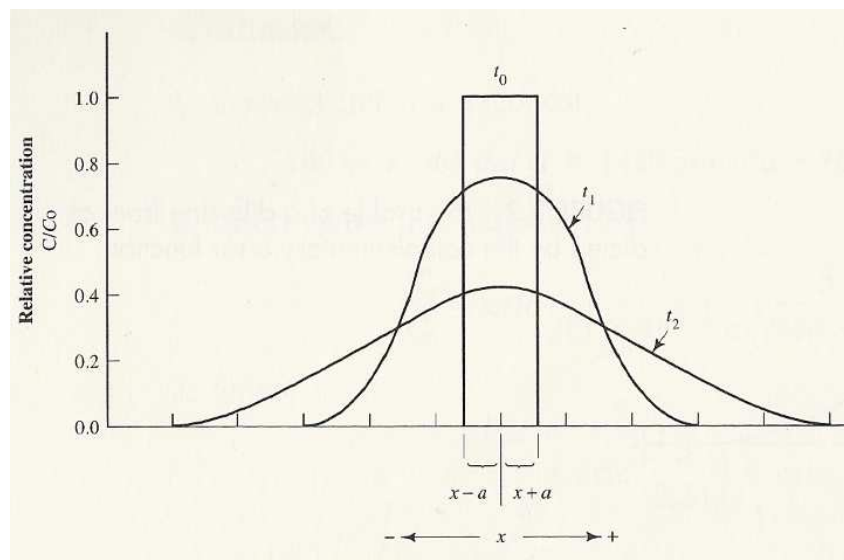


Figure 2.1 Spreading of a solute pulse with time (t), transport only due to diffusion. Solute pulse was injected into the aquifer at time t_0 with an initial concentration C_0 – reprinted from Fetter [1999]

Law describing diffusion based on the experimentally obtained results, has been published by Adolf Fick in his work “Über Diffusion” [On Diffusion, Fick, 1855]. From experimental data Fick established the relation that the mass of solute diffusing is proportional to the concentration gradient.

This relation is called Fick’s first law

$$F = -d_0 \left(\frac{\partial c}{\partial x} \right), \quad (2.1)$$

where F denotes mass flux of solute [$\text{mol}/\text{m}^2 \text{ s}$], d_0 is the molecular diffusion coefficient or diffusivity [m^2/s], c is the solute concentration [mol/m^3] and x is the length [m]. Negative sign on the right side of equation (2.1) indicates that a solute flux is from areas of higher concentration towards those with lower concentration.

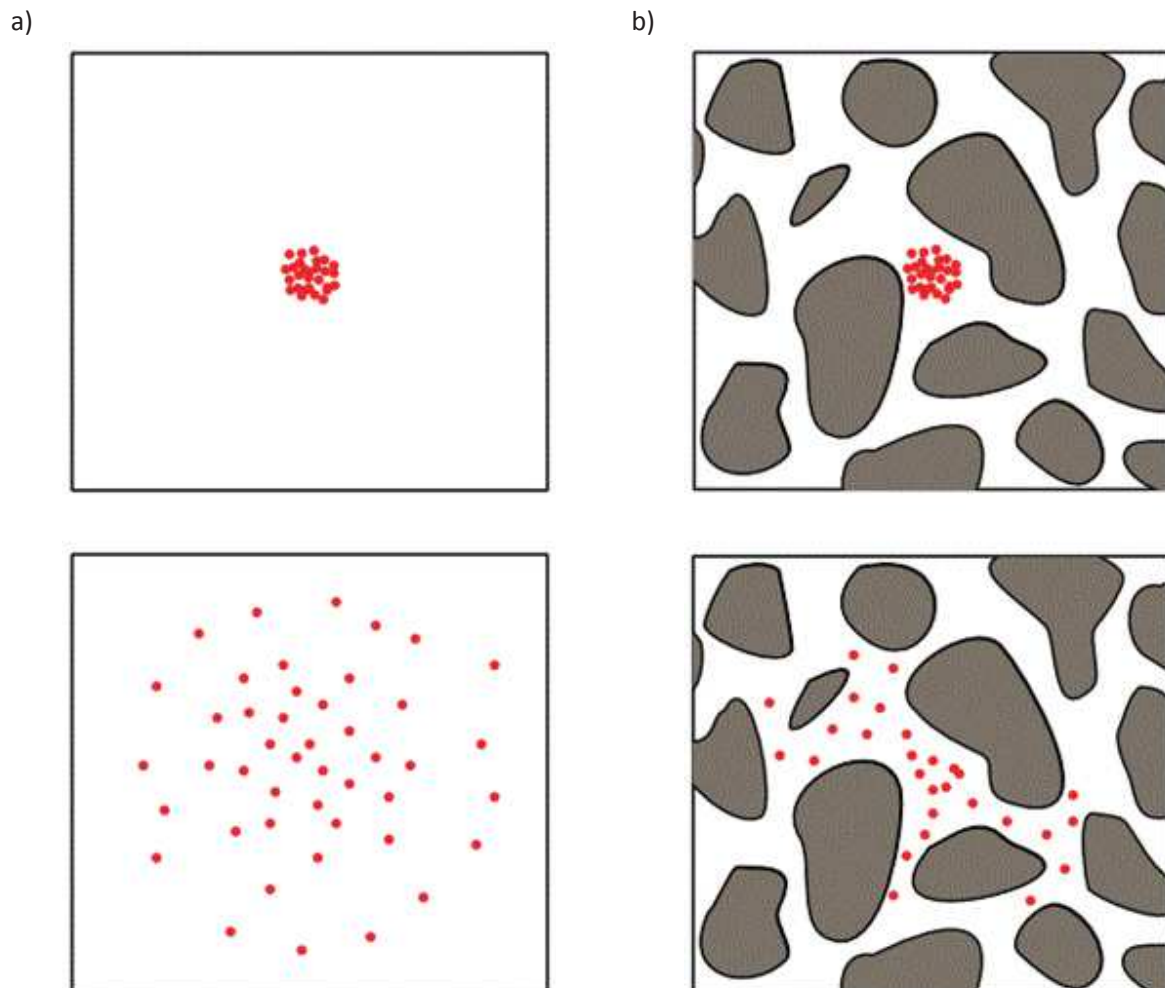


Figure 2.2 Illustration of diffusion a) free in space and b) in the pore space

Fick's second law predicts changes in the concentration with time (t) caused by diffusion

$$\frac{\partial c}{\partial t} = d_0 \left(\frac{\partial^2 c}{\partial x^2} \right). \quad (2.2)$$

Figure 2.2 illustrates the effect of the diffusion in liquids without any advection. In Figure 2.2 a) one can see spreading of particles in the space due to the concentration difference. However, spreading is mitigated in the porous media (Figure 2.2 b)), due to the complexity of the pore structure and smaller contact area between volumes with different concentrations. To account for slower diffusion in the porous media the molecular diffusion coefficient must be replaced by the effective diffusion coefficient ($d^{(e)}$) (detailed discussed in section 5.2.3)

$$d^{(e)} = \varpi d_0, \quad (2.3)$$

where ϖ is a coefficient related to the structure properties of the porous media (e.g. porosity, tortuosity..). The values of the diffusion coefficient d_0 in water for the main cations and tracer molecules range from $2 \cdot 10^{-10}$ to 10^{-9} m²/s.

2.2 Advective transport

Advection (or convection) is a process in which dissolved substances are carried along with the flowing water. It is easiest to imagine advection as a displacement of solute along the flow direction as illustrated in Figure 2.3. The total amount of transported solute is the function of its concentration and the total amount of flowing water. The total amount of flowing water is proportional to the average linear velocity and the effective porosity. The effective porosity ϕ_e consists of the interconnected pores in which water can flow. It is always lower than the total porosity since unconnected pores are excluded from the effective porosity. Because of the heterogeneity and anisotropy of pore network in rocks, the effective porosity can be different depending on the sampled volume and the geometry of the boundary conditions. We will see later that algorithms can be used to determine the connected porosity of imaged rock samples. The average linear velocity U_x is representing the velocity at which solute is transported through the porous medium; it can be calculated from the Darcy's law

$$U_x = \frac{k \Delta p}{\mu l}, \quad (2.4)$$

where k denotes permeability, μ fluid viscosity, p pressure and l is the distance between pressure observation points. The one-dimensional mass flux of solute F_x , due to advection can be calculated by equation (2.5):

$$F_x = U_x c. \quad (2.5)$$

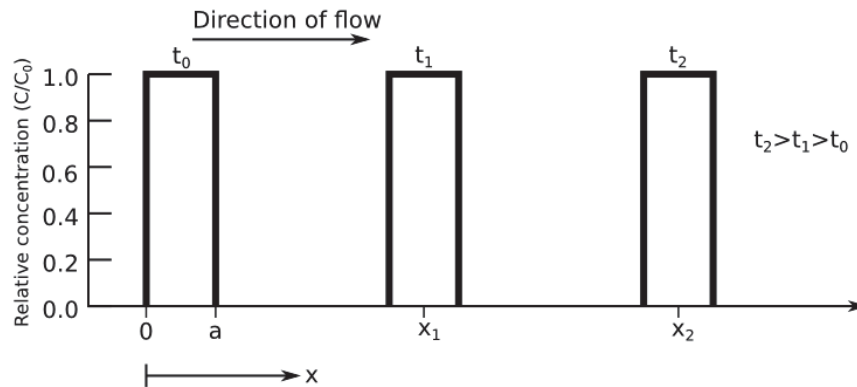


Figure 2.3 Illustration of advective transport in the porous medium with time. Solute pulse was injected at $x=0$ and at the time t_0 .

2.3 Asymptotic Fickian hydrodynamic dispersion

The illustration of a theoretical purely advective transport given in Figure 2.3 is made under assumptions that the flow field in the porous medium is homogeneous and that the diffusion is null. However, these assumptions are obviously not applicable to porous media. Water is moving through the porous medium at different rates using different flow path because of the heterogeneity of the pore-space (Figure 2.4). This causes hydrodynamic spreading of the tracer “particles”, while diffusion triggers tracer “particle” to jump from a given flow line to an (adjacent) other producing mixing.

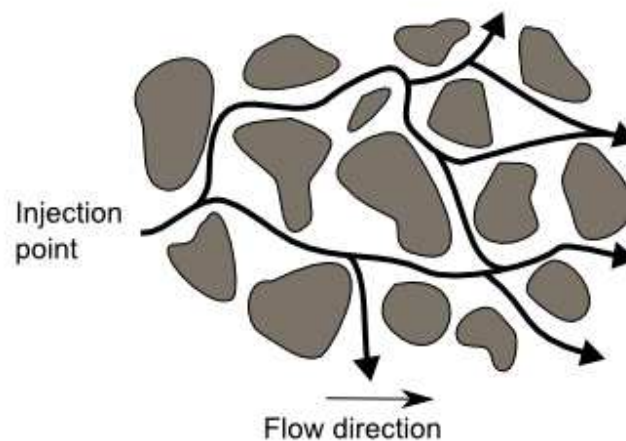


Figure 2.4 Illustration of different trajectories taken by solute traveling through the porous medium

The mechanical or kinematic dispersion is a common name for all mixing and spreading that happens due to advection (i.e parabolic velocity distribution in pores, different velocities in different flow paths and different lengths of flow paths covering same linear distance (Figure 2.5)). Elongation of the solute plume in the direction of flow is called longitudinal dispersion. Solute plume also have the tendency to spread in the directions normal to the flow direction. This happens due to diverging flow paths as illustrated on Figure 2.4. Spreading of the solute in the directions normal to flow-paths is called

transverse dispersion. Both longitudinal and transverse dispersion occur even in the most homogeneous porous medium, however spreading in the transverse direction is often 5 to 100 times less than in the flow direction [de Marsily, 1986].

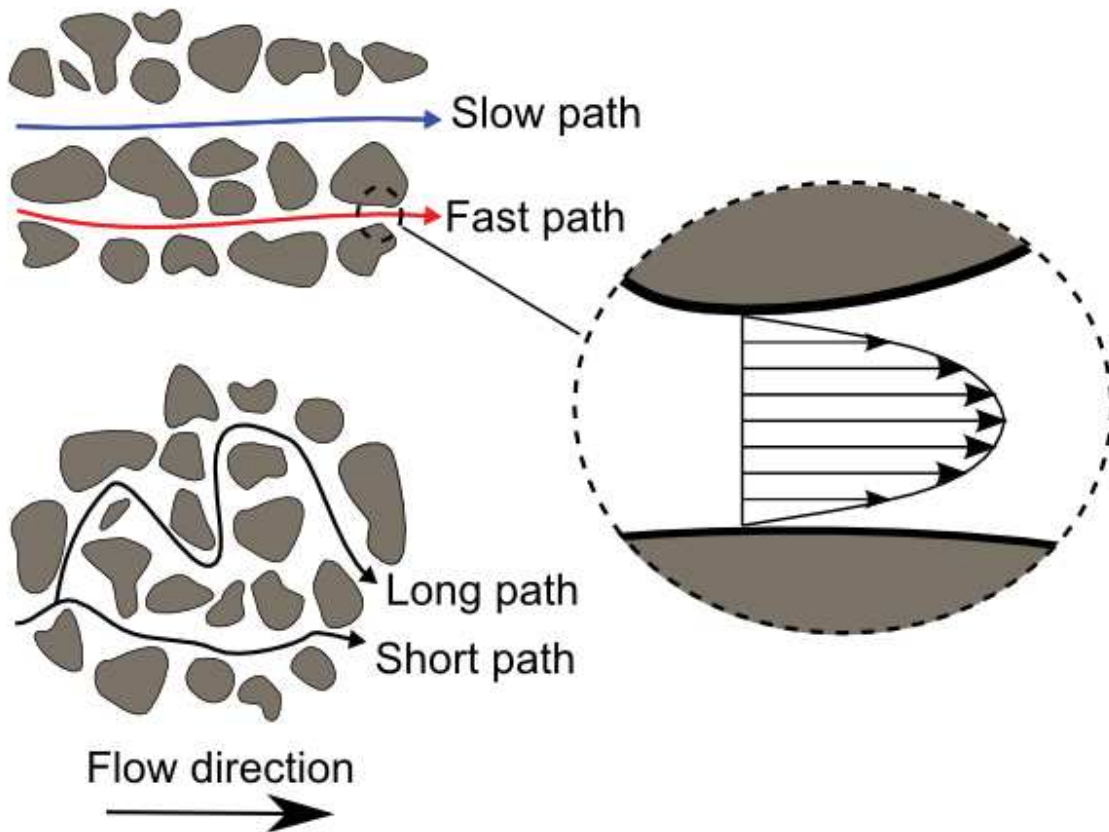


Figure 2.5 Illustration of the mechanical dispersion in the porous medium. On the illustration at the top, blue line denotes flow-path with lower velocity while red line denotes flow-path with faster flowing fluid. On the bottom image there is an illustration of two different paths taken by the solute, both paths have same starting and finishing points but the path length is significantly different. Magnified is example of the parabolic velocity distribution in one pore that causes Taylor dispersion.

However, dispersion in the porous media with flowing water is influenced by both diffusion and mechanical dispersion and they cannot be separated. Therefore both of these influences are defined together as hydrodynamic dispersion. Hydrodynamic dispersion coefficient as a function of mechanical dispersion and diffusion can be expressed as:

$$D_L = \alpha_L |U_x| + d^{(e)}, \quad (2.6)$$

$$D_T = \alpha_T |U_x| + d^{(e)}, \quad (2.7)$$

where D_L is the hydrodynamic dispersion coefficient in the direction of the flow, D_T is the hydrodynamic dispersion coefficient perpendicular to the flow direction, $d^{(e)}$ is the effective diffusion coefficient, α_L is

the dynamic dispersivity along the flow direction, α_T is the dynamic dispersivity transverse to the flow direction and U_x is the Darcy velocity.

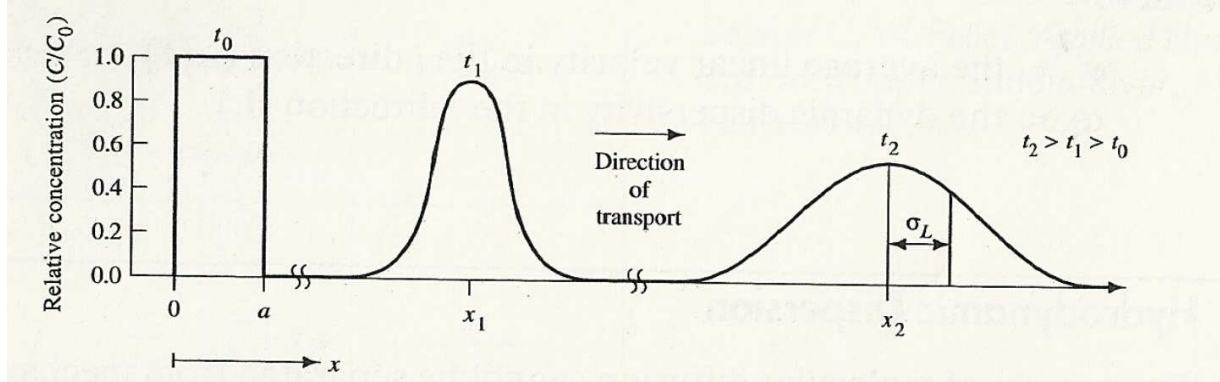


Figure 2.6 Illustration of the transport and spreading of the solute pulse in the porous medium with time, according to advection-dispersion theory. Solute pulse was injected at $x=0+a$ and at the time t_0 . Transported and spreading is due to advection and dispersion – reprinted from Fetter [1999]

Classically hydrodynamic dispersion in the homogeneous porous medium is described by the advection-dispersion equation (ADE) (2.8). The assumptions for the derivation of the ADE are that the porous medium is homogeneous, isotropic and fully saturated with fluid, also flow conditions have to be in the limits where Darcy's law is valid [Bear, 1972]. Macroscopically dispersion is assumed to be diffusion-like (Fickian) process (Figure 2.6). With the solute concentration c [g/m^3], the ADE is as follows

$$\phi \frac{\partial c}{\partial t} + \nabla \cdot (Uc) - \nabla \cdot (\mathbf{D}\nabla c) = 0, \quad (2.8)$$

where t denotes time [s], U is the macroscopic (Darcy) velocity [m/s] and \mathbf{D} is the dispersion tensor. The dispersion tensor expressed in its principal directions of anisotropy, is limited to three components

$$\mathbf{D} = \begin{pmatrix} D_L & 0 & 0 \\ 0 & D_T & 0 \\ 0 & 0 & D_T \end{pmatrix}, \quad (2.9)$$

while the average macroscopic velocity can be calculated from the Darcy's law by equation (2.4).

Two classical examples of interlaced influences of both diffusion and mechanical dispersion in the porous medium are Taylor and holdup dispersion. Taylor dispersion is a very simple and illustrative example of an evolution of the hydrodynamic dispersion starting as a pure mechanical dispersion and evolving due to the diffusion. First evidence of the dispersion due to the heterogeneity of a flow field in a capillary was published by Griffiths [1911]. However it was Taylor [1953; 1954] who mathematically described phenomenon later named after him.

Origin of Taylor dispersion is in the parabolic distribution of velocity in a capillary tube, given by Hagen-Poiseuille law

$$u(x) = \frac{\Delta p R^2}{l 4\mu} \left(1 - \frac{x^2}{R^2}\right), \quad (2.10)$$

where u denotes the velocity of the fluid in pores [m/s], x is the distance from the central axis of the tube [m], Δp is the pressure difference between tube ends, l is the tube length, R is the interior tube radius and μ is the viscosity of the fluid. Solute in the vicinity of the central axis travels significantly faster than one located near the boundaries. This causes spreading on solute plume in the longitudinal direction, but in the same time causing the difference in the concentration perpendicular to the flow direction. Due to this difference in the concentration solute starts to diffuse towards tube boundaries at the front edge of the solute plume and towards the central axis in back of the solute plume. Aris [1956] has extended Taylor's theory and proved that dispersion in a capillary tube will ultimately achieve Gaussian distribution if all conditions remain stable. Magnified area on Figure 2.5 shows parabolic velocity distribution that occurs in the pore.

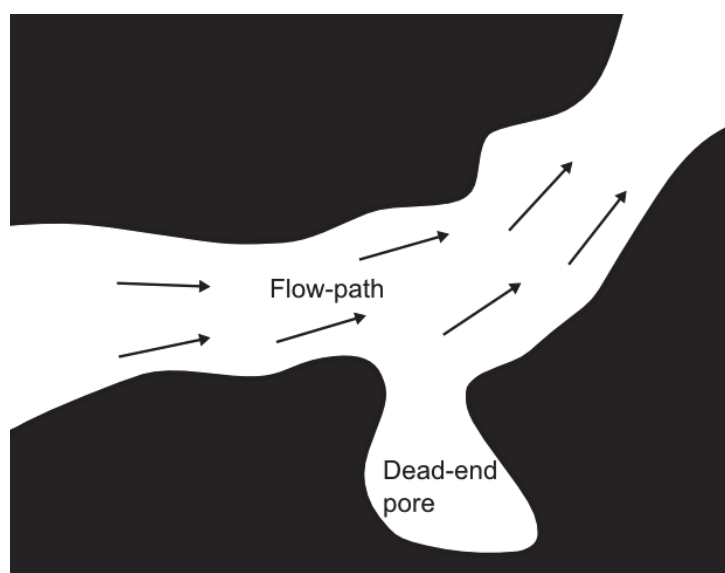


Figure 2.7 Illustration of dead-end pores in the natural porous medium

Hold-up dispersion is typical for the porous media. It is caused by solute diffusing into stagnant zones (e.g. dead-end pores). Stagnant zones are areas where there is virtually no fluid flow or where its velocity is negligible compared to the fluid velocity in the flow-paths. These zones exist in all porous media, even in the most homogeneous ones such as packed beads [e.g., Sederman et al., 1997; Reynolds et al., 2000], and their influence on the dispersion cannot be disregarded. Zinn et al. [2004] provides particularly nice visualization of influence of the stagnant regions over different transport regimes. Figure 2.7 illustrates typical dead-end pore. Solute is transported by convection through the flow-path and some particles diffuse into the dead-end pore. Particles which are in the stagnant zones can rejoin

flow path only by diffusion. Since diffusive transport happens from higher concentration to lower concentration, solute can diffuse back into the flow-path only when solute plume has passed. Also this release from stagnant zones is very slow due to small concentration difference.

2.4 Characterization of dispersion regime

Relative influence of the kinematic dispersion and diffusion on the hydrodynamic dispersion depends on the transport regime. Transport regime can be quantified by dimensionless Peclet number (Pe)

$$Pe = \frac{\bar{u}L}{d_0}, \quad (2.11)$$

where \bar{u} denotes mean microscopic velocity, L is the characteristic length and d_0 is the molecular diffusion coefficient. Relationship between dispersion coefficient and Peclet number has been established from experiments, exhaustive overview is given by Delgado [2007]. Based on these experimental results several authors defined five distinct transport regimes [e.g., de Marsily, 1986], corresponding to different relative influence of kinematic dispersion and diffusion. Some of experimental results are presented in Figure 2.8. On the same figure limits between different regimes are indicated with dashed lines. In each of these regimes empirical relation between longitudinal (D_L) and transversal (D_T) dispersion coefficients and Peclet number is found. Sahimi [1993] even gave approximate limits between regimes; however these limits are just tentative.

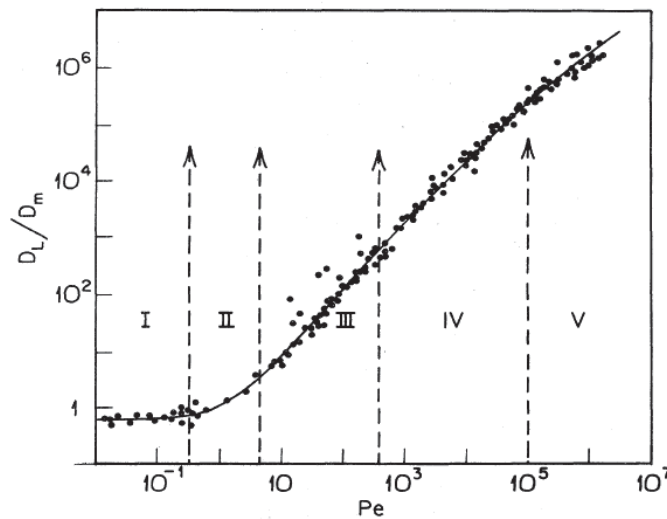


Figure 2.8 Experimental results showing relation between the longitudinal dispersion coefficient (D_L) and Peclet number (Pe). Dashed lines indicate limits between five different transport regimes – reprinted from Sahimi [1993]

- i) **$Pe < 0.3$** Pure molecular diffusion regime is characterized with very slow convection, and dispersion is almost completely controlled by diffusion. Since there is no convection the dispersion is isotropic and the dispersion coefficients are given by

$$\frac{D_L'}{d_0} = \frac{D_T'}{d_0} = \frac{1}{F_R \phi'} \quad (2.12)$$

where D_L' and D_T' are defined as

$$D_L' = \frac{D_L}{\phi} \quad \text{and} \quad D_T' = \frac{D_T}{\phi} \quad (2.13)$$

F_R is the formation factor, and ϕ is the total connected porosity of the medium. The formation factor F_R is a property that is originally defined from electrical conductivity measurements of fluid-saturated porous media. It is defined as the ratio of the resistivity of porous material, saturated with an electrolyte, to the bulk resistivity of the same electrolyte [Archie, 1942]. The ratio $1/F_R \phi$ is defined by the properties of the porous medium and commonly ranges between 0.15 and 0.7.

- ii) **0.3 < Pe < 5** Intermediate zone between pure diffusion and predominant kinematic dispersion, in which both convection and diffusion influences on the dispersion. In this regime the dispersion coefficient increases with increase of convection influences. To this day we still do not have valid formula that describes evolution of the dispersion coefficients in terms of the Peclet number in this transitory regime.
- iii) **5 < Pe < 300** This regime is characterized by predominant kinematic dispersion, however effect of diffusion cannot be neglected. Usually it is referred to as power-law regime since relation between the dispersion coefficients and the Peclet number are described by the empirical relations

$$\frac{D_L}{d_0} = \alpha_L Pe^{\beta_L}, \quad (2.14)$$

$$\frac{D_T}{d_0} = \alpha_T Pe^{\beta_T}, \quad (2.15)$$

where α_L and α_T [m] are known as intrinsic dispersion coefficients or dispersivity. Sahimi [1993] points out that the average values obtained from experiments are 1.2 for β_L and 0.9 for β_T . Saffman discovered existence of a diffusive layer near the solid surface; therefore, sometimes this regime is referred to as boundary-layer dispersion regime [Saffman, 1959].

- iv) **300 < Pe < 10⁵** For a porous medium that does not contain any stagnant zones (e.g., Figure 2.7) in this regime, transport is characterized as pure kinematic dispersion (i.e. completely dominated by convection). Due to negligible influence of diffusion, transport in this regime is usually referred to as mechanical dispersion, and the dispersion coefficient scales linearly with the Peclet number:

$$\frac{D_L}{d_0} = \alpha_L Pe, \quad (2.16)$$

$$\frac{D_T}{d_0} = \alpha_T Pe. \quad (2.17)$$

However stagnant zones exist in almost all porous medium, and actually contribute to the pore space with large percentage. Therefore application of power-law regime with its governing equations (2.14) and (2.15) is extended to this Peclet number range.

- v) $10^5 < Pe$ This regime is characterized by a turbulent flow, in contrast to the previous ones where a transport took place under laminar flow conditions. Kinematic dispersion is outside the domain where Darcy's law is valid. Since the flow turbulence also contributes to the dispersion, the dispersion coefficients depend on both Peclet and Reynolds numbers (see section 4.3.3 and equation (4.7)).

Yet, it is worth noticing that regimes *iv* and *v* are usually not encountered in natural systems, but may occurs very locally close to pumping well, for example.

2.5 Alternative Approaches

As mentioned earlier (Chapter 1) standard theory of transport in the porous medium fails to describe the real nature of dispersion for most of the natural conditions. Certainly the main issue is its inability to describe the effects of the flow field heterogeneity triggered by the more or less complex geometry of the porosity that occurs at virtually all scales. For a porous medium that one wishes to model at a given scale, there is always some scales below which heterogeneities are unresolved, and several studies stressed that these unresolved heterogeneities can have a key influence on the overall transport behavior [Berkowitz et al., 2006]. Consequently the use of average local properties (e.g., mean velocity and dispersion) measured at the modeling scale seems to be unjustified.

This led to the development of alternative models. Most of these models are based on non-local-in-time representations of hydrodispersive transport to take into account the fact that local mixing and spreading at a given time depend on previous conditions. The models closest to the "classical" ADE model are stochastic ADE models [e.g., Morales-Casique et al., 2006]. They are based on the premises that the transport can be accurately described at a given scale and that non-Fickianity arises from time and space depended fluctuations of the flow and transport properties. Averaging over an ensemble of velocity fields results in the representation of the non-Fickian transport behavior. Similarly Lagrangian framework models [e.g., Cushman and Ginn, 1993] average the solute particle motion over a random velocity field. Transport is then modeled by the ensemble average of nonlocal space-time representations. Non-local in space models have been developed for simulating long range correlations using for instance fractional ADE models [e.g., Benson et al., 2000]. Yet, the most used framework are the multi-rate mass transfer (MRMT) models (section 2.5.1) and the continuous time random walk (CTRW; section 2.5.2) that will be also at the center of the works presented in this document. Readers are directed towards detailed overviews given by Berkowitz et al. [2006] and Neuman and Tartakovsky [2009] for additional details on the non-Fickian transport model theories; in the following MRMT and CTRW approaches will be briefly presented.

2.5.1 Multi-Rate Mass Transfer Model (MRMT)

Molecular diffusion from the water-flowing portion of porous media to the stagnant zones (i.e. matrix diffusion) has been recognized and widely cited as a critical transport mechanism controlling the residence time. Prolonged residence time (e.g. tailing observed in the BTCs) is one of the most recognizable features of the anomalous transport. This premise led to development of simple transport models to account matrix diffusion, which can be divided into two main groups, first-order mass transfer models [e.g., Coats and Smith, 1964; van Genuchten and Wierenga, 1976] and rate-limited mass models [e.g., Rao et al., 1980; van Genuchten et al., 1984]. In both cases mass transfer between mobile and immobile domain is simulated with a single mass transfer type and rate at the time. Mathematically mass transfer is coupled with standard advection-dispersion equation by adding sink/source term. However in porous medium there is a large variety of different immobile domains (e.g. microporosity, stagnant zones, sorption...) with different properties and geometry (Figure 2.9a). Thus, they cannot be represented with a single mass transfer rate.

The MRMT models allow numerous types and rates of mass transfer to occur simultaneously [Haggerty and Gorelick, 1995; Carrera et al., 1998] as illustrated on Figure 2.9b. The mathematical expression of MRMT model is similar to his simpler predecessors. Moreover it has been demonstrated that spherical, cylindrical and layered diffusion models are just a special case of the MRMT model. The main difference is in the formulation of the sink/source term that accounts for the effect of the immobile domain. Usually mass transfer between mobile and immobile domain is modeled by linear mass exchange process, which can be expressed as the convolution product of a time dependent variations in concentration in the mobile domain and the memory function. The memory function (expressed as the inverse of time and noted hereafter $G(t)$) is a time-dependent function that denotes the intrinsic transport property of the immobile domain.

As stated earlier basic equation expressing the average solute concentration in the mobile domain (c_m) is standard ADE equation with added sink/source term (S), representing mass transfer between mobile and immobile domain [Carrera et al., 1998; Haggerty et al., 2001]

$$\xi_m \frac{\partial c_m}{\partial t} = \nabla \cdot (\mathbf{D}\nabla c_m) - U\nabla c_m - S, \quad (2.18)$$

where ξ_m denotes the volume fraction of the mobile domain which is equivalent to the macroscopic porosity (important to remind that this is only water-flowing portion of the porosity), t is the time, \mathbf{D} is the dispersion tensor and U is the Darcy velocity [m/s]. The sink/source term for linear mass transfer processes can be expressed as a convolution with the memory function (M):

$$S(\mathbf{x}, t) = \xi_{im} \frac{\partial}{\partial t} \int_0^t c_m(\mathbf{x}, t') M(t - t') dt', \quad (2.19)$$

where ξ_{im} denotes volume fraction of immobile domain (microporosity, dead-ends, stagnant and trapped water).

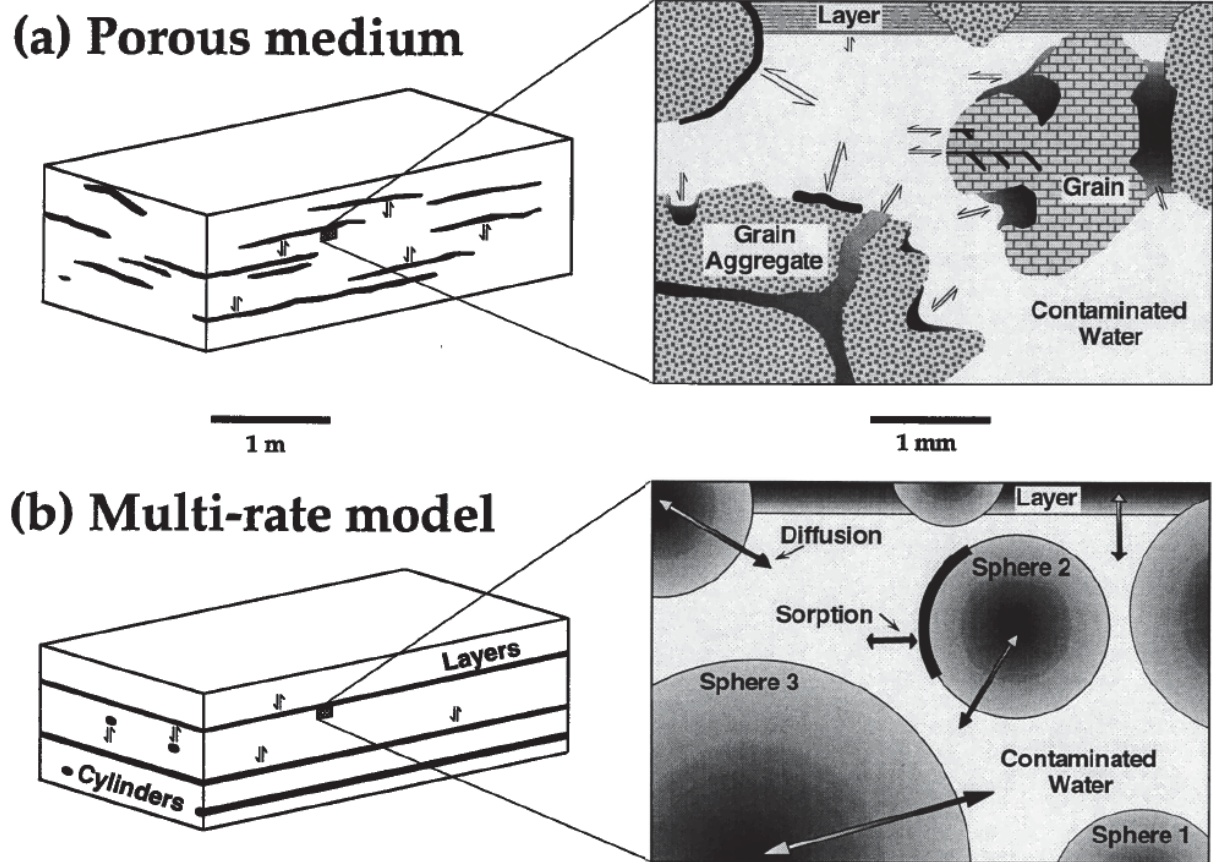


Figure 2.9 a) Illustration of “natural” heterogeneous porous medium with solute exchange between different phases indicated by arrows. Left image presents mass transfer between zones with different permeability (slow and fast flowing zones) and right presents mass exchange on the pore scale between porosity with different flow regimes (i.e. diffusion between stagnant and flowing zones), microporosity (e.g. clay pockets) and surface sorption. b) Illustration of different mass exchange processes incorporated in one multi-rate mass transfer model designed to simulate different mass exchange principles that happen in nature. – reprinted from Haggerty and Gorelick[1995]

The memory function depends on the properties of the immobile domain and specifically its heterogeneity. Heterogeneously distributed immobile domains with different mass transfer rates (λ) can be replaced with the homogeneous immobile domain with the probability distribution of the mass transfer rate ($P(\lambda)$). $P(\lambda)$ expresses the probability that the particle is in the immobile domain in a given time interval, generally it is controlled only by the volumetric distribution of the immobile region. Diffusive transfer rate between mobile and heterogeneous immobile domain is given by weighted average over the local memory function ($W(t, \lambda)$) [Haggerty et al., 2000].

$$M(t) = \int_0^{\infty} P(\lambda)W(t, \lambda)d\lambda. \quad (2.20)$$

Several authors have successfully used MRMT model to fit experimental data, trying to connect memory function with measurable rock properties [e.g., Haggerty et al., 2001; Haggerty et al., 2004;

Gouze et al., 2008b; Berkowitz et al., 2008]. However, the link between intrinsic properties of the rock and memory function is still debated. This is not surprising, knowing that mass transfer rate depends on many different factors, which contribution cannot be separated and evaluated individually. The MRMT class of model was developed for systems where it is possible to assume that two distinctly different transport modes coexist: a mobile domain (advection dominant) and an immobile domain (diffusion). In general these domains correspond to physical regions of the porous media (e.g., macroporosity and porous cement). Attempts have been made to use this approach to model the effects of the flow field heterogeneity, which means that the mobile and immobile volume fractions depend on the Peclet number [Liu and Kitanidis, 2012]. However, the justification of distinguishing a purely advective domain and a purely diffusive domain from a continuous distribution of velocities seems difficult and we should restrict the use of MRMT for cases where mobile and immobile domains can be clearly distinguished.

2.5.2 Continuous Time Random Walk (CTRW)

The CTRW framework has demonstrated an ability to successfully characterize non-Fickian transport behavior at different scales, as well as in both porous and fractured medium [e.g., Berkowitz et al., 2000; Cortis and Berkowitz, 2004; Le Borgne and Gouze, 2008; Cortis and Birkholzer, 2008; Kang et al., 2015]. It is a probabilistic approach, which uses the random walk framework to mimic particle transport in heterogeneous media. It describes a path as a series of successive uncorrelated random steps with no direct link to any geometrical or physical support. Continuous time was first introduced by Montroll and Weiss [1965] for modeling diffusion on lattice.

The CTRW framework aims at modeling anomalous transport in heterogeneous media. It is a random walk approach in which both space and time increments are random variables. Formally, the particle transitions depends on a joint probability (pdf) $\psi(\mathbf{s}, t)$ of the transition times, where \mathbf{s} denotes the position and t the time, but it is classically assumed that for hydrodynamic transport the decoupled form $\psi(\mathbf{s}, t) = \zeta(\mathbf{s}) \psi(t)$, where $\psi(t)$ is the probability rate for a transition time t between two sites. Detailed overview of the CTRW theory and mathematical framework is given in Berkowitz et al. [2006] and here we will present only the most important features.

Using the decoupled form presented above, the CTRW transport equation can be written in Laplace space:

$$\lambda \tilde{c}(\mathbf{s}, \lambda) - c_0(\mathbf{s}) = -\tilde{M}(\lambda) [\mathbf{v}_\psi \cdot \nabla \tilde{c}(\mathbf{s}, \lambda) - \mathbf{D}_\psi \cdot \nabla^2 \tilde{c}(\mathbf{s}, \lambda)], \quad (2.21)$$

where the sign \sim denotes the Laplace transform, λ is the Laplace variable, \mathbf{v}_ψ and \mathbf{D}_ψ are the apparent velocity vector and dispersion tensor respectively (both being respectively different from the average velocity and Fickian dispersion), and \tilde{M} is a memory function which depends on λ , $\tilde{\psi}(\lambda)$ and some transition time characteristics [Berkowitz et al., 2006 and references therein]. Note that in equation (2.21), c denotes the total concentration while the equation (2.18) written for the MRMT model gives the solution for the mobile concentration c_m . The common form for \tilde{M} is [e.g., Bijeljic et al., 2011a]:

$$\tilde{M}(\lambda) = \lambda \tau \frac{\tilde{\psi}(\lambda)}{1 - \tilde{\psi}(\lambda)}, \quad (2.22)$$

with τ a single characteristic transition time. Truncated power law for $\psi(t)$ is often used to model anomalous dispersion but other expressions for \tilde{M} and $\psi(t)$ can be investigated (see section 5.3). Note that for $\tilde{M}(\lambda) = 1$, i.e. an exponential form of $\tilde{\psi}(\lambda)$, the Fickian dispersion model (ADE Equation (2.8)) is retrieved. By performing inverse Laplace transform of Equation 22 one can obtain time domain transport equation:

$$\frac{\partial c(\mathbf{s}, t)}{\partial t} = - \int_0^t M(t - t') [\mathbf{v}_\psi \cdot \nabla c(\mathbf{s}, t') + \mathbf{D}_\psi \nabla^2 c(\mathbf{s}, t')] dt'. \quad (2.23)$$

As mentioned earlier, the transport behavior in the CTRW framework is controlled by the functional shape of the pdf. It depends on the probability rate of the transition times. For instance, a power law distribution of transition times may be used to model power law tailed breakthrough curves. In this case, CTRW formulation is mathematically equivalent to the MRMT approach [Dentz and Berkowitz, 2003; Schumer et al., 2003]. The numerical implementation of the 1D CTRW for modeling flow velocity heterogeneity and mobile-immobile mass transfers are detailed in section 5.3.

Chapter 3

Tracer experiments

3.1 Introduction and objectives

Experiments enable to observe natural behaviors in more or less controlled environments. Large scale experiments provide irreplaceable information source on transport as it happens in nature. However, they are long lasting, expensive, and often difficult to interpret because of the superposition of natural flow and the poor knowledge of the true reservoir heterogeneity. On the other hand laboratory experiments provide valuable insight into natural process with an ability to isolate different effects contributing the dispersion and usage of the well-known and investigated media. Laboratory experiments can in theory be performed under strictly regulated conditions, eliminating side effects that may lead to the misinterpretation of the results. Nevertheless, these objectives are often difficult to reach in practice and require quite sophisticated measurement equipment and protocols to minimize dispersion due to the experimental setup itself for instance. Also, it is important to perform tracer test over several order of magnitude in concentration to obtain a pertinent characterization of the non-Fickian dispersion behavior that is contained in the BTC tailing (i.e. at long time and for low concentration).

In this chapter we present series of 1D-like experiments performed on glass beads columns and Berea sandstone cores. The aim is to investigate tracer (pre-asymptotic) dispersion through relatively simple and well described porous media. Variations in the porous media structure, flow rate and experiment type (flow-through or push-pull) allows to distinguish contributions of different natural processes on the hydrodynamic dispersion.

3.2 Experiment setup

The experimental circuit is designed to support both flow-through and push-pull experiments without any changes in the circuit when changing experiment type. Actually the only part that needs to be changed between experiments is the sample and the protective cell around it when changing porous media type.

Experimental circuit layout is presented in Figure 3.1 and all components are detailed described in following subsections. Water is pumped into the circuit with two piston pumps, passes through tracer injection point, sample core and out of the system. Arrows indicate the direction of flow for different experiment stages. Blue arrows indicate flow direction in part of the circuit where flow direction is always the same, green arrows indicate flow direction during flow-through experiment and pull phase of push-pull experiment, while red arrows indicate flow direction during push phase of push-pull experiment. TELog is a high resolution optical sensor presented in details in subsection 3.2.5. It is installed below the experimental cell directly at the outlet from porous media. Data recording and TELog management is performed by personal computer which communicates with TELog through USB controlled signal converter.

In flow-through experiments water arrives at the top of the sample. Here we inject tracer at the injection point using micro-syringe to precisely dose trace volume and time of injection. It is important

not to inject too fast in order not to significantly disturb flow field. Solute then passes through porous media and outlet concentration is measured by TELog. For first (push) phase of push pull experiment flow direction valve is placed in position to direct flow at the bottom of cell. There is another injection point just between the TELog and the sample. Tracer is pushed for a period of time depending on flow rate, permeability and length of sample in order to investigate as much as possible of the porous media without any tracer leaving from porous media on the other side. At the end of the push period, the control valve is switched and water starts to flow from the top of the sample like in flow-through experiment. In order to emphasize dispersion due to diffusion in some experiments, we turned off the pumps for several minutes between push and pull phase.

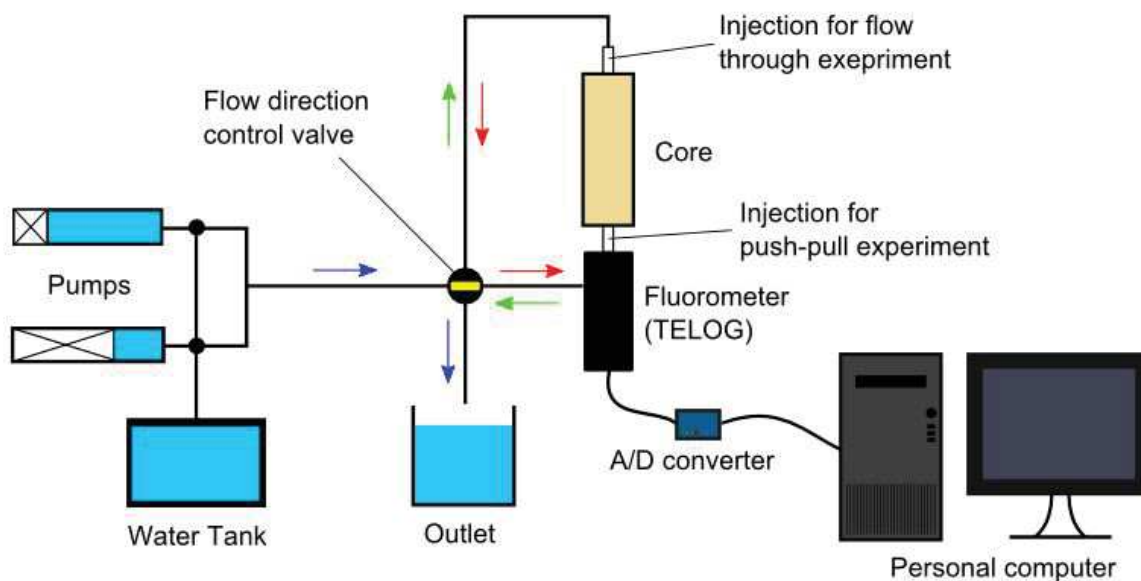


Figure 3.1 Schematic diagram of the experimental test-bench circuit layout with arrows indicating flow direction. Blue arrows – permanent flow direction; green arrows – flow direction for flow-through experiment and pull phase of push-pull experiment; red arrows – flow direction during push phase of push-pull experiment

3.2.1 Pumps

The main demand imposed for the pumps was to have constant flow rate without any fluctuations of chosen flow rate over several weeks. Two R2N piston pumps equipped with solenoid valves were chosen. Normally only one pump is used to inject water in the system while other one is waiting full or being recharged. When a pump is almost empty it starts to slow down the piston and decrease flow rate, at the same moment the other pump starts to move its piston maintaining combined flow rate from both pumps equal to chosen flow rate. The ratio in cumulated flow rate is being gradually increased in favor of the second pump until the first pump is completely stopped and the second pump takes over entire flow rate. First pump is being recharged and put in waiting for process to repeat.

Pumps are operated by acquisition program developed in LabVIEW by Richard Leprovost, mechanical engineer in the TMP team. Program monitors and controls pump status (on/off), position and speed of piston (controlling flow rate and recharge of pumps), status of the valves (open/closed). All relevant data are displayed on computer in real time.

Both pumps are exactly the same with internal diameter of 35,685 mm (cross section area 1000.14 mm²) and operating range from 1 to 500 cm³/h. Pumps calibration was performed at the beginning of the experiment to ensure that the actual flow rate is exactly the same as the imposed one.

3.2.2 Experimental materials and procedures

In this work we performed tracer experiments on both artificial (glass beads packing) and natural (Berea sandstone) porous media. Sample cell is designed to perform both flow-through and push-pull experiment and as well that changes between samples can be done fast and simple. As it can be seen in Figure 3.3 a) cell is placed vertical with injection points on the top and on the bottom. Measuring unit (TELog – details in section 3.2.5) is located directly at the bottom inlet/outlet of the sample.

Glass beads used in these experiments are originally intended for industrial application. Therefore, distribution of their diameter is relatively wide. To narrow glass beads diameter distribution we performed sorting process. The sorting process is performed on the vibrating sorting machine (Figure 3.2 b)), where sieves are positioned one above the other in order that upper sieve always has larger openings in the mesh. Glass beads are poured on the top sieve and beads smaller than openings in the mesh drop to lower sieve until they reach sieve with openings smaller than their diameter. Vibrations of the machine assist in the sorting process. At the end of the sorting process remaining beads on each sieve have diameter smaller than openings on the previous (top) sieve and smaller than openings on the sieve they are found on. Chosen glass beads for these experiments have diameters between 355 and 400 μm. Column filling with glass beads is made underwater with regular vibrations to ensure optimal homogeneous packing, as low as possible void content and to avoid air pockets (Figure 3.2 c)). First experiments to validate experimental procedure and bead packing were performed with the transparent coating (Figure 3.2 d)). Transparent coating in combination with high concentration tracer allowed monitoring tracer plume movement through the packed beads. During these experiments no side flow or other anomalous behavior was observed. However, the experiments for which results are presented in the section 3.3 were performed on the column with non-transparent coating to prevent light pollution of measurement and tracer decay due to light. Non-transparent cell used in the experiment is made of plastic material and by design is similar to one used for Berea sandstone cores (Figure 3.3 a)) except it does not have opening to apply external pressure. Both sides of cell are closed with thin highly permeable seals made of glass material.

Berea sandstone core was extracted from a block that is apparently homogeneous at centimeter scale. Core has 18 mm diameter and is 15 cm long (Figure 3.3 d)). Before placing core into the cell it has been coated with thermo-plastic material to prevent side flow. Procedure consists of placing core into “raw” thermo-plastic material which is later heated with heat gun. During heating process thermo-plastic material shrinks and adheres to a core, final result is presented in Figure 3.3 d)). Prepared core is

placed into metal coating and installed vertically on top of the TELog. A confining pressure (about 3 bar) is applied to the thermo-plastic jacket in order to prevent any leakage at the rock-jacket interface.

a)



c)



b)



d)

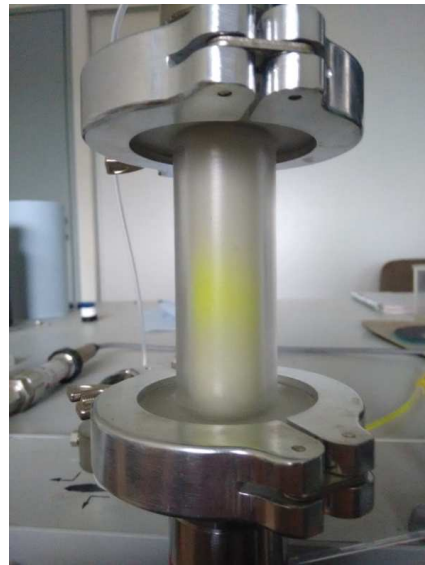
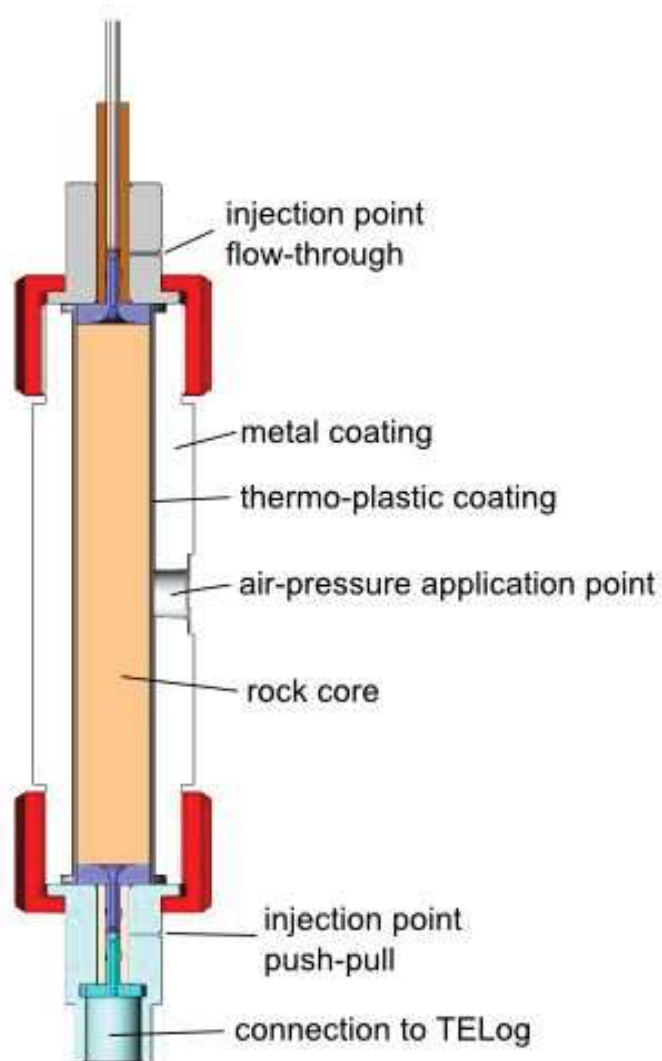


Figure 3.2 Different stages of glass bead column preparation for the experiments. a) microscopic image of glass beads; b) sorting machine at the Geosciences Montpellier laboratory and one of the sieves; c) underwater column filling with sorted glass beads; d) experiment on the transparent column with high fluorescein content in the tracer to visual check for side flow and other anomalies

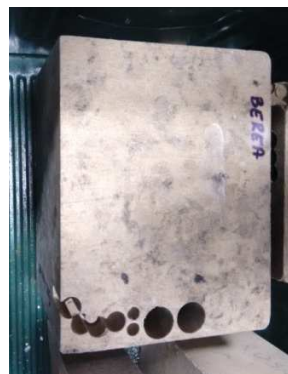
Measurement of TELOG can be impaired by several factors such as light pollution or changes in chemical composition of the water. The design of experimental cells and TELog provide good protection from light pollution and in order to ensure that water properties stayed the same during the whole experiment we used bottled water. We used “Eau de Source de montagne d’Auvergne” available in

French supermarkets. This water (pH is 7,3 and dry residual at 180°C is 52,2 mg/l) has a composition that prevent any chemical reaction with the studied material and specifically the cement material that are present in the Berea sandstone.

a)



b)



c)



d)



Figure 3.3 Cross section through experimental cell for laboratory tracer experiment (a) and different stages of preparing core samples; b) Berea sandstone block from which core is extracted; c) coring machine at Geosciences Montpellier laboratory and d) on the left Berea sandstone core and on the right same core coated with thermo-plastic coating

3.2.3 Tracer injection point

Injection of tracer is designed in order to minimize dispersion before tracer reaches the sample and in the same time to prevent disturbance in the flow. Figure 3.4 presents the cross section through the injection part installed at the top of the cell. The injection is made with a micro-syringe at injection point placed between tube 1 and diffuser. Needle (diameter 0.7 mm) penetrates through tube 2 which has an internal diameter exactly the same as the external diameters of tube 1 and diffuser. It is made of very dense rubber foam which self-closes the micro-hole after the needle is removed to prevent leakage from the system. Diffuser spreads just before the top of the sample ensuring that tracer can penetrate on the whole surface of the sample. At the cell bottom there is a similar device (with same working principle) for performing the injection during push-pull experiments.

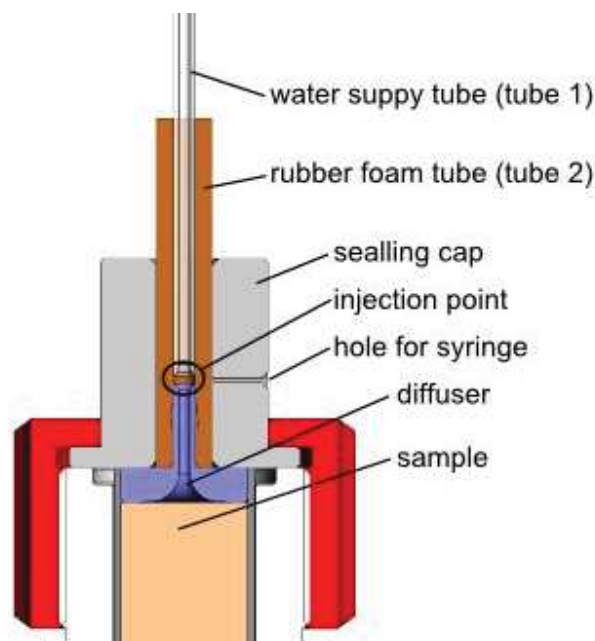


Figure 3.4 Schematic cross-section of injection part at the top of the cell with labeled essential parts

3.2.4 Fluorescein

Fluorescein is a synthetic organic compound frequently used in hydrogeological experiments. Usually we can find it in a form of disodium salt which is dark red powder also known as “uranin” or D&C Yellow no.8. Even small amount of fluorescein dissolved in the water gives a green color to the solution, while solutions with high fluorescein concentration are colored in orange or red (Figure 3.5). Although organics, sunlight and some chemicals can impair intensity of the dye it is one of the best non-toxic conservative tracers used for tracing of water pathways. A reason of its popularity and wide application is that its presence can be detected up to 0.001 $\mu\text{g/L}$ [Gaspar, 1987]. From chemical point of view fluorescein has only negative functional groups which mean that there is almost no sorption on negatively charged surfaces such as silica sand and sandstones [Kasnavia et al., 1999].

Measurement of fluorescein is based on intensity and wavelength distribution of emission spectrum after excitation by a certain spectrum of light [So and Dong, 2002]. In water, fluorescein has an absorption maximum at 494 nm and emission maximum of 521 nm. The molecular diffusion coefficient of fluorescein in water is $6.4 \times 10^{-10} \text{ m}^2/\text{s}$ [Galambos and Forster, 1998].



Figure 3.5 Fluorescein in various forms, on the right is disodium salt which is also known as “uranin” and on the left is dissolution in the water with typical bright green color.

For our experiment we can consider fluorescein as an ideal tracer since it has been proven that sorption can be neglected on positively charged surfaces, both glass beads and sandstones are positively charged. Density effect will be investigated in detail during the experiments.

3.2.5 The TELog sensor

TELog is a high resolution optical sensor primarily developed for field usage [Gouze et al., 2009]. It is in fact a special kind of fluorometer designed for continuous measurement of very low fluorescein concentration. Ability to measure at low concentrations is essential when studying dispersion of a passive tracer in order to avoid density effect and still be able to measure concentration over several orders of magnitude.

Measurement is based on the specific wave lengths absorbed and re-emitted by fluorescein. Figure 3.6 displays a schematic representation of the TELog head. Blue led is emitting short light pulses (less than 3 ms) every 10 ms, this light pulses passes the filter that filters all light with different wave length than $485 \pm 10 \text{ nm}$. Light beam then passes through the glass tube where the solute is flowing at the outlet from the sample. Fluorescein in the solute absorbs light and re-emits it. Re-emitted light passes through a second filter that eliminates all light with different wave length than $530 \pm 10 \text{ nm}$. Filtered light is detected by photomultiplier and the signal is processed by a computer. The TELog is operated by an acquisition software developed using LabVIEW by Olivier Maudens, electrical engineer in the TMP team. The sensitivity of the photomultiplier is defined by 8 pre-programmed scaling factors (gains). Starting from the lower gain value applied to the photomultiplier, the LabVIEW code determines incrementally the optimal gain to obtain the best sensitivity of the photomultiplier; the principle is explained in details in the section 3.2.6.

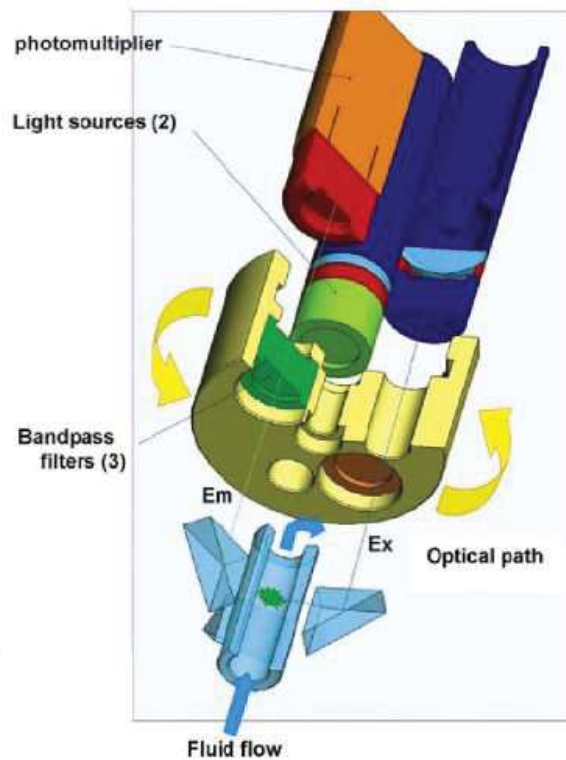


Figure 3.6 Schematic representation of the TELog measurement head displaying optical path - reprinted from Gouze et al. [2009].

Experiment stability and reproducibility is a very important issue. The use of bottled water, the stability of light source and the accuracy of the flow rate eliminates most of external factors that could cause false readings in final data. Furthermore the black signal (i.e. measure of the photomultiplier response without being illuminated) is used to monitor and correct if necessary light pollution coming from external light source and for the value of the dark signal of the photomultiplier.

3.2.6 TELog calibration and data readings

The photomultiplier installed in TELog detects light that passes through the tube containing fluid at the outlet of the sample. According to the light intensity and wavelength the photomultiplier produces different output voltage. To establish correlation between output voltage and fluorescein concentration we performed calibration. During the calibration process we injected solutions with known fluorescein concentrations and measured the output voltage.

The first step of the calibration process was to produce a set of solutions with known fluorescein concentrations. Solution concentrations are chosen in order that they cover the whole range of values that are expected to be measured (from 1ppm to 1ppt) and that they give enough information to enable interpolation values in between while keeping reasonable number of solutes. First solution is made by adding fluorescein in powder into the pure water.

Solute concentration (C_0) is calculated by equation:

$$C_0 = \frac{w_f}{w_{H_2O}}, \quad (3.1)$$

where w_f denotes the mass of the fluorescein and w_{H_2O} the mass of the water. The first solution had concentration of 1000 ppm and from this we produced first master solution C_1 . Second master solution C_2 is produced from C_1 ; all other solutions are produced from these two masters (as illustrated on Figure 3.7). Since new solutions are obtained by dilution from existing solutions rather than by adding fluorescein into the pure water, their concentration is calculated by equation:

$$C_x = \frac{w_f}{w_{ms} + w_{H_2O}}, \quad (3.2)$$

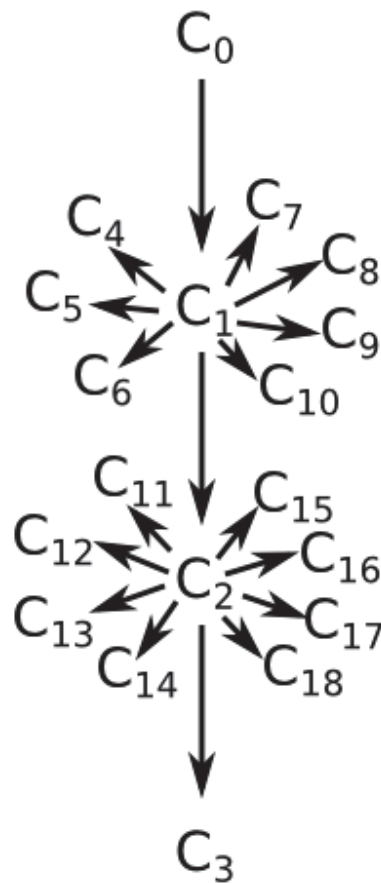
where C_x denotes the concentration of resulting solute, w_f is the mass of fluorescein in the master solute and w_{ms} is the total mass of the master solute. In order to facilitate calculations, in equation (3.2) the fluorescein mass is substituted by solute concentration, this gives equation (3.3)

$$C_x = \frac{\frac{w_{ms}}{(1 + 1/C_{ms})}}{\frac{w_{ms}}{(1 + C_{ms})} + w_{H_2O}}, \quad (3.3)$$

where C_{ms} denotes the concentration of master solution. Advantage of the approach with few master solutions to the approach where each solution is obtained by dilution from the first stronger solution is in minimizing cumulative errors and avoiding that the whole series of solutions have wrong concentration due to one mistake. However it requires more attention and very precise scales since resulting concentrations are up to 3 orders of magnitude lower than master concentrations. In order to meet these requirements we used two digital scales with different maximal load and precision. First one is Precise LX220a with the maximal load up to 220g and the precision of 0.001g. Second one covering all weights higher than 220g is Kern EG 2200-2NM with the maximal load up to 2200g and the precision of 0.01g. Made solutions are kept closed in bottles impermeable to light to prevent fluorescein decay due to light.

The calibration procedure consisted in injecting solutions directly into TELog and then flushing it with pure water and drying a tube with air. Solutions were injected starting from the lowest concentration towards highest ones. Each solution is injected three times with 7 minutes of the resting period in between, resulting in a total time of 21 minutes during which measurements were recorded. In the calibration mode TELog records a value every 3 seconds at different gain (i.e. different sensibility of photomultiplier). Recorded value is an average of 30 measurements made each 0.1s at the same gain and then TELog shifts to another gain. Injections every 7 minutes were made to prevent decay of the fluorescein concentration due to light effect, however no decay was observed even for the lowest concentrations. After each injection the system was flushed with pure water for 35 minutes, to remove all fluorescein from the system including some that may be trapped in the dead zones. After flushing,

the entire system is dried with compressed air. Drying phase is important since the injected volumes were relatively small and residual drops of water could significantly dilute the injected solution.



C_0	1000 ppm
C_1	1 ppm
C_2	1 ppb
C_3	1 ppt
C_4	500 ppb
C_5	100ppb
C_6	50 ppb
C_7	20 ppb
C_8	10 ppb
C_9	5 ppb
C_{10}	2 ppb
C_{11}	750 ppt
C_{12}	500 ppt
C_{13}	250 ppt
C_{14}	100 ppt
C_{15}	50 ppt
C_{16}	20 ppt
C_{17}	10 ppt
C_{18}	5 ppt

Figure 3.7 Schematic illustration of master concentration and its diluted products with list of all solutes concentrations.

Measured tension for different TELog gains at different fluorescein concentrations obtained during calibrations process are presented on Figure 3.8. Symbols present measured values, while lines are fitted functions for each gain used to process experimental results.

While in calibration mode tension is measured for all gains, during the experiment TELog was working in standalone mode that was always trying to achieve optimal photomultiplier sensitivity (optimal gain). Optimal photomultiplier sensitivity is achieved between 0.3 and 1.5 V (dashed red lines in Figure 3.8). In this range there is a power law relation between fluorescein concentration and output voltage with relatively small oscillations. A measurement begins with the lowest gain 1 (lowest photomultiplier sensibility) and switches to higher gain if output voltage is lower than 0.3V. Only exception is the highest gain 8 in which there is no lower limit. If during the experiment at any gain (except gain 1) output voltage exceeds 1.5V measurement is switched to gain with lower sensibility. Unlike calibration mode, in the standalone mode output is given as recorded values immediately registered every 0.1 s at given gain, without any additional treatment.

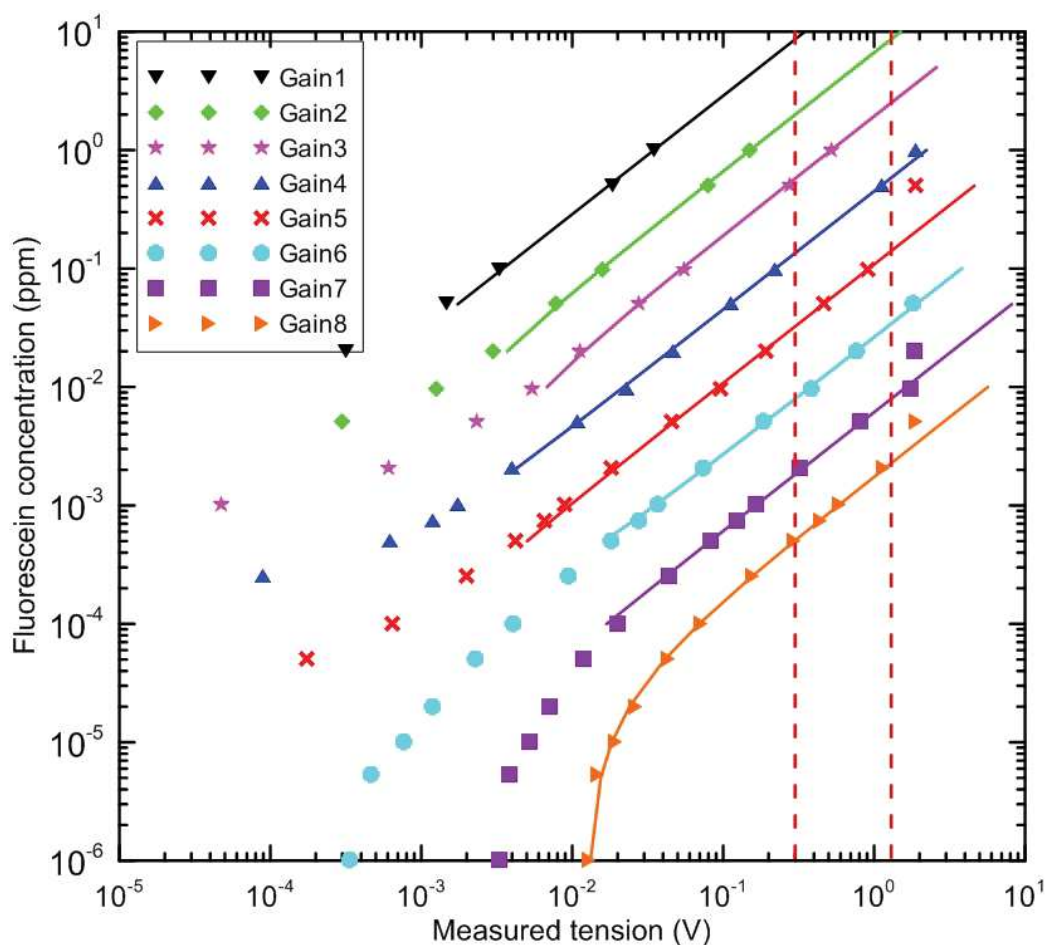


Figure 3.8 TLog calibration results. Symbols present measured tension output for given concentration at different gains (photomultiplier sensitivity), lines present functions used to transform voltage to fluorescein concentration for different gains (line color matches symbol color for same gain), two dashed red lines present limit of function application in standalone mode for all gains except gain 8.

Trend lines obtained from measured values during the calibration process can be expressed by power-law function equation; transformation from measured voltage at specific gain to fluorescein concentration is made by equation

$$C = B_i V + A_i, \quad (3.4)$$

where C denotes the concentration, i refers to gain value (i.e. photomultiplier sensitivity level), V is measured voltage output, A and B are coefficients of the calibration curves related to specific gain. Comparison of experimental results with ADE mode (e.g. Figure 1.1) is based on the CXTFIT model [Toride et al., 1995] incorporated into STANMOD software package.

3.3 Results and discussion

In this section we present results of the laboratory experiments performed on glass beads columns and Berea sandstone cores. All results are presented as breakthrough curves (BTC) showing the tracer concentration at the outlet of the sample.

After each experiment, retrieval rate is calculated as an area below BTC. Retrieval rate varies between 90 and 105% of tracer injected in the system. This difference (as well positive) is explained by the fact that injected volumes were relatively small (2 to 50 μL), so there might be small difference (uncertainties on the injected volume) between the planned and the actual injected volume.

3.3.1 Glass beads flow-through experiments

We performed series of experiment on the glass beads column. The column (200 mm long and 18 mm in diameter) was filled with glass beads with diameter between 355 and 400 μm . Flow rate was 50 cm^3/h for all experiments. At this flow rate, in the porous medium, there is a laminar flow regime with Reynolds number of 0.55 and the Peclet number is 853 according to equations (2.11) and (4.7) respectively. Porosity of packed beads is estimated at 0.38 [Dullien, 1992], characteristic length is taken as median bead diameter and is equal to 380 μm , water density is 1000 kg/m^3 , fluorescein molecular diffusivity is 6.4×10^{-10} m^2/s [Galambos and Forster, 1998] and water dynamic viscosity at 20 $^\circ\text{C}$ is 1.002×10^{-3} Pa s.

Section 3.2.4 shows that in certain experimental conditions, fluorescein can be considered as an ideal tracer. Since both glass beads and sandstones are positively charged surfaces, sorption of the tracer can be neglected, so the only thing that could impair experimental precision is density effect. Several authors studied dispersion behavior in cases when there is significant density difference between the resident fluid and tracer solution, such as e.g. contact interface between salt and fresh water [Hassanizadeh and Leijnse, 1995; Konz et al., 2009]. However density effect resulting from the weak density contrast (e.g. dissolved tracer in the same fluid as resident fluid) is often neglected. To our knowledge only Tenchine and Gouze [2005] investigated density effect for the weak density contrast. They observed that the density effect can influence the transport even if there is only 0.35 grams of the fluorescein sodium per liter.

Figure 3.9 presents the study of the possible density effect during the flow-through experiments performed on the packed glass beads column. Four different solutions ranging from 10^{-3} (1000 ppm) to 10^{-6} (1 ppm) grams of the fluorescein sodium per liter of the water are tested. All BTCs for different injection concentrations have similar shapes displaying non-Fickian behavior with emphasized tailing. Analysis of the peak arrival time (Table 3.1) reveals the influence of the density effect. Due to density effect higher concentrations have shorter peak arrival time than lower ones. The observed difference in the peak arrival time between 1000 ppm and 1 ppm is around 6%, and between 500 ppm and 1ppm is around 3%. It can be noted that the peak arrival time for the injected concentration of 50 ppm is slightly larger than the one for the 1ppm; however, the difference is in the range of the experimental error. We conclude that the differences in the peak arrival times are clear indications of density effect the tracer transport, for experimental setup where flow and gravity are oriented in the same direction.

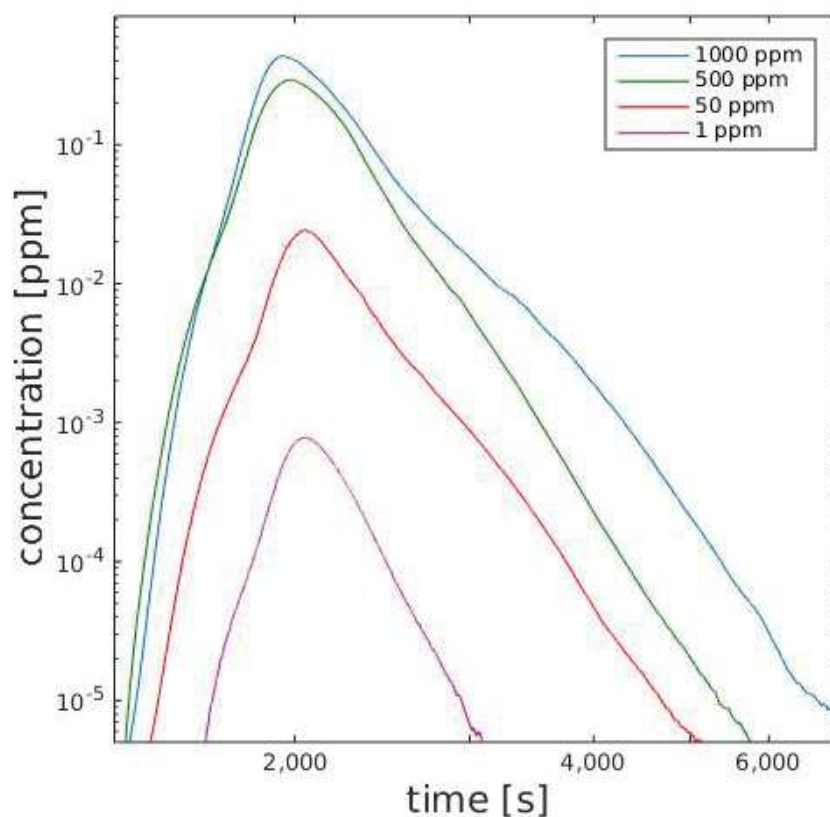


Figure 3.9 Experimental breakthrough curve data of tracer concentration at the outlet of the column packed glass beads ($L=20\text{cm}$ $\varnothing=18\text{mm}$), flow-through experiment, flow rate $50\text{cm}^3/\text{h}$. Comparison between different solution concentration of injected tracer ranging from 1 ppm to 1000 ppm.

Differences in the late time behavior are not so pronounced. In case of 1000 ppm, a density effect in very permeable and relatively short porous medium causes irregular tailing, tails observed for 500 ppm and 50 ppm at late times becomes parallel one to another with a slope of $t^{-10.6}$. While slope for 1 ppm ($t^{-13.4}$) is steeper than ones observed at late time for higher concentrations it is in good agreement with ones occurring just after the peak. From this one can conclude that in case of 1 ppm, resolution of the measurements is sufficient only to capture early times after the peak.

Concentration [ppm]	Peak arrival time [s]
1000	1925
500	1976
50	2049
1	2043

Table 3.1 Peak arrival time from the BTCs on Figure 3.9 for different concentrations of injected solution

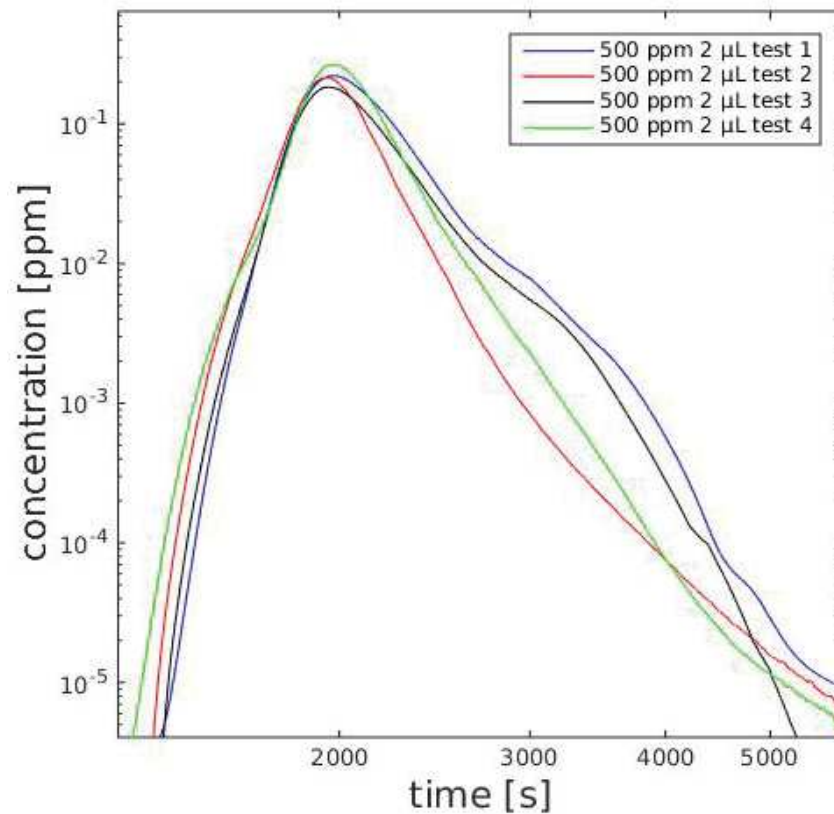


Figure 3.10 Experimental breakthrough curve data of tracer concentration at the outlet of the column packed glass beads ($L=20\text{cm}$ $\varnothing=18\text{mm}$), flow-through experiment, flow rate $50\text{cm}^3/\text{h}$. Displaying different tail behavior due to density effect in experiments with injection concentration 500ppm and tracer volume $2\mu\text{L}$.

The irregular late time behavior observed in the experiment with strongest concentration (1000ppm) of the injected solution (Figure 3.9) requires further investigations of the result reproducibility. In Figure 3.10 one can observe that for the same flow conditions and the same injected concentrations late time behavior can significantly differ. These behaviors appear to be unpredictable and are presumably due to occurrence of variable tracer localization in preferential channels induced by density effects. For all the four experiments peak arrival time differences are inside the experimental error range.

These effects do not occur at low value of the injected tracer concentration. For instance Figure 3.11 presents BTCs for two experiments with tracer concentration of 50ppm and with different tracer volumes of 2 and $10\mu\text{L}$, presented with blue and red curve respectively. Results for the two experiments are very consistent. The two BTCs are remarkable similar both in terms of early and late time behavior; the tail of both curves displays a characteristic local slope of $t^{-10.6}$. The only differences are a) a wider concentration distribution around the peak and b) a shift in the peak arrival time; the peak arrives later in the experiment with the larger volume injected. This can be explained by the longer injection period for the $10\mu\text{L}$ injection. Indeed, we observed (see section 3.3.2, Figure 3.14) that experimental results are sensitive to the solute injection rate and therefore slow injection rate (i.e. long injection periods) is used so that disturbance in the flow around injection point is low and at least similar in both cases (using the same tracer injection rate).

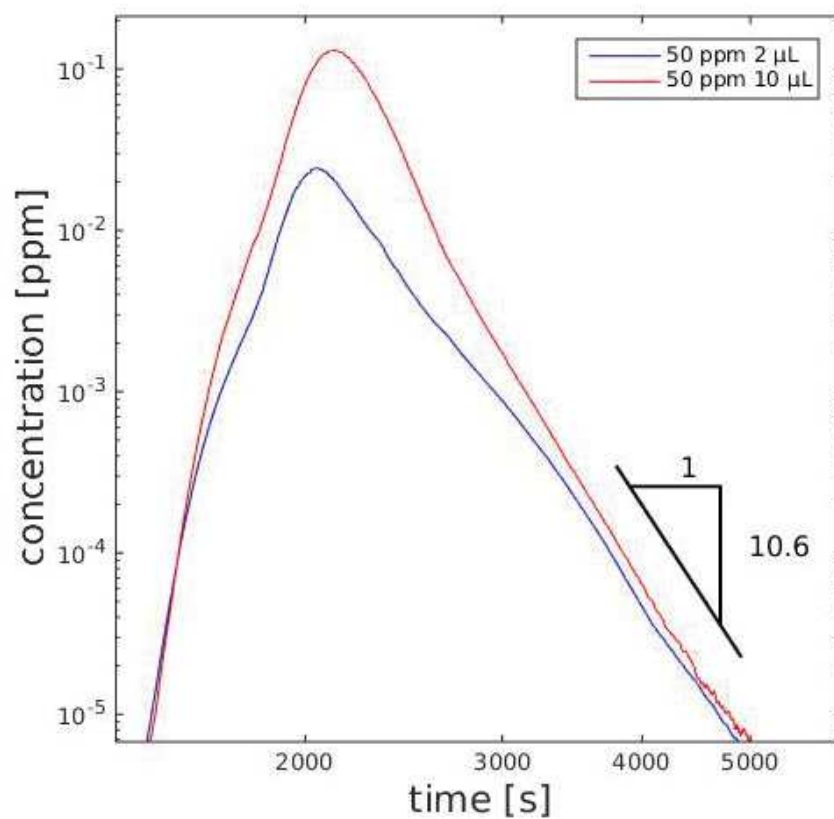


Figure 3.11 Experimental breakthrough curve data of tracer concentration at the outlet of the column packed glass beads ($L=20\text{cm}$ $\varnothing=18\text{mm}$), flow-through experiment, flow rate $50\text{cm}^3/\text{h}$. Displaying behavior for injected tracer with concentration of 50ppm , with two different tracer volumes $2\mu\text{L}$ (blue line) and $10\mu\text{L}$ (red line).

3.3.2 Glass beads push-pull experiments

Push-pull experiments on the glass beads packing are made on the same sample and with the same flow rate as the flow-through experiments described earlier. The only difference is that tracer is injected from the bottom of the sample (push phase) and then after a certain time flow direction is inverted and directed from the bottom (pull phase) of the sample. For some experiments between push and pull phase pumps are stopped to create no flow conditions. This period without flow hereafter will be referred to as the resting period. Desired flow rate is achieved in less than 10 s after turning on the pumps, while turning off is instantaneous. Therefore it can be considered that pump manipulations do not have effect on the results. Push period duration is estimated from the flow-through experiment with the aim to make it as long as possible, without causing any tracer leakage at the other side of the sample. It is crucial that there is no tracer leakage from the porous media since this could cause misinterpretation of experimental data. Longer push phase allows tracer to explore larger portions of the porous media. Push-pull experiments are performed in order to distinguish difference between reversible (spreading) and irreversible (mixing) parts of dispersion.

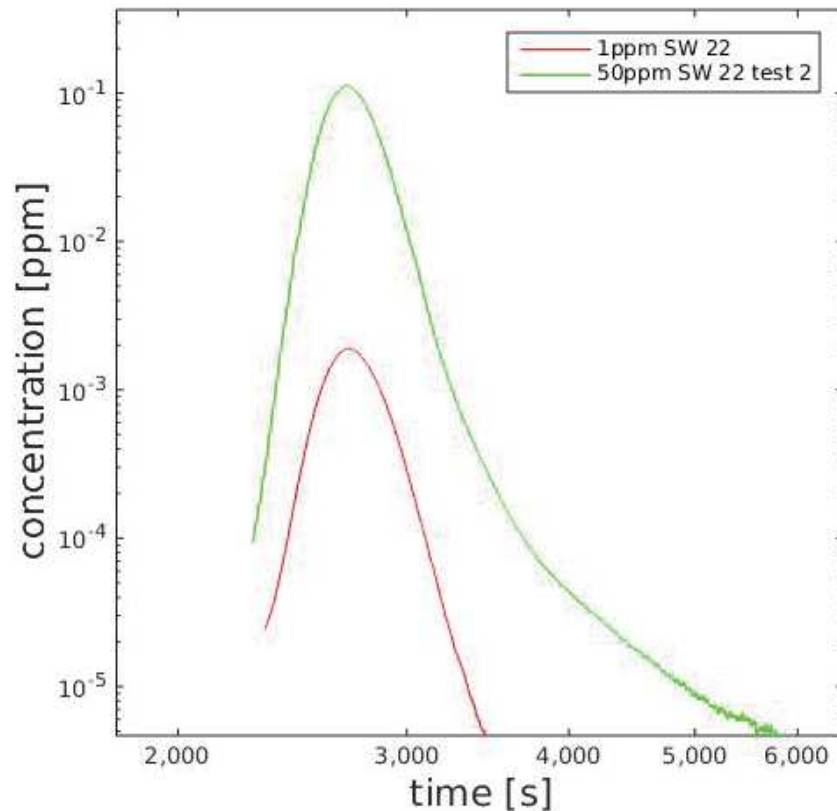


Figure 3.12 Experimental breakthrough curve data of tracer concentration at the outlet of the column packed glass beads ($L=20\text{cm}$ $\varnothing=18\text{mm}$), push-pull experiment, flow rate $50\text{cm}^3/\text{h}$, duration of push phase is 22 minutes, injected tracer volume $10\ \mu\text{L}$. Comparison between different concentrations of the injected solutions; 50 ppm (green line) and 1 ppm (red line).

Investigation of the density effect similar to one made for the flow-through experiment (section 3.3.1) is presented in Figure 3.12. However, for push-pull test only the two lowest concentrations are tested with push period lasting 22 minutes. The BTC curves for both tracer concentrations have similar peak arrival time and behavior just before and after the peak. This confirms conclusions from flow-through experiments that there is no visible density effect if tracer concentration is 50 ppm or less. At late times for the experiment with higher tracer concentration, one can observe occurrence of the tailing that is not visible in the experiment with the lower tracer concentration because of the resolution limit of the TeLoG sensor as already observed for the flow-through experiments. Therefore, further experiments will be made with a tracer concentration of 50 ppm.

Figure 3.13 presents push-pull experiments with different push phase and resting period duration. The aim of this comparison is to investigate solute transport behavior in relation with different time spent in the porous media and different distances that it explores. All experiments are performed at the same conditions (flow rate $50\text{cm}^3/\text{h}$, injected concentration solution 50 ppm) and on the same sample. As expected, difference in the peak arrival time is equal to the differences in the sum of the push and resting period durations. The peak concentration is lower in the experiment when peak arrival time is longer; this is due to the diffusion that has more time to influence on the plumb center.

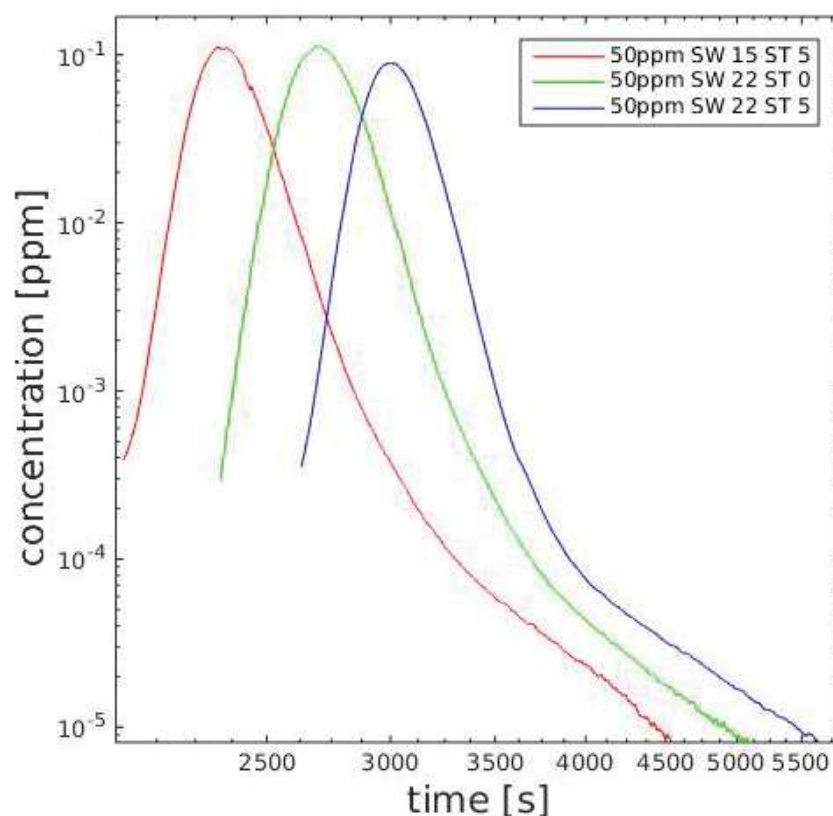


Figure 3.13 Experimental breakthrough curve data of tracer concentration at the outlet of the column packed glass beads ($L=20\text{cm}$ $\varnothing=18\text{mm}$), push-pull experiment, flow rate $50\text{cm}^3/\text{h}$, injected tracer concentration 50 ppm, injected tracer volume $10\ \mu\text{L}$. Differences between BTC's are in duration of push and resting period. Red curve – push duration 900s, resting duration 300s; green curve – push duration 1320s, resting period 0s; blue curve– push duration 1320s, resting period 300s. Times noted in legend are in minutes, SW stands for duration of push and ST for resting period.

It can be noticed that longer push and resting period does not affect BTC's shape tail since all three BTCs display similar late time slopes of $t^{-6.2}$. Experiments with longer duration of push and stagnant phases have tendency to faster converge between two slopes. This means that difference in the time spent in the system does not affect the late time behavior.

Comparing results to similar flow-through experiment (Figure 3.11), one can observe that in push pull there are two very distinct behaviors. Immediately after the peak, one can observe a faster decrease in the concentration which is explained by the fact that the reversible part (spreading) of hydrodynamic dispersion is cancelled. At later times, the second slope appears which is controlled by the irreversible dispersion (e.g. controlled by diffusion in slow flowing zones), whereas, in flow-through experiments, the concentration decrease rate is rather constant and its value is somewhere in between the two slopes that characterize the push-pull experiment. Clearly it is reasonable to expect that the concentration decrease in the flow-through experiment immediately after the peak is slower than in the push-pull experiment due to spreading of solute plume. However, it is also expected that BTC slopes at late time for both experiments have similar values; since late-time behavior is supposed to be controlled by the diffusion transfer between fast and stagnant (no) flowing zones. One can observe that the slope

in the flow-through experiment is significantly steeper than the second slope captured in the push-pull experiment. The reason for this difference is in the fact that in case of the flow-through experiments late time behavior is not captured and that the slope is still controlled by overlapping effects of flow field heterogeneity and mobile-immobile transfer.

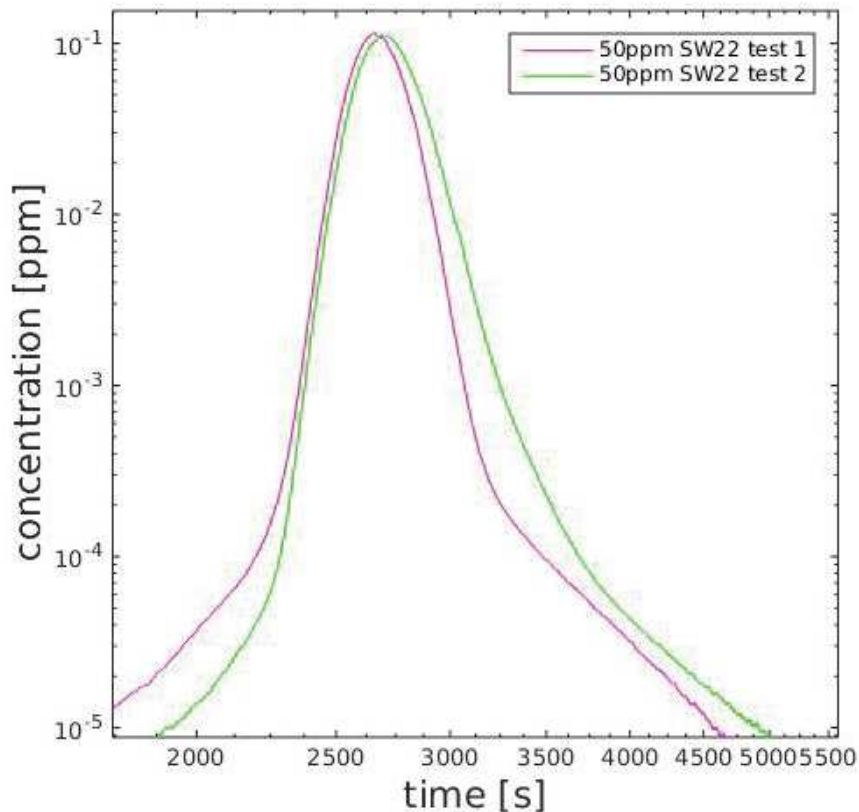


Figure 3.14 Experimental breakthrough curve data of tracer concentration at the outlet of the column packed glass beads ($L=20\text{cm}$ $\varnothing=18\text{mm}$), push-pull experiment, flow rate $50\text{cm}^3/\text{h}$, injected concentration solution 50 ppm, push duration 22min. Magenta curve – fast injection, Green curve – slow injection

As for flow-through experiments, repeatability is very important issue. Since the sample is relatively small, it is reasonable to assume that manipulations should be very precise to ensure good repeatability and ability to compare different experiments. Figure 3.14 presents BTC for two experiments performed with same injection concentration, injection volume, push period and flow rate. Difference is made in the injection procedure. Since tracer injection is made by human with a syringe it is impossible to expect that there will be two injections with exactly the same conditions. Therefore we compared two “extreme” injection cases. Magenta curve presents experiment where whole volume of the tracer is injected in 1 or 2 seconds (i.e. fast injection), while green curve represents slower injection in which tracer was injected during approximately 10 seconds. The BTC from the experiment with faster injection has earlier peak arrival time and narrower peak. Also concentration decreases faster immediately after the peak, however one can observe that late time behavior in both cases is the same, i.e. is not dependent on the solute injection uncertainties.

Despite precautions (e.g. bottled water, elimination of the light pollution...) taken during the designing and performing experiment we encountered unresolvable problem with measurement resolution. For unexplained reasons measurement equipment would decrease its resolution. Example can be seen on Figure 3.15 presenting two exactly identical push pull experiments performed in two consecutive days. Experiment performed on day before (blue line) had significantly lower resolution than second experiment. There were no differences in the water, room temperature and light conditions between two experiments. Only possible explanation can be in the fluctuations of the TElOG sensibility due to possible changes in the voltage or the temperature. However, this investigation has shown remarkable consistency at higher concentrations and excellent repeatability of the experiment results.

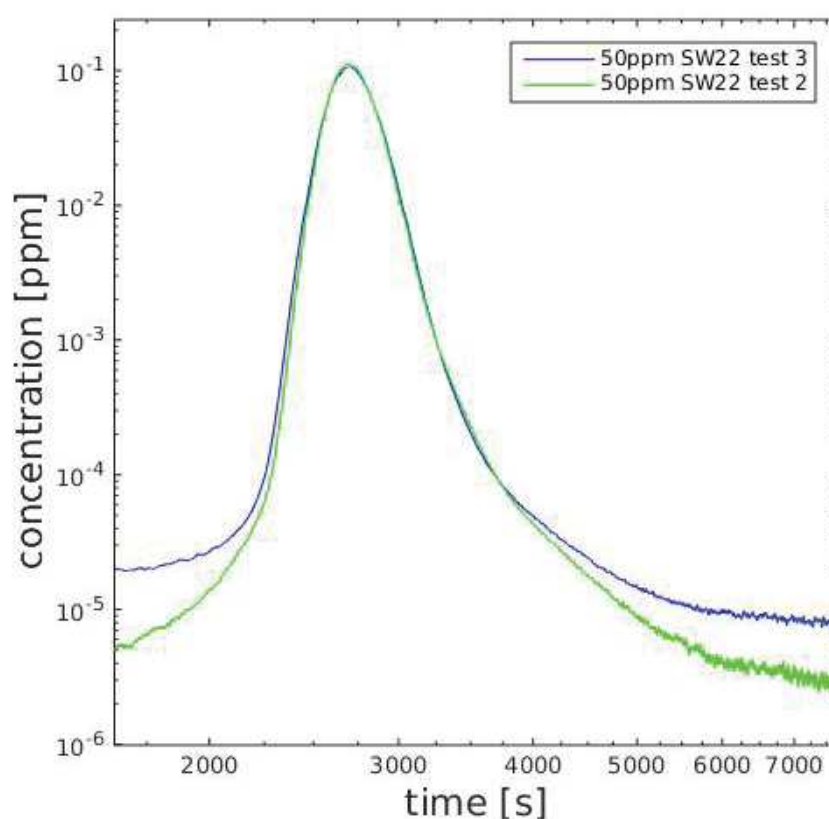


Figure 3.15 Experimental breakthrough curve data of tracer concentration at the outlet of the column packed glass beads ($L=20\text{cm}$ $\varnothing=18\text{mm}$), push-pull experiment, flow rate $50\text{ cm}^3/\text{h}$, injected concentration solution 50 ppm , injected volume $10\text{ }\mu\text{L}$, duration of push phase 22 min .

3.3.3 Berea sandstone flow-through experiments

In this section we present results of the flow-through experiment performed on the Berea sandstone core (length 15 cm , diameter 18 mm). We performed experiments at two different flow rates, 10 and $2\text{ cm}^3/\text{h}$. Calculated Peclet numbers (2.11) are ≈ 100 and ≈ 20 , with Reynolds number (4.7) ranging between 0.06 and 0.01 for given flow rates. To calculate Peclet and Reynolds numbers characteristic length ($\approx 110\text{ }\mu\text{m}$) is taken from calculations made on segmented images presented in

section 4.2.4. Porosity is 0.19; it was measured during mercury porosimetry test. Other parameters were taken from the literature; water density is 1000 kg/m^3 , fluorescein molecular diffusivity is $6.4 \times 10^{-10} \text{ m}^2/\text{s}$ [Galambos and Forster, 1998] and water dynamic viscosity at 20°C is 1.002×10^{-3} .

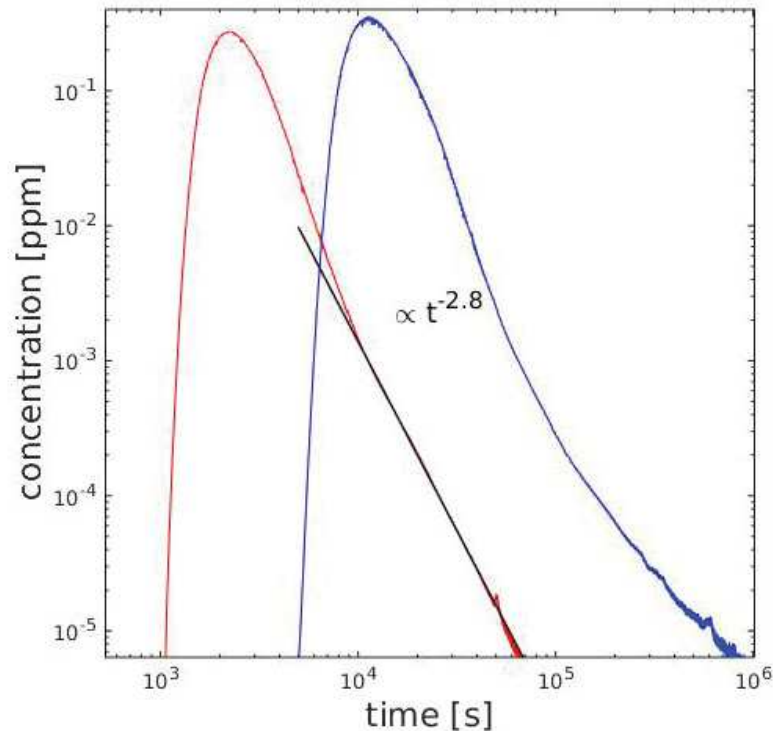


Figure 3.16 Experimental breakthrough curve data of tracer concentration at the outlet of the Berea sandstone core ($L=15\text{cm}$ $\varnothing=18\text{mm}$), flow-through experiment, injected concentration solution 50 ppm, injected volume $50 \mu\text{L}$. Comparison between two different flow rates $10 \text{ cm}^3/\text{h}$ (red line) and $2 \text{ cm}^3/\text{h}$ (blue line). Black line denotes power-law function that fits late time behavior of the experiment with higher flow rate.

Experimental results are presented in Figure 3.16. Red curve represents BTC for the experiment with higher flow rate and blue one BTC obtained at the lower flow rate. Both BTC displays signatures of anomalous transport with elongated tails. BTC resulted from the experiment with higher flow rate is characterized at the late time by constant slope that scales in time as a power law with a slope of -2.8 . On the other hand on the BTC obtained at lower flow rate the slope cannot be determined. BTCs tails scaling as a power law in time are commonly recorded in the conditions with higher Peclet number and late time behavior is more pronounced. However from the Figure 3.16 it is clear that the concentration decrease for slower flow rate is significantly slower than one noticed in at higher flow rate. This behavior is contrary to our expectations. In theory the late-time behavior is controlled by matrix diffusion and therefore is function of the porous medium properties and independent on the flow rate.

To understand this observed a priori incoherent behavior, first we have to explain a problem that occurred during the experiment with higher flow rate. Due to relatively high pressure at the injection points there was a leakage during the injection. Rubber foam tube (tube 2, see section 0 and Figure 3.4) started to leak at the position where needle had penetrated it. Yet, although the hole was closed in

couple of seconds with another needle a small volume of tracer leaked and therefore was not injected in the water flow. Note that the needle used to close the hole was clean and inserted just in the rubber tube in order to not disturb the flow. We believe that this small leakage did not influence the experimental results and BTCs shape; however, it is clear that the amount of tracer actually injected in the core sample was smaller than expected. It is difficult to have a precise appraisal of the amount of tracer that was lost. Nevertheless, we can make some rough estimation by noting that we approximately recover 14 % of the tracer in the higher rate experiment compared to the lower rate experiment (Figure 3.16). Although it seems quite large, since leakage was almost immediately stopped (one small drop leaked), it is worth reminding that the total injected volume is small as well (50 μL) and that excellent retrieval rate was measured in previous experiments. Figure 3.17 a) presents the scaled BTC according to the estimated injected volume. To explain the observed behavior it is compared with modeling results (modified Figure 11 from section 5.3). Figure 3.17 b) presents results of the transport simulations with different Peclet numbers ($Pe=1000$ pink symbols, $Pe=100$ green symbols) performed on the segmented images of the same Berea sandstone rock as used in the experiment (more details are in section 5.3). Connected symbols denotes simulations where both influences of the flow field heterogeneity and mass transfer to the microporous phase are considered, while unconnected symbols denotes simulations where mass transfer to microporous phase is neglected.

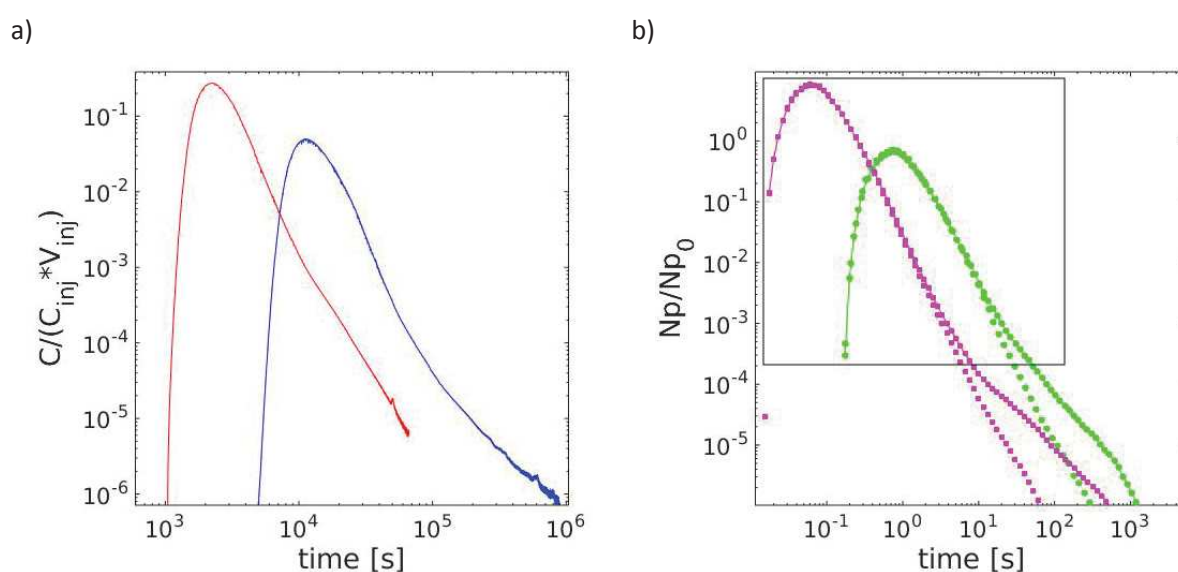


Figure 3.17 Scaled BTC according to the estimated tracer volume that is injected (a); red line 10 cm^3/h , blue line 2 cm^3/h . Compared with results of transport simulations performed on XRMT images of the same rock (b) at $Pe = 1000$ (purple symbols) and $Pe = 100$ (green symbols). Black rectangular limits resolution that can be observed in the experiments. Unconnected symbols denotes simulations in which mass transfer to microporosity is neglected, while connected symbols represents simulations that account for mass transfer into the microporosity – original figure is in section 5.3, Figure 11

Qualitative comparison between Figure 3.17 a) and b) reveals similarities in the observed behavior. The rectangular window (Figure 3.17 b)) represents the limits of the experiment resolution, so experimental BTCs are compared only with part of numerically obtained BTCs inside the limits of this window. BTC for the simulation with higher Pe have more pronounced slope after the peak and that

behavior influenced by matrix diffusion starts later than in the case of the lower Pe . The experimental BTC for higher Pe displays the same behavior, except that influence of the matrix diffusion is not visible due to resolution limitations. For lower Pe slowing of the concentration decrease rate observed in the experiments is visible also in the numerical simulations, but only ones that include matrix diffusion. This comparison reveals significant limitations in the experiment resolution, despite its ability to measure over more than 5 orders of magnitude. Due to these limitations it is not possible to study BTC behavior influenced only by the matrix diffusion (i.e. late-time behavior) and they can mislead to the conclusion that the heterogeneities in the flow field are exclusively responsible for non-Fickian behavior. However experimental results with lower Pe emphasize importance of inclusion matrix diffusion into transport calculations, which cannot be observed at higher Pe .

3.4 Summary and conclusion

In this section we presented an experimental set-up that allows studying dispersion of the non-reactive tracer. Test bench design allowed continuous measurement of the tracer concentration over several orders of magnitude. Improvements in the injection procedure minimized tracer dispersion in the system before entering the porous media. However it also caused leakage in experiments where a high pressure difference was imposed.

Series of experiments with different tracer concentrations performed on the glass beads column emphasize the importance of the density effect. The density effect is usually neglected, especially in the large scale experiments. However, we proved that density effect can impair experimental results even if the concentration is 500 ppm. Although, concentration (and consequently density) of the tracer decreases during the experiment, final results may be misinterpreted due to density effect in vicinity of the injection point. In this scope we demonstrated influence of different injection times (rates) on the BTCs shape.

Comparison between push-pull and flow-through experiments showed limitations of the experimental equipment when trying to capture late-time behavior. These limitations were confirmed on the flow-through experiments performed on the Berea sandstone. Also, qualitative comparison between experimentally and numerically obtained BTCs on the Berea sandstone emphasized the importance of inclusion both matrix diffusion and flow field heterogeneity in the pore-scale transport modeling.

Finally, one must admit that despite a tremendous effort for obtaining state-of-the-art core tracer test, the results cannot be used with confidence for parameterizing non-Fickian model. This conclusion is the results of a large set of experiments for testing 1) the effects of tracer concentration, injection procedure and optimization of the equipment and 2) the result reproducibility. Albeit there is still space for improvement of the equipment and protocol, we believe that tracer tests on cores must be analyzed with care because 1) a small experimental bias can produce large effects on the BTC and 2) technological barriers limit our possibilities of tackling part of the BTC tails. This is specifically obvious for low Peclet experiments corresponding to the most general case in natural geological situations. It follows that an apparently power law behavior defined over less than one order of magnitude in concentration can be just a transitional behavior between, for instance velocity heterogeneity effects and MRMT effects.

Pore-scale numerical simulations of the flow field

4.1 Introduction and framework

Recent development of pore-scale imaging techniques, computational fluid dynamics solvers and more powerful computers has allowed investigating origin of anomalous transport at pore scale. The common approach is to process X-ray microtomography (XRMT) images in order to distinguish the pore from the solid, then simulate the steady-state flow for incompressible fluid and finally solve the diffusion-advection in order to obtain the distribution of the tracer concentration according to specified boundary conditions [Ovaysi and Piri, 2011; Blunt et al., 2013].

XRMT acquisition and image processing is described in section 4.2. These images are then used to calculate flow field. Flow field is calculated using Navier-Stokes equation pre-programmed in computational fluid dynamics software OpenFOAM. Detailed procedure is described in section 4.3. Results of the flow simulations with emphasis on comparison between different mesh resolutions are shown in section 4.4. Transport results are presented in the first article in Chapter 5.

4.2 Rock structure imaging

4.2.1 X-ray microtomography (XRMT)

Internal geometry of the rock is the main input parameter needed for flow and transport simulations at pores scale. XRMT is a non-invasive imaging technique used to obtain realistic presentation of the pore space geometry. Image resolution can vary from few decimeters to the tenths of micrometers.

Figure 4.1 illustrates procedure of obtaining real 3D model of pore space from a rock sample using XRMT approach. X-ray beam is emitted from the source passing through the sample and captured by CCD camera placed behind sample. The image consists of the projection of the sample in terms of X-ray intensity. Projections of samples are taken from different angles ranging from 0° to 180° (or 360°) and the step change between projections does not exceed half degree. Recorded projections are transferred from the camera to the processor where they are filtered and reconstructed. Result is a set of 2D images representing sample slices in terms of X-ray attenuation per pixel. X-ray attenuation depends on chemical compound and density. For mono-crystalline rocks, XRMT images are actually maps of rock density (porosity), since there is no variation in chemical compound. Sets of 2D images are arranged and together form a 3D image of pore space. This 3D image is suitable for physical parameter analysis and pore-space geometry reconstruction.

For this work the high resolution XRMT image of the Berea sandstone core (10mm length and 6mm diameter) was acquired using the BM5 beamline at the European Synchrotron Radiation Facility (Grenoble, France). The 3D volume was reconstructed from 3495 projections acquired at an energy of 110 keV using a GGG:Eu 100 microns scintillator and a SCMOS-based 2048 x 2048 pixels detectors (model PCO edge; <http://www.pco.de>). The reconstruction was performed using the single distance phase retrieval algorithm described by Paganin et al. [2002] applying an unsharp filter before

reconstruction. Details on the reconstruction algorithm and performances can be found in [Iassonov et al., 2009]. The final 3D image is formed by $4667 \times 2130 \times 2099$ voxels of characteristic size $3.16 \mu\text{m}$ ($3.16 \cdot 10^{-6} \text{ m}$). The 16 bits encoded value associated to each of the voxels denotes the X-ray absorption integrated over a volume of $31.5 \mu\text{m}^3$.

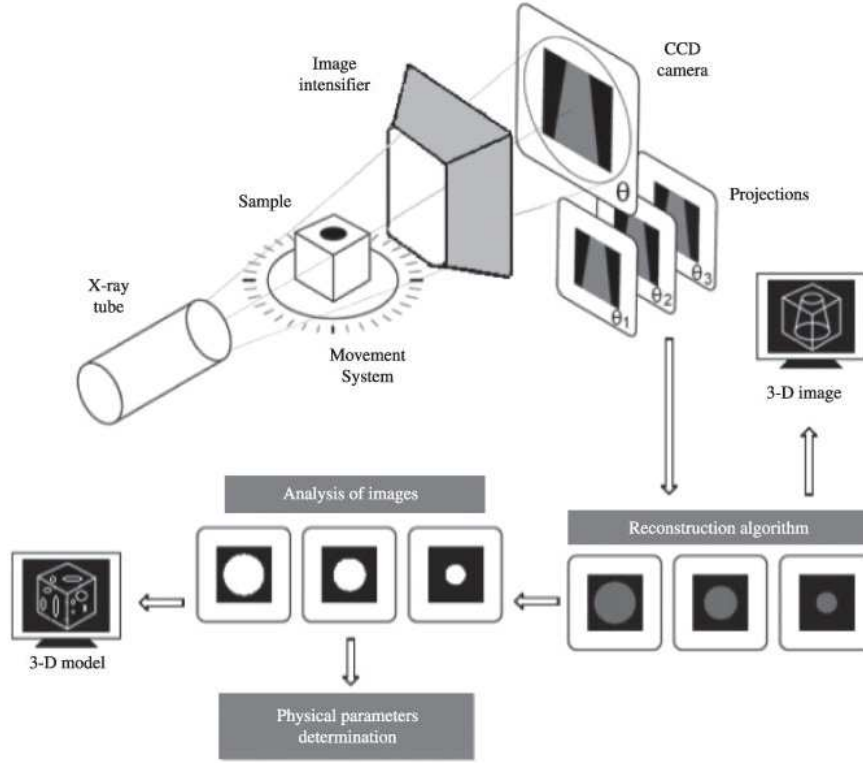


Figure 4.1 Image acquisition from X-ray microtomography to the final 3D model of heterogeneous media – reprinted from Fernandes et al. 2012

4.2.2 Segmentation

Analysis of the gray level histogram from raw XRMT images pointed out existence of three types of materials, denoted hereafter phases. The three phases correspond respectively to the macroporosity (i.e. the void space filled with air or liquid), the microporosity (voxels in which pores are smaller than image resolution) and the solid rock. Furthermore, existence of pores smaller than image resolution is confirmed by the Mercury Intrusion Porosimetry (MIP) test. MIP is a widely used technique for characterizing the pore size distribution in porous media. It is based on the premise that a non-wetting fluid; in our case mercury, will not intrude capillaries of a given diameter unless a given pressure is applied [Abell et al., 1999]. Relationship between the capillary pressure (P_s) and the pore radius (R) is given by Washburn equation (4.1) [Washburn, 1921]

$$P_s = \frac{2\gamma}{R} \cos \theta, \quad (4.1)$$

where γ is the surface tension and θ is the angle of contact.

Throat size distribution is determined from volume of mercury intruded at each step. Figure 4.2 shows results of MIP test for Berea sandstone. Red dashed line denotes image resolution ($3.16\ \mu\text{m}$) and all pores with radius smaller than this (left from the line) are considered as microporosity. Blue line marks average pore size ($11.71\ \mu\text{m}$) for given sample.

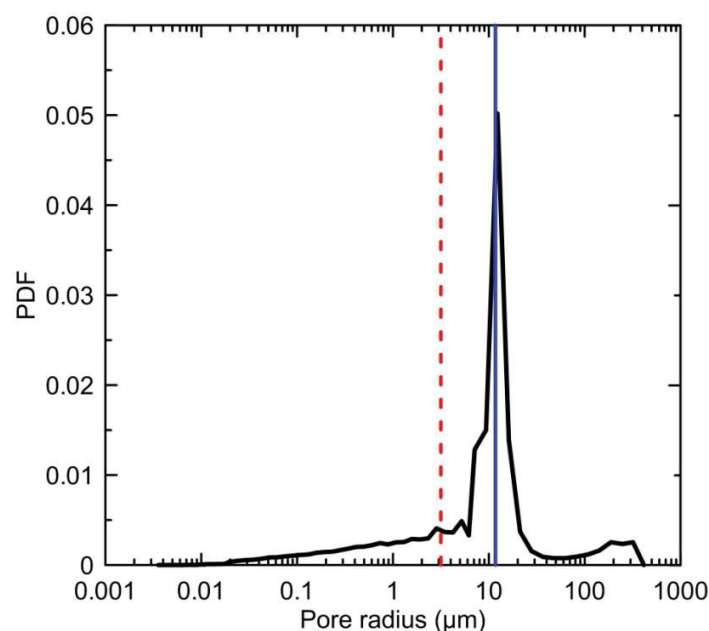


Figure 4.2 Mercury Intrusion Porosimetry test results for Berea sandstone (black line). Dashed red line denotes XRMT image resolution ($3.16\ \mu\text{m}$), delimitating microporosity and macroporosity, blue line marks average pore size ($11.71\ \mu\text{m}$)

The identification and then labeling of the different phases is called segmentation. There are different methods for performing image segmentation, none of them producing strictly equivalent results. Segmentation is consequently a critical step in accurate simulations of flow and transport at pore-scale [Iassonov et al., 2009; Schlüter et al., 2014; Scheibe et al., 2015].

One of the most common approaches to image segmentation is applying global threshold. This simple approach consists in deciding a grey scale value that marks separation point in X-ray attenuation between two phases on the basis of image histogram analysis. However, by definition, the microporous material can display a large range of gray level values denote pixels sampling both solid and voids. Consequently it is a priori not pertinent to use the global thresholding method for porous materials in which the existence of microporosity is known. Several alternative methods have been developed in order to improve the accuracy of the segmentation. A comparative study of different approaches has been presented by Iassonov et al. [2009].

For our study we used the so called “region growing” method based on the assumption that all the voxels belonging to a given phase cluster are connected and they are similar in term of gray level [Siprkovska, 1993; Noiriél et al., 2005]. A significant difficulty of growing methods is the need for carefully defining the grey level thresholds that defines boundaries between regions. This is typically done manually from analyzing the histogram. However, the image histogram does not contain enough information to properly identify the different phases and relatively small differences in thresholds may

lead to noticeable errors on the determination of the phase fraction and structure of pore space. For this reason in the present work we applied method proposed by Mangane et al. [2013]. It consists in conditioning the determination of the threshold values by the value of the total porosity measured by laboratory techniques.

Delimitation of 3 phases is done in two steps. In the first step we perform standard segmentation in which 2 thresholds are applied. All values that are smaller than lower threshold belong to first phase. Values larger than higher threshold are assigned to second phase, while the algorithm decides on assigning pixels with values between threshold limits to one of two phases. For 3 phase segmentation we have to perform this procedure two times to obtain two images, consequently we need 4 thresholds. Two images differ in arrangement of segmented phases. Phase one at first image is denoting void, while microporosity and solid are combined in second phase. On the second image void and microporosity are combined together in first phase while second phase contains only solid. Second step is overlapping and addition of two images. Areas that are marked as first phase on both images are considered as void, if the area is marked by second phase on first image and by first phase on second image it is considered as microporosity and finally all area that are marked with second phase on both images are considered as rock.

Described procedure is applied to perform 3 phase segmentation on Berea sandstone. From gray scale level distribution of raw image presented in Figure 4.3, 4 thresholds were defined. After finished segmentation the total porosity (ϕ_t) of the segmented image is calculated by equation:

$$\phi_t = \xi_v + (\xi_\mu \phi_\mu), \quad (4.2)$$

with ξ_v and ξ_μ denoting fraction of the void and of the microporous phase respectively, and ϕ_μ denoting the intrinsic porosity. The convergence toward a satisfactory agreement between the total porosity of segmented images and the connected porosity obtained by MIP is obtained by an iterative procedure. Threshold values were adjusted until the total porosity was in good agreement with the experimentally obtained porosity. Final threshold values are presented on Figure 4.3. Blue dashed lines are denoting thresholds used to delimitate between void and microporosity, while red dashed lines denotes thresholds delimitating microporosity and rock.

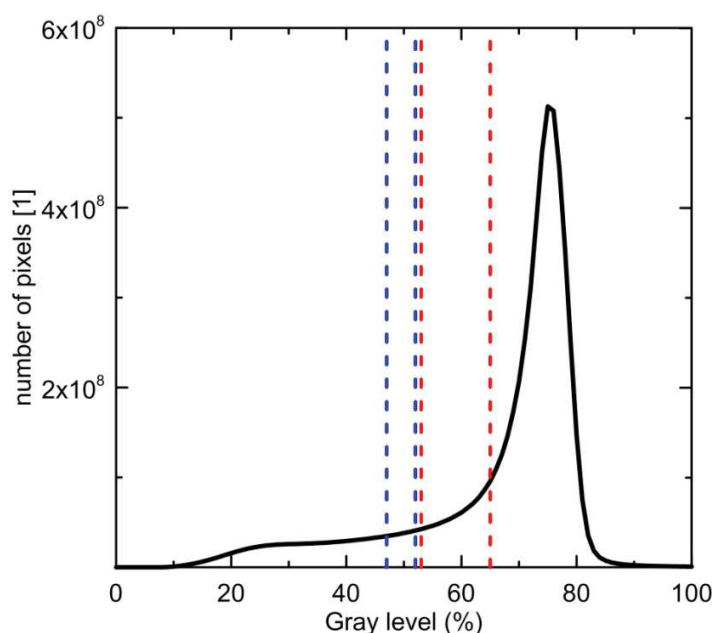


Figure 4.3 Gray scale level distribution for Berea sandstone (black line), dashed lines marks threshold values used for segmentation. Blue lines are for void-microporosity interface and red lines are for solid-microporosity interface

Procedure was applied assuming that the mineralogical composition of the microporous cement is homogeneous and second that the intrinsic porosity of microporous phase range from 0.01 to 60 %. Assumption of maximal intrinsic porosity is based on the fact that above 60 %, material cannot be cohesive. Whole procedure is based on comparing the experimental porosity to the total porosity (4.2). Certainly XRMT images may contain pixels belonging to the unconnected porosity which cannot be measured by MIP test. However, we performed measurement of this unconnected porosity a posteriori (details in section 4.2.3) and found that share of unconnected porosity is lower than 0.8% for all extracted sub-volumes. Accordingly one can consider that this value represents the error in the segmentation.

On XRMT images there are some voxels located directly on the interface between void and rock phases. Gray level of these pixels is similar to gray level of microporosity and during segmentation they are assigned to microporous phase. In order to avoid the appearance of microporous layer with thickness of one voxel on all void-rock interfaces we performed one layer abrasion during segmentation process. This abrasion is applied during first step on the image where microporosity and rock are place together in the same phase.

With the procedure described in this section we obtained realistic pore space geometry representations of the Berea sandstone (Figure 4.4). The fraction of the different phases are 79.45, 18.15 and 2.4 for solid, void (macroporous) and microporous phase respectively. The intrinsic porosity of microporous phase is heterogeneously distributed between 0.01 and 60%. Distribution is obtained directly from XRMT images as explained in section 4.2.1 .



Figure 4.4 3-dimensional visualization of pore-space network (blue) and connected microporosity (yellow)

4.2.3 Percolation clusters

The first step of segmented-data processing consist in eliminating unconnected pores since they do not participate in solute transport through porous medium. Network of interconnected pores that spans through the whole sample volume in the flow direction connecting boundaries is called percolation cluster. In this work percolation cluster were defined by cluster-labeling method proposed by Hoshen and Kopelman [1976].

Connected clusters were determined with two different assumptions, first that microporosity is percolating and second that it is not. Figure 4.5 illustrates differences between two approaches. White color represents macroporous zone that is percolating in both cases and this zone will be referred as mobile domain. Immobile domain consists of microporous zone denoted in orange and macroporosity that is connected only through microporosity that is colored in blue. In the mobile domain flow field can be calculated with standard approach using Stokes equation and transport is driven by both velocity and diffusion. Flow calculations in the immobile domain are feasible [e.g., Brinkman, 1949], but not very common on pore-scale. However, even if flow field is calculated, fluid velocities are significantly lower than in mobile phase and transport is dominated by diffusion. Inclusion of the immobile domain increases porosity on average by 5.3 % in the segmented sub-volumes of Berea sandstone; while macroporosity connected only through microporosity contributes in this increase with around 40 %.

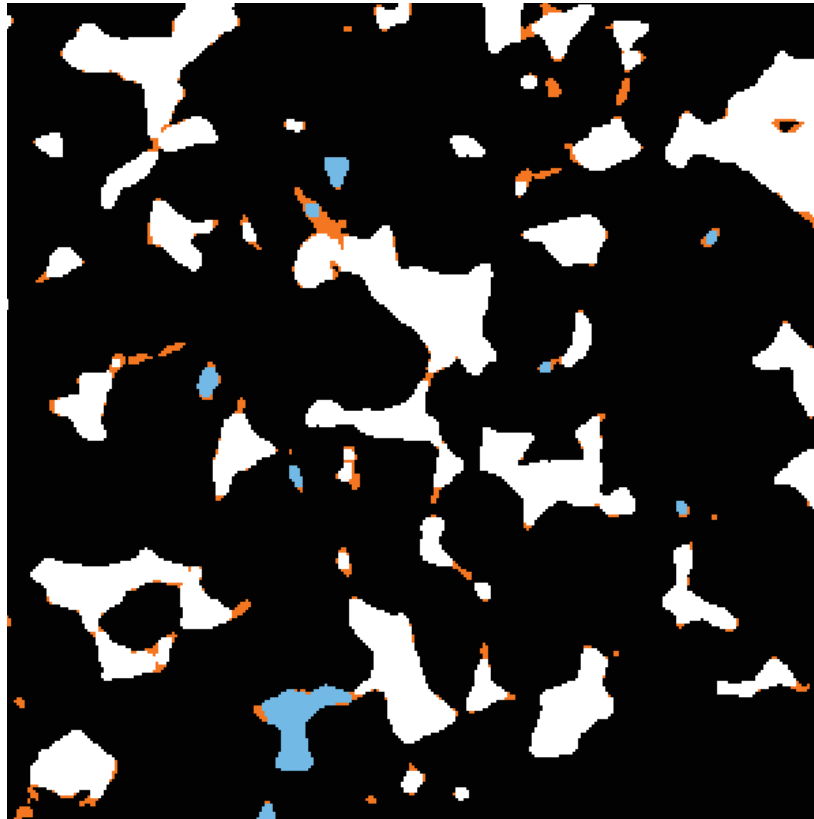


Figure 4.5 Cross section through segmented Berea sandstone displaying pore-space structure of connected clusters (i.e. all unconnected porosity is eliminated). Black filled areas denote the solid phase, white colored areas denote connected macroporosity, orange colored areas indicate the microporous phase and blue areas denote macroporosity that is connected with percolation cluster only through microporous phase

4.2.4 Characteristic length

The characteristic length (L) is the property of porous media necessary to calculate Reynolds (4.7) and Peclet (2.11) numbers, which is usually expressed as average grain (experiments with unconsolidated porous media) or pore diameter. At pore scale it is usually associated with the average pore diameter in the relation with the definition of the Peclet number in a capillary [Taylor, 1953].

For heterogeneous porous medium the characteristic length can be defined from the variogram of the mobile domain porosity. The variogram for Berea sandstone is presented in Figure 4.6 where dashed red line marks distance ($\approx 110 \mu\text{m}$) at which one can consider that the variogram reached asymptotic value. This is considered as the characteristic length.

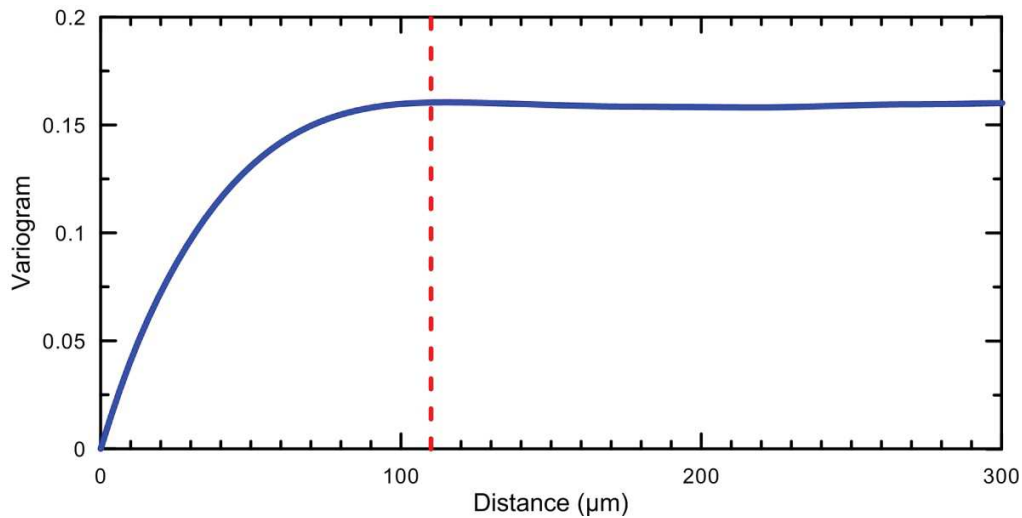


Figure 4.6 Rock structure variogram for Berea sandstone

Mostaghimi et al. [2012] proposed alternative way to calculate the characteristic length based on the cubic packing of regular spheres. For this idealized system, the characteristic length (L) can be associated with the sphere diameter

$$L = \frac{\pi V}{A}, \quad (4.3)$$

where V is the bulk volume of the porous medium (void and solid) and A is the interface area between the void and solid. Applying this method on Berea sandstone we obtain characteristic length equal to 124 μm .

We note that characteristic lengths calculated with both methods are in good agreement with characteristic lengths calculated on Berea sandstone in other relevant studies: 100 μm [Bijeljic et al., 2004], 131.13 μm [Mostaghimi et al., 2012] and 150 μm [Berkowitz et al., 2006].

4.3 Obtaining flow field

4.3.1 Representative elementary volume

To obtain a realistic velocity field of heterogeneous medium it is necessary to satisfy two opposite conditions. First one is to have a high resolution in order to capture all geometrical properties and the second one is to have a domain that is large enough to capture all heterogeneities of porous media. Increase in resolution is resulting in an increase of computational cell number and therefore reduces the size of the media that can be simulated, thus it is essential to achieve a good balance between resolution and domain size.

Properties of a heterogeneous medium vary in space and therefore the volume on which simulations are performed should be large enough to capture average properties of medium. Volume that satisfies this minimal requirement is usually called the representative elementary volume (REV). One of the most popular methods to define REV is through studying the scale dependence of the

porosity [Bear, 1972]. Figure 4.7 presents a diagram to determine REV in terms of porosity. Dashed line at ΔU_0 marks when the REV is achieved since porosity values are stabilized.

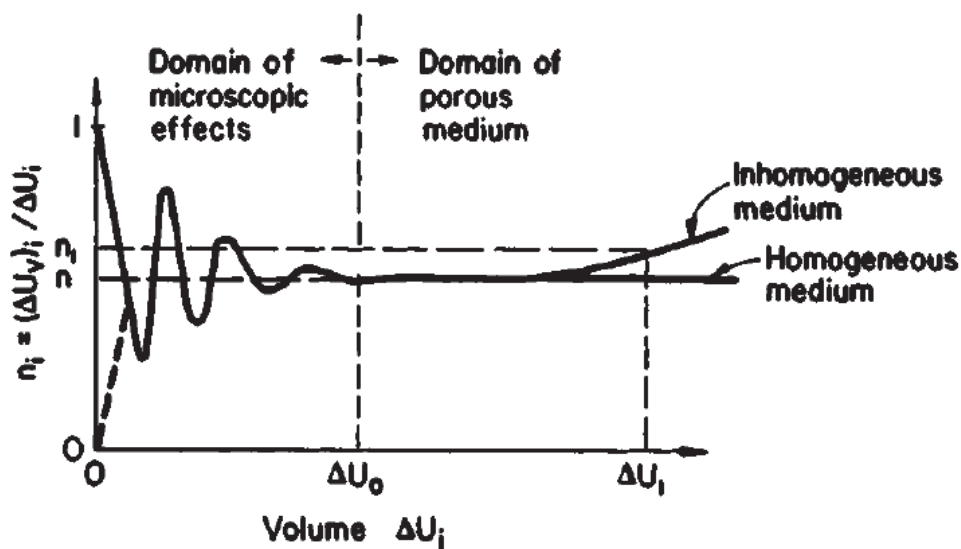


Figure 4.7 Definition of the representative elementary volume as a function of porosity – reprinted from Bear [1972]

To evaluate REV of Berea sandstone images, six points were chosen completely randomly in the whole image. From these starting points, cubes of different volumes were extracted. For each cube, connected porosity is calculated and divided by the total porosity of the whole image. Similarly volume of each cube was divided by volume of the cube with side dimensions of $300 \times 300 \times 300$ pixels since this size is chosen for numerical simulations presented in this work. Figure 4.8 presents results of investigation of the REV in terms of porosity. We observe that the porosity starts to become consistent with the total porosity at volumes that are twice smaller than the chosen volume and continuous this trend for larger volumes. Dashed red line presents volume equal to $300 \times 300 \times 300$ block (0.85 mm^3).

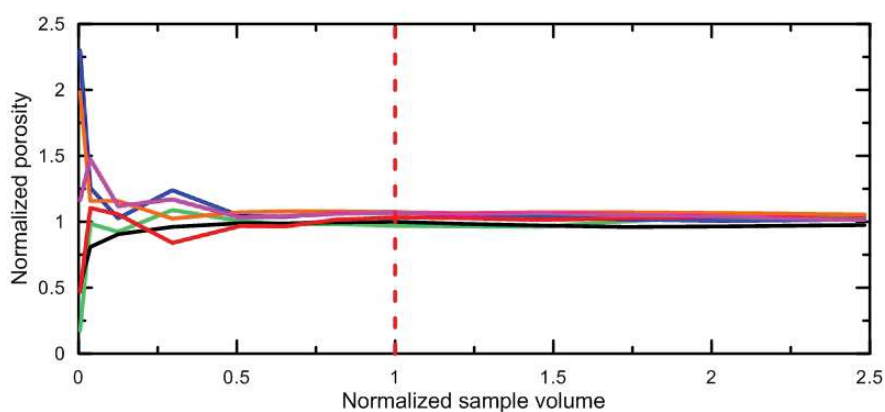


Figure 4.8 Normalized porosity in function of the normalized sample volume

However porosity-defined REV size can differ in terms of the hydrodynamic properties of the porous media that is being observed. Therefore we decided to investigate REV in terms of permeability. We randomly choose one series of blocks originating from same point used in porosity comparison. On each block flow simulations are performed and permeability [m²] k is calculated from Darcy's Law by equation

$$k = \frac{\mu Q l}{\Delta p A_x}, \quad (4.4)$$

where μ is fluid viscosity [Pa s], Q is total flux [m³/s], l is length [m] of block in the flow direction, p is pressure [Pa] and A_x is area [m²] of cross section perpendicular to flow direction. Figure 4.9 presents results of permeability calculation for cubes with different volumes. Sample volumes are normalized to the volume of 300x300x300 pixel (0.85 mm³) cube, which is represented by dashed red line. Permeability is normalized to the permeability of the referent cube and we observe that it starts to become uniform from cubes that are 40% smaller than referent. From both of these investigations we can conclude that cubes with side length of 0.95 mm used for the simulations are large enough to have good representation of Berea sandstone sample. Estimated value is in a good agreement with the REV investigations performed by other authors on the same rock, who estimated that cubes with side length larger than 1.2 mm [Ovaysi and Piri, 2010] or 0.68 mm [Okabe and Oseto, 2006] can be considered as representative.

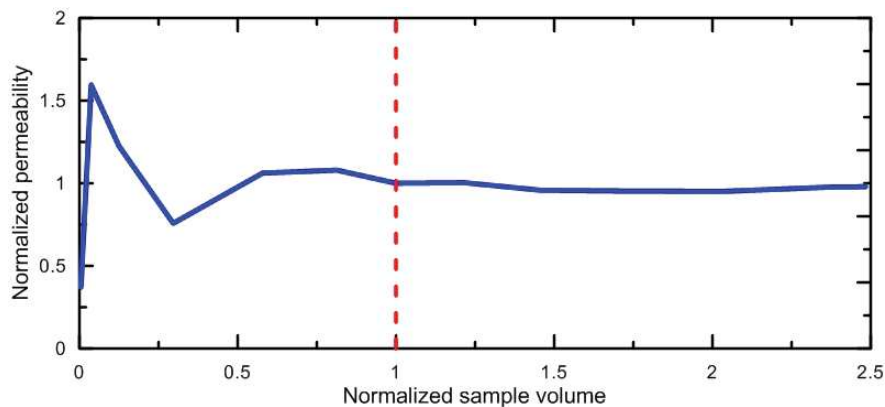


Figure 4.9 Normalized permeability in function of normalized sample volume

4.3.2 Mesh generator

Solving partial differential equations using CFD simulators requires that the domain is divided in smaller sub-domains. Inside these sub-domains the governing equations are discretized and solved. The sub-domains are usually called cells and collection of cells is called a mesh or a grid. There are different types of meshes which are usually classified as structured and unstructured meshes. Structured meshes are the ones made with always the same elements that have the same size, while in unstructured meshes cells varies in size and shape.

Mesh generation is quite complex and time consuming task which has direct influence on the simulation convergence as well as accuracy of the final result. Therefore it is essential to obtain a mesh with a good quality for given problem. Good quality mesh captures the system/problem of interest in a discrete manner with enough resolution to enable capturing enough information while retaining reasonable number of cells.

In this work we use structured mesh made of cubes (regular hexahedra). Such a decision is based on a fact that cubic mesh easily captures pore structure from segmented XRMT images and it is suitable for post processing to obtain necessary input data for the transport simulations. Pore scale simulations on XRMT image commonly use image resolution as mesh resolution, which means that cells are the same size as voxels. However a recent study of flow properties by Guibert et al. [2015] has shown that mesh resolution should be smaller than XRMT image resolution.

Mesh generation utility provided with OpenFOAM is called snappyHexMesh. This utility enables to generate structured and unstructured 3D meshes automatically from triangulated surface geometries saved in Stereolithography (.stl) format. To produce *.stl file we used the commercial image processing software Avizo, however this software treats each voxel in XRMT images as a point with coordinates but without a real volume. This causes changes in the pore structure between original image and resulting *.stl file. Also this approach is very memory consuming, thus limiting maximal size of domain that can be meshed.

To resolve this problem we developed our own mesh generator that reads XRMT images and produces mesh with the same geometry as original image. One of the features of this mesh generator is that each voxel can be divided by any integer in all three directions creating a structured mesh with several times higher resolution than the original image.

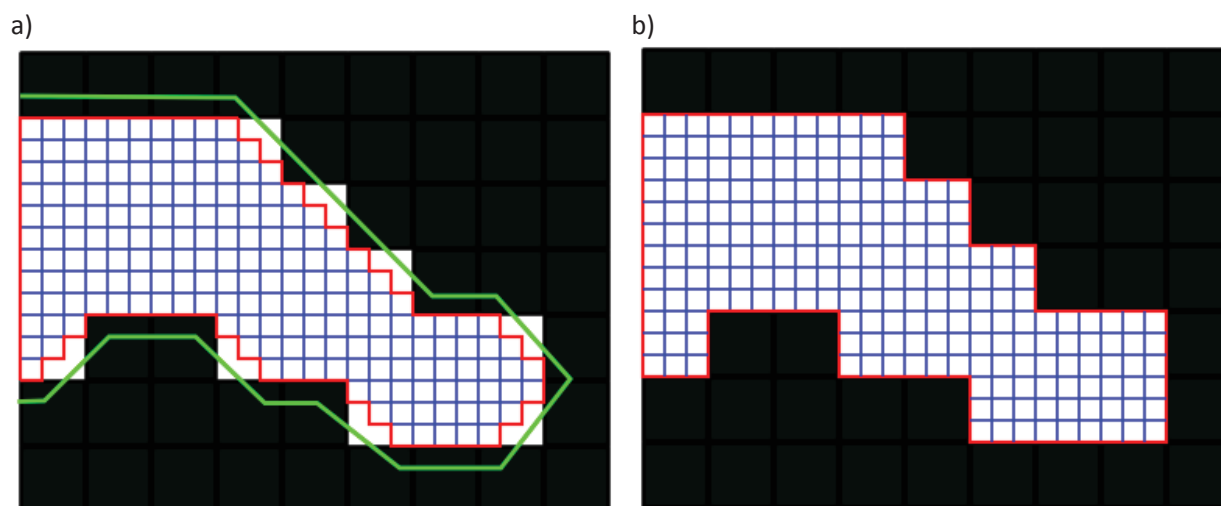


Figure 4.10 Graphical illustration of differences between two mesh generation approaches. Left image (a) presents mesh generated from *.stl file (green line) with snappyHexMesh and right image (b) is presenting mesh made by developed mesh generator. Black – solid phase; white – void phase; green – surface from *.stl file; blue – internal mesh boundaries; red – external mesh boundaries

Comparison of mesh generators is presented on the Figure 4.10. On the left side (Figure 4.10 a)) is the mesh made with snappyHexMesh. Black area is representing solid phase, white parts are void spaces, green line is surface made by Avizo (*.stl file), blue lines are internal mesh boundaries between neighboring cells and red lines are external boundaries between void and solid phase. It can be observed that there are some void spaces that are not included in the mesh. On the right there is a mesh made with our software. We can see that mesh external boundaries (red line) are at the same position as boundaries between void and solid in the XRMT image. Comparison on the same geometry and in the case when each voxel is divided into 27 equal cells shows that approximately 7% of void phase is not included in the approach when using snappyHexMesh.

Figure 4.11 illustrates impact of the mesh resolution to the flow simulation results on an example of a throat with diameter equal to one voxel in two dimensions. In laminar flow, velocity distribution is not uniform due to friction with side walls. According to the Poiseuille's Law velocity has a parabolic distribution [Adler, 1992] as illustrated on Figure 4.11 a) with fast moving fluid in the middle of the throat and almost stagnant. Figure 4.11 b) illustrates a case in which cell size is equal to the XRMT image size. Parabolic velocity distribution is substituted with only one value and in this case velocity distribution in the throat is neglected. On Figure 4.11 c) there is presented a case in which the mesh resolution is three times smaller than image resolution. In this case we see that velocity in the middle cell is larger than in the ones next to the boundary. It is possible to capture part of the throat velocity distribution. In ideal case mesh resolution would be small enough to capture full parabolic velocity distribution. However this would mean a very big mesh and consequently would make simulations extremely long and demanding in terms of computer power usage. Therefore it is necessary to find a mesh resolution that captures the most important flow field properties while creating a mesh that can be handled by available computer resources.

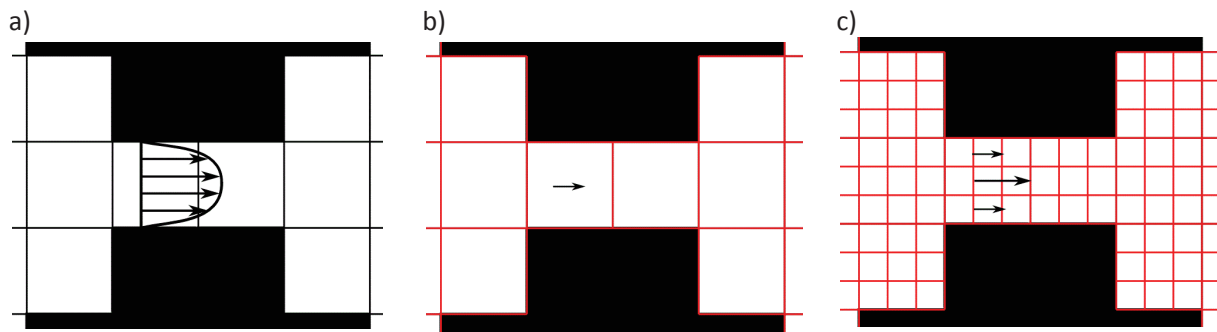


Figure 4.11 Velocity distribution in the pore throat with diameter equal to the XRMT image resolution a) parabolic velocity profile in real conditions; b) velocity distribution when mesh resolution is equal to image resolution; c) velocity distribution when mesh resolution is three times smaller than image resolution

Investigation to determine optimal mesh resolution is made on the 150x150x150 voxel image extracted from the one of the subsamples used in the numerical simulations and with approximate porosity as the whole image. We made 7 simulations with different cell size, every time voxels were divided by an integer in all three directions. After each simulation permeability is calculated (4.4) and results are presented in Table 4.1. Pixel divided column denotes integer used to divide voxel, e.g. by 3 denotes that voxel is divided by 3 in each direction and that each voxel contains 27 cells. We observe that permeability decreases with increase in the mesh resolution which is consistent with similar studies [Guibert et al., 2015].

Pixel divided	Permeability [mD]	Relative Difference [%]	Maximal sample volume [mm ³]	Characteristic length [1]
by 1	736	+22.3	2.84	25.8
by 2	657	+9.1	1.42	12.9
by 3	630	+4.7	0.948	8.6
by 4	617	+2.5	0.711	6.5
by 5	610	+1.3	0.569	5.2
by 6	605	+0.5	0.474	4.3
by 7	602		0.406	3.7

Table 4.1 Comparison of permeability to the mesh resolution, relative difference of calculated permeability compared to the finest mesh resolution, maximal sample volume that can be processed with available computational resources and characteristic lengths contained in maximal sample volume

The control of the refinement level on the computed permeability value is larger for coarser mesh and it decreases as mesh is refined. Permeability difference between coarsest and finest mesh is more than 22%, while difference between two finest meshes is less than 0.5%. We decided to use mesh that is refined by 3 from the original image and relative difference of less than 5% from the finest mesh resolution. Maximal sample volume for each refinement level in Table 4.1 shows that refinement by 3 gives a good compromise between simulation results quality and sufficiently large volumes of observed medium.

The boundary conditions at the edges of the computational domain are set to mimic an experimental permeameter: on the inlet and outlet sides of the sample a pressure difference is imposed, and no-flow conditions are specified on the other faces of the sample. No-slip condition is set at the solid-void interface. Twenty layers (21 μm) of void voxels have been added to the porous volume at the inlet and outlet boundaries in order to minimize the boundary effects [Guibert et al., 2015]. Figure 4.12 shows the final mesh of pore space structure for Berea sandstone including inflow and outflow manifolds.

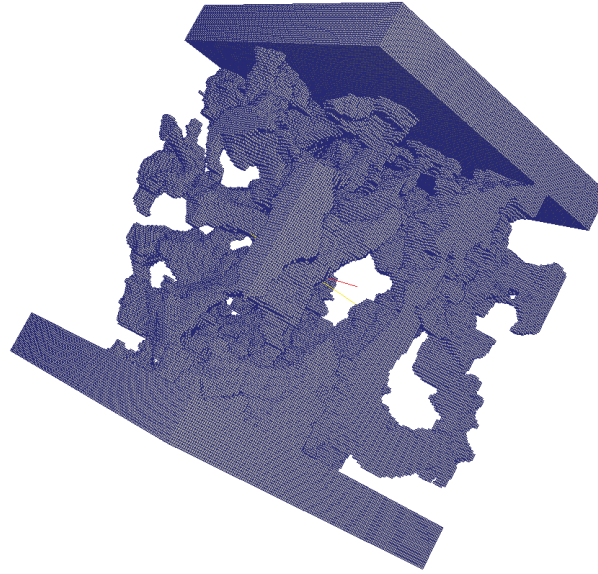


Figure 4.12 Mesh generated in pore space of Berea sandstone used for flow simulations, including manifolds on inlet and outlet boundaries

4.3.3 Solving flow

Pore scale flow field is obtained by direct CFD simulations performed on segmented XRMT images using open source CFD software package OpenFOAM® [OpenFOAM Foundation, 2014]. We solved the mass conservation equation (4.5) and the Navier-Stokes equation (4.6), for single phase flow with constant density and viscosity.

$$\nabla \cdot u = 0, \quad (4.5)$$

$$\rho \left(\frac{\partial u}{\partial t} + u \cdot \nabla u \right) = -\nabla p + \mu \nabla^2 u, \quad (4.6)$$

where u denotes superficial velocity [m/s], ρ is the fluid density [kg/m^3], t is the time [s], p is the pressure [Pa] and μ is dynamic fluid viscosity [Pa s].

OpenFOAM solver is based on a finite volume method which enables solving system of non-linear equations. The pressure and velocity are solved iteratively by a steady-state solver based on Semi-Implicit Method for Pressure-Linked Equations (SIMPLE) algorithm [Patankar, 1980]. SIMPLE algorithm belongs to Pressure-Based Method techniques to deal with pressure-velocity coupling in numerical simulations of the fluid flow. Detailed procedure has been described in Patankar and Spalding [1972], Caretto et al. [1972] and Patankar [1975].

The iterative procedure to couple Navier-Stokes equations can be summed up as follows:

1. Set the boundary conditions
2. Solve the discretized momentum equation to compute the intermediate velocity field
3. Compute the mass fluxes at the cell faces
4. Solve the pressure equation and apply under-relaxation
5. Correct the mass fluxes at the cell faces
6. Correct the velocities on the basis of the new pressure field
7. Update the boundary conditions
8. Repeat until convergence

In our case simulations are pressure driven, which means that pressure is imposed on inlet and outlet of the system as mentioned above. Since simulations are steady-state, pressure value at the boundaries is constant and flow is driven only by pressure difference (Δp) between inlet and outlet. Example of flow field is given in Figure 4.13. Blue color denotes regions with low local velocity while red color is used for regions with high local velocities.

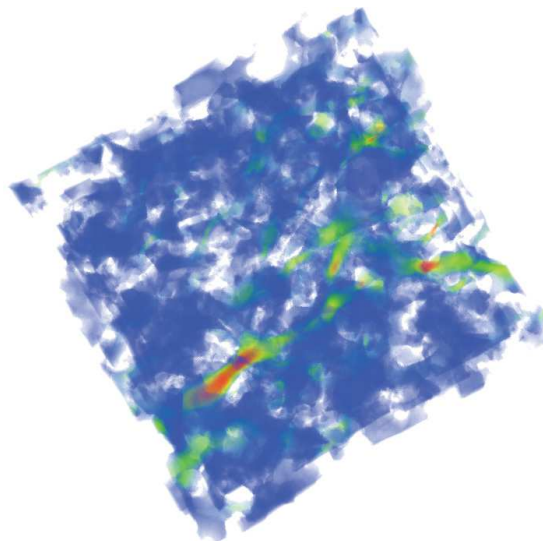


Figure 4.13 Flow field obtained from OpenFOAM, blue color denotes areas with low velocities while red denotes areas with high velocities

All the simulations are run for laminar flow condition; precisely with Reynolds number significantly lower than 1 ($Re \ll 1$). Reynolds number is a dimensionless unity used to distinguish different flow regime, described by equation [de Marsily, 1986]:

$$Re = \frac{\rho \bar{u} L}{\mu}, \quad (4.7)$$

where ρ denotes the fluid density [kg/m^3], \bar{u} is the average pore velocity [m/s], L is the characteristic length [m] and μ is the dynamic fluid viscosity [Pa s]. It defines ratio of inertial forces to

viscous forces. Low Reynolds number indicates dominance of viscous forces, thus occurrence of laminar flow regime which is associated with low velocities in the flow field.

When $Re \ll 1$ Stokes flow occurs and Navier-Stokes equation can be simplified to Stokes equation. However comparison between built-in solvers in OpenFOAM shows that the solver for full Navier-Stokes equation based on SIMPLE algorithm is much more efficient than comparable one for Stokes equation.

Convergence criterion

A convergence criterion in steady-state numerical simulations is always an arbitrary issue. Since every problem that needs to be simulated is different, there is no straight forward answer what is the optimal setup. For flow simulations in this work we decided to use two criteria to estimate when simulations are fully converged.

First criterion is based on mass balance and we monitored inlet and outlet flux from the domain. Standard utilities to calculate flux at the boundaries built-in the OpenFOAM are not appropriate for running in the same time with simulations, therefore we used a plug-in swak4Foam that prints inlet and outlet flux in real time.

Second criterion is based on initial residual values. Initial residual value presents relative differences in flow field parameters (e.g. velocity, pressure...) between the current iteration and the previous one. To determine initial residual values below which we have fully converged simulations, we run simulation till initial residuals for pressure and all three velocity components were lower than 10^{-9} . Permeability is calculated by equation (4.4) every time the residual is lower or equal to threshold. Figure 4.14 present the evolution of permeability with decreasing values of the initial residual. Permeability is stabilized when initial residual level is lower that 10^{-4} . To be sure that we use adequate convergence criteria that is still reasonable in terms of computational time all simulations in this thesis are stopped when initial residuals are below 10^{-5} .

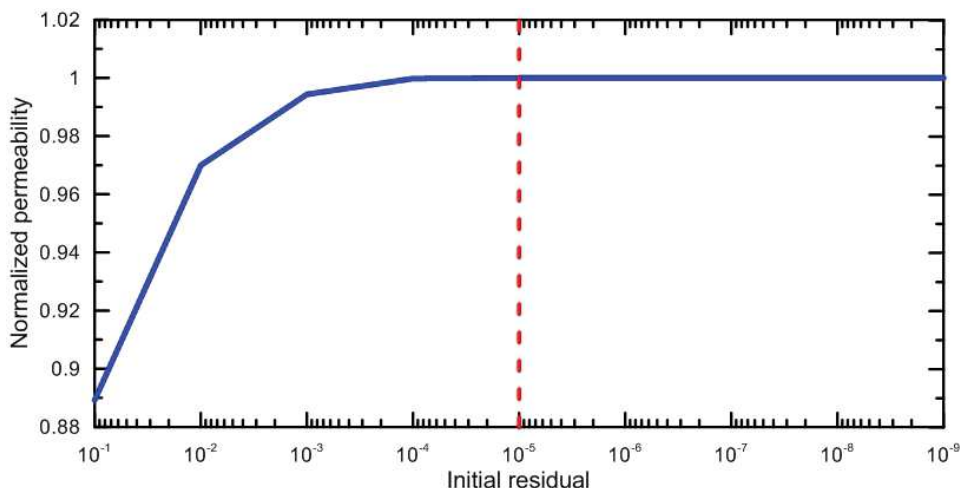


Figure 4.14 Normalized permeability in function of initial residual, red dashed line denotes initial residual level chosen as convergence criterion of all OpenFOAM simulations

Parallelization performance

Optimal usage of available computer resources reduces time needed to perform numerical simulations. Simulations were performed on a large memory computer using four 24-cores Intel Xeon (2.3 GHz) processors with 1,5 TB of RAM. To optimize our simulations, we performed scalability test on the simulation with same geometry, boundary conditions, convergence criteria and solver setup, only variable that changes is number of nodes used for calculations. All cases used simple method for mesh decomposition provided in OpenFOAM. Figure 4.15 presents results of parallelization performance investigations on mesh similar to ones used in the simulations. We observe a significant speed-up when increasing the number of *process* up to 16, while speed-up is negligible when increasing *process* number up to 24. All the simulations were performed using 18 to 24 *process* and they converged in less than three days.

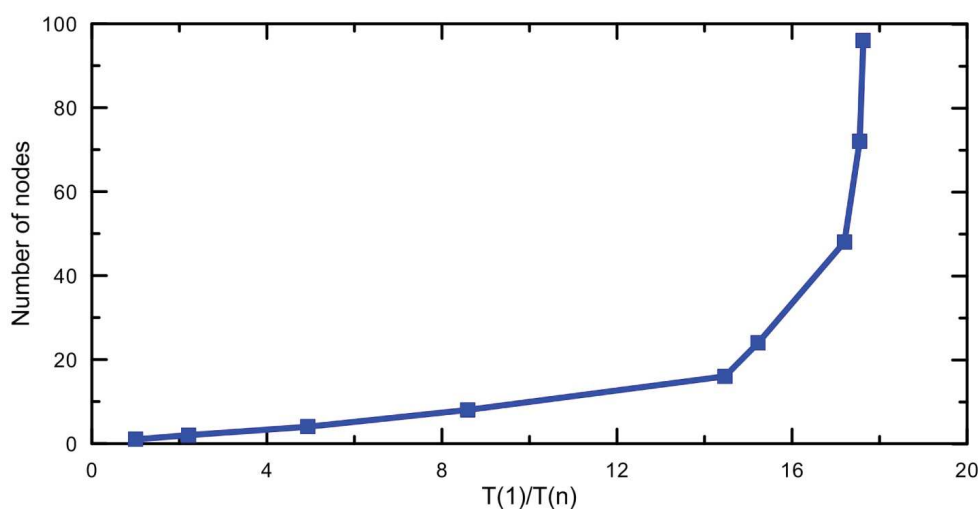


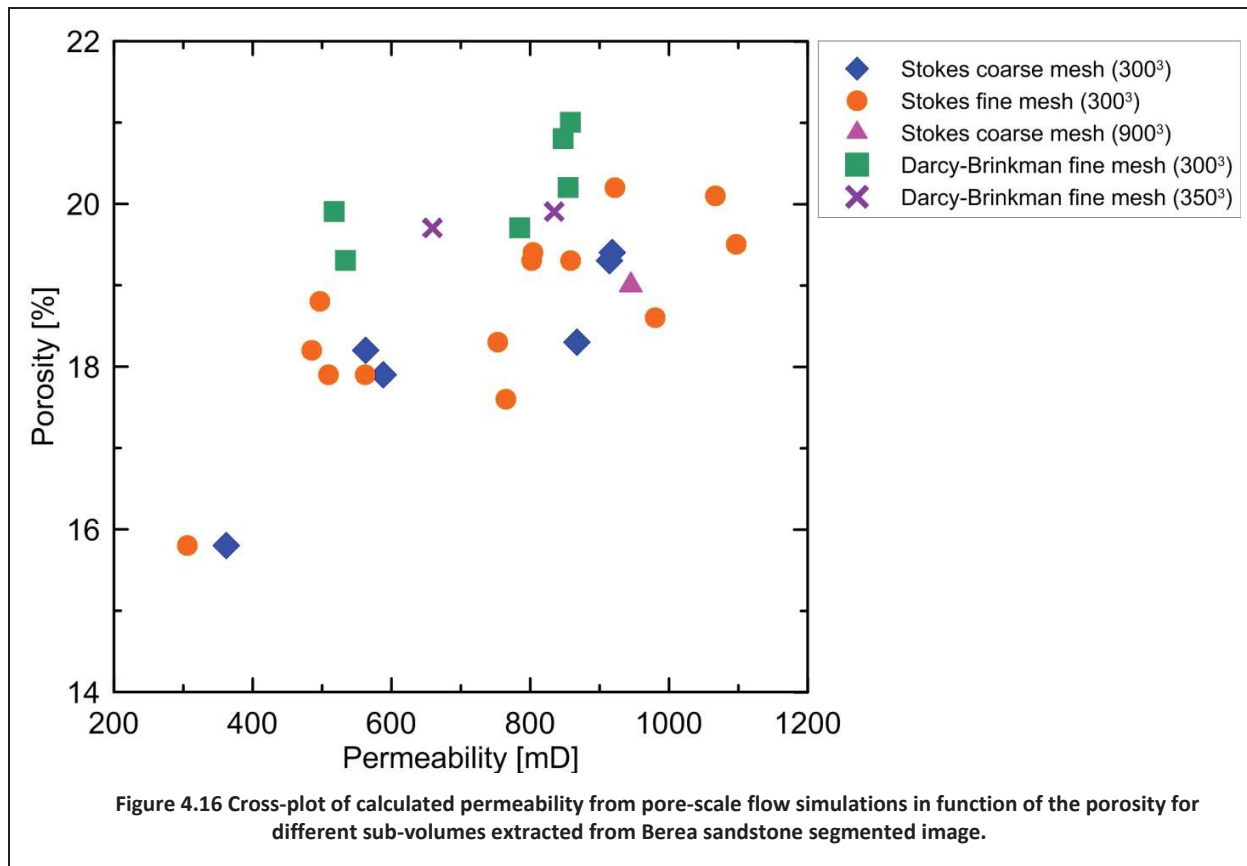
Figure 4.15 Results of OpenFOAM parallelization performance investigation, times are printed as relative speed-up compared to the simulation time of non-parallelized simulation

4.4 Results and discussion

In this section we focus mostly on the flow statistics and properties, since transport results are presented in Chapter 5. Figure 4.16 presents a cross plot between porosity and calculated permeability made on the Berea sandstones sub-volumes with different mesh resolutions and using different simulation approaches. Mesh resolution is discussed in details in section 4.3.2 and in this comparison we use three different mesh resolutions. The coarse mesh has same resolution as image and the fine mesh is obtained by dividing each voxel by 3 in all directions.

Regarding simulation approaches we used a conservative approach which implies solving Stokes equation in the mobile zone as presented in the section 4.3.3. These results are then compared with the Darcy-Brinkman approach that allows flow computations in the microporous zone as well. More details regarding the Darcy-Brinkman solver implemented in OpenFOAM and comparison with the Stokes solver are presented in Chapter 6.

As expected, there is globally a weak positive correlation between porosity and permeability (Figure 4.16). It can be noted that adding flow calculation in the microporosity does not have a significant influence on the permeability while it induces a noticeable change of the porosity. This is reasonable since velocities in the microporous zone have one or several orders of magnitude lower values than in macroporous zone and there is only very few zones where the connectivity is controlled by microporous clusters.



4.4.1 Mesh comparison

Mesh resolution has significant effect on the flow simulation results. Table 4.1 presents influence of seven different mesh resolutions on the permeability of the small sub-volume of Berea sandstone. Here we present a more detailed investigation focused on coarse and fine mesh resolution. Table 4.2 shows differences in the permeability between two mesh resolutions for six different sub-volumes of Berea sandstone. Permeability calculated from the coarse mesh is always higher than the one calculated from the fine mesh by 14 to 18.3%. These results are in good agreement with previous investigation (Table 4.1) and relevant studies [Guibert et al., 2015].

	Porosity (%)	Permeability (mD)		Relative difference (%)
		coarse mesh	fine mesh	
SubV1	19.4	918	804	14.2
SubV2	19.3	914	802	14.0
SubV3	18.3	867	753	15.1
SubV4	18.2	563	485	16.1
SubV5	17.9	588	509	15.5
SubV6	15.8	362	306	18.3

Table 4.2 Comparison of permeability calculated from flow simulations performed on coarse and fine mesh. Six different sub-volumes extracted from segmented image of Berea sandstone.

Differences between two mesh resolutions are also visible at high velocities in the probability density function (section 5.3, Figure 9), where probability of achieving higher velocity is higher in coarser mesh. That was in conflict with our assumption shown in the Figure 4.11 where one could expect lower maximal velocities in the coarse mesh due to averaging errors.

Figures from 4.17 to 4.22 show average (a), maximal (b) and minimum (c) velocities per slice perpendicular to the flow direction for different sub-volumes and different mesh resolution. Blue line is always denoting fine mesh; orange line is for coarse mesh and dashed black line represents local porosity. There is clear negative correlation between porosity and average velocity, however there is no correlation between porosity and minimal and maximal velocities.

When comparing averages velocities per slice there is a clear offset and average velocities are always higher in the coarser mesh. There is no significant variation in differences between average velocities. Observed offset of around 10-15% is in accordance with permeability differences and also cross plot between coarse grained average velocity from fine mesh and corresponding velocity in coarse mesh (section 5.3, Figure 9).

Comparison between maximal and minimal velocities (Figures 4.17-4.22 b) and c)) shows that in all situations maximal velocity is higher in the coarse mesh. Similar minimal velocity per slice is lower in the coarse mesh; however this difference is even less highlighted. Although it is clear that coarser mesh causes greater differences in velocity distribution, deviation is relatively small.

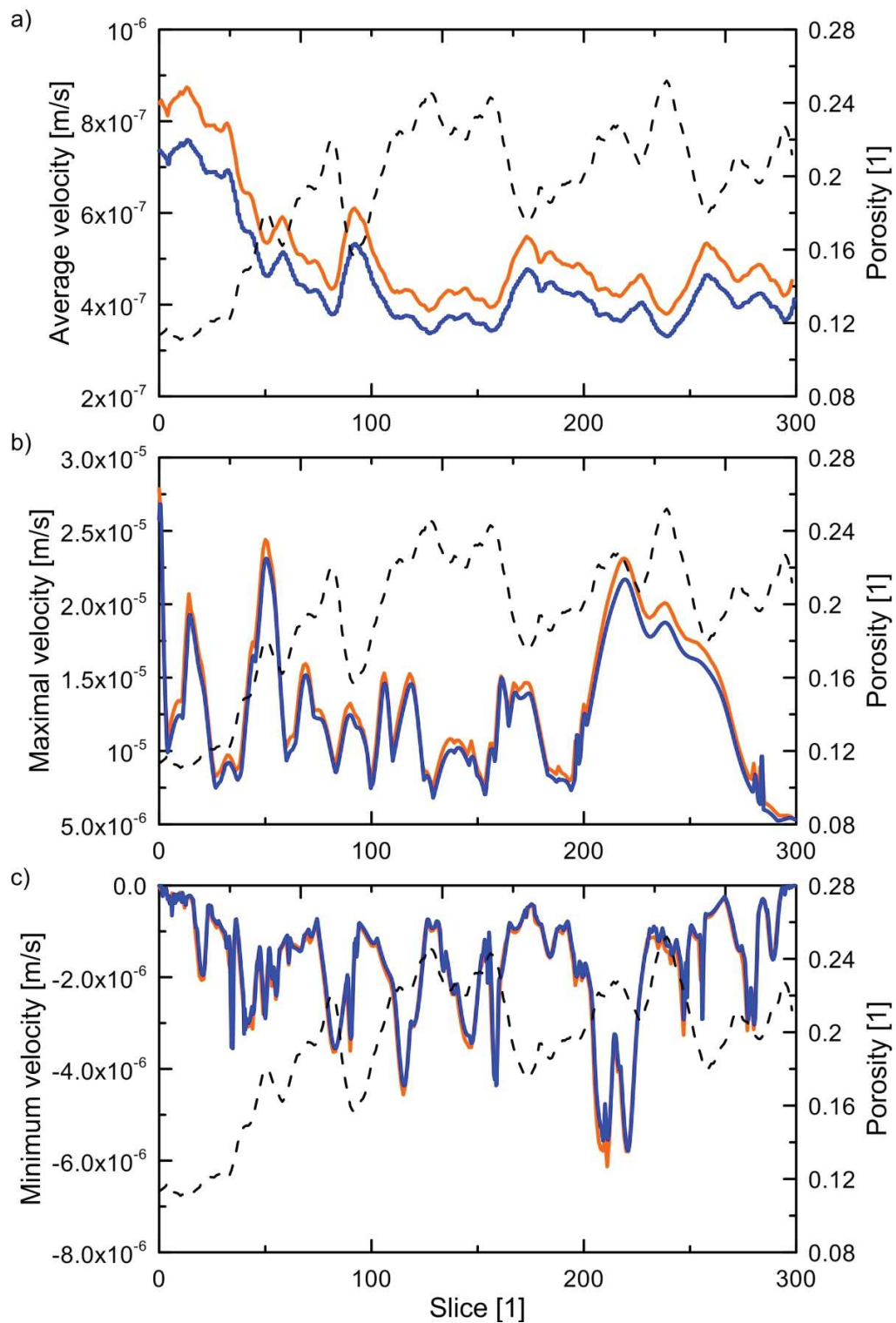


Figure 4.17 SubV1. Comparison of a) average, b) maximal and c) minimal velocity per cross-section profiles perpendicular to the flow direction for coarse (orange line) and fine mesh (blue line) with corresponding local porosity (black dashed line).

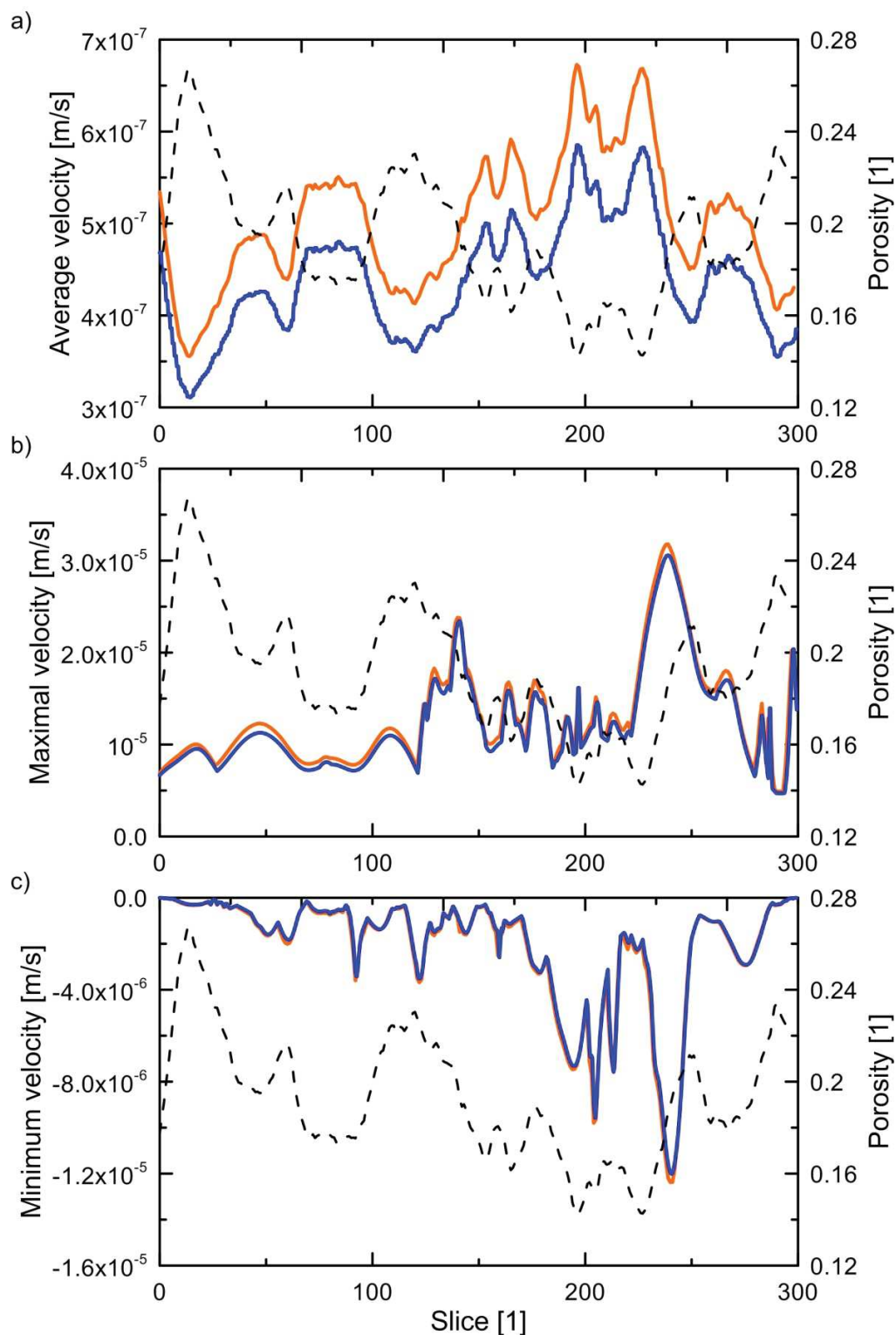


Figure 4.18 SubV2. Comparison of a) average, b) maximal and c) minimal velocity per cross-section profiles perpendicular to the flow direction for coarse (orange line) and fine mesh (blue line) with corresponding local porosity (black dashed line).

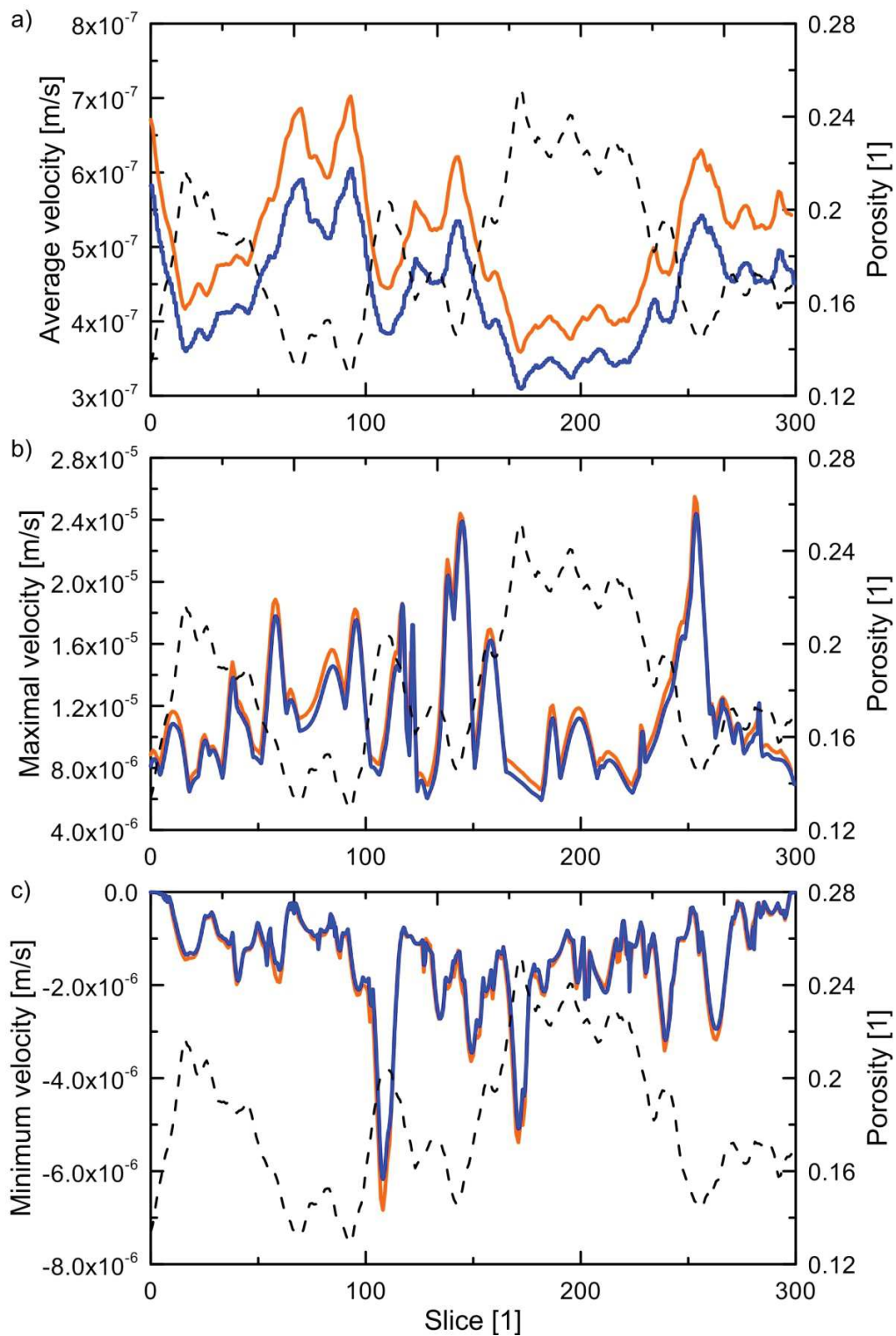


Figure 4.19 SubV3. Comparison of a) average, b) maximal and c) minimal velocity per cross-section profiles perpendicular to the flow direction for coarse (orange line) and fine mesh (blue line) with corresponding local porosity (black dashed line).

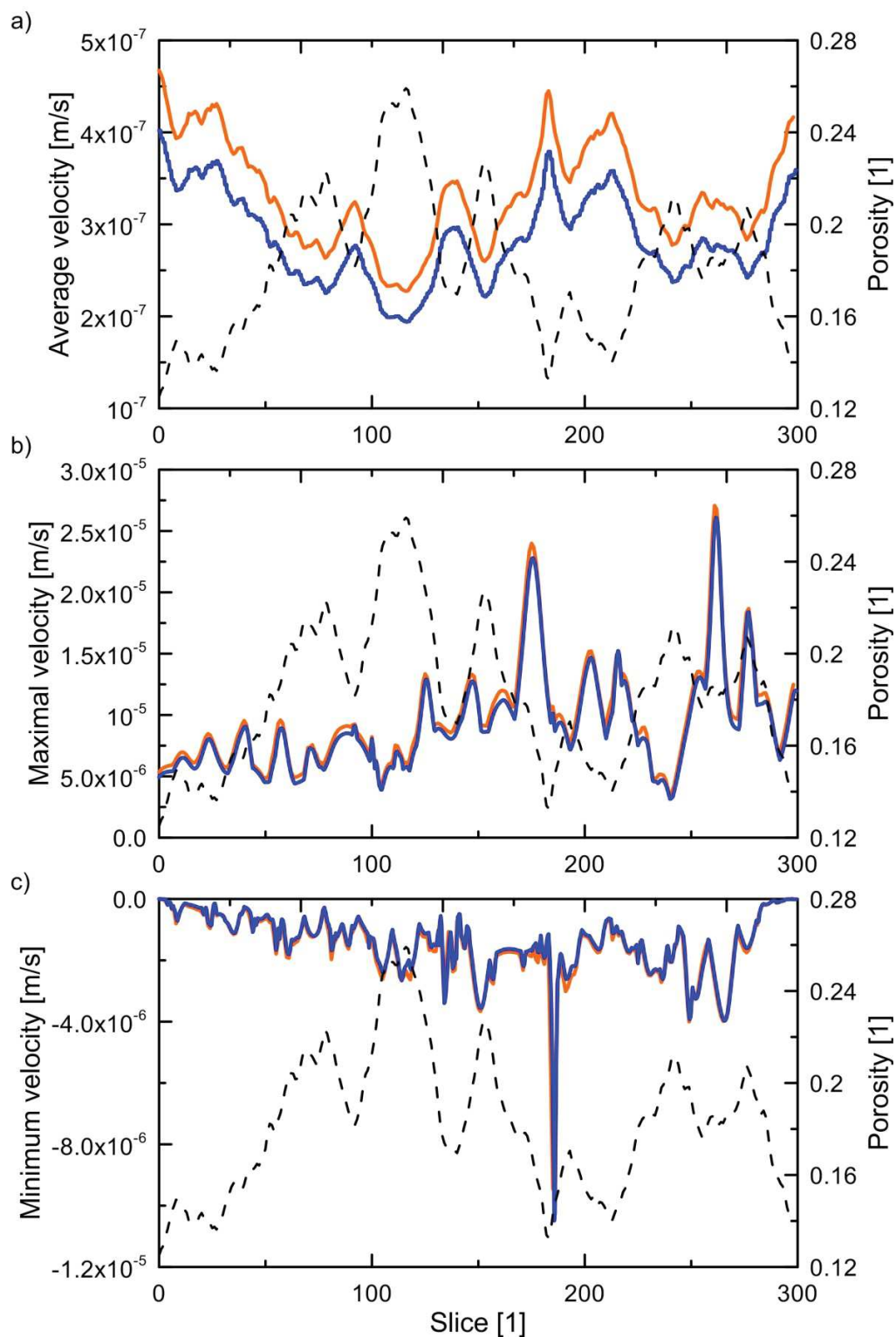


Figure 4.20 SubV4. Comparison of a) average, b) maximal and c) minimal velocity per cross-section profiles perpendicular to the flow direction for coarse (orange line) and fine mesh (blue line) with corresponding local porosity (black dashed line).

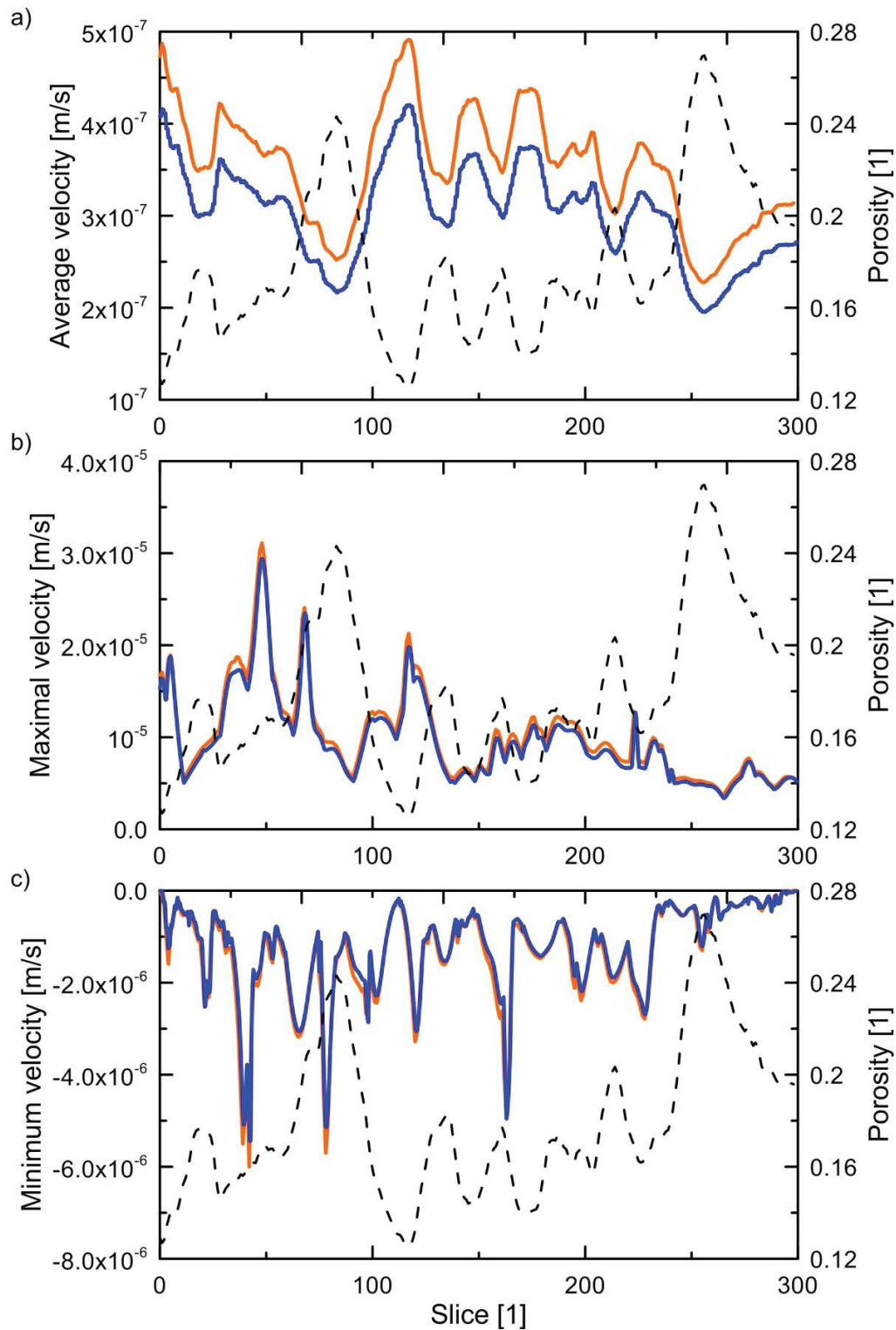


Figure 4.21 SubV5. Comparison of a) average, b) maximal and c) minimal velocity per cross-section profiles perpendicular to the flow direction for coarse (orange line) and fine mesh (blue line) with corresponding local porosity (black dashed line).

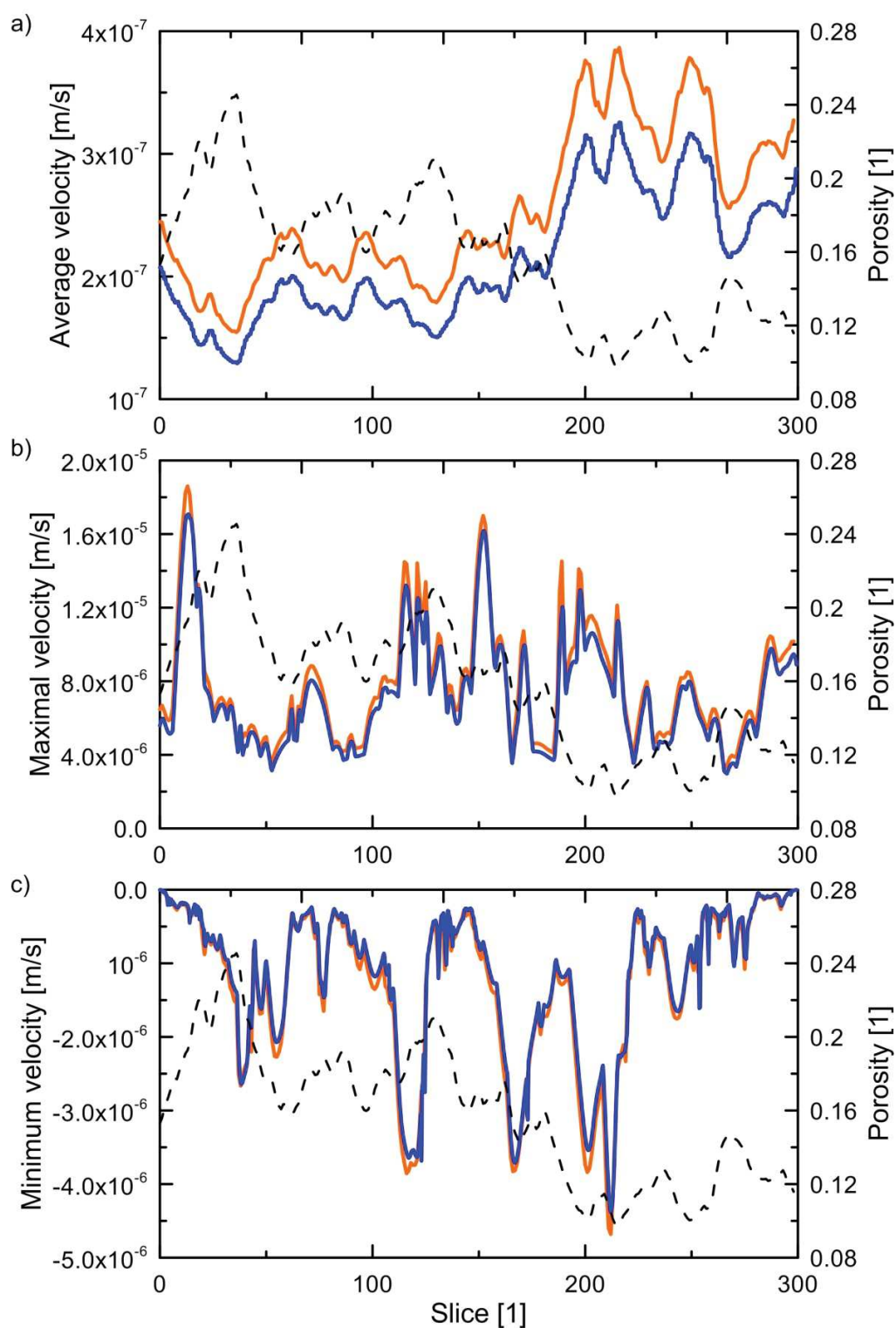


Figure 4.22 SubV6. Comparison of a) average, b) maximal and c) minimal velocity per cross-section profiles perpendicular to the flow direction for coarse (orange line) and fine mesh (blue line) with corresponding local porosity (black dashed line).

To gain even better understanding of the mesh resolution impact on the velocity field distribution we created 3D artificial structure simulating a synthetic throat between two pores (Figure 4.23). The structure is completely symmetric and it gradually decreases in area perpendicular to the flow direction until it reaches the size of one pixel. The coarsest mesh has same resolution as the original structure, and all other meshes are gradually finer. Resolution is increased by principle explained in the section 4.3.2.

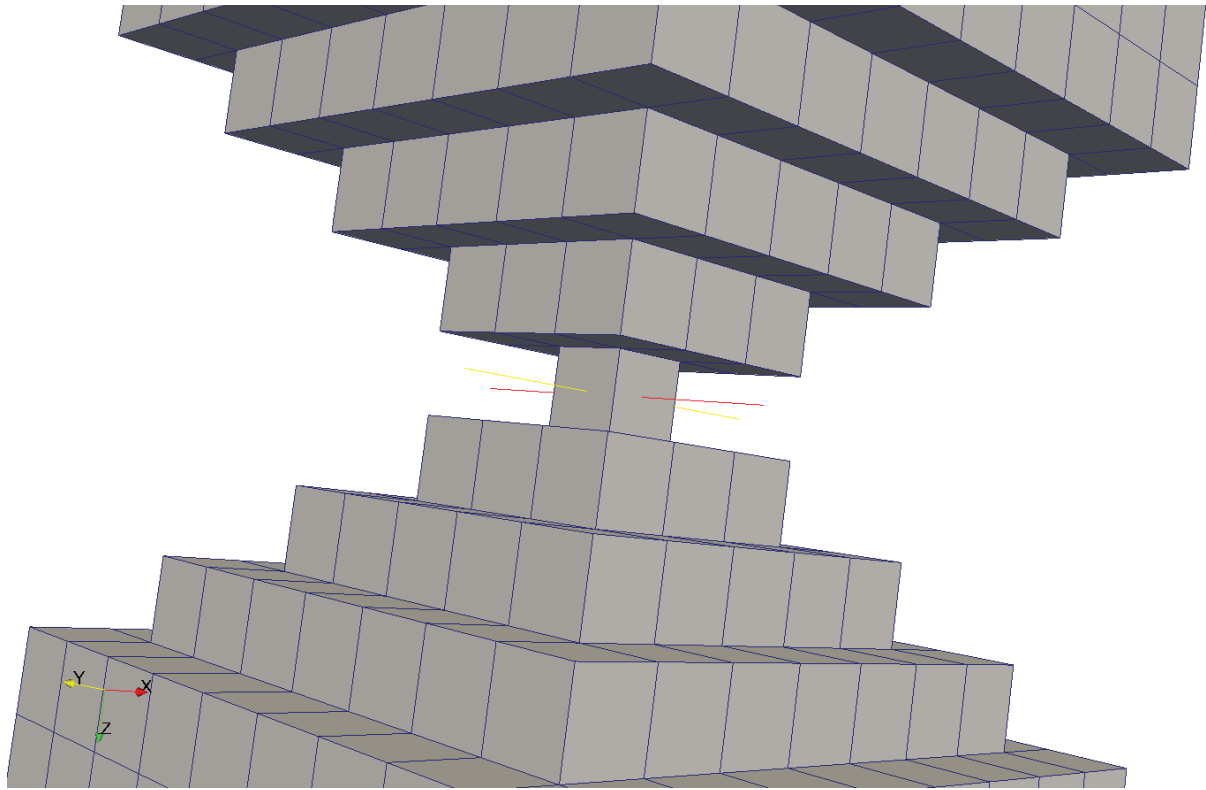


Figure 4.23 Artificial 3d symmetric structure, designed to investigate flow-through smallest possible throat (1 pixel)

Permeability and maximal velocity for different mesh resolutions are summarized in Table 4.3. Relative differences are calculated regarding to finest mesh results. Again one can observe a gradual decrease in the absolute permeability that is in accordance with relevant studies and previous investigations presented in this thesis (Table 4.1). However, differences in this case are more pronounced. This is probably due to the structure geometry which is designed to investigate case where largest differences are expected. From the table it can be noticed that maximal velocities in the meshes where pixels were divided by even number are lower than comparable meshes where pixels are divided by odd number. This is due to the fact that meshes where pixels are divided by even integer fail to capture the maximal velocity in the middle of the throat.

Pixel divided	Permeability (mD)	Relative difference (%)	Max velocity (m/s)	Relative difference (%)
by 1	77.2	+175	$1.825 \cdot 10^{-5}$	+19.4
by 2	44.9	+60.4	$1.19 \cdot 10^{-5}$	-22.1
by 3	36.1	+28.9	$1.644 \cdot 10^{-5}$	+7.3
by 4	32.2	+15	$1.443 \cdot 10^{-5}$	-5.6
by 5	30.1	+7.5	$1.557 \cdot 10^{-5}$	+1.9
by 6	28.9	+3.2	$1.472 \cdot 10^{-5}$	-3.6
by 7	28		$1.528 \cdot 10^{-5}$	

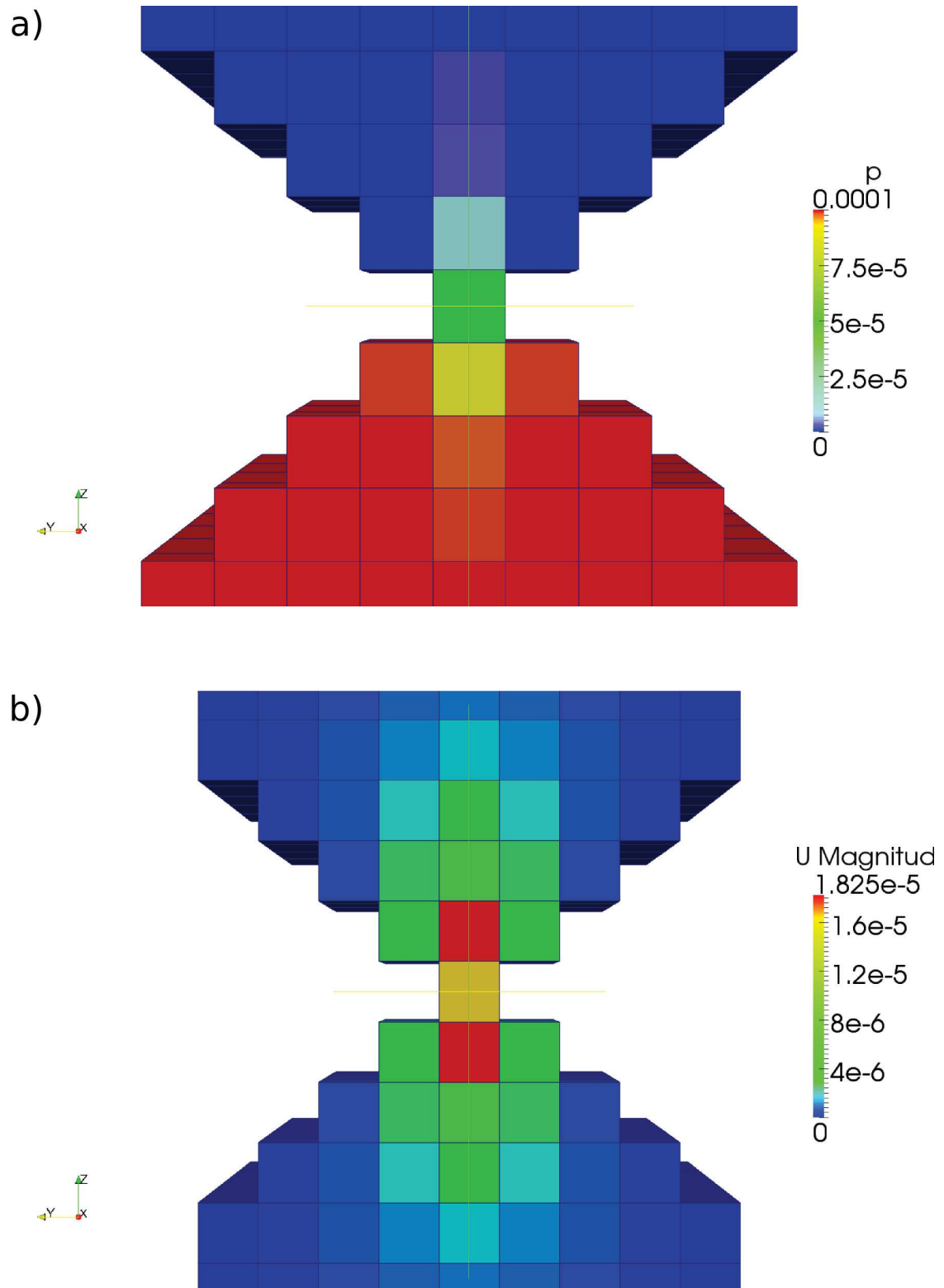
Table 4.3 Comparison of the permeability and the maximal velocity at different mesh resolution. Simulations are performed on the 3D symmetric artificial structure simulating smallest possible throat in porous media

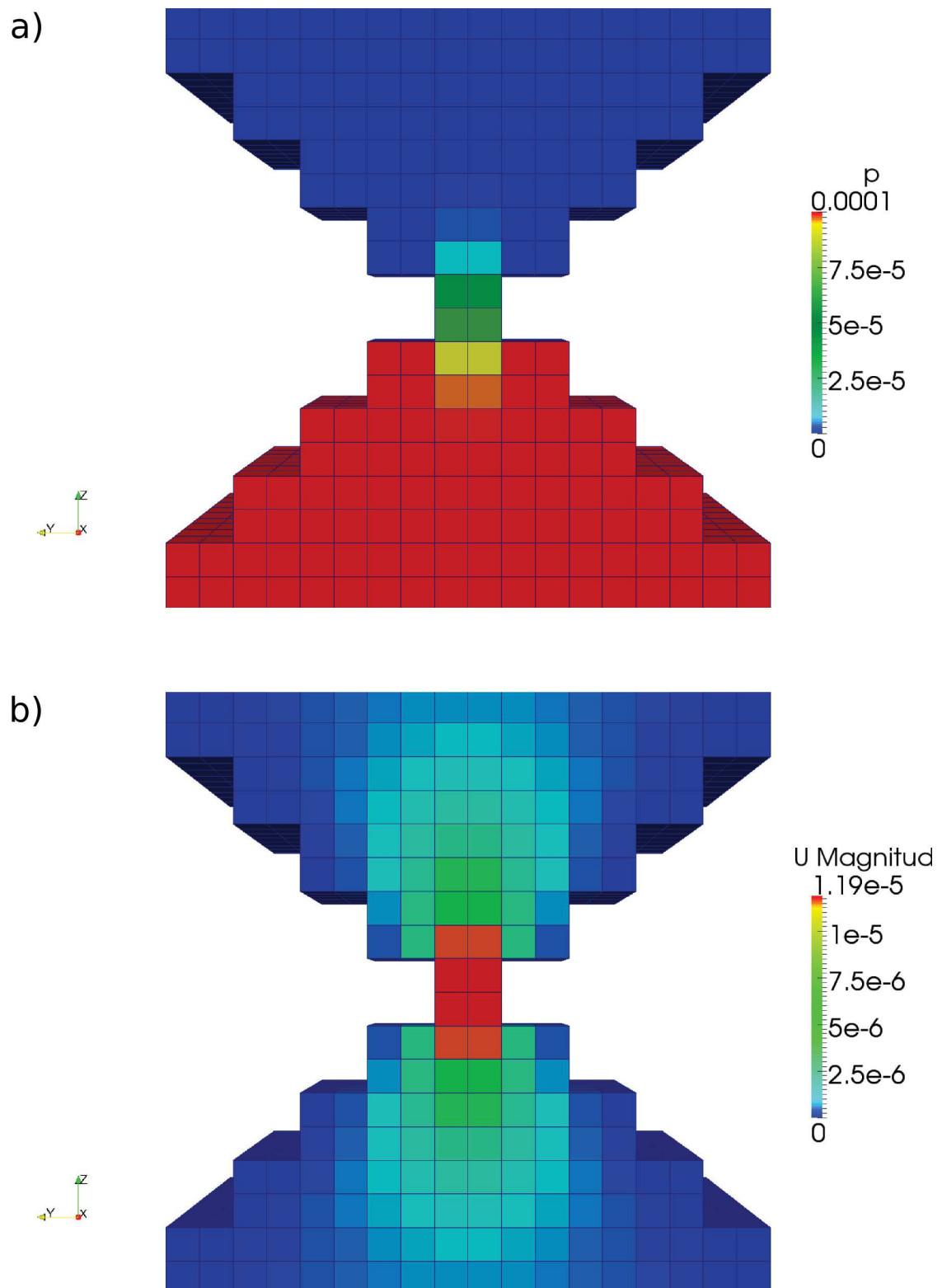
Figures 4.24-4.27 shows the pressure (a) and velocity field (b) distribution for different mesh resolutions. Figure 4.27 presents flow field results for finest mesh (each pixel divided by 7 in all 3 directions), it is considered as the best approximation of the real flow field. One can observe that if mesh has same resolution as image (Figure 4.24), it completely fails to reproduce realistic pressure and velocity distribution. Even more worrying is that maximal velocities occur in cross sections before and after the narrowest one. Therefore, mass conservation is questionable, although fluxes at inlet and outlet of the system at the end of simulation are the same. We repeated the simulation several times with different pressure gradients and increasing convergence criterion, however results are always the same. Detailed investigation of the relative cell divergence revealed that divergence in the cross section before throat is equal to 7×10^{-4} , while divergence in finer meshes never reaches 6×10^{-6} . However this does not fully explain the value of 9 % lower local velocity in the throat compared to neighboring cross sections. Relative cell (i) divergence (div) is calculated by equation

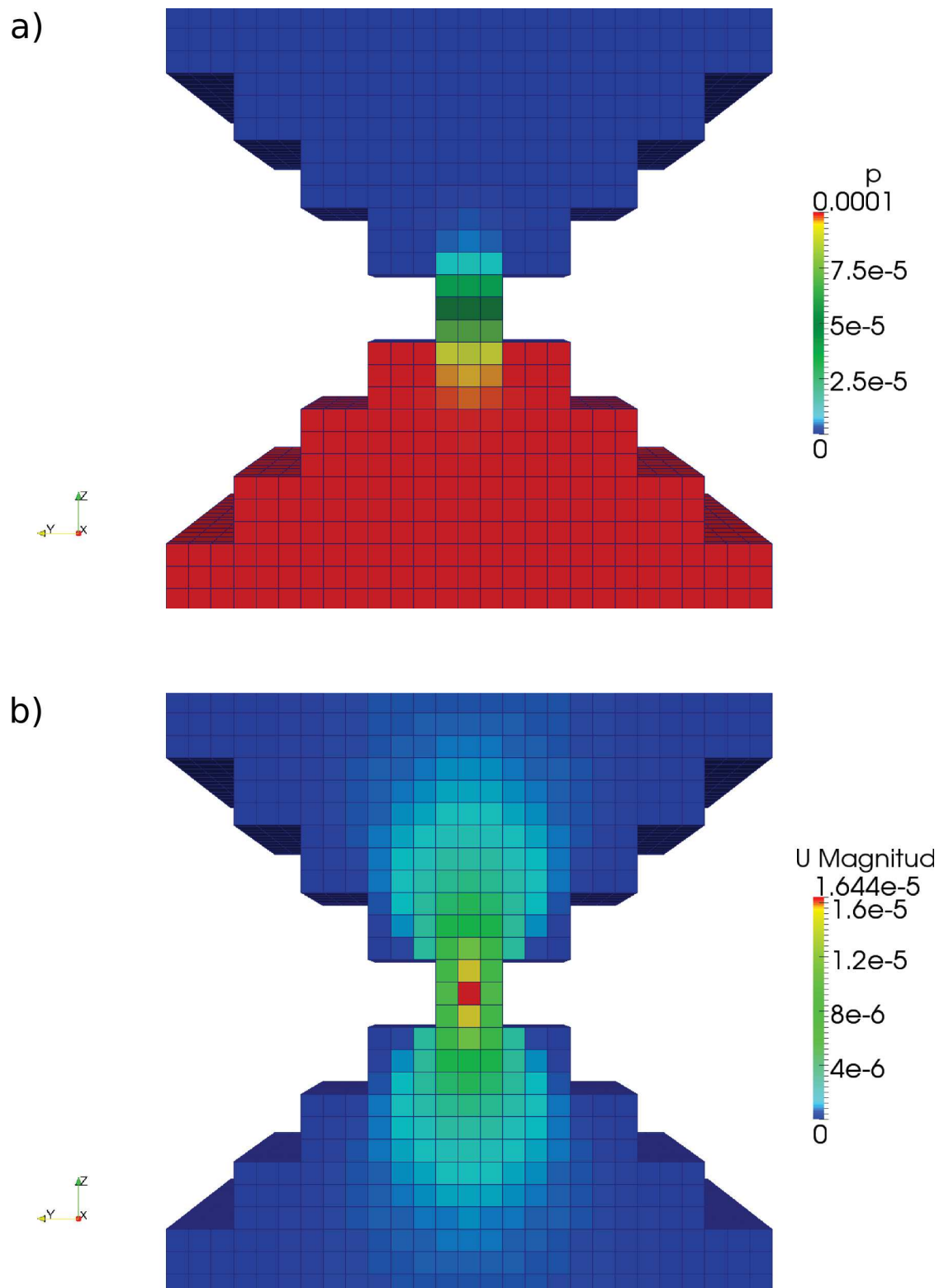
$$div_i = \frac{\sum_{j=6}^j \vec{q}_{j_i}}{u_i}, \quad (4.8)$$

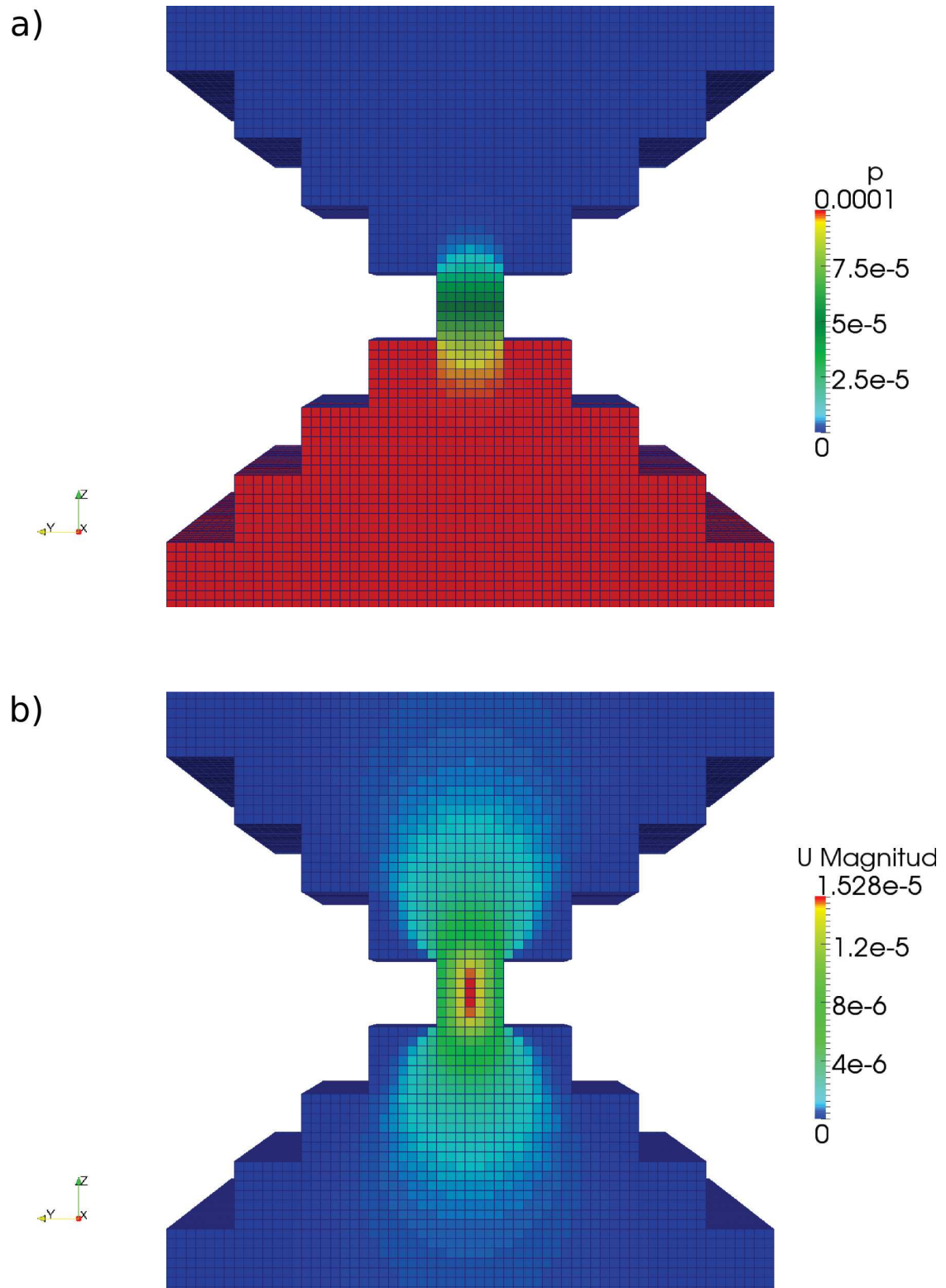
where $\sum_{j=6}^j \vec{q}_{j_i}$ is the sum of the fluxes at all six faces of the cell and u is magnitude of the velocity in the cell centre.

Pressure distribution for the second mesh (pixels divided by 2) is significantly better (Figure 4.25 a)). However the velocity distributions map (Figure 4.25 b)) shows that at this resolution there are still significant misinterpretations of velocities in the throat. Contrary to the coarser mesh, in case when mesh has a three times higher resolution than the original image, pressure and velocity distributions (Figure 4.26) are in good agreement with the finest mesh.









4.5 Summary and conclusion

In this section the methodology used for solving flow from the XRMT images is presented. Starting from image acquisition, followed by the segmentation and removal of non-connected porosity, to the Navier-Stokes solver implemented in the OpenFOAM software package, which allowed flow field calculations. Also different ways for calculating the characteristic length and representative elementary volume are presented.

Development of mesh generator allowed transferring pore geometry directly from the segmented images to the numerical solver. Also it allowed investigating the mesh resolution influence on the accuracy of the flow simulations. This issue was recently accentuated by Guibert et al. [2015] and in this work we expand their investigation by investigating further refinements of the mesh size and discretization.

Similar to the other authors it has been observed a decrease in the permeability with the mesh refinement (Table 4.1). We showed that common practice where one image voxel is modeled by one mesh cell induces significant deviations from the results using meshes with higher discretization of the same structure. Also in some cases (e.g. modeling one pixel sized throat) flow field representation is completely unrealistic. It has been shown that the optimal mesh resolution is if each voxel is represented by 27 mesh cells in the case of our Berea sandstone image

Similar scaling of the permeability to mesh resolution observed in our investigation is expected in other porous media displaying dissimilar complexity and pore geometry characteristic. However, the mesh refinement factor necessary to obtain satisfactory results may differ significantly due to the image resolution and porous medium properties. As a general rule for porous medium with very narrow throats it is advisable to use odd mesh refinement factor (e.g. 3,5,7..) in order to achieve more realistic flow field approximations.

5.1 Introduction

This section presents transport simulations performed directly on the X-ray microtomography images focusing on the dispersion of ideal tracer in a porous medium. Image processing and flow simulations are presented in the previous chapter (Chapter 4). Selected sub-volumes (300^3 voxels) were post processed after flow simulations and used as an input data for transport simulations.

The hydrodiffusive transport of a passive tracer is modeled by random walk particle tracking method in which solute concentration field is represented by the ensemble average of particles. Actually these particles are random walkers, which are considered to be without mass, infinitesimally small and that they do not interact between each other or with the porous medium. In the random walk methods a large number of particle moves through the medium taking random steps that may vary in distance, direction and time need to make a step. Although path taken by each particle is not representative; the ensemble average of the motion of a large number of particles represents the solute transport behavior for given boundary conditions.

There are numerous different random walk methods and in this work we decided to use the time domain random walk (TDRW). TDRW proved to be very efficient tool since it is based on the particle movements with constant length, while stochasticity arises from the direction of the step and time between two consecutive steps. Constant step size makes TDRW very suitable to use in the discretized media with complex geometry; where other methods with stochastic distribution of step size would cause numerous missteps and thus have negative influence on the duration of simulations.

Main results, discussion and conclusions are presented in form of an article (see section 5.3) accepted in Water Resources Research. Expanded theory and assumptions taken into account during modeling transport in microporous domain are presented hereafter (section 5.2).

5.2 Immobile region properties

5.2.1 Percolation threshold of microporosity

Similar as discussed in section 0 for macroporosity, there is also a fraction of unconnected porosity in the microporous phase which is inaccessible for solute transport. Contrary to macroporosity, unconnected microporosity cannot be detected from XRMT images, since pores are smaller than image resolution. In terms of continuous model, intrinsic porosity of microporous phase has to be higher than percolation threshold (ϕ_θ) in order that microporosity is accessible to flow and transport.

Figure 5.1 presents an illustration of percolation threshold effect. In this illustration it is assumed that solute is diffused into immobile domain from mobile domain (blue) at the top. Figure 5.1 a) shows distributed intrinsic porosity of microporous phase without percolation threshold applied. Gray level denotes value of intrinsic porosity, where darker colors represent areas with lower intrinsic porosity while lighter colors are used for areas with higher intrinsic porosity. Influence of low percolation threshold is shown on Figure 5.1 b) where one can see yellow areas that are considered to be

inaccessible for diffusion since intrinsic porosity is lower than percolation threshold. Here we observe that inaccessible microporosity is scattered in microporous phase and lacunarity is increased. As a consequence of lacunarity (i.e. heterogeneity of microporous phase), macroscopic tortuosity in microporous phase is increased as presented on the Figure 5.1 c). Red arrows denote flow paths taken by solute in microporosity. This increase of heterogeneity in microporous phase means that transient time that solute experience when diffuse into microporous phase is increased. Consequently tails in break through curve is elongated. Finally when percolation threshold is increased so that most of microporosity is inaccessible to diffusion (Figure 5.1 d)), the influence of the microporosity on transport is reduced because smaller volume is accessible to diffusion.

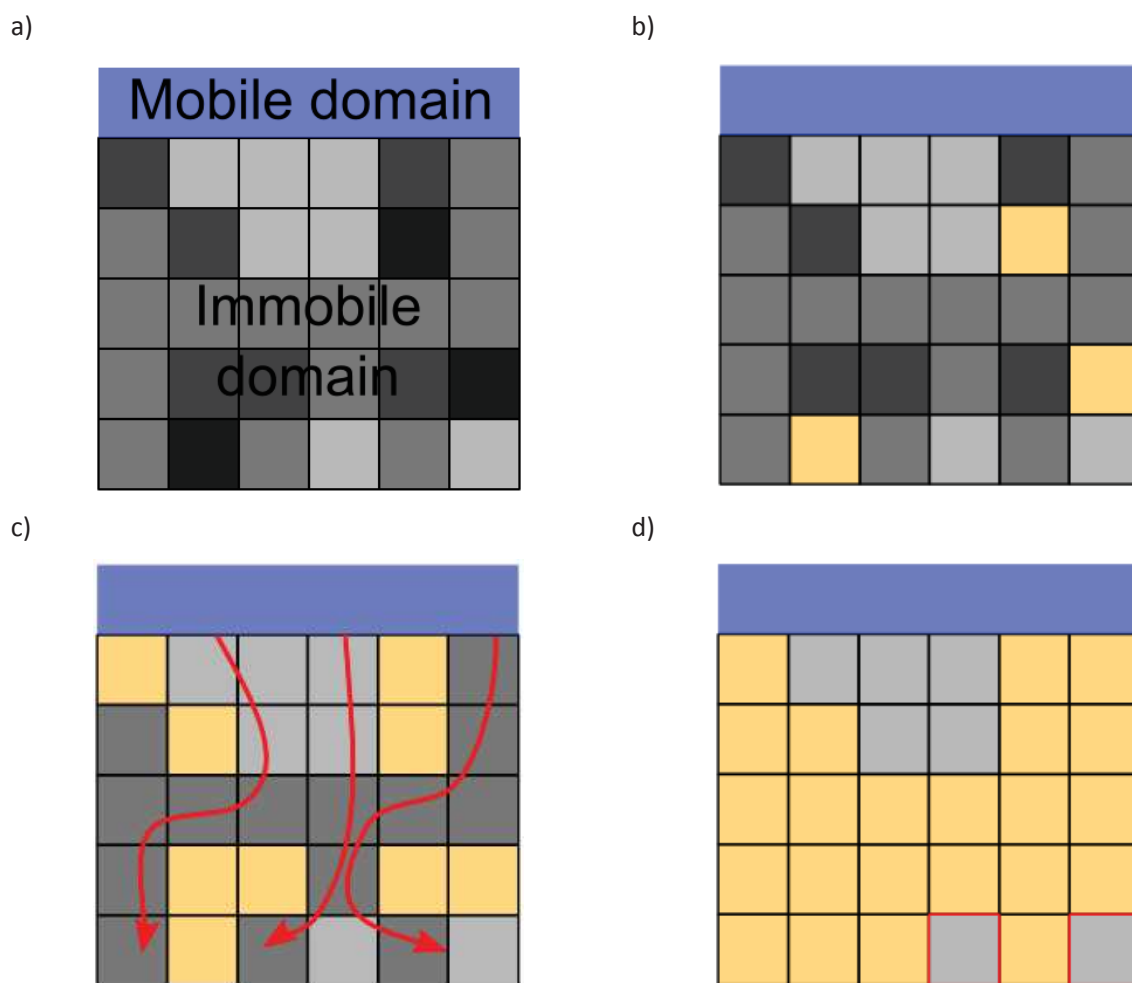


Figure 5.1 Illustration of evolution of percolation threshold in microporous phase. Blue color denotes mobile domain from which solute diffuses in microporosity, microporous phase is represented with gray pixels where gray level represents intrinsic porosity (darker gray lower intrinsic porosity and vice versa) and yellow color denotes areas with intrinsic porosity lower than percolation threshold; a) no percolation threshold applied, b) low percolation threshold level, c) medium percolation threshold level and d) high percolation threshold

5.2.2 Tortuosity

In this work we will not calculate the tortuosity explicitly; however since it is an important parameter that strongly influences the transport in the 3-phase segmented porous medium, we will briefly present the theory standing behind. The concept of the tortuosity (τ) was introduced by Carman [1937], who defined it as square of the ratio of the effective average path length (l_e) to the shortest distance (l) as presented on the Figure 5.2 and with equation (5.1).

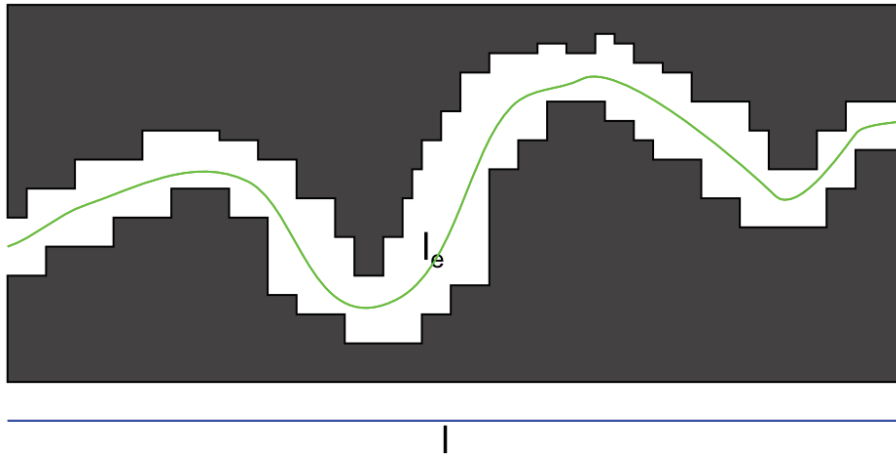


Figure 5.2 Illustration of tortuosity definition by Carman (1937). Effective average path (l_e) in the porous media (green line) and shortest possible distance measured along transport direction (l) (blue line)

$$\tau = \left(\frac{l_e}{l}\right)^2. \quad (5.1)$$

Many authors developed other definitions of tortuosity (e.g. Bear and Bachmat, 1986); however, there is still no universal definition [Lorenz, 1961; Dullien, 1992; Clennel, 1997]. Different definitions of the tortuosity is used by physicists, engineers and geologists to describe the sinuosity and interconnectedness of the pore space that affects transport processes taking place in a porous medium. Some of the most common definitions of the tortuosity are geometrical, electrical, hydraulic and diffusional tortuosity. With the exception of the geometrical tortuosity which can be measured only if the 3D geometry of the pore space is known, the other definitions of tortuosity refer to different mechanisms of mass or energy transport. It follows that relations between these definitions of tortuosity are not simple because they come distinctly different types of measurement or computation [Clennel, 1997].

In this work tortuosity is considered as one of the parameters contributing to the reduction of the molecular diffusivity in the immobile domain (see section 0). Therefore, the most suitable definition for our problem is the diffusional tortuosity. It can be defined as a ratio between molecular diffusivity (d_0) and the effective diffusivity $d^{(e)}$

$$\tau_D = \frac{d_0}{d^{(e)}}. \quad (5.2)$$

In bulk solution the rate of molecular diffusion is defined by the molecular properties of the fluid and the tracer as well as the temperature and pressure in the system. However under same conditions, the spreading of a passive tracer in a porous medium is significantly slower than in free fluid due to the inhibiting effects of the complex structure that slow down spreading in all directions. The diffusional tortuosity can be modeled with a random walk method; however in case of the microporosity defined in our images it is not possible since pores are smaller than the image resolution, and therefore we must define the effective diffusion coefficient from a model.

5.2.3 Effective diffusion in the microporosity

Diffusive mass transfer rate in microporosity varies spatially due to structure complexity of microporosity. Complexity arises from different intrinsic porosity and tortuosity structure at different locations and thus causing spatial variations of effective diffusion coefficient($d^{(e)}$). Diffusive mass transfer into microporosity domain (μ) is described by diffusion equation:

$$\phi_{\mu}(\mathbf{x}) \frac{\partial c_{\mu}(\mathbf{x}, t)}{\partial t} = \nabla \cdot [d^{(e)}(\mathbf{x}) \nabla c_{\mu}(\mathbf{x}, t)], \quad (5.3)$$

where initial concentration in microporosity is 0 ($c_{\mu}(\mathbf{x}, t = 0) = 0$) and boundary condition at the interface between macro and microporous domain $c_{\mu}(\mathbf{x}, t)|_{x \in \partial\Omega} = c_m(\mathbf{x}, t)$. Diffusion coefficient depends on the local properties that are the intrinsic porosity $\phi_{\mu}(\mathbf{x})$ and the tortuosity $\tau_{\mu}(\mathbf{x})$. It is defined by equation:

$$d^{(e)}(\mathbf{x}) = \tau_{\mu}^{-1}(\mathbf{x}) \phi_{\mu}(\mathbf{x}) d_0. \quad (5.4)$$

The tortuosity of the microporous phase cannot be determined from XRMT images. Many authors [Avallandea and Torquato, 1991; Clennel, 1997; Dias et al., 2006] suggested that the inverse of tortuosity scales as a power law of porosity. This approximation is confirmed for porosities ranging from 0.4 to 0.5. To the best of our knowledge, this approach has not been validated for lower porosities. However, due to lack any other information or means to calculate tortuosity in the microporous phase, we consider the above-mentioned relation to be valid even for low intrinsic porosity. Therefore, in equation (5.4) tortuosity term can be expressed as power law of intrinsic porosity $\tau_{\mu}(\mathbf{x}) = \phi_{\mu}(\mathbf{x})^{-m}$, and accordingly the effective diffusion can be rewritten:

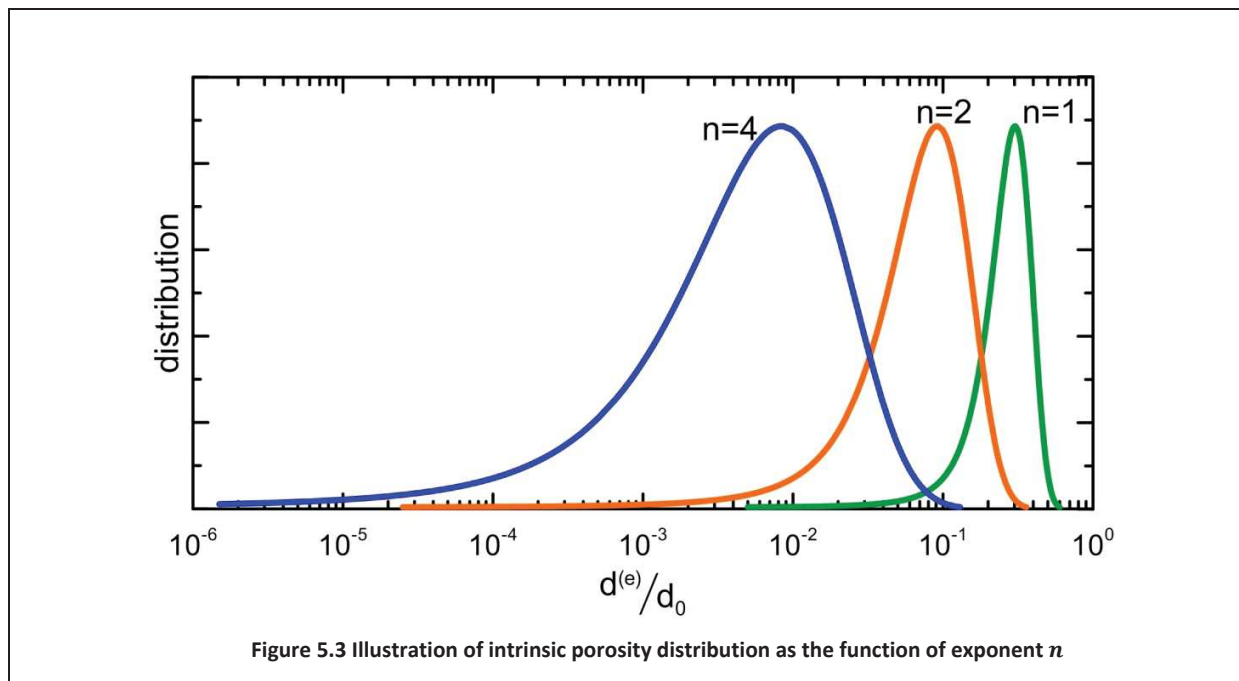
$$d^{(e)}(\mathbf{x}) = \phi_{\mu}(\mathbf{x})^{1+m} d_0. \quad (5.5)$$

In section 5.2.1 we discussed the regions of microporosity inaccessible to mass transfer because they display low porosity values so low that they do not permit percolation. It follows that the formulation for the effective diffusion is:

$$d^{(e)}(\mathbf{x}) = \begin{cases} \phi_{\mu}(\mathbf{x})^n d_0 & \text{for } \phi_{\mu} > \phi_{\theta} \\ 0 & \text{for } \phi_{\mu} < \phi_{\theta} \end{cases} \quad (5.6)$$

where $n = 1 + m$. In this work we will perform sensitivity analysis with different values of n from $n = 1$ to $n = 4$, since we have no information on the exact value, following the methodology proposed by

Gouze et al. [2008b]. The effect of the exponent n in terms of intrinsic porosity distribution is illustrated on Figure 5.3. As one can see, increasing the value of n widens the distribution and decreases effective intrinsic porosity.



5.3 Article 1 – Dual control of flow field heterogeneity and immobile porosity on non-Fickian transport in Berea sandstone



RESEARCH ARTICLE

10.1002/2015WR017645

Key Points:

- We simulate pore-scale flow and anomalous transport in Berea sandstone
- We show that both flow heterogeneity and diffusion in immobile domain control BTC shape
- We upscale successfully the 3-D transport behavior by a new 1-D effective CTRW model

Correspondence to:

F. Gjetvaj,
filip.gjetvaj@gm.univ-montp2.fr

Citation:

Gjetvaj, F., A. Russian, P. Gouze, and M. Dentz (2015), Dual control of flow field heterogeneity and immobile porosity on non-Fickian transport in Berea sandstone, *Water Resour. Res.*, 51, doi:10.1002/2015WR017645.

Received 3 JUN 2015

Accepted 21 SEP 2015

Accepted article online 23 SEP 2015

Dual control of flow field heterogeneity and immobile porosity on non-Fickian transport in Berea sandstone

Filip Gjetvaj¹, Anna Russian¹, Philippe Gouze¹, and Marco Dentz²

¹Géosciences Montpellier, Université de Montpellier, UMR 5243 CNRS, Montpellier, France, ²Spanish National Research Council (IDAEA-CSIC), Barcelona, Spain

Abstract Both flow field heterogeneity and mass transfer between mobile and immobile domains have been studied separately for explaining observed anomalous transport. Here we investigate non-Fickian transport using high-resolution 3-D X-ray microtomographic images of Berea sandstone containing microporous cement with pore size below the setup resolution. Transport is computed for a set of representative elementary volumes and results from advection and diffusion in the resolved macroporosity (mobile domain) and diffusion in the microporous phase (immobile domain) where the effective diffusion coefficient is calculated from the measured local porosity using a phenomenological model that includes a porosity threshold (ϕ_0) below which diffusion is null and the exponent n that characterizes tortuosity-porosity power-law relationship. We show that both flow field heterogeneity and microporosity trigger anomalous transport. Breakthrough curve (BTC) tailing is positively correlated to microporosity volume and mobile-immobile interface area. The sensitivity analysis showed that the BTC tailing increases with the value of ϕ_0 , due to the increase of the diffusion path tortuosity until the volume of the microporosity becomes negligible. Furthermore, increasing the value of n leads to an increase in the standard deviation of the distribution of effective diffusion coefficients, which in turn results in an increase of the BTC tailing. Finally, we propose a continuous time random walk upscaled model where the transition time is the sum of independently distributed random variables characterized by specific distributions. It allows modeling a 1-D equivalent macroscopic transport honoring both the control of the flow field heterogeneity and the multirate mass transfer between mobile and immobile domains.

1. Introduction

Flow and solute transport in water-saturated porous rock and porous material in general have been the focus of intense research over several decades. The quantification and prediction of observed flow and transport phenomena plays a central role in many areas of science and engineering including groundwater hydrology (e.g., pollution risk analysis and remediation), nuclear waste disposal, underground storage of CO₂ and shale gas exploration [Gouze *et al.*, 2008a; Yoon *et al.*, 2015; Russian *et al.*, 2015], but also transport in biological tissues [Sen and Basser, 2005], for example. The main focus of traditional approaches to quantify effective transport, has been the development of macrodispersion models [Dentz *et al.*, 2011, and literature therein]. The advection-dispersion equation (ADE) is traditionally used to describe transport of nonreactive dissolved chemicals (i.e., tracers) at the Darcy scale. The ADE approach is based on the assumption that the hydrodynamic dispersion, triggered by the combination of the diffusion and the variability of the advective fluxes along the flow paths within the pore space, behaves macroscopically as a diffusion-like (Fickian) process [Bear, 1972]. With $c(\mathbf{x}, t)$ the concentration of the tracer at position \mathbf{x} and time t , the ADE reads:

$$\phi \frac{\partial c(\mathbf{x}, t)}{\partial t} - \nabla \cdot [\mathbf{D}\nabla + \phi \bar{\mathbf{u}}] c(\mathbf{x}, t) = 0, \quad (1)$$

where \mathbf{D} , $\bar{\mathbf{u}}$ and ϕ denote the effective dispersion coefficient that quantifies spreading and mixing, the average velocity and the connected porosity respectively. All these parameters are defined at the scale of the support volume, the representative elementary volume (REV), where full mixing of the tracer is assumed [Bear, 1972].

However, many experimental tracer tests, both from in situ [Adams and Gelhar, 1992; Meigs and Beauheim, 2001; Becker and Shapiro, 2003; Gouze *et al.*, 2008b] and laboratory [Kandhai *et al.*, 2002; Levy and Berkowitz,

2003; Scheven *et al.*, 2005; Moroni *et al.*, 2007; Gouze *et al.*, 2009], display strongly asymmetric breakthrough curves (BTCs) with long tails that usually decrease as a power-law of time, whereas the ADE predicts fast concentration decrease. Non-Fickian dispersion manifests itself in power-law tailing of BTCs as well as anomalous scaling of the mean and the variance of the spatial tracer distribution and early arrivals in BTCs [Berkowitz *et al.*, 2006; Neuman and Tartakovsky, 2008]. These numerous experiments indicate that Fickian models fail to capture the real nature of the dispersion in systems macroscopically heterogeneous systems as well as in macroscopically homogeneous such as glass bead columns [e.g., Datta *et al.*, 2013; Holzner *et al.*, 2015].

The apparently ubiquitous non-Fickianity of dispersion in porous media is generally interpreted as the result of the large variability of fluid velocity that is evidently linked to the inherent complexity of the geological formations at all scales. Several authors have explored different approaches (both theoretical and numerical) for characterizing and modeling the processes that control non-Fickian dispersion in relation with the geometry of the pore space [e.g., Bijeljic and Blunt, 2006; Le Borgne *et al.*, 2011; de Anna *et al.*, 2013; Holzner *et al.*, 2015] and at larger scale to the heterogeneous distribution of the hydraulic conductivity field [e.g., Ederly *et al.*, 2014].

In the present paper we focus on macroscopic non-Fickian behavior arising from (stationary) pore-scale Navier-Stokes flow of a Newtonian fluid in a relatively simple natural porous rock. It has been possible only recently to systematically investigate these type of problems due to the possibility of accurately imaging natural porous structures by X-ray micro-tomography (XRMT) tools [Ovaysi and Piri, 2011; Blunt *et al.*, 2013]. The common approach is to process XRMT images in order to distinguish the pore from the solid, then simulate the steady-state flow of an incompressible fluid and finally solve the diffusion-advection equation in order to obtain the distribution of the tracer concentration according to specified boundary conditions [Blunt *et al.*, 2013]. Then, the tracer spreading is analyzed in relation with the flow field properties for different values of the average velocity that determines the contribution of the diffusion in the tracer transport [Bijeljic *et al.*, 2013a]. The pertinence of the analysis depends strongly on the accuracy of the calculations and the representativeness of the domain size, which in turn are strongly dependent both on the technological XRMT and computational limitations [Arns *et al.*, 2005; Guibert *et al.*, 2015a] and on the relevance of the image data processing [Schlüter *et al.*, 2014]. Nevertheless this approach is unmatched for investigating spreading and mixing processes arising from the wide range of transit times experienced by the tracer when transported across the pores of different size and shape.

Few recent studies have focused on the investigation of the relations between the (wide) velocity variability and consequently the (wide) range of transit times of a transported inert tracer using direct pore flow simulations in simple structures [e.g., Le Borgne *et al.*, 2011; de Anna *et al.*, 2013], glass bead packs [e.g., Maier *et al.*, 2008; Holzner *et al.*, 2015], sandstones [e.g., Kang *et al.*, 2014] and carbonate rock [e.g., Bijeljic *et al.*, 2013a, 2013b]. For instance, Bijeljic *et al.* [2011] studied the transport of a passive tracer in small volumes of Berea sandstone (the same rock type as the one used in the present paper) and a Portland limestone following the methodology presented above (i.e., based on the direct calculation of the Stokes flow on digitized XRMT images). The authors (op. cit.) computed the average travel time distribution as the function of the Peclet number using a streamline-based random walk approach. Finally, these transition time distributions were modeled as truncated power-laws [Dentz *et al.*, 2004] and then used to parametrize a continuous time random walks (CTRW) model. Kang *et al.* [2014] studied the purely advective transport of a tracer in a small volume of Berea sandstone as well. However, these authors (op. cit.) interpreted the anomalous dispersion as the results of correlation features of the Lagrangian velocities that can be accounted for in a CTRW model. CTRW characterized by a correlated random time increment was initially proposed by Le Borgne *et al.* [2011] and [de Anna *et al.*, 2013] to model transport in simple 2-D structures where the anomalous dispersion arises from the competition between distribution and correlation effects of the velocity.

Matrix diffusion represents another critical transport process that controls the late-time behavior of BTCs [e.g., Haggerty and Gorelick, 1995; Carrera *et al.*, 1998; Shapiro, 2001; Zhou *et al.*, 2007; Gouze *et al.*, 2008a]. The tracer transit times by diffusion in the matrix are usually orders of magnitude larger than the average transit time in the connected porosity controlling the medium permeability. If a fraction of the medium is formed of the matrix where diffusion is dominant, then dual-porosity models can be conveniently used. Mass transfer between mobile and immobile zones and the separation of characteristic transport time scales in the mobile and immobile regions gives rise to non-Fickian transport behaviors. These mechanisms

are quantified by the multirate mass transfer ADE model (MRMT-ADE) [Haggerty and Gorelick, 1995; Carrera *et al.*, 1998; Haggerty *et al.*, 2000], which can be formulated as

$$\xi_v \frac{\partial c(\mathbf{x}, t)}{\partial t} - \nabla \cdot [\mathbf{D} \nabla + \xi_v \bar{\mathbf{u}}] c(\mathbf{x}, t) + S(\mathbf{x}, t) = 0 \quad (2)$$

with the sink-source term

$$S(\mathbf{x}, t) = \xi_\mu \frac{\partial}{\partial t} \int dt' M(t-t') c(\mathbf{x}, t'), \quad (3)$$

where ξ_v and ξ_μ denote the volume fraction of the mobile domain (i.e., the macroscopic connected porosity) and the volume fraction of the immobile domain respectively; and $M(t)$ is the memory function that contains all the information on the mass transfer process, the geometry and the volume fraction of the immobile domain as well as its accessibility to tracer particles issued from the mobile domain. A power-law designed memory function will trigger the power-law tail of the BTCs. Specifically, a power law tailed BTC that decays as $\propto t^{-\beta-1}$ corresponds to $M(t) \propto t^{-\beta}$. This behavior would persist infinitely if the tracer could assess longer diffusion paths as time increases, such as in fractal systems. However, a maximum diffusion length is expected in natural porous media displaying finite size immobile domains and $M(t)$ decays exponentially fast to zero when the maximum residence time in the immobile domain is reached and the system evolves toward asymptotic Fickian dispersion according to (2). The MRMT-ADE approach accounts also for the heterogeneity of the matrix, and has been successfully applied to model field and laboratory experiments [Haggerty *et al.*, 2001, 2004; Gouze *et al.*, 2008a]. The MRMT-ADE and the CTRW approaches are equivalent under certain conditions as discussed in Dentz and Berkowitz [2003] and Schumer *et al.* [2003].

In the studies cited above the origin of the non-Fickian dispersion has been investigated either considering the void and the solid phases to tackle the effects of the velocity distribution in the mobile domain, or considering the effect of an immobile domain while the dispersion was assumed Fickian in the mobile domain. Here we will investigate both mechanisms by considering simultaneously the presence of the matrix where transport is controlled by diffusion and the velocity variability in the mobile domain. The presence of microporous material in reservoir rocks, for instance detected by XRMT imaging, and its control on the connectivity and consequently its permeability has been documented in recent studies [Gouze *et al.*, 2008a; Mangane *et al.*, 2013; Garing *et al.*, 2014; Hebert *et al.*, 2015]

The paper is organized as follow. Section 2 describes image acquisition and segmentation. In section 3, we present the methods used to perform flow simulations, and the particle tracking methods. Section 4 is dedicated to the analysis of the results of the particle transport simulations and their discussion. Conclusions are presented in section 5.

2. Rock Sample Imaging

Berea sandstone has been used extensively as a sandstone reservoir proxy because it is relatively homogeneous, cohesive, well characterized and easily available [Churcher *et al.*, 1991; Øren and Bakke, 2003; Tanino and Blunt, 2012]. Berea sandstone is composed of quartz grains that are cemented together by silica, dolomite, feldspar, and clayey minerals. Grains are well sorted (ranging in size between 70 and 400 μm) and well rounded (only around 20% of grains are not spherical) [Churcher *et al.*, 1991]. Cement fraction in Berea sandstone ranges from 1.8 to 9% [Øren and Bakke, 2003; Tanino and Blunt, 2012]. Here we intentionally chose a sample with the lowest cement fraction in order to determine if a low fraction of immobile domain can produce a key control on the dispersion together with the velocity heterogeneity in the mobile domain.

2.1. Image Acquisition

The high resolution X-ray microtomography (XRMT) image of the core (10 mm length and 6 mm diameter) was acquired using the BMS beamline at the European Synchrotron Radiation Facility (Grenoble, France). The 3-D volume was reconstructed from 3495 projections acquired at an energy of 110 keV using a GGG:Eu 100 microns scintillator and a SCMOS-based 2048 \times 2048 pixels detectors (model PCO edge; <http://www.pco.de>). The reconstruction was performed using the single distance phase retrieval algorithm described by Paganin *et al.* [2002] applying an unsharp filter before reconstruction. Details on the reconstruction algorithm and performances can be found in Sanchez *et al.* [2012]. The final 3-D image is formed by 4667 \times

2130×2099 voxels of characteristic size $3.16 \mu\text{m}$ ($3.16 \times 10^{-6} \text{m}$). The 16 bits encoded value associated to each of the voxels denotes the X-ray absorption integrated over a volume of $31.5 \mu\text{m}^3$.

2.2. Identification of the Different Type of Porosity

Analysis of the raw XRMT images pointed out the existence of three types of material, denoted hereafter phases. The three phases correspond respectively to the macroporosity (i.e., the void space filled with water or air), the microporosity (voxels in which pores are smaller than image resolution) and the solid rock. The identification and then labeling of these three phases is called segmentation. There are different methods for performing image segmentation, none of them producing strictly equivalent results. Segmentation is consequently a critical step of the data processing [Iassonov et al., 2009; Schlüter et al., 2014; Scheibe et al., 2015].

Global thresholding is often applied; this simple approach consists in deciding a gray scale value separating two material types on the basis of image histogram analysis. However, by definition the microporous material can display a large range of gray level values depending on its porosity, while intermediate gray level values denote pixels sampling both solid and voids. Consequently, it is a priori not pertinent to use the global thresholding method for the present study where the presence of heterogeneous microporous material is known. Several alternative methods have been developed in order to improve the accuracy of the segmentation; see the comparative study by Iassonov et al. [2009].

Here we use the so called "region growing" methods based on the assumption that all the voxels belonging to a given phase cluster are connected and are similar in terms of gray levels [Špirková, 1993]. A significant difficulty of region growing methods is the need for carefully defining the initial gray level range, limiting the seed regions for each phase, which is typically done manually from analyzing the histogram. However, the image histogram does not contain enough information to properly identify the different phases, and relatively small differences on the threshold values may induce noticeable errors on the determination of the phase fractions. Here we applied the method proposed by Mangane et al. [2013] that consists in conditioning the determination of the threshold values (delimiting the initial gray level range for each phase) by the value of the total porosity measured independently using laboratory techniques. For delimiting the three phases four thresholds values must be determined. The convergence toward a satisfactory agreement between the measured total porosity and that obtained by the segmentation procedure (ϕ_t) is obtained from an iterative procedure, where ϕ_t is:

$$\phi_t = \xi_v + (\xi_\mu \phi_\mu) \quad (4)$$

with ξ_v and ξ_μ the volume fraction of the void phase (macroporosity) and of the microporous material, respectively, and ϕ_μ the intrinsic porosity of the microporous phase. Here we used the porosity evaluated from mercury intrusion porosimetry (MIP) as the reference total connected porosity. This procedure was applied to the gray level image assuming that first the mineralogical composition of the microporous cement is homogeneous, and second that the porosity of the microporous phase range from 0.01 to 60%. This latter assumption is based on the fact that above 60% the material cannot be cohesive. The procedure is based on comparing the experimental porosity to the total porosity (4) where ξ_v may contains pixels belonging to porosity unconnected to the percolating cluster. However, we measured the value of this unconnected porosity a posteriori (see in section 2.3) and found that it was always lower than 0.8% for each of the studied subvolumes. Accordingly one can consider that this value represents the error on the segmentation. The average porosity of the microporous phase is 24.93%, and the total porosity calculated by equation (4) is 18.8%. Figure 1 illustrates the pore network and microporosity obtained by three phase segmentation.

2.3. Microporosity and Connected Clusters

Figure 2 illustrates the throat radius distribution obtained by MIP test. The throat radius distribution for the Berea sandstone under consideration is quite narrow compared to other rocks, especially carbonates. Most throat radii are between 8 and $20 \mu\text{m}$, but there is a significant portion of throats with smaller radii. The dashed line in Figure 2 marks the XMRT image voxel size. All throats and pores with smaller radii cannot be distinguished on the XRMT images and are assigned to the microporous phase.

In the following, flow and transport will be studied on 4 nonoverlapping subvolumes (SV1, SV2, SV3, and SV4) of $300 \times 300 \times 300$ voxels randomly extracted from the full core image. In order to investigate the

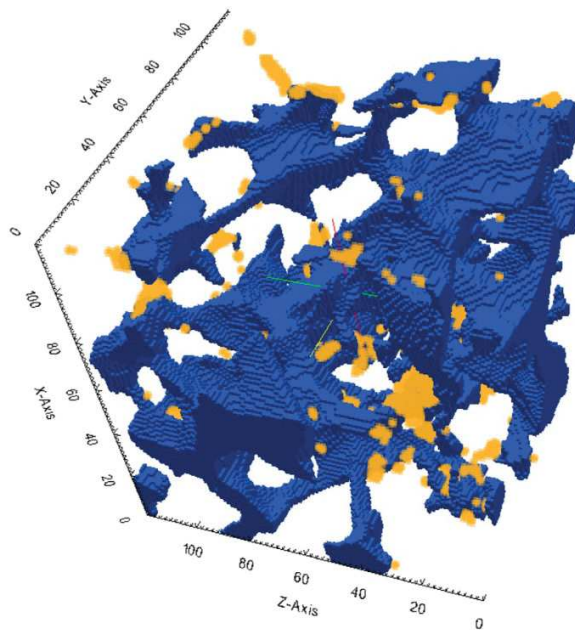


Figure 1. Three-dimensional visualization of the pore network (blue) and the connected microporosity (yellow) for a subvolume of $120 \times 120 \times 120$ voxels.

perpendicular to the flow direction in subvolume SV1 for the two-phase segmented image (Figure 3a) and for the three-phase segmented image (Figure 3b). One can see, for example in the area marked by the green circle, that the three-phase image contains a fraction of macroporosity connected that is connected by microporous material (in orange), a feature that does not exist in the two-phase image. The porosities for the four subvolumes are given in Table 1. The total porosity ϕ_t of the three-phase subvolumes calculated by (4) is on average increased by 5.3% when compared to the equivalent two-phase volume. This corresponds to an average

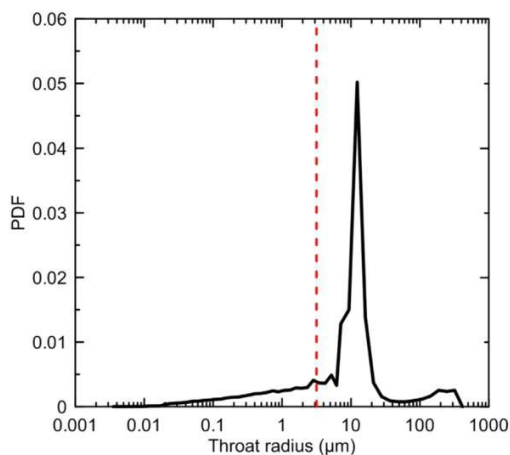


Figure 2. Throat radius PDF obtained from mercury intrusion porosimetry for Berea sandstone. The vertical dashed line marks the XMRT image voxel size.

influence of microporosity on solute transport we compare flow and transport computed on the three-phase segmented volumes, and two-phase images where the microporous phase is assigned to the solid phase.

The first step of the segmented-data processing consists in the determination of the percolating clusters, i.e., the computation of the network of pores that spans through the whole volume and connects the boundaries in flow direction. Percolated clusters were identified using the method described in *Hoshen and Kopelman* [1976]. The mobile domain, in which the flow will be computed corresponds to the connected macroporosity, while the immobile domain corresponds to the microporosity as well as a fraction of the macroporosity that is connected by the microporous phase only. Figure 3 shows the same cross sections

perpendicular to the flow direction in subvolume SV1 for the two-phase segmented image (Figure 3a) and for the three-phase segmented image (Figure 3b). One can see, for example in the area marked by the green circle, that the three-phase image contains a fraction of macroporosity connected that is connected by microporous material (in orange), a feature that does not exist in the two-phase image. The porosities for the four subvolumes are given in Table 1. The total porosity ϕ_t of the three-phase subvolumes calculated by (4) is on average increased by 5.3% when compared to the equivalent two-phase volume. This corresponds to an average increase of a 2% of the macroporosity, which is made accessible by the microporous cement clusters. By definition, this fraction of the macroporosity belongs to the immobile domain because transport is only due to diffusion.

3. Modelling Tools

3.1. Mesh Generator

Guibert et al. [2015a] showed that the grid resolution is an important issue for ensuring meaningful permeability calculations. Here we want to investigate the influence of the grid resolution on the calculation of the transport properties as well. Therefore, we first programmed a new meshing algorithm that is capable to create regular hexahedron mesh compatible with OpenFOAM[®] strictly equivalent to the voxels of the segmented images. Applying this

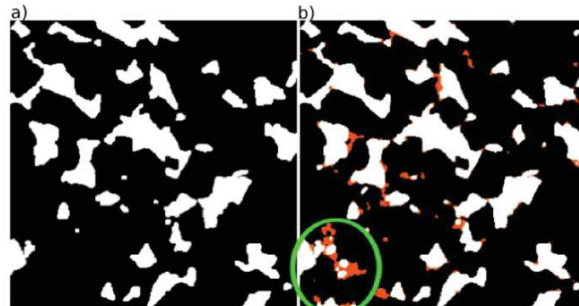


Figure 3. Comparison between a cross section (300×300 pixels) extracted from subvolume SV1 perpendicular to the flow direction for (a) a two-phase image and (b) a three-phase image. Black areas denote the solid phase (no advection and no diffusion), white areas denote the macroporosity, i.e., the mobile domain and areas colored in orange indicate the microporous phase where transport is assumed to be controlled by diffusion only.

algorithm we are able to avoid any averaging or smoothing that often occur in the course of the standard OpenFOAM[®] meshing procedure. Then we built two meshes with different resolution for each of the subvolumes (SV1–SV4). The hereafter called “coarse mesh” is made of cubic cells with the same size as the image voxels, while the “fine mesh” is obtained by dividing each voxel by 3 in all the directions, creating consequently 27 cubes of $1.05 \mu\text{m}$ size per image voxel.

3.2. Solving Flow

Single phase flow in porous media on pore-scale is classically calculated by the Navier-Stokes equation [Bear, 1972; de Marsily, 1986]. In this work, we computed the pore-scale flow field by solving the conservation equation (5) and the Navier-Stokes equation (6), for single-phase with a constant density and viscosity.

$$\nabla \cdot u = 0 \quad (5)$$

$$\rho \left(\frac{\partial u}{\partial t} + u \cdot \nabla u \right) = -\nabla p + \mu \nabla^2 u, \quad (6)$$

where u denotes the velocity vector (m/s), ρ is the fluid density (kg/m^3), t is the time, p is pressure (Pa) and μ is fluid viscosity (Pa s).

Equations are solved by using the steady-state solver based on the SIMPLE algorithm implemented in OpenFOAM[®] [Weller *et al.*, 1998]. OpenFOAM is a free, open source computational fluid dynamics software package with parallelization capabilities. The equations are discretized using the finite volume method. The SIMPLE (Semi-Implicit Method for Pressure-Linked Equations) algorithm presented by Patankar [1980], is one of the pressure-based method techniques to solve pressure-velocity coupling. It allows to iteratively solve Navier-Stokes equation and obtain the steady state pressure and velocity fields. For each step pressure and velocity field are calculated according the boundary conditions and the results from the previous step, until the difference between the current and previous steps is smaller than a given convergence criterion.

Table 1. Total Porosity (ϕ_t ; see (4)) for Two-Phase and Three-Phase Images, Columns 1 and 2, Respectively^a

	Total Porosity ϕ_t		Relative Difference (%)	
	Two-Phase	Three-Phase	$\Delta\phi_t$	$\Delta\xi_v$
SV1	19.36	20.37	5.25	1.97
SV2	19.32	20.23	4.68	1.56
SV3	18.26	19.18	5.03	2.04
SV4	18.21	19.33	6.14	2.51

^aColumn 3: relative difference between total porosity $\Delta\phi_t = [\phi_t^{(3P)} - \phi_t^{(2P)}] / \phi_t^{(3P)}$. Column 4 reports the relative difference between the fraction of the void phase included in the total porosity: $\Delta\xi_v = [\xi_v^{(3P)} - \xi_v^{(2P)}] / \xi_v^{(3P)}$. This difference denotes the fraction of macroporosity made accessible to diffusion due to the presence of the microporous phase.

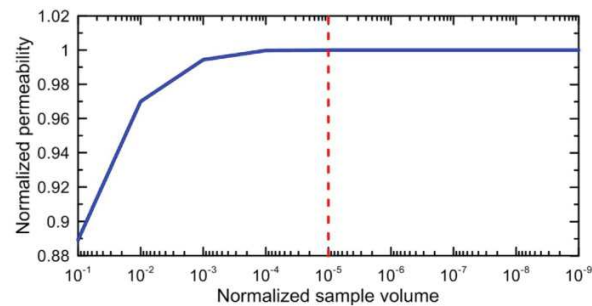


Figure 4. Normalized permeability as a function of the sample volume for different residual convergence criteria.

Constant pressure is applied to the inlet and outlet boundaries while all other boundaries including the void-rock interface are considered as no-flow boundaries (no-slip condition at the void-rock interface). Twenty layers of void voxels have been added to the porous volume at the inlet and outlet boundaries in order to minimize the boundary effect [Guibert *et al.*, 2015b]. Fluxes at the inlet and outlet boundaries and residual convergence were used to evaluate if the simulations have fully converged. To determine the residual convergence criterion, we made several simulations on the same structure while constantly decreasing the convergence criterion until the computed permeability converged to a stationary value. For the Navier-Stokes flow simulations described below, the computation duration, using a 24-cores Intel Xeon (2.3 GHz) PC, ranged from about 10 h for a 300^3 voxels mesh to about 75 h for a 900^3 voxels mesh.

Permeability k was calculated from Darcy's law

$$k = \frac{\mu Q L_z}{\Delta p A_z} \quad (7)$$

where Q is the total flux (m^3/s), L_z length of the block in flow direction, and A_z (m^2) is the area of the cross section perpendicular to the flow direction.

Figure 4 displays the permeability values obtained for different values of the residual convergence criterion. We observed that the computed permeability value increases with the decrease of the fixed convergence residual and eventually stabilizes after the initial residual falls below 10^{-4} . Based on these results we decided to use 10^{-5} as the residual convergence criteria which has proved to give completely converged calculations with reasonable computation times.

All simulations were made with low Reynolds numbers of $Re \cong 10^{-6}$. The Reynolds number is defined as the ratio of viscous and inertial forces, $Re = (\rho \bar{u} L) / \mu$, where \bar{u} is the average superficial velocity [m/s] and L is characteristic length [m]. For such low values of Re flow is laminar, and formation of eddy-currents, which could create anomalous dispersion, is minimized.

Figure 5a presents the probability density function (PDF) of velocity in flow direction. We observe that velocity values are mainly positive. Yet the small portion of negative values emphasizes the complexity of the pore network. The PDF of velocities perpendicular to the flow direction are displayed in Figure 5b, where we observe similar distributions of negative and positive velocities, as expected for an macroscopically homogeneous, isotropic volume of rock.

3.3. Solving Transport

Pore-scale transport in the mobile domain is computed by solving the advection-diffusion equation

$$\frac{\partial c(\mathbf{x}, t)}{\partial t} - \nabla \cdot [d_0 \nabla + \mathbf{u}(\mathbf{x})] c(\mathbf{x}, t) = 0, \quad (8)$$

where d_0 is the diffusion coefficient of the tracer in water and $\mathbf{u}(\mathbf{x})$ is the flow velocity. Here we solve (8) using the time domain random walk (TDRW) method [Noetinger and Estebenet, 2000; Delay and Bodin, 2001; Delay *et al.*, 2005]. Details about the implementation of the TDRW approach, starting from the discretization of the transport equation up to the random walk algorithm implementation can be found in Dentz *et al.*

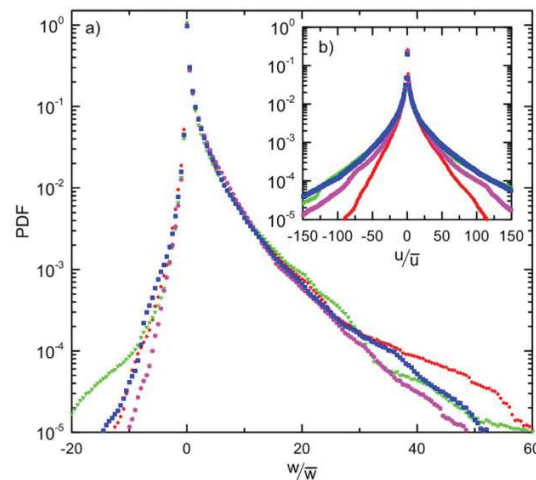


Figure 5. PDFs of normalized velocity for the four subvolumes (a) along the main flow direction (w) and (b) perpendicular to the main flow direction (u) for subvolume 1 (red rhombi), subvolume 2 (green triangles), subvolume 3 (magenta circles), subvolume 4 (blue squares).

[2012]. The domain discretization is the same as the one used for computing the flow field and corresponds to the image voxels (coarse mesh) or the image voxel divided in 27 cubes (fine mesh) as explained in section 3.1. The TDRW approach models particle motions in space and time by the following recursive relations

$$\mathbf{x}_i(n+1) = \mathbf{x}_j(n) + \xi_{ij}, \quad t(n+1) = t(n) + \tau_j. \quad (9)$$

The probability w_{ij} for a transition of length $|\xi_{ij}|$ from pixel j to pixel i , and the transition time τ_j associated to pixel j are given by

$$w_{ij} = \frac{b_{ij}}{\sum_{|jk|} b_{kj}}, \quad \tau_j = \frac{1}{\sum_{|jk|} b_{kj}}, \quad (10)$$

where the notation $\sum_{|jk|}$ denotes summation over the nearest neighbors of pixel j . The b_{ij} are defined as follows,

$$b_{ij} = \frac{\hat{d}_{ij}}{\xi_{ij}^2} + \frac{|u_{ij}|}{2\xi_{ij}} \left(\frac{|u_{ij}|}{|u_{ij}|} + 1 \right), \quad (11)$$

where $\xi_{ij} = |\xi_{ij}|$; \hat{d}_{ij} is the harmonic mean of the diffusion coefficients of pixels i and j ; u_{ij} denotes the velocity component of \mathbf{u}_j in the direction of pixel i , $u_{ij} = \mathbf{u}_j \cdot \xi_{ij}$. If $u_{ij} > 0$, pixel i is downstream from pixel j , and correspondingly, if $u_{ij} < 0$ pixel i is upstream from pixel j .

The TDRW method is used to solve transport in both the mobile and the immobile domains, where for the latter the velocity is zero. Accordingly the transport equation in the immobile domain (i.e., in the microporous phase) is:

$$\phi_\mu(\mathbf{x}) \frac{\partial c(\mathbf{x}, t)}{\partial t} - \nabla \cdot [d^e(\mathbf{x}) \nabla c(\mathbf{x}, t)] = 0, \quad (12)$$

where d^e is the spatially distributed effective diffusion coefficient in the immobile domain:

$$d^e(\mathbf{x}) = \tau_\mu^{-1}(\mathbf{x}) \phi_\mu(\mathbf{x}) d_0, \quad (13)$$

where τ denotes the tortuosity of the immobile domain, which is usually expressed as a power-law of the porosity, $\tau_\mu \equiv \phi_\mu^{-m}$ [Pisani, 2011]. Furthermore, for porosity values smaller than the porosity ϕ_0 at the percolation threshold, no more diffusion can take place. Thus, the effective diffusion coefficient d^e takes the following form,

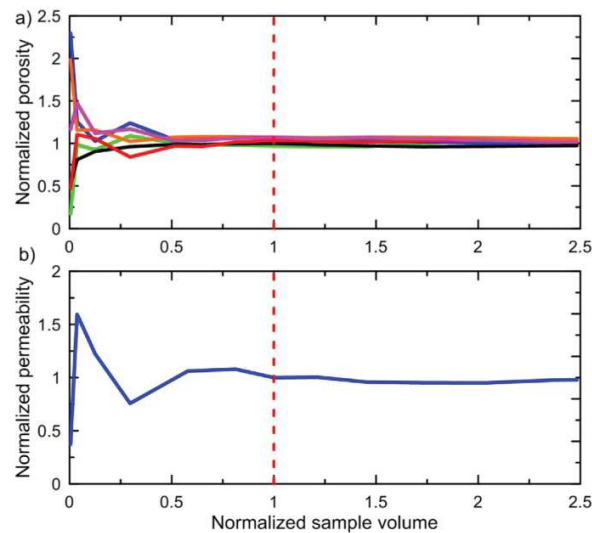


Figure 6. (a) Normalized porosity and (b) permeability versus the sample volume normalized by the reference volume of 300^3 voxels.

$$d^e(\mathbf{x}) = \begin{cases} \phi_\mu(\mathbf{x})^n d_0 & \text{for } \phi_\mu > \phi_\theta \\ 0 & \text{for } \phi_\mu < \phi_\theta \end{cases} \quad (14)$$

with $n = m + 1$. In the following we will test different values of n from $n = 1$ up to $n = 4$ [Gouze *et al.*, 2008a], because we have no information on the exact value of n . Note that ϕ_θ is a characteristic property of the porous material under consideration and requires an experimental approach to be determined precisely. In our case the value of ϕ_θ is not known. In the following, we test the sensitivity of the results to this parameter for different values ranging from $\phi_\theta = 0$ up to $\phi_\theta = 0.4$.

3.4. Representativeness of the Samples

For simulating flow and transport in heterogeneous porous media it is essential that the support volume used for the calculations is large enough to be representative of the medium. The minimum volume required is the representative elementary volume (REV) [Bear, 1972]. To evaluate the representativeness of the 300^3 voxel subvolumes SV1–SV4, we made calculations of the porosity and the permeability of the mobile domain for increasing size of the support volume. For porosity we randomly chose 6 locations in the core and measured the mobile domain porosity for cubes of increasing size. For permeability we followed the same procedure, but starting from one location only, in order to keep this study tractable in terms of computational times. For the same reason we performed the Navier-Stokes computations using the coarse mesh (i.e., mesh cells of the same size as the image voxels) in order to be able to increase the support volume sufficiently for a sound evaluation of the size effect.

Figure 6a presents results of the mobile domain porosity as a function of the support volume. The plotted porosity values are normalized to the porosity of the whole image and the volume values are normalized to the volume of the 300^3 voxel subvolumes (i.e., 0.95 mm^3). Although there are small differences in the asymptotic porosities (which denotes large scale variability of the porosity in the core) depending on the initial location, we concluded that porosity stabilizes for volumes of about 0.5 times that of the 300^3 voxel sample. Similar behavior was observed for the permeability calculations; the relative difference in permeability is staying below 5% for all subvolumes larger than 300^3 . Together with the observations made on the velocity PDF (section 3.2), one can conclude that 300^3 voxels subvolumes can be considered as a good approximation of a REV in terms of porosity and flow in the mobile domain, albeit they may display weak differences in their macroscopic properties.

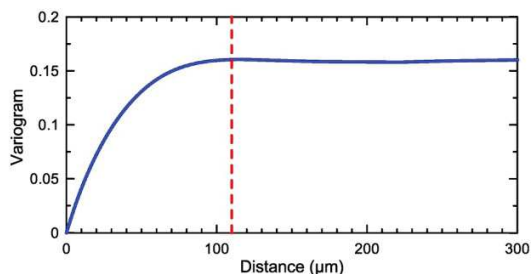


Figure 7. Porosity variogram for the Berea sandstone sample.

3.5. Transport Characterization

At the pore-scale, tracer transport is driven by both advection and diffusion. The relative importance of these two mechanisms is quantified by the Peclet number Pe [de Marsily, 1986]:

$$Pe = \frac{\bar{u}L}{d_0} \quad (15)$$

where d_0 is the coefficient of molecular diffusion (set here to $10^{-9} \text{ m}^2\text{s}^{-1}$) and \bar{u} the average pore velocity. The characteristic length L is usually associated with the average pore diameter in relation with the definition of Pe in a capillary [Taylor, 1953]. For the heterogeneous pore structure under consideration here, we define the characteristic length L from variogram of the porosity of the mobile domain, which is displayed in Figure 7. The dashed line indicates the length ($\approx 110 \mu\text{m}$) at which the variogram reaches its asymptotic value. This is considered here as the characteristic length L . In order to make our results comparable to those of Mostaghimi *et al.* [2012], we applied also the simplified method they proposed, which is based on the assumption that the sandstone is made of regularly packed spheres. For this idealized system, the characteristic length can be associated with the sphere diameter $L = \pi V \sigma^{-1}$, where V is total volume and σ is the interface area between the mobile domain and the solid phase. Applying this method to our subvolumes one obtains values ranging from 122.1 to 125.6 μm , which are similar to those obtained from the variogram method. We note that this evaluation of L is in good argument with the characteristic lengths calculated for Berea sandstone in other studies ($L = 131.13 \mu\text{m}$ [Mostaghimi *et al.*, 2012], $L = 100 \mu\text{m}$ [Bijeljic *et al.*, 2004]) and $L = 150 \mu\text{m}$ [Øren and Bakke, 2003]).

4. Results and Discussion

Here we present and discuss the results obtained from the calculation of tracer transport in subvolumes SV1–SV4. Figures 8–16 show the breakthrough curves (BTC) at the outlet of the subvolumes. The BTC measures the number Np of particle observed at the outlet normalized by the total number Np_0 of particle injected at the inlet. The simulations use $Np_0 = 10^6$ particles. The computation time for the transport simulations discussed below ranged from about 10 min to 30 h using a 12-cores Intel Xeon (2.6 GHz) computer, and depends mainly on the value of the Peclet number and the presence and properties of the immobile domain.

We first study the influence of the mesh resolution on the resulting BTCs and then analyze the respective controls of advection and diffusion in the mobile domain, and mass transfer between the mobile and the immobile domains. The results depend on the Peclet number that characterizes the relative strength of diffusion and advection in the mobile domain, and the parameters which characterize the effective diffusion in the immobile domain, i.e., the exponent n and the percolation threshold ϕ_{ij} in (14).

4.1. Influence of the Mesh Resolution

For all the simulations presented here, we fixed the value of Pe by multiplying the flow velocity by a coefficient in order to obtain the required average velocity. Nevertheless, when comparing meshes with different resolutions one must take into account that the permeability computed by equation (7), and consequently the average velocity, are slightly different depending on the voxel size. For subvolume SV3 the permeability

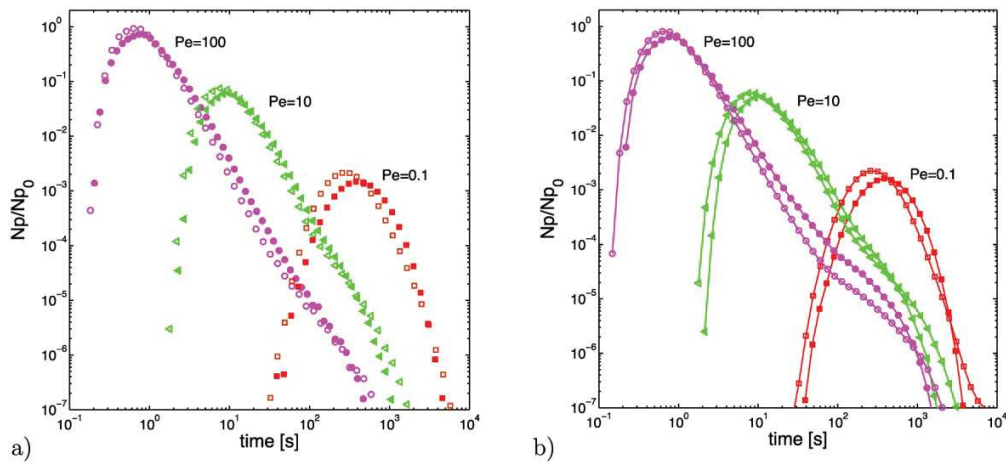


Figure 8. BTC obtained with the coarse mesh (300^3 cells, open symbols) and fine mesh (900^3 cells, full symbols) for subvolume 3 for $Pe = 100$ (pink circles), $Pe = 10$ (green triangles), and $Pe = 0.1$ (red squares). (a) The BTCs for mobile transport only, and (b) mobile transport and diffusion in the microporous phase.

is 867 mD for coarse mesh and 753 mD for fine mesh. This decrease of permeability with the voxel size was already mentioned by *Guibert et al.* [2015a]. To make the comparison meaningful, we first calculate the multiplication factor for the targeted Pelet number for the fine mesh and used the same coefficient to multiply the flow velocity for the coarse mesh.

Figure 8 displays the BTCs for the coarse and fine meshes for different transport regime ($Pe=0.1, 10$ and 100). Figure 8a shows BTCs for transport in the mobile domain only, while Figure 8b shows BTCs for transport in the presence of mass transfer between the mobile and immobile domains.

For both cases (i.e., with and without immobile domain) we observe that for advection dominated transport ($Pe=100$) the peak arrival time for the fine mesh is around 20% larger than for the coarse mesh. This is a

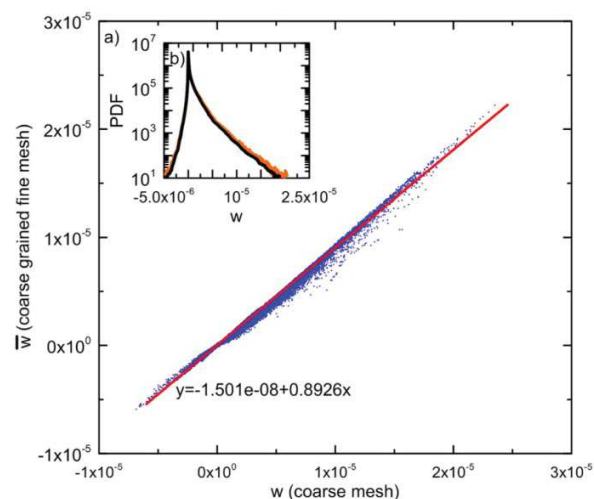


Figure 9. (a) Cross plot of coarse grained velocities for subvolume 3 versus the velocity average over the coarse cell obtained from the fine mesh data (blue points) together with the best-fit (red line). (b) Inset: PDFs of velocity along the main flow direction w for the (black) fine mesh and (orange) coarse mesh.

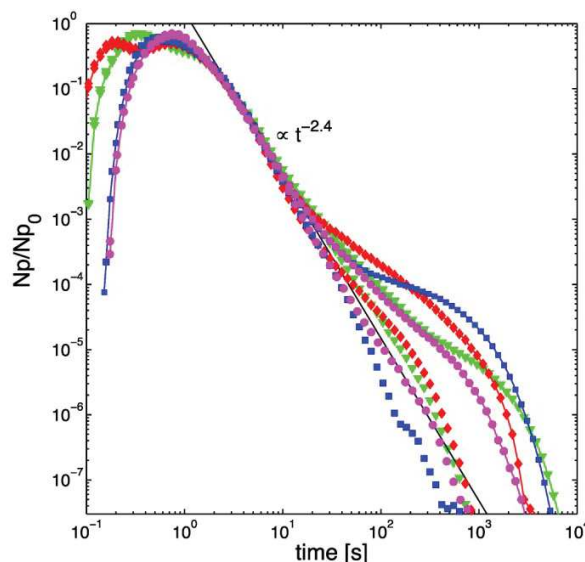


Figure 10. BTC for subvolumes SV1 (red rhombi), SV2 (green triangles), SV3 (pink curves), and SV4 (blue squares) for $Pe = 100$. Unconnected symbols denote simulations with transport in the mobile domain only and line-connected symbols denote simulations with diffusion in the immobile domain, setting $n=1$ and $\phi_{ij}=0$ in equation (14).

direct consequence of the higher average velocity and permeability in the coarse mesh. There are also slight differences in the concentration decay after the peak, which are more marked for the mobile-immobile case. For diffusion dominated transport characterized by $Pe=0.1$, the peak arrival time for the fine mesh is around 50% longer than for the coarse mesh. This 50% difference in the peak concentration arrival time is larger than the difference in the permeability. The BTC for the coarse mesh and $Pe=0.1$ (Figure 8b)

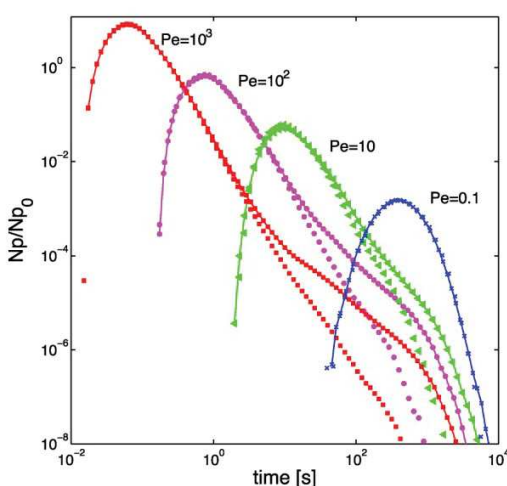


Figure 11. BTC for subvolume 3 (SV3) computed with transport in the mobile domain only (unconnected symbols), and with the immobile domain (connected symbols) for $Pe = 1000$ (squares), $Pe = 100$ (circles), $Pe = 10$ (triangles), and $Pe = 0.1$ (crosses) with $n = 1$ and $\phi_{ij} = 0$ in equation (14).

also displays an extended tailing. Regarding the maximum concentration values one observes that they are always higher for the coarse mesh than for the fine mesh, with differences ranging between 18% and 29% in the simulations without immobile domain and 15–20% for the case with mobile-immobile mass transfer. These results indicate that an insufficient mesh resolution can lead to an overestimation of the anomalous transport characteristics by increasing peak concentrations, decreasing peak arrival times, and increasing tailing; these effects are more pronounced at low Peclet numbers. However, the origin of these differences is not clear. Figure 9 presents a detailed investigation of the differences in the flow field for different mesh resolutions. For the fine mesh we performed a coarse graining process in which the mean velocity is calculated from the 27 mesh cells (dividing by each voxel by 3 in for each direction) which belong to each of the void

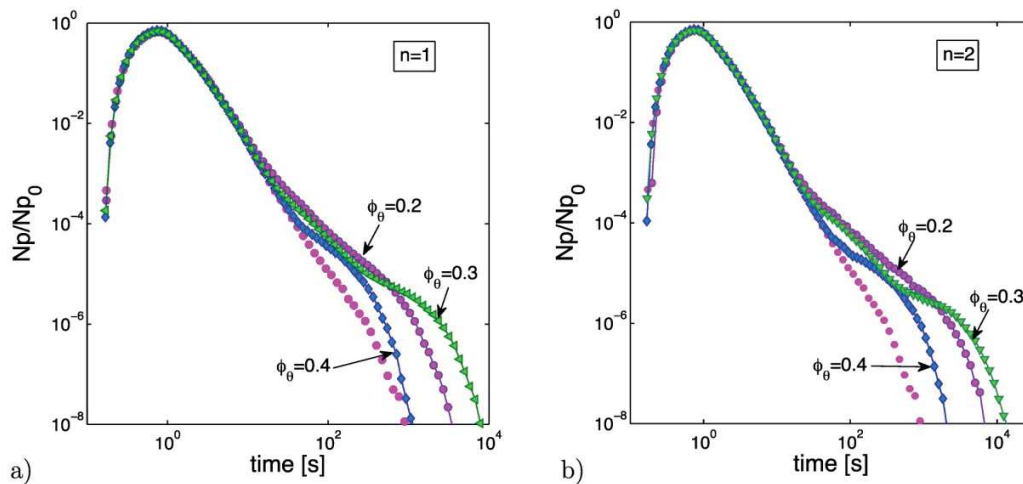


Figure 12. BTC computed in subvolume 3 (SV3) for $Pe = 100$ and threshold values $\phi_\theta = 0.2$ (connected pink circles), $\phi_\theta = 0.3$ (green triangles), and $\phi_\theta = 0.4$ (blue rhombus) with (a) $n = 1$ and (b) $n = 2$. For comparison the unconnected pink circles denote the BTC in the absence of the microporous phase.

voxel of original image. The cross plot between coarse grained mean velocity from the fine mesh and its corresponding velocity in the resampled coarse mesh is presented in Figure 9a. These data are fitted by a linear trend of slope 0.89 indicating that, on average, velocities on the fine mesh are around 10% lower than those for the coarse mesh.

Figure 9b displays the comparison of the PDFs for the two different mesh resolutions. While no noticeable difference for low velocities is evidenced, the difference is more marked for higher velocity values. Whereas it can be conjectured that these differences in the higher velocity explain the difference in the BTC maximum concentration arrival time, the increase of the BTC tailing for the coarse mesh cannot be directly explained by the difference in the velocity PDF without a more detailed analysis of, for instance, the velocity correlation. This, however, is not the scope of this paper. Nevertheless, these results indicate clearly that refining the mesh

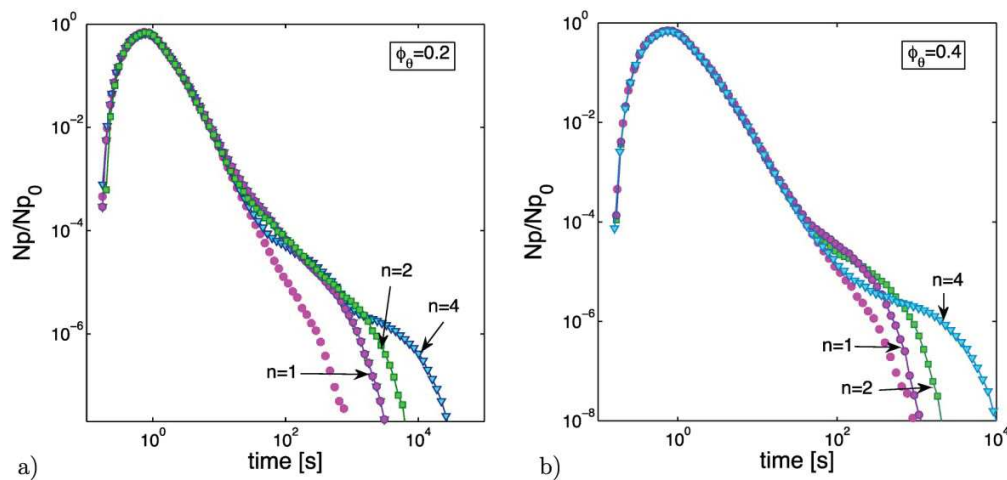


Figure 13. BTC for subvolume 3 (SV3) with $Pe = 100$. The parameters n and ϕ_θ defined in equation (14) for the effective diffusion coefficient are set to: $n = 1$ (connected pink circles), $n = 2$ (green squares) and $n = 4$ (blue triangles); for (a) $\phi_\theta = 0.2$, and (b) $\phi_\theta = 0.4$. For comparison, the unconnected pink circles denote the BTC in the absence of the microporous phase.

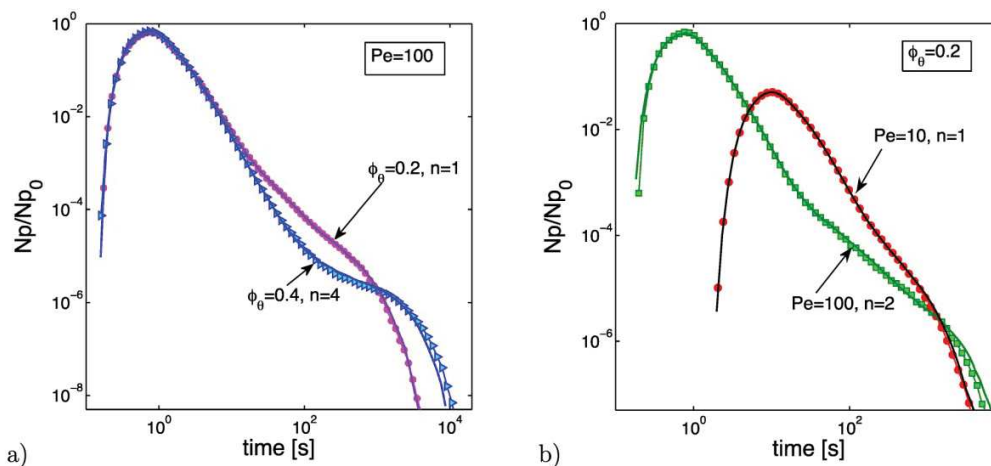


Figure 14. Comparison of the BTC in subvolume 3 (SV3) for a heterogeneous microporous phase characterized by spatially variable porosity $\phi_p(\mathbf{x})$ (connected symbols) and in a homogeneous microporous phase characterized by the harmonic mean of $\phi_p(\mathbf{x})$ (continuous thick line). (a) BTC with $Pe = 100$ for $\phi_0 = 0.4$, $n = 4$ (heterogeneous: blue triangles, homogeneous: blue thick line) and $\phi_0 = 0.2$ and $n = 1$ (heterogeneous: pink circles, homogeneous: violet thick line). (b) BTCs with $\phi_0 = 0.2$ for $Pe = 10$ and $n = 1$ (heterogeneous: red circles, homogeneous: black thick line) and $Pe = 100$, $n = 2$ (heterogeneous: green squares, homogeneous: green tick line).

is not only important for improving the accuracy of flow field computation, but also for improving transport computation precision. Accordingly, all the following results were obtained using the fine mesh.

4.2. Control of the Microporous Material on Transport

In this section, we investigate the control of the immobile domain on the overall transport of a passive tracer. Figure 10 displays the simulation results presented as the comparison of the BTC for the 4 subvolumes with and without the immobile domain for $Pe = 100$.

We observe very similar transport behaviors for all subvolumes in the case of mobile transport only. The BTCs are characterized by long-time tails with slope of $t^{-2.4}$ for all four subvolumes indicated by the unconnected symbols in Figure 10. Conversely, when including the immobile domains (connected symbols) we observe that the difference from one subvolume to the other is much more marked than for transport in the mobile domain only.

The most significant difference between the mobile-only and mobile-immobile simulations appears in the tails. We observe a stronger tailing due to a larger proportion of slow transport, and the presence of two inflection points at the time t_1 , which marks the transient regime characterized by slopes smaller than $t^{-2.4}$,

and the cut-off time t_2 which denotes the diffusion time scale at which the mobile and immobile zones equilibrate. However both the slope and the value of t_2 differ between subvolumes.

From the data reported in Table 2 we observe that the influence of the immobile domain on the intermediate slope of the BTC tail, which appears to be related mainly to the surface area σ_{m-im} of the interface between the mobile and immobile domains, albeit the influence of the immobile domain volume V_{im} is less clear-cut. Nevertheless, one can observe that SV4 is characterized by the largest values of both σ_{m-im} and V_{im} while the corresponding BTC (blue squares in Figure 10) displays a lower slope and value of t_2 .

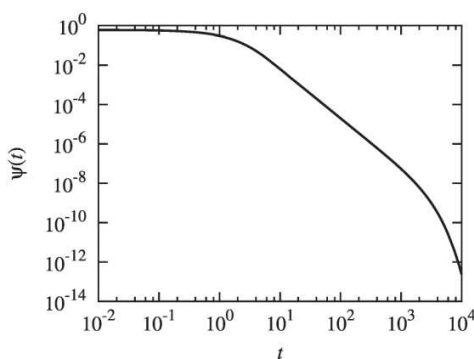


Figure 15. Illustration of the truncated power-law PDF (24) for $\tau'_\nu = 1$ and $\tau_c = 10^3$.

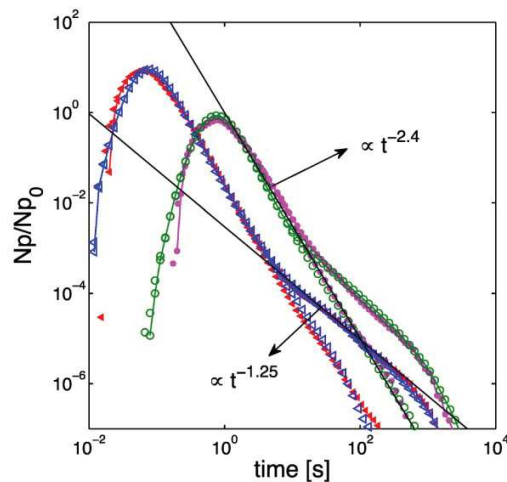


Figure 16. BTC for subvolume 3 (SV3) for $Pe=10^3$ (filled red triangles), and $Pe=10^2$ (filled pink circles) compared to the BTC obtained from the 1-D CTRW model (unfilled triangles and circles). Unconnected symbols denote the BTCs in the absence of the microporous phase. Connected symbols denote the BTCs in the presence microporous phase with $n = 1$ and $\phi_{ij}=0$. The parameters for the 1-D CTRW model are $b = 0.7$, and $a = 0.3$, $\alpha = 1.4$, $\epsilon = 6 \times 10^{-5}$ for the PDF (24) of mobile times, a trapping frequency of $\gamma = 0.05 \text{ s}^{-1}$, and $\beta = 0.25$, $\tau_1 = 3 \text{ s}$ and $\tau_2 = 700 \text{ s}$ for the PDF (26) of trapping times.

Figure 11 displays the comparison between the simulation (for SV3) of the mobile-only and the mobile-immobile cases for different values of the Peclet number ($Pe = 0.1, 10, 100$, and 1000). The elongation of the BTC tail and the occurrence of a second slope between t_1 and t_2 are clearly visible for $Pe \geq 10$. As expected, the difference between the two cases becomes insignificant for diffusion dominated transport ($Pe \leq 0.1$); the only difference when adding the immobile domain is a small increase of about 5% (see Table 1) of the overall diffusional volume. The additional tailing behavior increases with the value of Pe .

These results clearly demonstrate the importance of the immobile domain, or in other words, the necessity of taking into account the presence of the microporous material, even if it represents a small fraction of the porosity. Also, the results indicate that the area of the interface between the mobile and the immobile domains is a critical parameter. The area of this interface determines the efficiency of mass transfer between these two domains, while the volume of the clusters which form the immobile domain should control the maximum (and average) trapping time in the immobile domain [Haggerty and Gorelick, 1995; Carrera et al., 1998]. However, this last statement cannot be verified by comparing the four subvolumes, because first the difference in terms of V_{im} is probably not significant and second we do not have precise information on the size of the immobile domain clusters.

4.3. Effect of the Immobile Domain Properties on the BTC

As explained in section 3.3, the effective diffusion coefficient in the microporous material is evaluated from the distributed porosity (which is the only known property of this material) using the model described by

Table 2. Area σ of (Column 1) the Interface Between the Mobile Domain and the Microporous Material (σ_{m-im}), (Column 2) the Mobile Domain and the Solid (σ_{m-s}) and (Column 3) the Solid and the Immobile Domain (σ_{s-im}) for Subvolumes SV1–SV4^a

	Area in mm^2			Volume in $10^6 \mu\text{m}^3$	
	σ_{m-im}	σ_{m-s}	σ_{s-im}	V_m	V_{im}
SV1	0.77	1.62	1.10	164.9	24.9
SV2	0.76	1.61	1.04	164.6	23.1
SV3	0.71	1.71	1.04	155.5	21.8
SV4	0.84	1.58	1.19	155.2	26.4

^aColumns 4 and 5 gives the volume of the mobile domain (V_m) and of the immobile domain (V_{im}) respectively.

(14). This model requires fixing both the porosity threshold ϕ_θ and the exponent n of the power law model (13). Here both these parameters are unknown. Yet their pertinent range can be deduced from the literature, which allows us to propose a meaningful sensitivity analysis of these parameters, here performed on subvolume SV3.

Figure 12 displays the BTCs for different percolation thresholds $\phi_\theta=0.1, 0.3$ and 0.4 for $n=2$ and 4 . Figure 13 displays the BTCs for different values of the exponent n ranging from 1 to 4 for $\phi_\theta=0.2$ and 0.4 . Note that the BTCs for $\phi_\theta=0.2$ and $\phi_\theta=0$ are identical, compare Figure 11 and Figure 12. This is so because setting the value of ϕ_θ to 0.2 removes only a relatively small fraction of the microporous material, which is already difficult to be reached by the tracer due to its low diffusivity. Consequently, this does not modify noticeably the diffusion properties of the immobile domain. We observe a stronger tailing of the BTC as the value of ϕ_θ increases. Increasing the value of ϕ_θ means increasing the nondiffusive portion of the microporous region, and thus the its tortuosity. As a consequence, the tortuosity of the particle paths leads to an increase in the characteristic retention times and thus the observed stronger tailing of the BTC for $\phi_\theta=0.3$ compared to $\phi_\theta=0.2$. Note that increasing the value of ϕ_θ also means decreasing the microporous domain volume. Thus, as the value of ϕ_θ is further increased, the immobile domain volume decreases to a point that its impact on transport becomes negligible. We observe this in Figure 12. For $\phi_\theta \leq 0.4$ the BTC tailing is less pronounced than for $\phi_\theta=0.3$. Conversely, Figure 13 shows that increasing the value of n increasing the value of t_2 (and to a lesser extent of t_1), and decreases the slope of the intermediate regime bounded by t_1 and t_2 . This can be explained by the fact that increasing n corresponds to an increase of the width of the distribution of the effective diffusion coefficient in the immobile domain. Thus a larger fraction of low diffusion coefficient leads to a stronger particle retention and a larger cut-off time, which is set by the smallest diffusion coefficients.

4.4. Equivalent Homogeneous Microporosity

Here we evaluate if the distributed porosity $\phi_\mu(\mathbf{x})$ in the microporous phase can be simplified by an equivalent homogeneous porosity ϕ_μ^* . For this purpose, we compare simulations using a spatially variable porosity in the microporous phase with simulations that are characterized by the arithmetic, geometric and harmonic means of $\phi_\mu(\mathbf{x})$. Figure 14 shows that the spatially-distributed porosity in the microporous phase can be in general replaced by a constant porosity value equal to the harmonic mean. The effect of this simplification on the BTC shape is negligible for $\phi_\theta=0.2$ and $n=1$, while in other cases (e.g., for $\phi_\theta=0.4$, $n=4$ and $Pe=10$) second-order differences on the late-time BTC shape can be identified.

From Figure 14 we can conclude that in general the spatially variable $\phi_\mu(\mathbf{x})$ can be substituted by an equivalent homogeneous value equal to harmonic mean of the spatial distribution of $\phi_\mu(\mathbf{x})$.

4.5. Effective 1-D CTRW Model

We model the observed breakthrough curves by an effective $d=1$ dimensional CTRW that accounts for both the impact of heterogeneous advection in the pore-space and particle retention due to mass transfer in the immobile domain. Particle transitions are modeled by the recursion relations

$$x_{n+1}=x_n+\Delta x_n, t_{n+1}=t_n+\Delta t_n \quad (16)$$

The increments Δx_n are identical independently distributed random variables which are characterized by the PDF

$$p_x(\Delta x)=(1-p_v)\delta(\Delta x-\ell)+p_v\delta(\Delta x+\ell), \quad (17)$$

where the probability p_v to move upstream is given by

$$p_v=\frac{1}{2+Pe_\ell}. \quad (18)$$

We defined here $Pe_\ell=v\ell/d_0$, where ℓ is the transition length and $v=b\bar{u}$ the effective flow velocity with b a modeling parameter of the order of 1 and \bar{u} the average pore velocity. Before specifying the transition length ℓ , we recall that the particle velocities at subsequent steps in this modeling framework are assumed to be independent. We choose $\ell=78.75 \mu\text{m}$, which corresponds to half of the characteristic length L computed from the Berea sandstone pore structure (see section 3.5). Note that ℓ is larger than the maximum pore radius ($20 \mu\text{m}$), which we deem to be a suitable decorrelation length [de Anna et al., 2013; Kang et al., 2014].

To account for particle transitions in the mobile and immobile regions, the transition times Δt are modeled as [Margolin et al., 2003; Benson and Meerschaert, 2009; Dentz et al., 2012]

$$\Delta t = \tau_m + \sum_{j=1}^{n_{\tau_m}} \tau_{im,j}. \quad (19)$$

The mobile times τ_m and immobile times $\tau_{im,i}$ are each identical independently distributed random variables characterized by the PDFs $\psi_m(\tau_m)$ and $\psi_{im}(\tau_{im})$, respectively. Note that n_{τ_m} is the number of trapping events that occur in the time τ_m . It is a Poisson random variable characterized by the probability distribution

$$p_n(n|\tau_m) = \frac{(\gamma\tau_m)^n \exp(-\gamma\tau_m)}{n!}, \quad (20)$$

where the trapping frequency γ is a modeling parameter that in principle may be related to the medium characteristics [Dentz et al., 2012]. Note that the average number of trapping events is given by $\gamma\tau_m$, i.e., it depends on the mobile time, and thus on the flow conditions. The mobile time is modeled as

$$\tau_m = \tau_0 \eta, \quad (21)$$

in which τ_0 is an exponentially distributed random variable such that

$$\psi_0(\tau_0) = \frac{\exp(-\tau_0/\tau_v)}{\tau_v}, \quad \tau_v = \frac{\ell/v}{1+2Pe_\ell}. \quad (22)$$

The time τ_v is the characteristic transition time for a Fickian model that is characterized by $\eta = 1$. In this case, the CTRW (16) describes advective-diffusive transport in a $d = 1$ dimensional homogeneous medium characterized by the dispersion coefficient d_0 and velocity \bar{u} . Note that the time τ_v depends on both the average flow velocity as well as the diffusion coefficient. Thus, a change in the flow regime manifests directly in the distribution of transition times in the mobile domain.

The dimensionless time η accounts for a broad distribution of transport time scales and is here modeled by the truncated Pareto distribution

$$\psi_\eta(\eta) = \frac{\alpha}{a(1-\epsilon^\alpha)} \left(\frac{\eta}{a}\right)^{-1-\alpha}, \quad (23)$$

for $a < \eta < a\epsilon^{-1}$; where a and ϵ are a modeling parameter that in principle can be related to the smallest and the largest particle velocities. Thus, the PDF of mobile transition times τ_m is given by

$$\psi_m(\tau_m) = \frac{\alpha}{\tau'_v(1-\epsilon^\alpha)} \left(\frac{\tau_m}{\tau'_v}\right)^{-1-\alpha} F_c(\tau_m, \tau'_v, \tau_c), \quad (24)$$

where we defined $\tau'_v = a\tau_v$ and the cutoff time $\tau_c = \tau'_v/\epsilon$. The cut-off function $F_c(\tau_m, \tau'_v, \tau_c)$ is defined by

$$F_c(\tau_m, \tau'_v, \tau_c) = \int_{\tau_m/\tau_c}^{\tau_m/\tau'_v} d\tau \tau^\alpha \exp(-\tau). \quad (25)$$

This distribution is constant for $\tau_m < \tau'_v$, then it decreases as the power-law $\sim \tau_m^{-1-\alpha}$ until it is cut-off exponentially fast for times $\tau_m > \tau_c$, as illustrated in Figure 15. Thus, the fast time scales are delineated by the time scale τ'_v , which scales with the mean flow velocity \bar{u} and the Peclet number. The upper cutoff scale is related to the smallest particle velocity

The immobile times τ_{im} are modeled a the truncated power-law PDF of the same shape as (24),

$$\psi_{im}(\tau_{im}) = \frac{\beta}{\tau_1(1-\epsilon_{im}^\beta)} \left(\frac{\tau_{im}}{\tau_1}\right)^{-1-\beta} F_c(\tau_{im}, \tau_1, \tau_2), \quad (26)$$

where $\tau_1 < \tau_{im} < \tau_2$. The ratio between the lower and upper cut-off scales is denoted by $\epsilon_{im} = \tau_1/\tau_2$. The trapping rate and average trapping time may be related to the volume fraction χ_{im} of the immobile domain as $\chi_{im} = \gamma\langle\tau_{im}\rangle$. The cutoff scales τ_1 and τ_2 as well as the exponent β are characteristic for the heterogeneity

of the immobile regions [Gouze *et al.*, 2008a]. Their values are estimated here from the simulated breakthrough curves.

This $d = 1$ dimensional CTRW model provides a good description of the breakthrough curves obtained numerically from the flow and transport simulations in the heterogeneous pore structure as illustrated in Figure 16. Specifically, it reproduces very well the occurrence of two anomalous time regimes. The first reflects the velocity heterogeneity in the mobile medium portions in which the BTC scales as $t^{-2.4}$, while the second is characteristic of particle retention in the microporous immobile regions. In this regime, the BTC scales as $t^{-5/4}$.

The velocity heterogeneity in the CTRW model (16)–(26) is characterized by the exponent α , which here is found to be $\alpha = 1.4$. The heterogeneity of the immobile zones is reflected by the exponent of β , which here is estimated as $\beta = 1/4$ from the simulation data. This value indicates strong particle retention in the immobile regions. Note that mass transfer between a single type of homogeneous immobile region and the mobile domain is characterized by an exponent of $\beta = 1/2$, which leads to a BTC scaling as $t^{-3/2}$. The heterogeneity of the microporous immobile regions triggers stronger tailing than expected for homogeneous immobile regions.

The parameter values are estimated for the data set with $Pe = 10^2$ and listed in the caption of Figure 16. The same parameters are used for the data set with $Pe = 10^3$, which provides an equally good fit. Thus, the modeling parameters of the effective CTRW model are characteristic of the medium heterogeneity because they do not change with the flow and transport conditions.

5. Conclusion

We presented a numerical study of pore-scale flow and transport of a passive tracer in porous sandstones based on high-resolution 3-D XRMT images of Berea sandstone samples. This rock contains a small fraction of a micro-porous phase which is defined as a porous material with pore smaller than the XRMT resolution. The simulations were performed on a set of subsamples, whose volumes are sufficiently large to be a pertinent approximation of the REV of the media. We obtained a suite of results that allowed us to determine and discuss, as far as we know for the first time, the respective role of the flow field heterogeneity in the macro-pore network, and mass transfer between the mobile and immobile domains.

The main results presented in this paper are:

1. As expected, the mesh resolution has an important influence on the transport results, independently of the presence of the micro-porosity; a coarse mesh tends to increase the non-Fickian behavior and specifically over-estimates the BTC tailing. However, we observed that the differences in non-Fickian behaviors for different mesh resolutions are more pronounced for low Peclet numbers. This is a priori counter-intuitive because a major implication of refining the mesh was a change (decrease) in permeability. Yet the differences in the PDFs of velocity between the coarse mesh and the fine mesh (corresponding to the subdivision of the cells of the coarse mesh in 27 subcells) appears to be small and consists mainly in a general shift of the velocity PDF, i.e., a change of the average velocity.
2. In the absence of mass transfer between the mobile and immobile domains, i.e., for transport localized in connected porosity only, we observed that the heterogeneity of the flow field triggers BTC late-time slopes scaling as $t^{-2.4}$.
3. Marked additional tailing of the BTCs is observed when one takes into account the immobile domain which is formed by the microporous material and some macropores connected by this microporous phase. Specifically, at high Pe a second time regime develops in which the BTC scales as $t^{-5/4}$. Furthermore, the results show that the increase in the late-time component of the BTC is (1) positively correlated to the volume of the micro-porous phase and to the surface area of the mobile-immobile interface, and (2) more pronounced at high Peclet numbers, but cannot be neglected even in the case of diffusion dominated transport.
4. As the only information on the microporous phase given by the XRMT images is its porosity, we employed the parametric model (14) to relate porosity to the effective dispersion coefficients in the immobile region. We probed the impact of the porosity threshold ϕ_{ij} , which denotes the minimum porosity required for percolation in the microporous phase, and the exponent n which is used to model

the tortuosity-porosity power-law dependence and determines the width of the distribution of effective diffusion coefficients. The results showed that: (1) The BTC tailing shows a nonmonotonic behavior with an increase of ϕ_0 . The tailing behavior first increases with the value of ϕ_0 because of an increase of the diffusion path tortuosity, which is triggered by an increase in the lacunarity of the microporous phase. As ϕ_0 increases further the volume of the microporous phase becomes more and more negligible compared to that of the mobile domain and its impact on the BTC diminishes dramatically. (2) Increasing n increases the BTC tailing and affects the cut-off time scale t_2 . This is due to the fact that increasing the value of n decreases the average effective diffusion coefficient and increases the width of its distribution. The larger fraction of low effective diffusion coefficients leads to the increased tailing and the observed increase in t_2 .

5. The spatially variable $\phi_\mu(\mathbf{x})$ can be replaced with its constant harmonic mean, $\bar{\phi}_\mu(\mathbf{x})$. This may be convenient for simplifying the sensitivity analysis of the transport results to the parameters of the immobile domain in case that the distribution of the porosity in the immobile domain is difficult to evaluate due to low quality XMRT data, for example.
6. We built a macroscopic 1-D CTRW model that captures the dual control of flow field heterogeneity and mass transfer between the mobile and immobile domains on non-Fickian transport. The transition time is modeled as the sum of the mobile transition time and the retention time in the immobile domain. The distribution of mobile transition times depends both on the average flow rate and the diffusion coefficient in the mobile region. The broad distribution of transport time scales in the mobile domain, which is a consequence of the velocity heterogeneity, is modeled by a truncated power-law whose characteristic time scales are related to the characteristic advection and diffusion times in the mobile zones.

The number of trapping events in the microporous phase per transition is modeled as a Poisson process whose mean is proportional to the mobile transition time, and thus dependent on the flow rate. The total retention time in the immobile domain then is given by the sum of random trapping times. The distribution of trapping time scales, which is related to the heterogeneous diffusion in the immobile zones, is modeled as a truncated power-law whose cutoff scales can be related to the characteristic diffusion times in the microporous domains.

The CTRW model represents well the observed breakthrough behavior and predicts the existence of two time regimes for large Péclet numbers, as observed in the numerical simulations. The modeling parameters of the presented CTRW approach adjusted from the BTCs for a given Péclet number provide equally good fits when changing the flow and transport regimes. Thus, we suggest that they are characteristic of the medium heterogeneity.

7. All together, the results presented in this paper demonstrate the critical role of both the velocity field heterogeneity and particle retention due to diffusion-dominated transport in the microporosity on observed non-Fickian transport behaviors, even in a rock for which the micro-porous cement represents only a small fraction of the connected porosity. We can anticipate that the non-Fickian behavior due to the presence of the immobile domain should be even more significant in sandstone reservoirs containing larger fractions of microporous cements and in carbonate reservoirs where the microporosity usually represents several percents of the domain accessible to the tracer transport [Garing *et al.*, 2014].

Acknowledgments

The authors wish to thank Paul Tafforeau for his help in the X-ray microtomography data acquisition at the European Synchrotron Radiation facility (ESRF, France). All data used in this work are available upon from the corresponding author, while details and codes for OpenFOAM are available at <http://openfoam.org/>. MD acknowledges the support of the European Research Council (ERC) through the project MHetScale (617511).

References

- Adams, E. E., and L. W. Gelhar (1992), Field study of dispersion in a heterogeneous aquifer, 2. Spatial moment analysis, *Water Resour. Res.*, **28**, 3293–3308.
- Arns, C. H., et al. (2005), Pore scale characterization of carbonates using X-ray microtomography, *SPE J.*, **10**, 475–484.
- Bear, J. (1972), *Dynamics of Fluids in Porous Media*, Am. Elsevier, N. Y.
- Becker, M. W., and A. M. Shapiro (2003), Interpreting tracer breakthrough tailing from different forced-gradient tracer experiment configurations in fractured bedrock, *Water Resour. Res.*, **39**(1), 1024, doi:10.1029/2001WR001190.
- Benson, D. A., and M. M. Meerschaert (2009), A simple and efficient random walk solution of multi-rate mobile/immobile mass transport equations, *Adv. Water Resour.*, **32**(4), 532–539, doi:10.1016/j.advwatres.2009.01.002.
- Berkowitz, B., A. Cortis, M. Dentz, and H. Scher (2006), Modeling non-Fickian transport in geological formations as a continuous time random walk, *Rev. Geophys.*, **44**, RG2003, doi:10.1029/2005RG000178.
- Bijeljic, B., and M. J. Blunt (2006), Pore-scale modeling and continuous time random walk analysis of dispersion in porous media, *Water Resour. Res.*, **42**, W01202, doi:10.1029/2005WR004578.
- Bijeljic, B., A. H. Muggeridge, and M. J. Blunt (2004), Pore-scale modeling of longitudinal dispersion, *Water Resour. Res.*, **40**, W11501, doi:10.1029/2004WR003567.
- Bijeljic, B., P. Mostaghimi, and M. J. Blunt (2011), Signature of non-fickian solute transport in complex heterogeneous porous media, *Phys. Rev. Lett.*, **107**, 204502, doi:10.1103/PhysRevLett.107.204502.

- Bijeljic, B., P. Mostaghimi, and M. Blunt (2013a), Insights into non-Fickian solute transport in carbonates, *Water Resour. Res.*, *49*, 2714–2728, doi:10.1002/wrcr.20238.
- Bijeljic, B., A. Raeini, P. Mostaghimi, and M. Blunt (2013b), Predictions of non-Fickian solute transport in different classes of porous media using direct simulation on pore-scale images, *Phys. Rev. E*, *87*, 013011-1–013011-9, doi:10.1103/PhysRevE.87.013011.
- Blunt, M., B. Bijeljic, H. Dong, O. Gharbi, S. Iglauer, P. Mostaghimi, A. Paluszny, and C. Pentland (2013), Pore-scale imaging and modelling, *Adv. Water Resour.*, *51*, 197–216, doi:10.1016/j.advwatres.2012.03.003.
- Carrera, J., X. Sánchez-Vila, I. Benet, A. Medina, G. Galarza, and J. Guimerà (1998), On matrix diffusion: Formulations, solution methods, and qualitative effects, *Hydrogeol. J.*, *6*, 178–190.
- Churcher, P., P. French, J. Shaw, and L. Schramm (1991), Rock properties of Berea sandstone, baker dolomite and Indiana limestone, paper SPE 21044 presented at the SPE International Symposium on Oilfield Chemistry, Soc. of Pet. Eng., Richardson, Tex.
- Datta, S. S., H. Chiang, T. S. Ramakrishnan, and D. A. Weitz (2013), Spatial fluctuations of fluid velocities in flow through a three-dimensional porous medium, *Phys. Rev. Lett.*, *111*, 064501, doi:10.1103/PhysRevLett.111.064501.
- de Anna, P., T. L. Borgne, M. Dentz, A. M. Tartakovsky, D. Bolster, and P. Davy (2013), Flow intermittency, dispersion, and correlated continuous time random walks in porous media, *Phys. Rev. Lett.*, *110*(18), 184502, doi:10.1103/PhysRevLett.110.184502.
- Delay, F., and J. Bodin (2001), Time domain random walk method to simulate transport by advection-diffusion and matrix diffusion in fracture networks, *Geophys. Res. Lett.*, *28*, 4051–4054.
- Delay, F., P. Ackerer, and C. Danquigny (2005), Simulating solute transport in porous or fractured formations using random walk particle tracking, *Vadose Zone J.*, *4*, 360–379.
- de Marsily, G. (1986), *Quantitative Hydrogeology: Groundwater Hydrology for Engineers*, Academic, San Diego, Calif.
- Dentz, M., and B. Berkowitz (2003), Transport behavior of a passive solute in continuous time random walks and multirate mass transfer, *Water Resour. Res.*, *39*(5), 1111, doi:10.1029/2001WR001163.
- Dentz, M., A. Cortis, H. Scher, and B. Berkowitz (2004), Time behavior of solute transport in heterogeneous media: Transition from anomalous to normal transport, *Adv. Water Resour.*, *27*(2), 155–173.
- Dentz, M., T. Le Borgne, A. Engler, and B. Bijeljic (2011), Mixing, spreading and reaction in heterogeneous media: A brief review, *J. Contam. Hydrol.*, *120-121*, 1–17, doi:10.1016/j.jconhyd.2010.05.002.
- Dentz, M., P. Guoze, A. Russian, J. Dweik, and F. Delay (2012), Diffusion and trapping in heterogeneous media: An inhomogeneous continuous time random walk approach, *Adv. Water Resour.*, *49*, 13–22, doi:10.1016/j.advwatres.2012.07.015.
- Ederly, Y., A. Guadagnini, H. Scher, and B. Berkowitz (2014), Origins of anomalous transport in heterogeneous media: Structural and dynamic controls, *Water Resour. Res.*, *50*, 1490–1505, doi:10.1002/2013WR015111.
- Garing, C., L. Luquot, P. A. Pezard, and P. Guoze (2014), Electrical and flow properties of highly heterogeneous carbonate rocks, *AAPG Bull.*, *98*(1), 49–66.
- Guoze, P., Y. Melean, T. Le Borgne, M. Dentz, and J. Carrera (2008a), Non-Fickian dispersion in porous media explained by heterogeneous microscale matrix diffusion, *Water Resour. Res.*, *44*, W11416, doi:10.1029/2007WR006690.
- Guoze, P., T. Le Borgne, R. Leprovost, G. Lods, T. Poidras, and P. Pezard (2008b), Non-fickian dispersion in porous media: 1. Multiscale measurements using single-well injection withdrawal tracer tests, *Water Resour. Res.*, *44*, W06426, doi:10.1029/2007WR006278.
- Guoze, P., R. Leprovost, T. Poidras, T. L. Borgne, G. Lods, and P. A. Pezard (2009), Cofis and telog: New downhole tools for characterizing dispersion processes in aquifers by single-well injection-withdrawal tracer tests, *C. R. Geosci.*, *341*(10-11), 965–975, doi:10.1016/j.crte.2009.07.012.
- Guibert, R., M. Nazarova, P. Horgue, G. Hamon, P. Creux, and G. Debenest (2015a), Computational permeability determination from pore-scale imaging: Sample size, mesh and method sensitivities, *Transp. Porous Media*, *107*, 641–656.
- Guibert, R., P. Horgue, G. Debenest, and M. Quintard (2015b), A comparison of various methods for the numerical evaluation of porous media permeability tensors from pore-scale geometry, *Math. Geosci.*, 1–19, doi:10.1007/s11004-015-9587-9.
- Haggerty, R., and S. M. Gorelick (1995), Multiple-rate mass transfer for modeling diffusion and surface reactions in media with pore-scale heterogeneity, *Water Resour. Res.*, *31*, 2383–2400.
- Haggerty, R., S. A. McKenna, and L. C. Meigs (2000), On the late time behavior of tracer test breakthrough curves, *Water Resour. Res.*, *36*, 3467–3479.
- Haggerty, R., W. S. Flemin, L. C. Meigs, and S. A. McKenna (2001), Tracer tests in a fractured dolomite 2. Analysis of mass transfer in single-well injection-withdrawal tests, *Water Resour. Res.*, *37*, 1129–1142.
- Haggerty, R., C. F. Harvey, C. F. von Schwerin, and L. C. Meigs (2004), What controls the apparent timescale of solute mass transfer in aquifers and soils? A comparison of experimental results, *Water Resour. Res.*, *40*, W01510, doi:10.1029/2002WR001716.
- Hebert, V., C. Garing, L. Luquot, P. A. Pezard, and P. Guoze (2015), Multiscale X-ray tomography analysis of carbonate porosity, *Geol. Soc. Lon. Spec. Pub.*, *406*(1), 61–79, doi:10.1144/SP406.12.
- Holzner, M., M. Willmann, V. Morales, and M. Dentz (2015), Intermittent Lagrangian velocities and accelerations in three-dimensional porous medium flow, *Phys. Rev. E*, *92*, 013015.
- Hoshen, J., and R. Kopelman (1976), Percolation and cluster distribution. I. Cluster labeling technique and critical concentration algorithm, *Phys. Rev. B Solid State*, *14*(8), 3438–3445.
- Iassonov, P., T. Gebrenegus, and M. Tuller (2009), Segmentation of X-ray computed tomography images of porous materials: A crucial step for characterization and quantitative analysis of pore structures, *Water Resour. Res.*, *45*, W09415, doi:10.1029/2009WR008087.
- Kandhai, D., D. Hlushkou, A. G. Hoekstra, P. M. A. Sloot, H. Van As, and U. Tallarek (2002), Influence of stagnant zones on transient and asymptotic dispersion in macroscopically homogeneous porous media, *Phys. Rev. Lett.*, *88*, 234501-1–234501-4, doi:10.1103/PhysRevLett.88.234501.
- Kang, P., P. de Anna, J. Nunes, B. Bijeljic, M. Blunt, and R. Juanes (2014), Pore-scale intermittent velocity structure underpinning anomalous transport through 3-D porous media, *Geophys. Res. Lett.*, *41*, 6184–6190, doi:10.1002/2014GL061475.
- Le Borgne, T., D. Bolster, M. Dentz, P. de Anna, and A. Tartakosky (2011), Effective pore-scale dispersion upscaling with a correlated continuous time random walk approach, *Water Resour. Res.*, *47*, W12538, doi:10.1029/2011WR010457.
- Levy, M., and B. Berkowitz (2003), Measurement and analysis of non-Fickian dispersion in heterogeneous porous media, *J. Contam. Hydrol.*, *64*(3-4), 203–226, doi:10.1016/S0169-7722(02)00204-8.
- Maier, R. S., M. R. Schure, J. P. Gage, and J. D. Seymour (2008), Sensitivity of pore-scale dispersion to the construction of random bead packs, *Water Resour. Res.*, *44*, W06503, doi:10.1029/2006WR005577.
- Mangano, P. O., P. Guoze, and L. Luquot (2013), Permeability impairment of a limestone reservoir triggered by heterogeneous dissolution and particles migration during CO₂-rich injection, *Geophys. Res. Lett.*, *40*, 4614–4619, doi:10.1002/grl.50595.

- Margolin, G., M. Dentz, and B. Berkowitz (2003), Continuous time random walk and multirate mass transfer modeling of sorption, *Chem. Phys.*, *295*, 71–80.
- Meigs, L. C., and R. L. Beauheim (2001), Tracer tests in a fractured dolomite: 1. Experimental design and observed tracer recoveries, *Water Resour. Res.*, *37*, 1113–1128, doi:10.1029/2000WR900335.
- Moroni, M., N. Kleinfelder, and J. H. Cushman (2007), Analysis of dispersion in porous media via matched-index particle tracking velocimetry experiments, *Adv. Water Resour.*, *30*(1), 1–15, doi:10.1016/j.advwatres.2006.02.005.
- Mostaghimi, P., B. Bijeljic, and M. Blunt (2012), Simulation of flow and dispersion on pore-space images, *Math. Geosci.*, *17*, 1131–1141.
- Neuman, S. P., and D. M. Tartakovsky (2008), Perspective on theories of anomalous transport in heterogeneous media, *Adv. Water Resour.*, *32*, 670–680, doi:10.1016/j.advwatres.2008.08.005.
- Noetinger, B., and T. Estebenet (2000), Up-scaling of double porosity fractured media using continuous-time random walks methods, *Transp. Porous Media*, *39*, 315–337.
- Øren, P.-E., and S. Bakke (2003), Reconstruction of Berea sandstone and pore-scale modelling of wettability effects, *J. Pet. Sci. Eng.*, *39*(3-4), 177–199, doi:10.1016/S0920-4105(03)00062-7.
- Ovaysi, S., and M. Piri (2011), Pore-scale modeling of dispersion in disordered porous media, *J. Contam. Hydrol.*, *124*, 68–81, doi:10.1016/j.jconhyd.2011.02.004.
- Paganin, D., T. E. Mayo, S. C. and Gureyev, P. R. Miller, and S. W. Wilkins (2002), Simultaneous phase and amplitude extraction from a single defocused image of a homogeneous object, *J. Microsc.*, *206*, 33–40.
- Patankar, S. V. (1980), *Numerical Heat Transfer and Fluid Flow*, Hemisphere Publ. Corp.
- Pisani, L. (2011), Simple expression for the tortuosity of porous media, *Transp. Porous Media*, *88*, 193–203.
- Russian, A., P. Gouze, M. Dentz, and A. Gringarten (2015), Multi-continuum approach to modelling shale gas extraction, *Transp. Porous Media*, *109*, 109–130, doi:10.1007/s11242-015-0504-y.
- Sanchez, S., P. E. Ahlberg, K. M. Trinajstić, A. Mirone, and P. Tafforeau (2012), Three dimensional synchrotron virtual paleohistology: A new insight into the world of fossil bone microstructures, *Microsc. Microanal.*, *18*, 1095–1105.
- Scheibe, T. D., W. A. Perkins, M. C. Richmond, M. I. McKinley, P. D. J. Romero-Gomez, M. Ostrom, T. W. Wietsma, J. A. Serkowski, and J. M. Zachara (2015), Pore-scale and multiscale numerical simulation of flow and transport in a laboratory-scale column, *Water Resour. Res.*, *51*, 1023–1035, doi:10.1002/2014WR015959.
- Scheven, U. M., D. Verganelakis, R. Harris, M. L. Johns, and L. F. Gladden (2005), Quantitative nuclear magnetic resonance measurements of preasymptotic dispersion in flow through porous media, *Phys. Fluids*, *17*(11), 214504-1–214504-5, doi:10.1063/1.2131871.
- Schlüter, S., A. Sheppard, K. Brown, and D. Wildenschild (2014), Image processing of multiphase images obtained via X-ray microtomography: A review, *Water Resour. Res.*, *50*, 3615–3639, doi:10.1002/2014WR015256.
- Schumer, R. D., M. Benson, M. Meerschaert, and B. Baeumer (2003), Fractal mobile/immobile solute transport, *Water Resour. Res.*, *39*(10), 1296, doi:10.1029/2003WR002141.
- Sen, P., and P. J. Basser (2005), Modeling diffusion in white matter in the brain: A composite porous medium, *Magn. Reson. Imaging*, *23*, 215–220.
- Shapiro, A. M. (2001), Effective matrix diffusion in kilometer-scale transport in fractured crystalline rock, *Water Resour. Res.*, *37*, 507–522, doi:10.1029/2000WR900301.
- Spirkowska, L. (1993), A summary of image segmentation techniques, technical report, National Aeronautics and Space Administration (NASA) Technical Memorandum 104022, Ames Research Center, Moffett Field, Calif.
- Tanino, Y., and M. J. Blunt (2012), Capillary trapping in sandstones and carbonates: Dependence on pore structure, *Water Resour. Res.*, *48*, W08525, doi:10.1029/2011WR011712.
- Taylor, S. G. (1953), Dispersion of soluble matter in solvent flowing slowly through a tube, *Proc. R. Soc. London, Ser. A*, *219*, 186–203.
- Weller, H., G. Tabor, H. Jasak, and C. Fureby (1998), A tensorial approach to computational continuum mechanics using object-oriented techniques, *J. Comput. Phys.*, *12*, 620–631, doi:10.1063/1.168744.
- Yoon, H., Q. Kang, and A. J. Valocchi (2015), Lattice Boltzmann-based approaches for pore-scale reactive transport, *Rev. Mineral. Geochem.*, *80*, 393–431.
- Zhou, Q., H.-H. Liu, F. J. Molz, Y. Zhang, and G. S. Bodvarsson (2007), Field-scale effective matrix diffusion coefficient for fractured rock: Results from literature survey, *J. Contam. Hydrol.*, *93*(1-4), 161–187, doi:10.1016/j.jconhyd.2007.02.002.

5.4 Summary and conclusion

In this chapter we presented transport simulations performed directly on the XRMT images. Image processing and flow field calculations necessary to calculate transport are explained earlier in Chapter 4. The transport is simulated with a stochastic particle tracking method based on the random walk approach; more precisely we used time domain random walk (TDRW) [Dentz et al., 2012]. In the TDRW distance that particle makes in each step is constant and stochasticity arises from different time needed for the step and the direction. The constant step length makes it suitable to use in a discretized system with complex structure.

Once again, mesh resolution proved to be an important factor. In transport simulations inadequate mesh resolution lead to overestimating the anomalous transport and the error in the results appears to increase with decreasing Peclet number values. Comparison between transport simulations including only flow field heterogeneity and ones including both flow field heterogeneity and mobile-immobile mass transfer emphasizes their concomitant control in the intermediary domain of the BTC tail while, as expected, the mobile-immobile mass transfer control the late time behavior which is, as discussed in section 3.3.3, difficult to tackle experimentally.

From XRMT images we cannot extract a lot of information regarding the microporosity (e.g. tortuosity, percolation threshold). Actually only thing that can be estimated is its intrinsic porosity: the quality of this estimation depends on the quality of the 3-phase segmentation procedure. Therefore we performed a parametric analysis of the percolation threshold and effective diffusion on the BTC shape. Increase of the percolation threshold at the lower values increases the particle resident time in the immobile domain, while at higher values it significantly decreases the fraction of immobile domain accessible to the particles which results in shorter resident time and decreased tailing of the BTC. Conversely, the decrease of the effective diffusion causes increase in the particle residence time in the immobile domain increasing the BTC tailing.

An interesting point evidenced by the result analysis is that if one assumes that the properties of the microporous zone are positively correlated with intrinsic porosity, heterogeneous distribution of the microporous zone can be substituted with its equivalent homogeneous distribution. In this case the single diffusion coefficient for the microporosity must be equal to the harmonic mean of the heterogeneously distributed microporosity.

Finally we proposed an upscaled 1D model based on the continuous time domain random walk approach able to capture behavior caused by both flow field heterogeneity and mobile-immobile mass transfer. This is achieved by having two different power law distributions for representing transit times in mobile and immobile domain.

Chapter 6

Simulations of flow in both the macroporosity and the microporosity: the Darcy-Brinkman approach

6.1 Introduction

Numerical calculations of a flow field at pore scale are usually based on solving the Navier-Stokes equation (see 4.3) on two-phase segmented images. However in Chapters 4 and 5, we already showed that the microporosity cannot be neglected and demonstrated its influence on the anomalous transport behavior. However, in the first article (section 5.3), advection in the microporous phase was neglected, assuming that transport in this zone is completely driven by diffusion; this simplification was based on assumption that the velocities in this region is an order or two lower than in the macroporous zone.

The emphasis of this chapter is on the flow calculation in the microporous zone. There is no question that flow in the microporous zone has significant effect in the porous medium with high microporosity content (e.g. carbonates...). However, the idea is to prove importance of inclusion of the microporous phase into the flow calculations even if the microporous domain is only a fraction of the total medium volume. Problem of the flow calculations in the microporous domain could be solved by using high resolution X-ray microtomography images which can capture pore geometry even in such low pore size regions. Performing flow simulations with such high spatial resolution for volume corresponding to the macroporosity REV far beyond the actual computational possibilities, but it could be used for characterizing the “macroscopic” diffusivity for small volumes of the microporous phase. Yet, we believe that anyway it would be difficult (highly costly in term of computational effort) to evaluate the variability of the microporous phase at the scale of the macroporosity REV. Accordingly, we use here the same Berea sandstone images which were segmented by three phase segmentation (see section 4.2.2). The percolation clusters were determined as in section 4.2.3 with the assumption that microporosity is always percolating (i.e. percolating threshold in the microporous zone is 0). Note that this assumption can be easily avoided, but in this preliminary work the objective is to evaluate the maximum difference in terms of permeability and flow distribution between the two models.

In the present chapter, the used approach is based on the Darcy-Brinkman equation that allows solving Stokes equation in the macroporosity and an equivalent to Darcy flow in the microporous zone. In this approach, a further assumption has to be made which consists in using an heuristic model relating the permeability to the porosity in the microporous material. The Darcy-Brinkman solver compatible with OpenFOAM software package was developed by Cyprien Soullaine from Stanford University. Results are presented in form of a paper which is currently in preparation for submission.

6.2 Article 2 – Effect of microporosity on pore-scale simulation of flow using X-ray microtomography images

Effect of microporosity on pore-scale simulation of flow using X-ray microtomography images

C. Soullaine^a, F. Gjetva^b, C. Garing^a, S. Roman^a, A. Russian^b, H. Tchelepi^a, P. Gouze^b

^aStanford University
^bGéosciences Montpellier

Abstract

This work assesses the effect of microporosity on the fluid flow properties of a Berea sandstone using direct pore-scale simulations. The pore structure of a rock sample is obtained using high resolution X-ray microtomography ($3.16^3 \mu\text{m}^3/\text{voxel}$). Image analysis reveals that about 2% of the connected porosity corresponds to subvoxel porosity, or microporosity. The classic approach based on Stokes equations to solve the flow on three-dimensional images has been modified to incorporate the identified microporous regions. Instead, Darcy-Brinkman equations are used to model a Darcean flow in the microporous zone and a Stokes flow in the macroporosity. Simulation results are in good agreement with experimental core measurements. A cube of 1 mm^3 can be reasonably considered as a Representative Elementary Volume large enough to contain all the heterogeneities of the Berea sandstone sample considered in the present study. Pore-scale simulation, Darcy-Brinkman, microporosity, Berea sandstone, X-ray microtomography

1. Introduction

The rapid advances in three-dimensional (3D) pore-scale imaging and computation have driven a strong interest in digital rock physics, with application to reservoir engineering, subsurface hydrology, and CO_2 sequestration. Specifically, the recent improvements in X-ray microtomography (micro-CT) permits 3D imaging of the pore structure of a rock samples of a few cubic millimeters with a resolution up to the micron (images of 2000^3 voxels with a voxel size of 1 micrometer) [29, 6]. Simultaneously, Computational Fluid Dynamic (CFD) has invested a great deal of effort in developing flexible and highly efficient software platforms for numerical simulation of complex flows that can handle very large grids. Combined with modern High-Performance Computing techniques, flow simulators can now handle up to billion cells on highly complex geometries [27]. It is now quite common to solve the Stokes equations using realistic 3D pore-scale geometry directly computed from micro-CT images to obtain the local flow distribution, \mathbf{v} . The computation of pore scale flow has become a routine step to investigate flow and transport phenomena in

porous media and to evaluate effective parameters such as the permeability tensor, K , of a Representative Elementary Volume (REV) of a porous material [4, 18, 30, 19, 6, 21, 1, 2, 15].

However, some rocks such as carbonates contain a lot of heterogeneities distributed over multiple length scales of characteristic size (much) smaller than the resolution of the micro-CT devices [4, 11, 16]. For rocks that exhibit a multi-modal pore-size distribution, the segmentation of the raw images is a crucial step that can lead to completely different pore space geometries depending on the method used. The use of multi-thresholding segmentation algorithms allows to differentiate the voxels occupied by solid minerals only, those identified as void space only and the remaining ones defined as microporous (voxels composed of both solid and voids). Not taking into account the microporosity can lead to a reduction of the actual pore space or a loss of connectivities as illustrated in Figure 1. In this figure, red and blue regions correspond to zones that are unambiguously identified as void and solid mineral phases respectively, while the purple and green areas denote microporous zones. For instance, the flow resistance in this specific throat will be overestimated if during the segmentation process the purple region is identified as solid phase and thus the flow rate will be higher in the adjacent pore throats, resulting in a complete redistribution of the overall preferential flow pathways. Furthermore, microporous material can act as connecting macropores such as illustrated by the green region in figure 1. We see clearly that in such configurations, an ill-processed segmentation of the raw image can artificially remove connectivities and thus yield in an erroneous local velocity distribution, \mathbf{v} , and hence result to a totally wrong estimate of the sample permeability. Actually, this situation is not restricted to carbonates. For instance, it has been demonstrated that Berea sandstones may contain between 2 and 10% of microporosity [8, 26].

Regarding tracer transport, it is now well-accepted that the diffusion in the microporous matrix can partly explain the non-Fickian dispersion (see Gouze et al. and reference therein [12]). Actually, all the works published so far assume that the transport mechanism in the microporosity is driven by diffusion only. The validity of this assumption however can be put in doubt if the microporous region is located in a percolating pathway, as illustrated by the green region in figure 1. In such a case, convection in the microporosity might play an important role and should be included into the modeling for tracer transport.

The aim of this study is to modify the classic approaches used to obtain the flow through a pore space (*i.e.* by directly solving Stokes equations or using a Lattice Boltzmann Method) in order to incorporate the microporous fraction of porous media, which is defined here as the fraction of material containing pores of size smaller than the voxel size. For that we develop a hybrid solver that solves Stokes equations in the regions identified as void domain and Darcy's law in the microporous domain. The Darcy-Brinkman

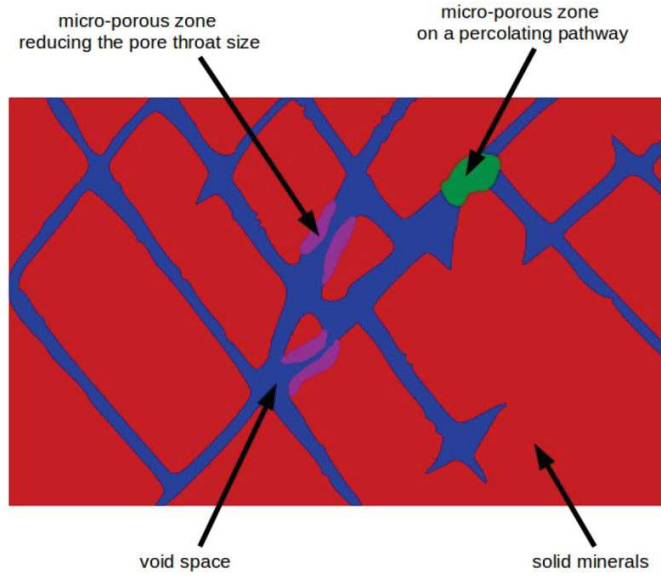


Figure 1: Schematic of a micro-CT rock sample image where red and blue regions are identified as solid minerals phase and void spaces respectively, and green and purple areas denote microporous regions.

approach seems appropriate for the incorporation of microporosity in the flow calculation of a bi-modal porosity medium [3, 20]. A particular attention must be paid to the estimate of the permeability of the micro-porous domain noted k_{micro} . In absence of external knowledge of the geometrical structure of this sub-voxel porosity coming from higher image resolution for example, k_{micro} has to be modeled with the only information provided by the imaging process. At least, it should at least be a function of the image inputs, namely the microporosity and image resolution.

In this paper, we first describe the investigated rock sample, the imaging method and the data processing used to determine the different components (i.e. the void, the solid and the microporous phase). Then we present the Darcy-Brinkman solver and the heuristic law used to estimate k_{micro} from the porosity of the micro-porous phase evaluated from the X-ray microtomography images. Finally, the results of simulations performed on 8 sub-volumes of the scanned rock sample are presented and the impact of the microporosity on the distribution of local velocity and permeability estimate is discussed.

2. Materials and methods

This section introduces the X-ray microtomography technique used to scan the Berea sandstone sample, the mathematical model developed to obtain the velocity distribution in the resulting void space and the simulations setup.

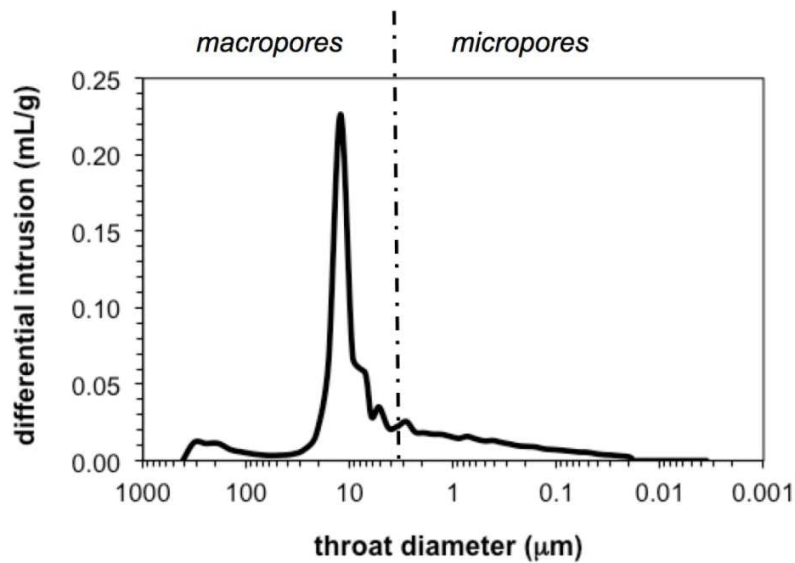


Figure 2: Pore throat size distribution of the studied Berea sandstone determined with mercury injection test (presented as the differential intrusion). The limit pore size separating macropores and micropores in this study (3.16 microns) is displayed as a dashed line.

2.1. X-ray microtomography

X-ray microtomography is a non-invasive imaging technique reconstructing a 3D image of the studied object from a set of two-dimensional (2D) radiographs of the X-ray attenuation properties of the materials forming the object. Each voxel value in the final volume corresponds to a quantitative measurement of linear absorption coefficients, which for a porous medium depends on the solid matrix composition and the porosity.

Sample

The studied rock sample is a Berea sandstone cored into a block presenting porosity and permeability values around 0.20 and 500 mD respectively. A mercury intrusion porosimetry test was conducted on a sample cored aside the scanned one with an AutoPore IV 9500 V1.06 from Micromeritics Instrument Corporation. It provided a porosity value of 19.41% and a mean pore entry (throat) diameter of 11.7 μm . The curve of the differential intrusion, which can be assimilated to the pore throat size distribution, is displayed in Figure 2. The limit size separating the pores that we refer to as macropores (diameter above 3.16 μm) and micropores (diameter below 3.16 μm) is also displayed on the graph. The Figure suggests that the studied sample may comprise a fairly low fraction of microporous material.

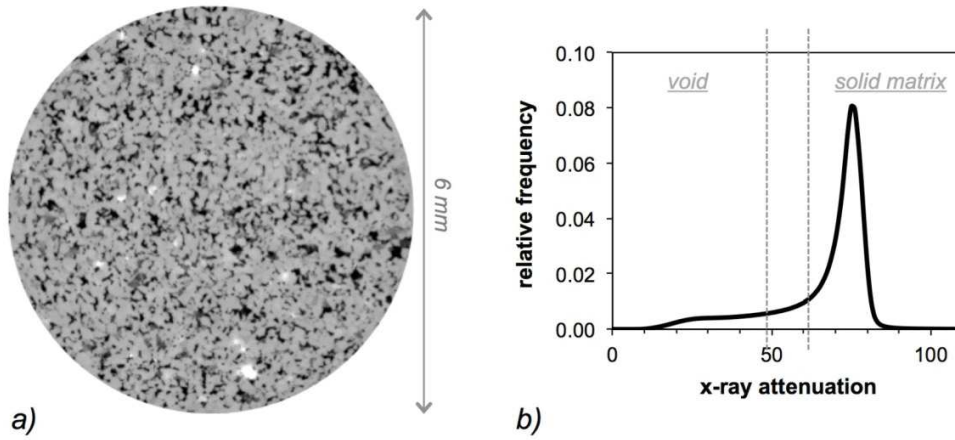


Figure 3: a) Cross section through the 3D volume. b) X-ray attenuation histogram for the entire sample

Data acquisition

The sample of 6 mm diameter and 6 mm length was imaged at the BM5 beamline of the European Synchrotron Radiation Facility (ESRF), Grenoble, France. Synchrotrons provide very high flux of monochromatic white beam and collimated x-rays, resulting in high quality low-noise images at micron/sub-micron resolution. A total of 3495 projections of the sample were taken every 0.051 degree for an angle ranging from 0 to 180 degrees using an exposure time of 0.1 s and an X-ray beam energy of 30 keV. The voxel size was $3.16 \mu\text{m}^3$.

The radiographs were corrected for the variation of the X-ray beam intensity and background noise and then the 3D volume of $4667 \times 2130 \times 2099$ voxels was reconstructed from the radiographs using a single distance phase retrieval algorithm [23, 25]. Figure 3a presents a numerically computed cross-section through the 3D volume. The black colour denotes the macroporosity phase (void only), lighter grey denotes the solid matrix, and the intermediate grey levels denotes the microporous phase (voxels composed of both solid and void). The X-ray attenuation histogram for the entire sample is displayed in Figure 3b. It shows an intermediate attenuation range between the pore and the solid peaks that can be associated to the microporous phase.

Data processing

In order to quantify the volume fraction and distribution of each phase of interest, the grey-scale images require to be segmented so that each phase is identified by a single integer. Since the grey level histogram (Figure 3b) does not show well-separated peaks characterizing the pore phase and the mineral phase, a three-phase segmentation is required in order to identify the microporous phase in addition to the solid matrix

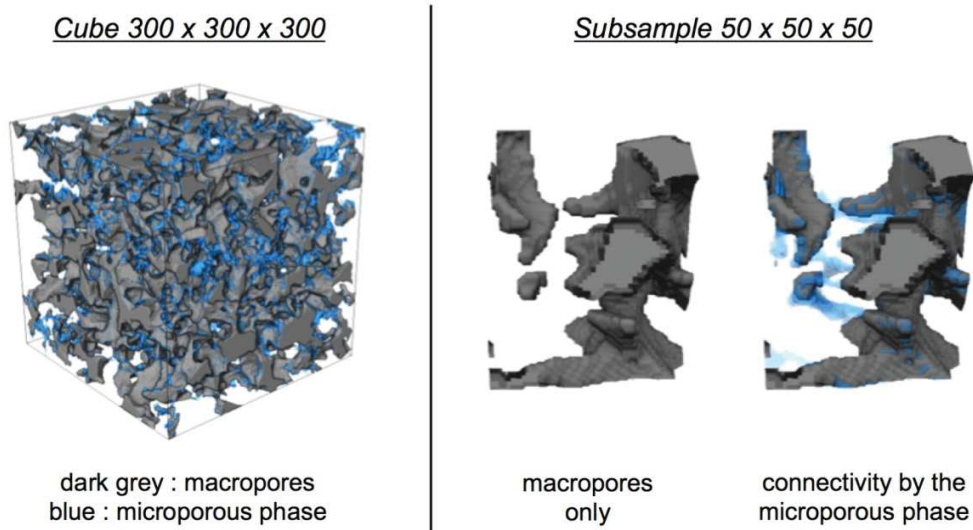


Figure 4: Three-dimensionnal representation of the connected macroporosity and microporous phase on a cube of $300 \times 300 \times 300$ voxels (left) and close-up on macropores only connected through microporous material (right)

and the macroporosity. It was done using the iterative growing-region algorithm described in Noiriél et al. [22] with two sets of thresholds values. A one voxel erosion was performed when distinguishing between voids (macroporosity) and the rest of the sample in order to remove edges artifacts that would then be incorporated in the microporous phase. The fraction of the different phases are 79.45, 18.15 and 2.4 % for the solid, macroporosity and microporous phase respectively. The microporosity has a mean intrinsic porosity of 49.4 %, leading to a total porosity of 19.36 % for the entire sample.

Six cubic sub-volumes of $300 \times 300 \times 300$ voxels (0.948^3 mm^3) and two of $350 \times 350 \times 350$ voxels (1.11^3 mm^3) were extracted from different locations within the 3D image representing the entire sample. For each sub-volume, the connectivity of the macroporosity and microporous phase was investigated using a modified version of the Hoshen-Kopelman algorithm [17]. The fractions of the connected macropores and of the total connected porous network, considering that the micropores comprised in the connected part of the microporous phase are also well connected, are detailed in Table 2 for all sub-volumes. The connected porosity (macropores and micropores) ranges from 17.9 to 21.0%, with a mean value around 19.8%. A close look at the distribution of the connected phases within the sub-volumes indicates that some macropores are only connected through microporous material, as shown in Figure 4 .

2.2. Mathematical model

Once the image analysis process is done, the solid structure is mapped by the microporosity field, $\varepsilon_{\text{micro}}$. It corresponds to the void fraction in each voxel and varies from 0 to 1. If $\varepsilon_{\text{micro}} = 1$ then the voxel contains void only and the flow is governed by a Stokes problem. On the contrary, if $\varepsilon_{\text{micro}} = 0$ then the cell is entirely composed of solid minerals and there is no flow. Intermediate values, *i.e.* $0 < \varepsilon_{\text{micro}} < 1$, denote microporous regions where the characteristic length is below the voxel size. In these regions, the flow resistance with regard to the microporous solid structure is modelled by a Darcy's law. To simulate the flow in an volume that includes microporosity (or microporous regions), two different approaches exist:

1. The two domains approach, where two domains with different physics (namely Stokes and Darcy models) are considered and communicate through coupled boundary conditions. For this approach the type of conditions one should impose at the interface between the free fluid and the porous part is still an open debate. Most of the time the effective conditions experimentally proposed by Beavers and Joseph [5] are used to simulate the pressure jump between the two domains.
2. The single domain approach for which it is assumed that a single equation, the Darcy-Brinkman equation [7], holds in both the free flow and the porous medium domains. The model arises from the integration of Stokes equations over a control volume (here, a voxel) in presence of solid material. Unlike the first approach, it does not involve coupling conditions. Indeed, the use of a single equation makes stresses and velocities continuous within the entire domain and the transition across a transition zone is denoted by spatial variations of properties, such as permeability and porosity. With such a formulation, the physics at the interface between the domains is an approximation of the reality. It has been shown from upscaling considerations, however, that this approximation can be considered as valid for moderate and low permeability [13].

In this work we adopt the second approach, which we estimate to be more convenient and flexible. As the microporosity field, $\varepsilon_{\text{micro}}$, denotes the average amount of void in each voxel, one can define the voxel averaged pressure and velocity fields, \bar{p} and $\bar{\mathbf{v}}$ as,

$$\bar{\mathbf{v}} = \frac{1}{V_{\text{voxel}}} \int_{V_{\text{voxel}}} \mathbf{v} dV \quad \text{and} \quad \bar{p} = \frac{1}{V_{\text{voxel}}} \int_{V_{\text{voxel}}} p dV. \quad (1)$$

These two unknown variables satisfy the locally averaged Stokes equations [28],

$$\nabla \cdot \bar{\mathbf{v}} = 0, \quad (2)$$

and

$$0 = -\nabla\bar{p} + \frac{\mu}{\varepsilon_{\text{micro}}}\nabla^2\bar{\mathbf{v}} - \mu k_{\text{micro}}^{-1}\bar{\mathbf{v}}, \quad (3)$$

where the latest term of the right-hand side of Eq (3) is a drag force that represents the momentum exchange term between the fluid and the solid phase, *i.e.*, the Darcy resistance term. It has meaning only if a voxel contains solid minerals. Conversely, if the control volume is occupied by fluid only, there is no friction of the fluid against any solid structure, and this term tends towards zero. The drag force coefficient, k_{micro} , represents the permeability of the microporous regions, hereby denoted as micropermeability. It is a function of $\varepsilon_{\text{micro}}$ such that the resistance flow term $\mu k_{\text{micro}}^{-1}\bar{\mathbf{v}}$ vanishes in the free zone and is dominant in the microporous medium. With such considerations the locally averaged Stokes momentum equation, Eq (3), tends towards:

- Stokes when $\varepsilon_{\text{micro}} = 1$. In that case, $\bar{\mathbf{v}} = \mathbf{v}$,
- Darcy when $0 < \varepsilon_{\text{micro}} < 1$. In that case, the resistance flow term is dominant and $\bar{\mathbf{v}} = -\frac{k_{\text{micro}}}{\mu}\nabla\bar{p}$.

To summarize: below a certain resolution which is imposed by the image acquisition set-up and sample size, the solid structure is modelled by a microporous medium. Yet, the estimation of the micropermeability (permeability of the microporous regions) is not trivial and very likely to be rock-dependent. We can imagine a multi-scale approach where a very high resolution imaging of the microporosity allows an estimate of its local micropermeability. However, this kind of approach is costly and requires advanced equipment such as a laboratory nano-CT. Instead, for a given voxel, we can use the information of the image acquisition process, namely its size and the volume fraction of void in this voxel to estimate the microporosity. The Kozeny-Carman equation,

$$k_{\text{micro}}^{-1} = \frac{180}{d^2} \frac{(1 - \varepsilon_{\text{micro}})^2}{\varepsilon_{\text{micro}}^3}, \quad (4)$$

seems an appropriate candidate since $k_{\text{micro}}^{-1} \rightarrow \infty$ for very low values of microporosity (solid only) and $k_{\text{micro}}^{-1} = 0$ in the free zone. In Eq (4), d represents a characteristic length which is usually associated to the grain size. In absence of satisfactory values, d is assimilated to the voxel size. This will clearly over-evaluate the characteristic length and therefore the estimate of micropermeability values. Except perhaps in the case where the microporous region are located on a percolating pathway (green region in Figure 1), the main contribution of the permeability, K , comes from the macropores that are explicitly described in this approach (blue regions in Figure 1). Therefore, one can believe that a gross approximation of the micropermeability will not have a strong impact on the overall permeability tensor. It is worth noting that the two asymptotic values

of the micropermeability, $k_{\text{micro}}^{-1} = 0 \text{ mD}^{-1}$ (fully permeable) and $k_{\text{micro}}^{-1} = \infty \text{ mD}^{-1}$ (impermeable) define bounding configurations regardless the microporosity/micropermeability relationship, $k_{\text{micro}} = f(\varepsilon_{\text{micro}})$ and therefore, define bounding values for the permeability, K .

Porosity and permeability can be deduced from these simulations by an integration of the results over the sample volume, V . The porosity of the medium reads,

$$\varepsilon = \frac{1}{V} \int_V \varepsilon_{\text{micro}} dV, \quad (5)$$

and the components of the absolute permeability tensor in the j -axis read,

$$K_{ij} = \mu \left(\frac{\Delta P}{L} \right)_j^{-1} \left(\frac{1}{V} \int_V \bar{v}_i dV \right) \quad \text{with } i = x, y, z, \quad (6)$$

where $\left(\frac{\Delta P}{L} \right)_j$ is the pressure loss in the j direction. To obtain the full tensor, three simulations are required: $j = x, y, z$. In the present study, however, only the main component in z -axis, K_{zz} , is investigated.

2.3. Numerical implementation and simulation setup

The mathematical model formed by Eq (2) and (3) can be easily solved in the framework of the Semi-Implicit Method for Pressure Linked Equations (SIMPLE) algorithm [24]. This algorithm is an iterative procedure for solving steady-state equations for velocity and pressure. To improve the stability of the computation, it requires user-defined under-relaxation factors, α_p and α_U . The first one limits the amount which the pressure changes from one iteration to the next by modifying the pressure field directly. The second one limits the amount of velocity variation by under-relaxating the solution matrix prior to solving for the velocity field. This algorithm is embedded in most CFD softwares, so the effort to implement the model is relatively minimal. In the present study the finite volume toolbox OpenFOAM®(www.openfoam.org) is used. The SIMPLE solver of this package, *simpleFoam*, which has demonstrated a good scalability for parallel computing of single phase flow in a pore space [15], is customized to incorporate the flow resistance term, $\mu k_{\text{micro}}^{-1} \bar{\mathbf{v}}$, into the momentum equation. For a better stability, this term is treated as an implicit source term adding its contribution into the diagonal coefficients of the velocity matrix.

The computational domain is based on the X-ray microtomography segmented image, cropped as a cube of volume V . In order to save computational time and memory, the voxels that are identified as containing solid only, *i.e.* $\varepsilon_{\text{micro}} = 0$, are not represented and a no-slip condition at the solid/fluid boundary is specified. The boundary conditions at the edges of the computational domain are set to mimic an experimental

permeameter: a pressure difference, ΔP_z , is imposed on the inlet and outlet sides of the sample, and no-slip conditions are specified on the other faces of the samples [15, 14]. To specify these inlet and outlet boundary conditions, the computational domain is complemented with two manifolds of $21 \mu\text{m}$ thick. Since there is no flow resistance in these manifolds, the pressure drop in the boundary regions can be neglected compared with the pressure loss through the porous structure. Hence, the overall pressure drop in the rock sample is $\frac{\Delta P_z}{L_z}$, where L_z denotes the length of the sample in the z direction without the manifolds. The mean velocity used to estimate the permeability with Eq (6) is computed excluding the velocity distribution in the manifolds.

The gridding process is a major step considering its strong influence on the results accuracy. Former studies have based their computational grids directly on the image voxels, *i.e.*, one cell of the simulation grid corresponds to one voxel of the micro-CT image [4, 21]. However, because a porous medium skeleton consists in numerous narrow throats, one has first to ensure that the smallest throat of the domain contains enough cells in order to get an accurate flow profile in this capillary. Guibert et al. [15] performed mesh convergence analysis to investigate the influence of the size of the mesh on the simulation results. They reported that a computational grid made of the image voxels can exhibit up to 50% relative error on the computed permeability. Table 1 summarizes the mesh convergence study we performed on a 150^3 voxels sub-volume of the scanned Berea sandstone sample. The sub-volume does not contain any microporous regions. In this study, the image voxels were divided by n^3 with n varying from 1 to 7. Without refinement, a computational grid based on the image voxels only leads to up to 22% error in the absolute permeability assessment. This preliminary study leads us to choose simulation grids consisting of cells 3^3 finer than the image voxels, which offers a good compromise between accuracy (less than 5% error) and simulation cost.

n	1	2	3	4	5	6	7
K_{zz} (mD)	736	657	630	617	610	605	602
standard deviation (%)	22.4	9.1	4.7	2.5	1.3	0.5	0

Table 1: Mesh convergence study performed on a 150^3 voxels sub-volume of the scanned Berea sandstone sample

Computational domains are decomposed into 256 subdomains and simulations are carried out in parallel with 256 cores on Stanford Center for Computational Earth & Environmental Sciences cluster, 148 compute nodes, Dual E5-2660 Intel cpus (8 cores, 2.2GHz 8.0GT/s 20mb 95W DDR3-1600), 64 GB memory. Convergence is considered reached when the residuals go below 10^{-6} . The relaxation factors α_p and α_U are set to 0.2 and 0.9 respectively. Indeed, for Stokes problem the simulations require up to twice as less iterations to converge to the solution with $\alpha_U = 0.9$ as with the usual recommended value $\alpha_U = 0.8$. In every cases, simulations converge to the solution within 2 hours.

3. Results and discussion

This section presents the simulation results for the different sub-volumes. A first study investigates the influence of sub-voxel porosity on the pore-scale simulation results and shows that even with only 2% of microporosity, the prediction can be far from the expected value if the image is not properly segmented and the sub-voxel porosity is not accounted for in the flow modeling. In a second part, the simulation results of the single phase flow in the 8 sub-volumes of the Berea sandstone sample with distributed microporosity throughout the domain are presented and discussed.

3.1. Influence of sub-voxel porosity

To investigate the influence of microporosity on pore-scale simulations, a sub-volume of the image, denoted SubV0, was extracted and segmented into three different phases: void, solid and microporous. The connected pore structure of this sub-volume corresponds to 19.7% of macroporosity and 2.6% of microporosity. Regions identified as microporous are colored in red in Figure 5a. We observe that in some areas, according to the value of microporosity, $\varepsilon_{\text{micro}}$, some pathways can switch from percolating to non-percolating. In this part, it is assumed that the value of $\varepsilon_{\text{micro}}$ is the same for all the voxels identified as microporous phase.

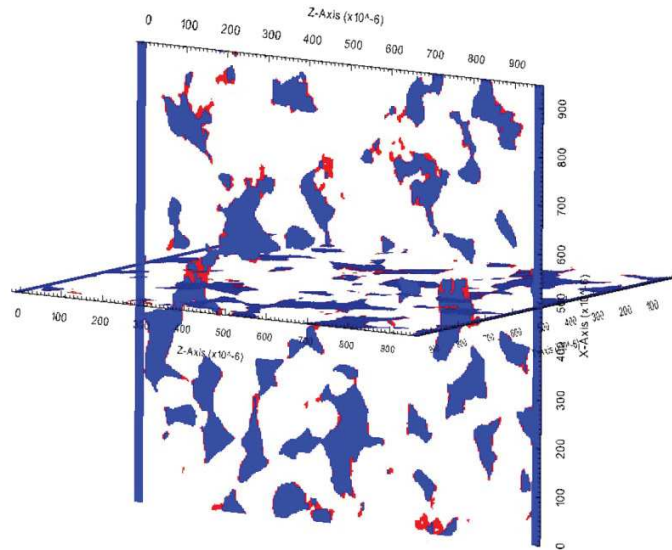


Figure 5: Map of the microporous regions for subsample SubV0 (blue=void, red=microporosity).

Several simulations are performed for $\varepsilon_{\text{micro}}$ ranging from 0.001 to 1. For these two extreme values, the permeability is evaluated to 702 mD and 1366 mD respectively. These two limit values of $\varepsilon_{\text{micro}}$ denote specific

situations where the microporous phase is identified as fully solid ($\varepsilon_{\text{micro}} = 0.001$) or fully void ($\varepsilon_{\text{micro}} = 1$). Because of the asymptotic values of the associated micropermeability, $k_{\text{micro}}^{-1} = 0$ or $\infty \text{ mD}^{-1}$ for these two bounding cases (here, ∞ stands for 10^7 mD^{-1} , which ensures that there is no flow in the microporous zone when $\varepsilon_{\text{micro}} = 0.001$), the resulting velocity distributions, and thus permeability, are independent of the relation that relates microporosity and micropermeability. Therefore, the discussion regarding the validity of Eq (4) does not apply for these cases.

Table 2 presents the computed permeability, K_{zz} , and porosity, ε , of SubV0 for different values of microporosity. As expected, K_{zz} increases when pore throats size is larger, *i.e.* for higher value of microporosity. The results clearly show that according to the segmentation process, the computed absolute permeability can be up to twice as high or low as the actual value.

$\varepsilon_{\text{micro}}$	0.001	0.25	0.5	0.75	0.9	1
$k_{\text{micro}}(\text{mD})$	0	2	27	365	3944	∞
ε	0.197	0.204	0.210	0.216	0.220	0.223
$K_{zz}(\text{mD})$	702	798	839	950	1168	1366

Table 2: Summary of simulation results for different microporosity values. Micropermeability, k_{micro} , is estimated with Eq (4).

The Probability Density Functions (PDFs) of the normalized velocity distribution, $\frac{|\mathbf{v}|}{|\frac{1}{V} \int_V \mathbf{v} dV|}$, are plotted for the different value of $\varepsilon_{\text{micro}}$ in Figure 6. In all cases, 99% of the cells contains velocities up to twice the superficial mean velocity and the PDFs present a quasi exponential decay reminiscent of recent numerical and experimental works [10, 9]. About 0.9% contains velocity between 2 and 4 times the mean velocity. The PDFs are shifted towards the right when reducing the microporosity value. Below a certain threshold, here close to $\varepsilon_{\text{micro}} = 0.75$, the PDFs become superimposed. This suggests that for simulations above this value ($\varepsilon_{\text{micro}}$ from 0.75 to 1), the presence or absence of microporous regions significantly changes the flow pathways. The flow resistance in some area becomes so important that it locally redistributes the flow, favoring other pores. In contrary, for simulations with $\varepsilon_{\text{micro}}$ below 0.75, the flow pathways are always the same, regardless the microporosity value. In such cases, the magnitude of the velocity field increases with the reduction of the pore-space, as expected. The velocity profiles plotted in Figure 7 illustrate this situation.

3.2. Simulation results for distributed microporosity

The situation presented so far where the value of sub-voxel porosity is the same throughout the entire rock sample is a bit artificial and only aimed to emphasize that if the length scale below the image resolution are not considered into the modeling, the velocity distribution obtained by pore-scale simulation can be

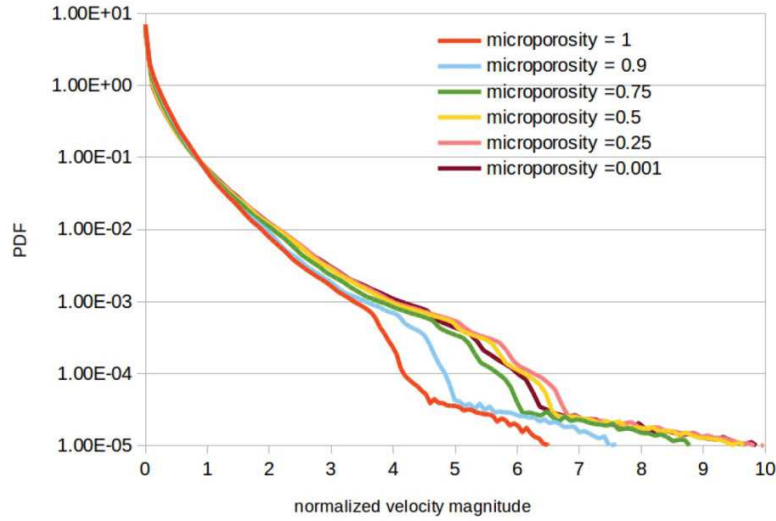


Figure 6: Plot of the Probability Density Functions of the normalized velocity distribution for $\varepsilon_{\text{micro}}$ ranging from 0 to 1.

totally wrong. In general, the microporosity has values heterogeneously distributed in the rock. In this section, the microporosity domain, $\varepsilon_{\text{micro}}$, is defined as a distribution of porosity values, and subsequently permeability values using equation 4, obtained from the distribution of grey level in the micro-porous phase (see an example in Figure 8a). The velocity distributions and permeability of the 8 sub-volumes is computed according to the procedure described in Section 2. The computational grid for the 6 cubes of $300 \times 300 \times 300$ voxels and for the 2 cubes of $350 \times 350 \times 350$ voxels contains approximately 220×10^6 and 330×10^6 cells respectively.

Figures 8b and 8c display the magnitude velocity distribution and the pressure field in the void space of a $300 \times 300 \times 300$ voxels sub-volume. These simulation results are then volume averaged following equation 6 to deduce the permeability of the different sub-volumes. Table 3 summarizes the simulation results for the different investigated sub-volumes. The calculated porosity is 0.20 ± 0.02 , as measured in laboratory on the Berea sandstone rock sample. Computed permeabilities range from 518 mD to 858 mD, and the mean value of the 8 simulations is 692 mD. These results are in good agreement with the 500 mD given by core measurements.

Sample	SubV1	SubV2	SubV3	SubV4	SubV5	SubV6	SubV7	SubV8
resolution	300 × 300 × 300						350 × 350 × 350	
ε	0.210	0.208	0.197	0.199	0.193	0.202	0.197	0.199
K_{zz} (mD)	858	848	785	518	534	855	659	835

Table 3: Values of porosity and permeability computed for the different sub-volumes.

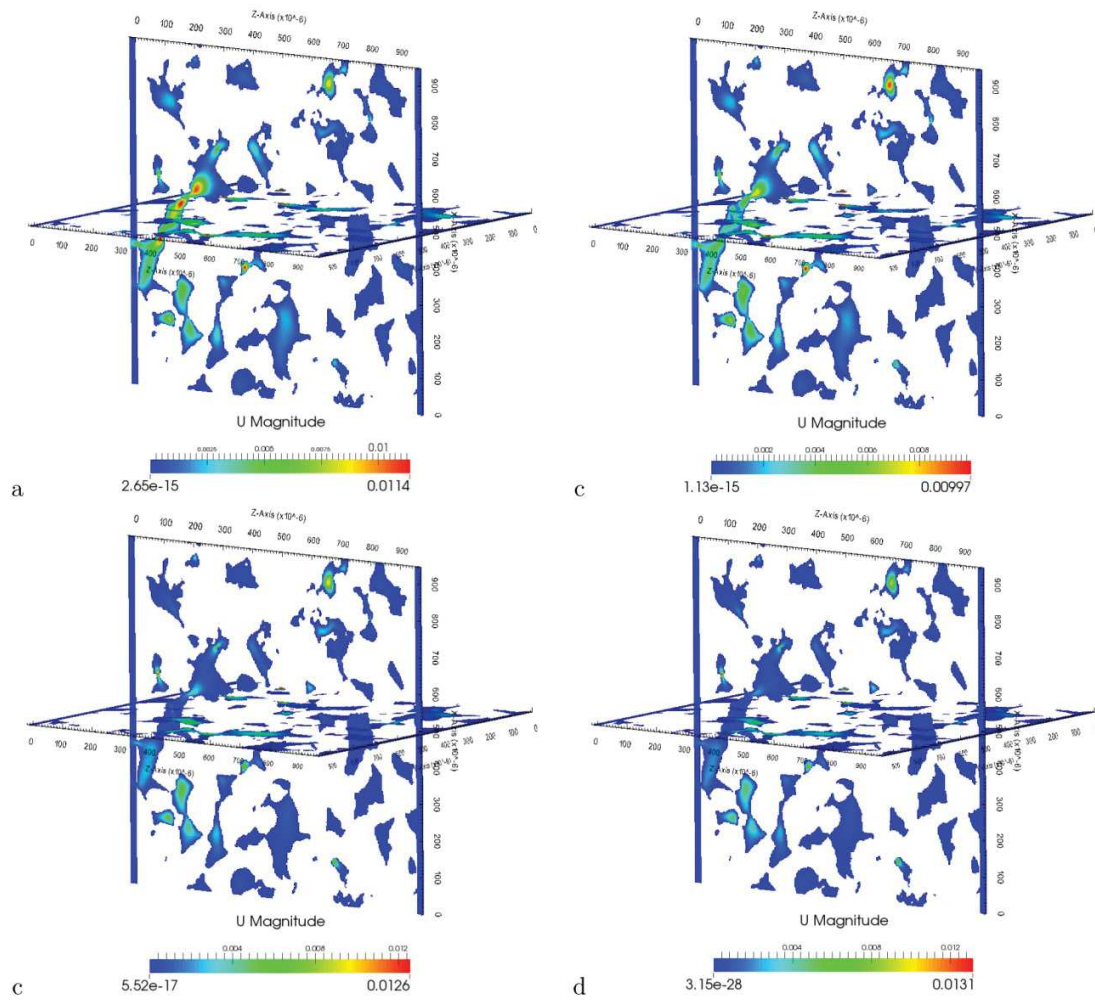


Figure 7: Plot of the velocity distribution for different sub-voxel porosity values: *a*) $\epsilon_{\text{micro}} = 1$, *b*) $\epsilon_{\text{micro}} = 0.9$, *c*) $\epsilon_{\text{micro}} = 0.5$, *d*) $\epsilon_{\text{micro}} \approx 0$.

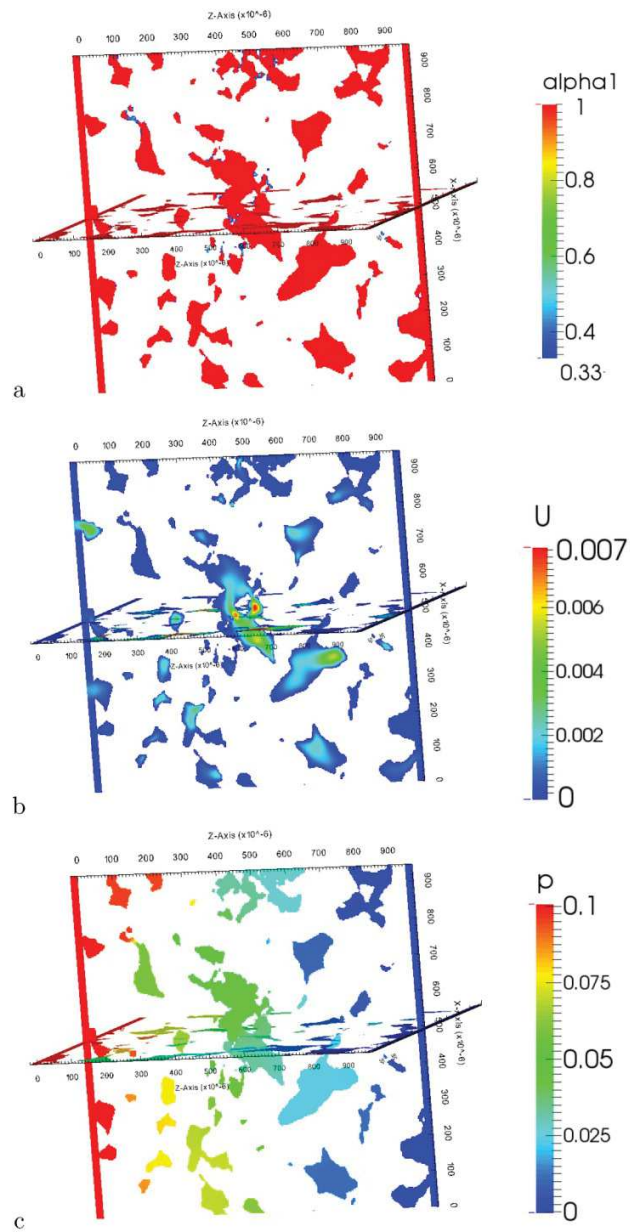


Figure 8: Plot of the simulation results for a $300 \times 300 \times 300$ voxels sub-volume. *a)* microporosity distribution, *b)* velocity distribution, *c)* pressure field.

The Probability Density Functions of the normalized velocity distribution for the different sub-volumes are plotted in Figure 9. The PDFs display similar trend for all simulations and 99% of the cells contains velocities up to X times the superficial mean velocity. These results confirm that for this Berea sandstone a cube of 1 mm^3 can be reasonably considered as a Representative Elementary Volume large enough to contain all the heterogeneities of the porous medium.

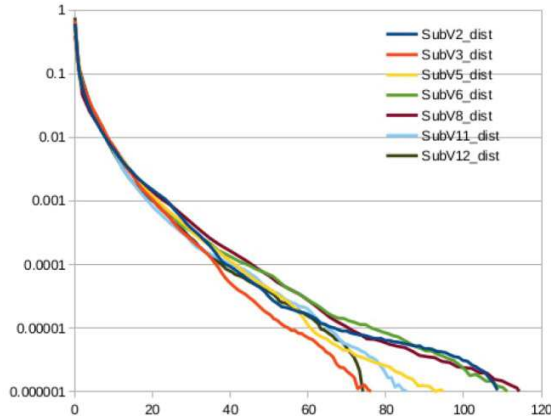


Figure 9: Probability Density Functions of the velocity distribution for the different sub-volumes.

4. Conclusion

With the improvement of imaging techniques and simulation capabilities, a recent trend tends to use pore-scale simulations as an alternative to lab measurements. The foundation of these simulations is an high fidelity representation of the solid skeleton. However, because of the multiple length scale nature of porous media, some structures are much smaller than the image resolution and can not be explicitly represented in the image. In this paper, we have proposed a general framework based on Darcy-Brinkman equations to incorporate this sub-voxel porosity into pore-scale simulations.

Simulations of flow in a Berea sandstone have shown that even with only 2% of microporous regions, the sub-voxel porosity plays an important role in the flow distribution within the pore network with evident consequences on the evaluation of the permeability tensor. In particular, some microporosity links macropores and if it is not included properly into the modeling, connectivities can be artificially removed. This has direct implications for tracer transport modeling since it suggests that the transport mechanism in the sub-voxel porosity can be driven not only by diffusion but also by convection. Future works in this direction will quantify this contribution.

The extension of this framework to multiphase system is clearly an open question that needs to be addressed if one wish to use pore-scale simulation to replace core-flooding experiments.

Acknowledgments

We wish to acknowledge (**TOTAL STEMS project, EFRC DOE**) for financial support. We thank Stanford Center for Computational Earth & Environmental Sciences for computational support. We also thank Paul Tafforeau for his help in the X-ray microtomography data acquisition at the European Synchrotron Radiation facility (ESRF, France).

References

- [1] Heiko Andrä, Nicolas Combaret, Jack Dvorkin, Erik Glatt, Junehee Han, Matthias Kabel, Youngseuk Keehm, Fabian Krzikalla, Minhui Lee, Claudio Madonna, Mike Marsh, Tapan Mukerji, Erik H. Saenger, Ratnanabha Sain, Nishank Saxena, Sarah Ricker, Andreas Wiegmann, and Xin Zhan. Digital rock physics benchmarks part i: Imaging and segmentation. *Computers & Geosciences*, 50(0):25 – 32, 2013. Benchmark problems, datasets and methodologies for the computational geosciences.
- [2] Heiko Andrä, Nicolas Combaret, Jack Dvorkin, Erik Glatt, Junehee Han, Matthias Kabel, Youngseuk Keehm, Fabian Krzikalla, Minhui Lee, Claudio Madonna, Mike Marsh, Tapan Mukerji, Erik H. Saenger, Ratnanabha Sain, Nishank Saxena, Sarah Ricker, Andreas Wiegmann, and Xin Zhan. Digital rock physics benchmarks part ii: Computing effective properties. *Computers & Geosciences*, 50(0):33 – 43, 2013. Benchmark problems, datasets and methodologies for the computational geosciences.
- [3] Saeid Norouzi Apourvari and Christoph H. Arns. An assessment of the influence of micro-porosity for effective permeability using local flux analysis on tomographic images. *International Petroleum Technology Conference, 19-22 January, Doha, Qatar*, 2014.
- [4] C.H. Arns, F. Baugé, A. Limaye, A. Sakellariou, T.J. Senden, A.P. Sheppard, R.M. Sok, L.I. Berge W.V. Pinczewskiband S. Bakke, and M.A. Knackstedt P.-E. Oeren. Pore-scale characterization of carbonates using x-ray microtomography. *SPE Journal*, 10(4):475–484, 2005.
- [5] Gordon S. Beavers and Daniel D. Joseph. Boundary conditions at a naturally permeable wall. *Journal of Fluid Mechanics*, 30:197–207, 1967.

-
- [6] Martin J. Blunt, Branko Bijeljic, Hu Dong, Oussama Gharbi, Stefan Iglauer, Peyman Mostaghimi, Adriana Paluszny, and Christopher Pentland. Pore-scale imaging and modelling. *Advances in Water Resources*, 51:197–216, 2013.
- [7] H. C. Brinkman. A calculation of the viscous force exerted by a flowing fluid on a dense swarm of particles. *Appl. Sci. Res.*, A1:27–34, 1947.
- [8] PL Churcher, PR French, JC Shaw, LL Schramm, et al. Rock properties of berea sandstone, baker dolomite, and indiana limestone. *SPE*, 21044:20–22, 1991.
- [9] Sujit S. Datta, H. Chiang, T. S. Ramakrishnan, and David A. Weitz. Spatial fluctuations of fluid velocities in flow through a three-dimensional porous medium. *Phys. Rev. Lett.*, 111:064501, Aug 2013.
- [10] Pietro De Anna, Tanguy Le Borgne, Marco Dentz, Alexandre M Tartakovsky, Diogo Bolster, and Philippe Davy. Flow intermittency, dispersion, and correlated continuous time random walks in porous media. *Physical review letters*, 110(18):184502, 2013.
- [11] Charlotte Garing, Linda Luquot, Philippe A Pezard, and Philippe Gouze. Electrical and flow properties of highly heterogeneous carbonate rocks. *AAPG Bulletin*, 98(1):49–66, 2014.
- [12] Philippe Gouze, Yasmin Melean, Tanguy Le Borgne, Marco Dentz, and Jesus Carrera. Non-fickian dispersion in porous media explained by heterogeneous microscale matrix diffusion. *Water Resources Research*, 44(11):n/a–n/a, 2008.
- [13] B. Goyeau, T. Benihaddadene, D. Gobin, and M. Quintard. Averaged momentum equation for flow through a nonhomogenous porous structure. *Transport in Porous Media*, 28(1):19–50, 1997.
- [14] R Guibert, P Horgue, G Debenest, and M Quintard. A comparison of various methods for the numerical evaluation of porous media permeability tensors from pore-scale geometry. *Mathematical Geosciences*, March 2015.
- [15] R. Guibert, M. Nazarova, P. Horgue, G. Hamon, P. Creux, and G. Debenest. Computational permeability determination from pore-scale imaging: Sample size, mesh and method sensitivities. *Transport in Porous Media*, pages 1–16, 2015.
- [16] Vanessa Hebert, Charlotte Garing, Linda Luquot, PA Pezard, and Philippe Gouze. Multi-scale x-ray tomography analysis of carbonate porosity. *Geological Society, London, Special Publications*, 406(1):61–79, 2015.

- [17] Joseph Hoshen and Raoul Kopelman. Percolation and cluster distribution. i. cluster multiple labeling technique and critical concentration algorithm. *Physical Review B*, 14(8):3438, 1976.
- [18] M.E. Kainourgiakis, E.S. Kikkinides, A. Galani, G.C. Charalambopoulou, and A.K. Stubos. Digitally reconstructed porous media: Transport and sorption properties. In D.B. Das and S.M. Hassanizadeh, editors, *Upscaling Multiphase Flow in Porous Media*, pages 43–62. Springer Netherlands, 2005.
- [19] Faisal Khan, Frieder Enzmann, Michael Kersten, Andreas Wiegmann, and Konrad Steiner. 3d simulation of the permeability tensor in a soil aggregate on basis of nanotomographic imaging and lbe solver. *Journal of Soils and Sediments*, 12(1):86–96, 2011.
- [20] Marcin Krotkiewski, Ingeborg S. Ligaarden, Knut–Andreas Lie, and Daniel W. Schmid. On the importance of the stokes–brinkman equations for computing effective permeability in carbonate karst reservoirs. *Global Science*, 2015.
- [21] Peyman Mostaghimi, Martin J. Blunt, and Branko Bijeljic. Computations of absolute permeability on micro-ct images. *Math Geosci*, 2013.
- [22] Catherine Noiriél, Dominique Bernard, Ph Gouze, and Xavier Thibault. Hydraulic properties and microgeometry evolution accompanying limestone dissolution by acidic water. *Oil & gas science and technology*, 60(1):177–192, 2005.
- [23] David Paganin, SC Mayo, Tim E Gureyev, Peter R Miller, and Steve W Wilkins. Simultaneous phase and amplitude extraction from a single defocused image of a homogeneous object. *Journal of microscopy*, 206(1):33–40, 2002.
- [24] Patankar. *Numerical Heat Transfer And Fluid Flow*. Taylor & Francis, 1980.
- [25] Sophie Sanchez, Per E Ahlberg, Katherine M Trinajstic, Alessandro Mirone, and Paul Tafforeau. Three-dimensional synchrotron virtual paleohistology: a new insight into the world of fossil bone microstructures. *Microscopy and Microanalysis*, 18(05):1095–1105, 2012.
- [26] Y Tanino and Martin J Blunt. Capillary trapping in sandstones and carbonates: Dependence on pore structure. *Water Resources Research*, 48(8), 2012.
- [27] David Trebotich and Daniel T. Graves. An adaptive finite volume method for the incompressible navier–stokes equations in complex geometries. *Communications in Applied Mathematics and Computational Science*, 2015.

- [28] Stephen Whitaker. Flow in porous media i: A theoretical derivation of darcy's law. *Transport in Porous Media*, 1:3–25, 1986. 10.1007/BF01036523.
- [29] Dorte Wildenschild and Adrian P. Sheppard. X-ray imaging and analysis techniques for quantifying pore-scale structure and processes in subsurface porous medium systems. *Advances in Water Resources*, 51(0):217 – 246, 2013. 35th Year Anniversary Issue.
- [30] Xin Zhan, Lawrence Schwartz, Wave Smith, Nafi Toksöz, and Dale Morgan. Pore scale modeling of rock properties and comparison to laboratory measurements. In *SEG Houston 2009 International Exposition and Annual Meeting*, pages –. Society of Exploration Geophysicists, 2009.

6.3 Results – comparison with Navier-Stokes equation

In addition to the results presented in the previous section, Table 6.1 presents the comparison of the permeability values between simulations performed on the exactly same (300^3 voxel) blocks with Navier-Stokes and Darcy-Brinkman equations based approaches. For Navier-Stokes simulations the microporous phase is added to the solid phase, to obtain 2-phase images. Permeability and porosity are calculated by equations (4.4) and (4.2) respectively.

	Permeability [mD]			Porosity [%]		
	N-S	D-B	Δ [%]	2 phase	3 phase	Δ [%]
SubV1	804	858	6.7	19.4	21	14.2
SubV2	802	848	5.7	19.3	20.8	14.0
SubV3	753	785	4.3	18.3	19.7	15.1
SubV4	485	518	6.8	18.2	19.9	16.1
SubV5	509	534	4.9	17.9	19.3	15.5

Table 6.1 Comparison in permeability and porosity between simulations performed on 2-phase (Navier-Stokes) and 3-phase (Darcy-Brinkman) segmented images. All simulations are performed on exactly the same 300^3 voxel blocks, fine mesh.

Results reveal that the inclusion of the microporous phase into flow calculations leads to an increase in permeability ranging from 4 to 7 %, while we expect errors from the flow simulations to be lower than 1 %.

6.4 Summary and conclusion

Starting from 3-phase segmented XRMT images (see section 4.2.2) we performed 3D pore scale flow simulations both in the macro and microporosity. The new solver developed in the OpenFOAM framework has proved to be appropriate for simultaneously solving the flow in the macroporosity and the microporous domain. The approach is based on the Darcy-Brinkman equation, which uses single equation to calculate fluid velocity in both Stokes (i.e. macroporosity) and Darcy (i.e. microporosity) domain. It consists of adding Darcy resistance term in Stokes equation, which represents the friction between solid and void in the macroporous domain. In the macroporosity domain the Darcy resistance term is null and we solve standard Stokes equation. The most important part of defining the Darcy resistance term is in the determination of the permeability in the microporous domain. Since we have no real data on the microporosity properties (see sections 4.2 and 5.2), the permeability is estimated by Kozeny-Carman equation.

The aim of this work was to study the importance of the additional flow in the microporosity even in rocks with low microporosity content such as Berea sandstone (2 %). The increase in permeability due to the microporosity is around 5 % which is relatively small but still noticeable and we can anticipate that the contribution of the flow in the microporosity should become a major process in rocks with

higher fraction of microporosity such as altered sandstone and carbonates. Nevertheless it is worth recalling that the Darcy-Brinkman simulation results hang on the porosity-permeability model used in the microporous phase (here Kozeny-Carman relationship). The implications of using different models or model parameterization (e.g. using power law ϕ - k laws such as proposed by [Gouze and Luquot, 2011]) on the permeability and further on the solute transport will have to be tested in futures works. Also, as mentioned in section 6.1, high resolution microtomography (with pixel size smaller than 500 nm for instance) can be used to help determining appropriate ϕ - k laws for the microporosity.

Chapter 7

General conclusions and prospective

In this thesis we presented new insights into the flow and transport in porous media obtained from both laboratory experiments and pore-scale numerical modeling. The main focus was on the simultaneous study of the flow field heterogeneity and multi-rate mass transfer as coexisting mechanisms contributing to the control of anomalous transport.

Newly designed experimental bench allowed highly accurate measurements over several orders of the concentration magnitude. Small experimental scale enabled to notice the significant density effect occurring if the tracer concentration in the solute is 500 ppm or higher. The density effect may lead to the misinterpretation of the experiment results, and it is important to notice that this concentration is well below the ones used in standard tracer tests. Comparison between push-pull and flow-through experiments performed on the glass beads and Berea sandstone indicated that solute concentration should be measured over more than 5 orders of magnitude to capture late time behavior controlled by the mobile-immobile mass transfer.

All together we found that 1) meeting all the requirements for obtaining reliable results (including a good reproducibility) is quite difficult and 2) that the range of Peclet values that can be effectively investigated with a sufficient definition of the BTC tail is quite restricted. Specifically, for the low Peclet number situations generally encountered in natural system, tackling the power-law decrease characteristic of the mobile-immobile mass transfers seems unrealistic at laboratory scale even with state-of-the-art (optical) sensors such as used in this study, at least for the type of porous media studied here.

Concerning pore-scale modeling, we presented some improvements on the understanding of the mesh resolution influence on the local and macroscopic properties. To our knowledge we performed the first transport simulations on segmented X-ray microtomography (XRMT) images containing a microporous phase. Transport simulations in the microporous phase are enabled by the implementation of the particle tracking method based on the random walk principles with constant displacement length [Dentz et al., 2012]. Results emphasize that taking into account the microporosity in the transport calculations is crucial even in porous media with low microporosity content such as Berea sandstone. Further simulations must be made to conclude on the influence on the overall dispersion of assuming diffusion only in the microporous phase or taking into account advection as well. Nevertheless, we demonstrated the influence of the advection in the microporous phase on the bulk permeability and velocity distribution using a solver based on the Darcy-Brinkman equation.

Transport behavior was up-scaled within a 1-D model based on the continuous time random walk (CTRW) principles, which incorporates both flow field heterogeneity and mobile-immobile mass transfer effects simultaneously. This new model was used to fit pore-scale simulations and we showed its predictability in the case of the Berea sandstone.

Finally, we did not managed to make a formal link between the experimental data on Berea sandstone and the transport simulations performed on the XRMT images of the same rock, but we made some qualitative comparisons that proved that the implementation in the models of the mass transfer in

the microporosity is compulsory for explaining the observations. Furthermore, we identified the methodological requirements and necessary technologic upgrading that seem to be essential for improving the experimental setup. Specifically, modifications must be made 1) to allow higher Peclet flow rate in order to better investigate the flow velocity heterogeneity on the anomalous transport and 2) to even increase the concentration measurement accuracy and resolution.

Conversely, we believe that further developments should focus on a better characterization of the microporosity and velocity distribution in order to relate the CTRW model parameters to measurable properties. While the directions of research for characterizing the microporosity can be easily drawn (e.g., measuring microporosity cluster volume, interface area, ...), improving the characterization of the flow field with the objective of parameterizing CTRW is more challenging and will require probably to analyze the velocity correlations in a Lagrangian framework.

Bibliography

- Abell, A.B., Willis, K.L., and Lange, D.A., 1999. Mercury Intrusion Porosimetry and Image Analysis of Cement-Based Materials. *Journal of Colloid and Interface Science*, 211, pp.39-44.
- Adams, E.E. and Gelhar, L.W., 1992. Field Study of Dispersion in a Heterogeneous Aqifer 2. Spatial Moments Analysis. *Water Resources Research*, 28(12), pp.3293-307.
- Adler, P.M., 1992. *Porous Media: Geometry and Transport*. Stoneham, Massachusetts: Butterworth-Heinemann.
- Archie, G.E., 1942. The Electrical Resistivity Log as an Aid in Determining Some Reservoir Characteristics. *Petroleum Technology*, pp.54-62.
- Aris, R., 1956. On the dispersion of a solute in a fluid flowing through a tube. *Proceedings of the Royal Society of London. Series A, Mathematical and Physical Sciences*, 235, pp.67--77.
- Arns, C.H., Bauget, F., Limaye, A., Sakellariou, A., Senden, T.J., Sheppard, A.P., Sok, R.M., Pinczewski, W.V., Bakke, S., Berge, L.I., Oren, P.-E., and Knackstedt, M.A., 2005. Pore Scale Characterization of Carbonates Using X-ray Microtomography. *Society of Petroleum Engineers*.
- Avellandea, M. and Torquato, S., 1991. Rigorous link between fluid permeability, electrical conductivity, and relaxation times for transport in porous media. *Phys. Fluids A*, 3(11), pp.2529-40.
- Barenblatt, G.I., Zheltov, I.P., and Kochina, I.N., 1960. Basic concepts in the theory of seepage of homogeneous liquids in fissured rocks (Strata). *Journal of Applied Mathematics and Mechanics*, 24(5), pp.1286-303.
- Bear, J., 1972. *Dynamics of fluids in porous media*. 1st ed. New York: American Elsevier Publishing Company, Inc.
- Bear, J. and Bachmat, Y., 1967. A generalized theory on hydrodynamic dispersion in porous media. *Int. Union Geod. Geophys*, 1.
- Bear, J. and Bachmat, Y., 1986. Macroscopic Modelling of Transport Phenomena in Porous Media. 2: Applications to Mass, Momentum and Energy Transport. *Transport in Porous Media*, pp.241-69.
- Becker, M.W. and Shapiro, A.M., 2000. Tracer transport in fractured crystalline rock: evidence of nondiffusive breakthrough tailing. *Water Resources Research*, 36(7), pp.1677-86.
- Benson, D.A., Wheatcraft, S.W., and Meerschaert, M.M., 2000. The fractional-order governing equation of Lévy motion. *Water Resources Research*, 36(6), pp.1413-23.
- Berkowitz, B., Cortis, A., Dentz, M., and Scher, H., 2006. Modeling non-Fickian transport in geological formations as a continuous time random walk. *Rev. Geophys.*, (44).
- Berkowitz, B., Emmanuel, S., and Scher, H., 2008. Non-Fickian transport and multiple-rate mass transfer in porous media. *Water Resources Research*, 44.
- Berkowitz, B., Scher, H., and Silliman, S.E., 2000. Anomalous transport in laboratory-scale, heterogeneous porous media. *Water Resources Research*, 36(1), pp.149-58.

Bijeljic, B., Mostaghimi, P., and Blunt, M.J., 2011b. Signature of non-fickian solute transport in complex heterogeneous porous media. *Physical Review Letters*, 107.

Bijeljic, B., Mostaghimi, P., and Blunt, M.J., 2013. Insights into non-Fickian solute transport in carbonates. *Water Resources Research*, 49, pp.2714-28.

Bijeljic, B., Muggeridge, A.H., and Blunt, M.J., 2004. Pore-scale modeling of longitudinal dispersion. *Water Resources Research*, 40.

Bijeljic, B., Rubin, S., Scher, H., and Berkowitz, B., 2011a. Non-Fickian transport in porous media with bimodal structural heterogeneity. *Journal of Contaminant Hydrology*, 120, pp.213-21.

Blunt, M.J., Bijeljic, B., Dong, H., Gharbi, O., Iglauer, S., Mostaghimi, P., Paluszny, A., and Pentland, C., 2013. Pore-scale imaging and modelling. *Advances in Water Resources*, 51, pp.197-216.

Brinkman, H.C., 1949. A calculation of the viscous force exerted by a flowing fluid on a dense swarm of particles. *Applied Scientific Research*, A1, pp.27-34.

Caretto, L.S., Gosman, A.D., Patankar, S.V., and Spalding, D.B., 1972. Two Calculation Procedures for Steady, Three-Dimensional Flows with Recirculation. In *Proc. 3d Int. Conf. Num. Methods Fluid Dyn.* Paris, 1972.

Carman, P.C., 1937. Fluid flow through granulat beds. *Trans. Instn. Chem. Engrs.*, 15, pp.32-48.

Carrera, J., Sanchez-Vila, X., Benet, I., Medina, A., Galarza, G., and Guimera, J., 1998. On matrix diffusion: formulations, solution methods and qualitative effects. *Hydrogeology Journal*, 6, pp.178-90.

Clennel, B.M., 1997. Tortuosity: a guide through the maze. *Geological Society, Special Publications* 122.

Coats, K.H. and Smith, B.D., 1964. Dead-end pore volume and dispersion in porous media. *Society of Petroleum Engineers Journal*, 4(1), pp.73-84.

Cortis, A. and Berkowitz, B., 2004. Anomalous Transport in "Classical" Soil and Sand Columns. *Soil Science Society of America Journal*, 68(5), pp.1539-48.

Cortis, A. and Birkholzer, J., 2008. Continuous time random walk analysis of solute transport in fractured porous media. *Water Resources Research*, 44.

Cortis, A., Chen, Y., Scher, H., and Berkowitz, B., 2004. Quantitative characterization of pore-scale disordere effects on transport in "homogeneous" media. *Physical Review E*, 70.

Curcher, P.L., French, P.R., Shaw, J.C., and Schramm, L.L., 1991. Rock Properties of Berea Sanstone, Baker Dolomite, and Indiana Limestone. In *Proceedings of the SPE International Syposium on Oilfield Chemistry*. Anaheim, CA, 1991. Society of Petroleum Engineers.

Cushman, J.H., 1984. On Unifying the Concepts of Scale, Instrumentation, and Stochastics in the Development of MuTransport Theory. *Water Resources Research*, 20(10), pp.1668-76.

Cushman, J.H. and Ginn, T.R., 1993. Nonlocal dispersion in media with continuously evolving scales of heterogeneity. *Transport in Porous Media*, 13(1), pp.123-28.

- Dagan, G., 1989. *Flow and Transport in Porous Formations*. Heidelberg: Springer-Verlag.
- Datta, S.S., Chiang, H., Ramakrishnan, T.S., and Weitz, D.A., 2013. Spatial Fluctuations of Fluid Velocities in Flow through a Three-Dimensional Porous Medium. *Physical Review Letters*, 11, pp.064501-1-5.
- de Marsily, G., 1986. *Quantitative Hydrology: Groundwater Hydrology for engineers*. San Diego, California: Academic Press, Inc.
- Delgado, J.M.P.Q., 2007. Longitudinal and transverse dispersion in porous media. *Chemical Engineering Research and Design*, 85(A9), pp.1245-52.
- Dentz, M. and Berkowitz, B., 2003. Transport behavior of a passive solute in continuous time random walks and multirate mass transfer. *Water Resources Research*, 39(5).
- Dentz, M., Gouze, P., Russian, A., Dweik, J., and Delay, F., 2012. Diffusion and trapping in heterogeneous media: An inhomogeneous continuous time random walk approach. *Advances in Water Resources*, 49, pp.13-22.
- Dias, R., Teixeira, J.A., Mota, M., and Yelshin, A., 2006. Tortuosity variation in a low density binary particulate bed. *Separation Purification Technology*, 51, pp.180-84.
- Dullien, F.A.L., 1992. *Porous Media Fluid Transport and Pore Structure*. San Diego, California: Academic Press, Inc.
- Fernandes, J.S., Appoloni, C.R., and Fernandes, C.P., 2012. Determination of the Representative Elementary Volume for the study of sandstones and siltstones by X-ray microtomography. *Material Research*, 15(4), pp.662-70.
- Fetter, C.W., 1999. *Contaminant hydrogeology*. 2nd ed. Upper Saddle River, New Jersey: Prentice-Hall, Inc.
- Fick, A., 1855. Uber Diffusion. *Annalen der Physik*, 170, pp.59-86.
- Fourar, M. and Radilla, G., 2009. Non-Fickian Description of Tracer Transport Through Heterogeneous Porous Media. *Transport in Porous Media*, 80, pp.561-79.
- Freyberg, D.L., 1986. A Natural Gradient Experiment on Solute Transport in a Sand Aquifer 2. Spatial Moments and the Advection and Dispersion of Nonreactive Tracers. *Water Resources Research*, 22(13), pp.2031-46.
- Galambos, P. and Forster, F.K., 1998. Micro-Fluidic Diffusion Coefficient Measurement. In Harrison, J.D. and van den Berg, A. *Micro Total Analysis Systems '98*. Banff, Canada, 1998. Springer Netherlands.
- Garabedian, S.P., LeBlanc, D.R., Gelhar, L.W., and Celia, M.A., 1991. Large-Scale natural Gradient Tracer Test in Sand and Gravel, Cape Cod, Massachusetts 2. Analysis of Spatial Moments for a Nonreactive Tracer. *Water Resources Research*, 27(5), pp.911-24.
- Gaspar, E., 1987. *Modern Trends in Tracer Hydrology*. Boca Raton, Florida: CRC Press Inc.

Gouze, P., Le Borgne, T., Leprovost, R., Lods, G., Poidras, T., and Pezard, P., 2008a. Non-Fickian dispersion in porous media: 1. Multiscale measurements using single-well injection withdrawal tracer tests. *Water Resources Research*, 44(6).

Gouze, P., Leprovost, R., Poidras, T., Le Borgne, T., Lods, G., and Pezard, P.A., 2009. CoFIS and TELog: New downhole tools for characterizing dispersion processes in aquifers by single-well injection-withdrawal tracer tests. *C.R. Geoscience*, pp.965-75.

Gouze, P. and Luquot, L., 2011. On the characterization of porosity-permeability relationships and reactive surface areas during heterogeneous dissolution induced by CO₂ injection in limestone reservoir. *Journal of Contaminant Hydrology*, 120-121, pp.45-55.

Gouze, P., Melean, Y., Le Borgne, T., Dentz, M., and Carrera, J., 2008b. Non-Fickian dispersion in porous media explained by heterogenous microscale matrix diffusion. *Water Resources Research*, 44(11).

Griffiths, A., 1911. On the Movement of a Coloured Index along a Capillary Tube, and its Application to the Measurement of the Circulation of Water in a Closed Circuit. *Proc. Phys. Soc. London*, 23, pp.190-97.

Guibert, R., Horgue, P., Debenest, G., and Quintard, M., 2015. A comparison of various methods for the numerical evaluation of porous media permeability tensor from pore-scale geometry. *Mathematical Geosciences*, pp.1-19.

Guibert, R., Nazarova, M., Horgue, P., Hamon, G., Creux, P., and Debenest, G., 2015. Computational Permeability Determination from Pore-Scale Imaging: Sample Size, Mesh and Method Sensitivities. *Transp. Porous Med.*

Haggerty, R., Fleming, S.W., Meigs, L.C., and McKenna, S.A., 2001. Tracer tests in a fractured dolomite 2. Analysis of mass transfer in single well injection-withdrawal tests. *Water Resources Research*, 37(5), pp.1129-42.

Haggerty, R. and Gorelick, S.M., 1995. Multiple-rate mass transfer for modeling diffusion and surface reactions in media with pore-scale heterogeneity. *Water Resources Research*, 31(10), pp.1383-2400.

Haggerty, R., Harvey, C.F., von Schwerin, C.F., and Meigs, L.C., 2004. What controls the apparent timescale of solute mass transfer in aquifers and soils? A comparison of experimental results. *Water Resources Research*, 40.

Haggerty, R., McKenna, S.A., and Meigs, L.C., 2000. On the late-time behavior of tracer test breakthrough curves. *Water Resources Research*, 36(12), pp.3467-79.

Hassanizadeh, M.S. and Leijnse, A., 1995. A non-linear theory of high-concentration-gradient dispersion in porous media. *Advances in Water Resources*, 18(4), pp.203-15.

Hoshen, J. and Kopelman, R., 1976. Percolation and cluster distribution. I. Cluster multiple labeling technique and critical concentration algorithm. *Physical Review B*, 14(8), pp.3438-45.

Iassonov, P., Gebrenegus, T., and Tuller, M., 2009. Segmentation of x-ray computed tomography images of porous materials: A crucial step for characterization and quantitative analysis of pore structures. *Water Resources Research*, 45(9).

Kandhai, D., Hlushkou, D., Hoekstra, A.G., Soot, P.M.A., Van As, H., and Tallarek, U., 2002. Influence of Stagnant Zones on Transient and Asymptotic Dispersion in Macroscopically Homogeneous Porous Media. *Physical Review Letters*, 88(23).

Kang, P.K., de Anna, P., Nunes, J.P., Bijeljic, B., Blunt, M.J., and Juanes, R., 2014. Pore-scale intermittent velocity structure underpinning anomalous transport through 3-D porous media. *Geophysical Research Letters*, pp.6184-90.

Kang, P.K., Le Borgne, T., Dentz, M., Bour, O., and Juanes, R., 2015. Impact of velocity correlation and distribution on transport in fractured media: Field evidence and theoretical model. *Water Resources Research*, 51(2), pp.940-59.

Kasnavia, T., Vu, D., and Sabatini, D.A., 1999. Fluorescent Dye and Media Properties Affecting Sorption and Tracer Selection. *Ground Water*, 37(3), pp.376-81.

Klise, K.A., Tidwell, V.C., and McKenna, S.A., 2008. Comparison of laboratory-scale solute transport visualization experiments with numerical simulation using cross-bedded sandstone. *Advances in Water Resources*, 31, pp.1731-41.

Konz, M., Younes, A., Ackerer, P., Fahs, M., Huggenberger, P., and Zechner, E., 2009. Variable-density flow in heterogeneous porous media - Laboratory experiments and numerical simulations. *Journal of Contaminant Hydrology*, 108, pp.168-75.

Le Borgne, T., Bolster, D., Dentz, M., de Anna, P., and Tartakovsky, A., 2011. Effective pore-scale dispersion upscaling with correlated continuous time random walk approach. *Water Resources Research*, 47.

Le Borgne, T. and Gouze, P., 2008. Non-Fickian dispersion in porous media: 2. Model validation from measurements at different scales. *Water Resources Research*, 44.

LeBlanc, D.R., Garabedian, S.P., Hess, K.M., Gelhar, L.W., Quadri, R.D., Stollenwerk, K.G., and Wood, W.W., 1991. Large-Scale Natural Gradient Tracer Test in Sand and Gravel, Cape Code, Massachusetts 1. Experimental Design and Observed Tracer Movement. *Water Resources Research*, 27(5), pp.895-910.

Levy, M. and Berkowitz, B., 2002. Measurement and analysis of non-Fickian dispersion in heterogeneous porous media. *Journal of Contaminant Hydrology*, 64, pp.203-26.

Liu, Y. and Kitanidis, P.K., 2012. Applicability of the Dual-Domain Model to Nonaggregated Porous Media. *Ground Water*, 50(6), pp.927-34.

Lorenz, P.B., 1961. Tortuosity in Porous Media. *Nature*, (189), pp.386-87.

Mackay, D.M., Freyberg, D.L., Roberts, P.V., and Cherry, J.A., 1986. A Natural Gradient Experiment on Solute Transport in a Sand Aquifer 1. Approach and Overview of Plume Movement. *Water Resources Research*, 22(13), pp.2017-29.

-
- Maier, R.S., Schure, M.R., Gage, J.P., and Seymour, J.D., 2008. Sensitivity of pore-scale dispersion to the construction of random bead packs. *Water Resources Research*, 44(6).
- Mangane, P.O., Gouze, P., and Luquot, L., 2013. Permeability impairment of a limestone reservoir triggered by heterogeneous dissolution and particles migration during CO₂-rich injection. *Geophysical Research Letters*, 40(17), pp.4614-19.
- Meigs, L.C. and Beauheim, R.L., 2001. Tracer test in a fractured dolomite 1. Experimental design and observed tracer recoveries. *Water Resources Research*, 37(5), pp.1113-28.
- Montroll, E.W. and Weiss, G.H., 1965. Random walks on lattices, II. *Journal of Mathematical Physics*, 6(2), pp.167-81.
- Morales-Casique, E., Neuman, S.P., and Guadagnini, A., 2006. Nonlocal and localized analyses of nonreactive solute transport in bounded randomly heterogeneous porous media: Computational analysis. *Advances in Water Resources*, 29(9), pp.1399-418.
- Moroni, M., Kleinfelder, N., and Cushman, J.H., 2006. Analysis of dispersion in porous media via matched particle tracking velocimetry experiments. *Advances in Water Resources*, 30, pp.1-15.
- Mostaghimi, P., Bijeljic, B., and Blunt, M.J., 2012. Simulation of Flow and Dispersion on Pore-Space Images. *SPE Journal*, pp.1131-41.
- Neuman, S.P. and Tartakovsky, D.M., 2009. Perspective on theories of non-Fickian transport in heterogeneous media. *Advances in Water Resources*, 32, pp.670-80.
- Noiriel, C., Bernard, D., Gouze, P., and Thibault, X., 2005. Hydraulic properties and microgeometry evolution in the course of limestone dissolution by CO₂-enriched water. *Oil and Gas Science and Technology*, 60(1-2), pp.177-92.
- Okabe, H. and Oseto, K., 2006. Pore-scale heterogeneity assessed by the Lattice-Boltzman method. In *Proceedings of the International Symposium, Society of Core Analysts*. Trondheim, Norway, 2006.
- OpenFOAM Foundation, 2014. *OpenFOAM*. [Online] Available at: www.openfoam.org [Accessed May 2014].
- Øren, P.-E. and Bakke, S., 2003. Reconstruction of berea sandstones and pore-scale modelling of wettability effects. *Journal of Petroleum Science and Engineering*, 39, pp.177-99.
- Ovaysi, S. and Piri, M., 2010. Direct pore-level modeling of incompressible fluid flow in porous media. *Journal of Computational Physics*, 229(19), pp.7456-76.
- Ovaysi, S. and Piri, M., 2011. Pore-scale modeling of dispersion in disordered porous media. *Journal of Contaminant Hydrology*, 124, pp.68-81.
- Paganin, D., Mayo, S.C., Gureyev, T.E., Miller, P.R., and Wilkins, S.W., 2002. Simltaneous phase and amplitude extraction from a single defocused image of homogeneous object. *Journal of Microscopy*, 206, pp.33-40.
- Patankar, S.V., 1975. Numerical Predictions in Three-Dimensional Flow. In Launder, B.E. *Studies in Convection: Theory, Measurement and Applications*. New York: Academic Press.

- Patankar, S.V., 1980. *Numerical Heat Transfer and Fluid Flow*. Washington: Hemisphere Publications.
- Patankar, S.V. and Spalding, D.B., 1972. A Calculation Procedure for Heat, Mass and Momentum Transfer in Three-Dimensional Parabolic Flows. *Int. J. Heat Mass Transfer*, 15, pp.1787-806.
- Quintard, M. and Whitaker, S., 1994. Transport in Ordered and Disordered Porous Media I: The Cellular Average and the Use of Weighting Functions. *Transport in Porous Media*, 14, pp.163-77.
- Rao, P.S.C., Rolston, D.E., Jessup, R.E., and Davidson, J.M., 1980. Solute Transport in Aggregated Porous Media: Theoretical and Experimental Evaluation. *Soil Science Society of America Journal*, 44(6), pp.1139-46.
- Reynolds, A.M., Reavell, S.V., and Harral, B.B., 2000. Flow and dispersion through a close-packed bed of spheres. *Physical Review E*, 62(3), pp.3632-39.
- Saffman, P.G., 1959. A theory of dispersion in porous media. *Journal of Fluid Mechanics*, 6(3), pp.321-49.
- Saffman, P.G., 1960. Dispersion due to molecular diffusion and macroscopic mixing in flow through a network of capillaries. *Journal of Fluid Mechanics*, 7(2), pp.194-208.
- Sahimi, M., 1993. Flow phenomena in rocks: from continuum models to fractals, percolation, cellular automata, and simulated annealing. *Reviews of Modern Physics*, 65(4), pp.1393-534.
- Scheibe, T.D., Perkins, W.A., Richmond, M.C., McKinley, M.I., Romero-Gomez, P.D.J., Oostrom, M., Wietsma, T.W., Serkowski, J.A., and Zachara, J.M., 2015. Pore-scale and multiscale numerical simulation of flow and transport in a laboratory-scale column. *Water Resources Research*, 51, pp.1023-35.
- Scheidegger, A.E., 1961. General Theory of Dispersion in Porous Media. *Journal of Geophysical Research*, 66(10), pp.3273-78.
- Scher, H. and Lax, M., 1973. Stochastic Transport in a Disordered Solid. I Theory. *Physical Review B*, 7(10), pp.4491-502.
- Scheven, U.M., 2013. Pore-Scale Mixing and Transverse Dispersivity of Randomly Packed Monodisperse Spheres. *Physical Review Letters*, 110.
- Scheven, U.M., Verganelakis, D., Harris, R., Johns, M.L., and Gladden, L.F., 2005. Quantitative nuclear magnetic resonance measurements of preasymptotic dispersion in flow through porous media. *Physics of Fluids*, 17(11), pp.117107-117107-7.
- Schlüter, S., Sheppard, A., Brown, K., and Wildenschild, D., 2014. Image processing of multiphase images obtained via x-ray micropomography: A review. *Water Resources Research*, 50(4), pp.3615-39.
- Schumer, R., Benson, D.A., Meerschaert, M.M., and Baeumer, B., 2003. Fractal mobile/immobile solute transport. *Water Resources Research*, 39(10).
- Sederman, A.J., Johns, M.L., Bramley, A.S., Alexander, P., and Gladden, L.F., 1997. Magnetic resonance imaging of liquid flow and pore structure within packed beds. *Chemical Engineering Sciences*, 52(14), pp.2239-50.

Seymour, J.D. and Callaghan, P.T., 1997. Generalized Approach to NMR Analysis of Flow and Dispersion in Porous Media. *Materials, Interfaces, and Electrochemical Phenomena Journal*, 43(8), pp.2096-111.

Siena, M., Hyman, J.D., Riva, M., Guadagnini, A., Winter, C.L., Smolarkiewicz, P.K., Gouze, P., Sadhukhan, S., Inzoli, F., Guedon, G., and Colombo, E., 2015. Direct numerical simulation of fully saturated flow in natural porous media at the pore scale: a comparison of three computational systems. *Computational Geosciences*.

Silliman, S.E. and Simpson, E.S., 1987. Laboratory Evidence of the Scale Effect in Dispersion of Solutes in Porous Media. *Water Resources Research*, 23(8), pp.1667-73.

Siprkovska, L., 1993. *A Summary of Image Segmentation Techniques*. Technical report. Moffett Field, California: Ames Research center NASA.

So, P.T. and Dong, C.Y., 2002. Fluorescence Spectrophotometry. In *Encyclopedia of Life Sciences*. Macmillan Publisher Ltd, Nature Publishing Groupe.

Taylor, G., 1953. Dispersion of Soluble Matter in Solvent Flowing Slowly through a Tube. *Proceedings of the Royal Society of London. Series A, Mathematical and Physical Sciences*, 219(1137), pp.186-203.

Taylor, G., 1954. The dispersion of matter in turbulent flow through a pipe. *Proceedings of the Royal Society of London, Series A*, 223, pp.446-68.

Tenchine, S. and Gouze, P., 2005. Density contrast effects on tracer dispersion in variable aperture fractures. *Advances in Water Resources*, 28, pp.273-89.

Toride, N., Leij, F.J., and van Genuchten, M.T., 1995. *The CXTFIT Code for Estimating Transport Parameters from Laboratory or Field Tracer Experiments*. Research Report No. 137. Riverside, California: U.S. Salinity Laboratory Agricultural Research Service U.S. Department of Agriculture.

van Genuchten, M.T., Tang, D.H., and Guennelon, R., 1984. Some Exact Solutions for Solute Transport Through Soils Containing Large Cylindrical Macropores. *Water Resources Research*, 20(3), pp.335-46.

van Genuchten, M.T. and Wierenga, P.J., 1976. Mass Transfer Studies in Sorbing Porous Media, I. Analytical Solutions. *Soil Science Society of America Journal*, 40(4), pp.473-80.

Washburn, E.W., 1921. The Dynamics of Capillary Flow. *The Physical Review*, XVII(3), pp.273-83.

Zinn, B., Meigs, L.C., Harvey, C.F., Haggerty, R., Peplinski, W.J., and Von Schwerin, C.F., 2004. Experimental Visualization of Solute Transport and Mass Transfer Processes in Two-Dimensional Conductivity Fields with Connected Regions of High Conductivity. *Environmental Science & Technology*, 38(14), pp.3916-26.

Résumé substantiel

Introduction

Les milieux poreux sont tout autour de nous et de notre vie quotidienne. Comprendre les mécanismes de transferts de masse et d'énergie qui se produisent dans ces milieux poreux est un objectif scientifique depuis longtemps. L'un des processus très important est le transport de substance dissoute, qui intervient dans de nombreux processus naturels, en particulier en géosciences (dispersion des polluants, exploitation des ressources souterraines, récupération assistée du pétrole, ...).

La théorie traditionnelle du transport de solutés dans les milieux poreux par diffusion et advection est basée sur les travaux de, par exemples Saffman [1959]; [1960]; Scheidegger, [1961]; Ours et Bachmat [1967]. La théorie de dispersion macrocosmique décrit le transport d'un traceur idéal dans un milieu poreux saturé satisfaisant aux conditions d'écoulement de la loi de Darcy et est décrite par l'équation d'advection-dispersion (EDA) (1,1). L'ADE représente le transport par un modèle similaire à la lois de Fick (Modèle Fickian) à une échelle à laquelle on suppose un mélange complet du soluté. Cependant, de nombreuses expériences de terrain, par exemple, Mackay et al., [1986], LeBlanc et al., [1991], Gouze et al., [2008a] et de laboratoire (par exemple, [Levy et Berkowitz, 2002; Gouze et al., 2009; Bijeljic et al., 2011a]) montrent des courbes de restitution de traceurs très asymétriques, avec la signature d'un transport anormal. L'EDA ne parvient pas à prédire les comportements observés expérimentalement car il ne peut pas reproduire les mécanismes réels qui contrôlent la dispersion pour les durées et / ou les échelles d'observation. La non-Fickianité du transport de solutés en milieux poreux est généralement expliqué par l'hétérogénéité de champ d'écoulement qui existe même dans les milieux macroscopiquement apparemment homogènes [Datta et al., 2013]. La dispersion non-Fickienne est un régime de pré-asymptotique; la dispersion devient Fickienne aux temps longs si l'échelle de l'hétérogénéité est finie, à savoir lorsque le traceur a visité l'hétérogénéité à toutes les échelles. Pourtant, dans les milieux naturels présentant une hétérogénéité à pratiquement toutes les échelles, le régime effectif de dispersion est en général non-Fickian.

Les propriétés de dispersion non-fickienne, leur origine et leurs relations avec l'hétérogénéité structurale de la porosité sont encore débattues. Pendant les quelques dernières décennies, de nombreux auteurs ont développé avec plus ou moins de succès différents modèles pour simuler et prévoir un transport non-Fickien. Beaucoup de ces modèles reposent largement sur la formulation de l'ADE et essaient d'adapter les résultats expérimentaux par les variations spatiales ou temporelles du coefficient de dispersivité. Cependant, les modèles alternatifs tels que le Continuous Time Random Walk (CTRW) ou Multi-Rate Mass transfer (MRMT) décrivant le comportement de transport anormal basé sur l'hypothèse que la dispersion non-Fickienne ont été développés. Ils sont basés sur la prise en compte de la distribution des temps de transition que le soluté rencontre dans les milieux poreux et se sont avérées très efficaces pour expliquer les comportements observés.

Les développements récents en ressources informatiques nous ont donné l'occasion d'étudier les mécanismes qui contrôlent le transport à l'échelle du pore. Par exemple, des techniques fiables pour l'imagerie tridimensionnelle des structures et de flux dans l'espace des pores sont maintenant utilisables. La résonance magnétique nucléaire (RMN) [par exemple, Scheven, 2013] et la microtomographie à

rayons X (XRMT) [par exemple, Fourar et Radilla, 2009; Klise et al., 2008] ont été utilisés pour visualiser directement les effets du transport dans les médias poreux naturel et artificiel. Toutefois, la contribution de ces méthodes pour caractériser les mécanismes de dispersion multi-échelles est plus qualitatif que quantitatif, similaire à d'autres techniques d'imagerie développées pour l'étude de la dispersion dans les milieux poreux transparent. Néanmoins, ces méthodes sont inégalement pour caractériser les modèles moyens de comportement et d'essais macroscopiques.

A l'inverse, une étude détaillée des processus de transport est maintenant possible par résolution numérique directe à l'échelle des pores. L'approche standard commence avec l'acquisition d'images à haute résolution de XRMT de la structure de pores. Les images segmentées sont ensuite utilisées pour mailler la porosité et calculer l'écoulement et le transport en utilisant des codes de dynamique des fluides calculée [Ovaysi et Piri, 2011; Blunt et al., 2013]. Cette approche donne des informations utiles sur les processus qui se déroulent à l'échelle des pores et de ses principales limites sont liées à la qualité et la résolution des images XRMT et les limitations de calcul pour résoudre les flux sur les grands domaines. En outre, les résultats sont très sensibles à la segmentation des images XRMT, la précision des calculs d'écoulement et à la représentativité de l'échantillon par rapport à l'objet macroscopique initial [Arns et al, 2005 [Schlüter et al, 2014.]. Guibert et al 2015. Sienne et al., 2015].

Transport en milieu poreux

Les deux modes de base de déplacement de solutés en milieu poreux sont miscibles et non miscibles. Dans ce travail, nous étudions le transport miscible d'un traceur idéal. Il est caractérisé par un seul fluide présent dans le milieu poreux, mais ses propriétés ou la composition peut varier dans l'espace et le temps. Deux mécanismes de transport principaux sont la diffusion moléculaire et l'advection. La diffusion moléculaire est un mécanisme ubiquiste de transport se produisant dans le milieu poreux dès que la concentration du soluté varie dans l'espace. Le traceur se déplace à partir d'une région de haute concentration pour une région de faible concentration. L'advection (ou convection) correspond au déplacement du traceur à la vitesse local de l'écoulement. L'advection provoque la dispersion du traceur en raison des différentes longueurs de trajet et les différences de vitesse. Ce processus est appelé dispersion mécanique. Cependant, la dispersion dans le milieu poreux avec de l'eau qui coule est influencée à la fois par la diffusion et la dispersion mécanique et ils ne peuvent pas être séparés. Par conséquent ces deux influences sont définies ensemble comme dispersion hydrodynamique. La contribution relative à dispersion hydrodynamique de dispersion et de diffusion mécanique est caractérisée par nombre de Peclet ($2,11$), qui est utilisé pour caractériser régime de dispersion.

Expériences de traçage

Le chapitre 2 présente montage expérimental et les résultats de l'expérience de laboratoire. Des expériences de laboratoire fournissent un aperçu précieux dans les processus naturels avec une capacité d'isoler les différents effets qui contribuent dispersion. Dans ce cas, l'expérience a été conçue pour permettre l'étude de la dispersion de traceur non-réactif (fluorescéine) dans des colonnes de billes de

verre et des carottes de grès de Berea dans des conditions strictement contrôlées. Le plan du circuit expérimental est présenté dans la figure 3.1. Il se compose de deux pompes à piston qui assurent un débit constant de flux, cellule d'échantillon, l'appareil de mesure (fluorimètre), la soupape de direction de l'écoulement, réservoir d'eau avec de l'eau propre et récipient pour l'eau de sortie. Le milieu poreux est placé dans la cellule qui est positionnée verticalement sur la partie supérieure du fluoromètre. Différentes vannes contrôlent la direction de l'écoulement (vers le bas ou vers le haut) à travers la cellule, ce qui permet d'effectuer des expériences push pull. Selon le type d'expérimentation le traceur est injecté dans le bas ou le haut de l'échantillon avec une seringue grâce à un système d'injection spécialement conçu (Figure 3.4).

Nous avons effectué série d'expériences sur la colonne de billes de verre ($L = 200 \text{ mm}$, $\varnothing = 18 \text{ mm}$). Les résultats en termes de courbes de percée (BreakThrough Curves, BTCs) sont présentés sur les figures 3.9 -3.15. Nous avons d'abord étudié le possible effet de la densité pour différentes concentrations de traceur. Il a été observé qu'il existe un effet significatif de densité se produit si la concentration du traceur est de 500 ppm ou plus. L'effet de la densité peut conduire à une mauvaise interprétation des résultats expérimentaux et par conséquent, toutes les autres expériences sont réalisées avec une concentration de traceur de 50 ppm. Expériences push-pull a révélé l'impact significatif de la durée de l'injection sur la forme des BTCs, mais il n'y a que peu d'effet sur le comportement aux temps long (tailing). En outre, il a été montré que le temps de résidence du traceur dans le système n'a aucun effet sur la pente des BTCs aux temps longs. En outre, nous avons comparé les résultats expériences en mode push-pull et des expériences standard et les résultats indiquent que le comportement aux temps long sont indentiques. Ces limitations ont été confirmés par deux expériences avec différents débits effectués sur la colonne de grès de Berea ($l = 150 \text{ mm}$, $\varnothing = 18 \text{ mm}$), i.e. la même roche que pour la modélisation numérique. Nous avons effectué la comparaison qualitative entre l'expérience et résultats de la modélisation (Figure 3.17), qui a souligné l'importance de l'inclusion à la fois la matrice de diffusion et le débit champ hétérogénéité dans la modélisation du transport pores échelle.

Enfin, il faut admettre que, malgré un effort considérable pour améliorer la résolution et le contrôle des expériences de laboratoire, les résultats ne peuvent pas être utilisés avec confiance pour le paramétrage modèle non-Fickian. Cette conclusion est le résultat d'un grand nombre d'expériences pour les essais 1) les effets de la concentration du traceur, la procédure d'injection et l'optimisation de l'équipement et 2) la reproductibilité des résultats.

Modélisation numérique du champ d'écoulement à l'échelle du pore

Dans le chapitre 4, nous présentons les procédures nécessaires qui doivent être effectuées afin d'effectuer écoulement et de transport des simulations sur la microtomographie à rayons X (XRMT) images. XRMT est une technique d'imagerie non invasive permettant d'obtenir la géométrie interne de la roche sur la base des faisceaux de rayons X passant à travers l'échantillon sous des angles différents. Le résultat de XRMT est un ensemble de 2D en niveaux de gris, où le niveau d'échelle de gris représente atténuation des rayons X par pixel. Pour les roches mono-cristallins tels que grès de Berea atténuation de rayons X ne dépend que de la densité de la roche (porosité). Ces images en niveaux de gris sont ensuite segmentées afin de distinguer les différentes phases (par exemple, rock, void). Processus de

segmentation dans ce travail a été effectué en utilisant ce qu'on appelle «région de croissance" algorithme [Siprkovska, 1993; . Noiriél et al, 2005]; dans lequel nous avons ajusté de manière itérative seuils pour obtenir la même porosité que dans l'essai de porosimétrie par intrusion de mercure effectuée sur la même roche [Mangane et al., 2013]. La nouveauté dans ce travail est que nous avons utilisé 3 phases segmentation de distinguer vide, rock et microporosité (c.-à-région avec des pores plus petits que la résolution de l'image); la place de la segmentation (seulement vide et rock) 2 phases habituellement utilisé dans la modélisation pores échelle [Ovaysi et Piri, 2010; Blunt et al., 2013]. Depuis porosité non connecté ne participe pas au transport, ils ont été éliminés par l'algorithme de marquage de la grappe sur la base de la méthode proposée par Hoshen Kopelman et [1976], qui identifie également des pores interconnectés qui enjambe à travers la totalité de l'échantillon. Sur les images segmentées nous avons calculé longueur caractéristique de deux manières différentes. Propriété définie comme le diamètre de pore moyen utilisé pour définir les régimes d'écoulement et de transport à travers Reynolds (4,7) et Peclet (2,11) respectivement des numéros. Les deux valeurs obtenues par la structure de la roche variogramme (≈ 110 um, Figure 4.6) et par la méthode proposée par Mostaghimi et al. [2012] (4.3) (124 um) sont en bon accord avec la littérature.

Pour obtenir une représentation réaliste de l'écoulement en milieu poreux, domaine de calcul doit être suffisamment grande pour capturer tous les hétérogénéités. Dans ce travail, le volume élémentaire représentatif a été étudié en fonction de la porosité (Figure 4.8) et la perméabilité (figure 4.9). Il a été extrait montrent que sous-volume de $300 \times 300 \times 300$ voxels peut être considérée comme représentative de milieu poreux sélectionné. Pour préparer milieu poreux pour les simulations de flux de domaine doit être discrétisée. Dans ce travail, nous utilisons maillage structuré en hexahédars réguliers, qui capte facilement la structure des pores à partir d'images de XRMT segmentés et il est adapté pour le post-traitement nécessaire pour les simulations de transport. Champ d'écoulement Pore échelle est obtenue en résolvant conservation de la masse (4.5) et Navier-Stokes (4.6) équations, pour l'écoulement monophasé avec la densité et de la viscosité constante. Ces équations sont construits dans une base de solveur l'état d'équilibre de la méthode semi-implicite pour les équations de pression-Lié (simple) [Patankar, 1980] algorithme qui fonctionne à l'intérieur du progiciel OpenFOAM. Algorithme simple utilise procédure itérative pour coupler de Navier-Stokes équation et obtenir champ d'écoulement pour des conditions aux limites données.

Figure 4.16 présente un graphique de corrélation de la perméabilité calculée en fonction de la porosité pour toutes les simulations effectuées dans la portée de ce travail. Reste de la section de résultat est dédié à l'étude de l'influence de la résolution de maillage. Nous avons confirmé les résultats publiés par Guibert et al. [2015] en ce qui concerne la diminution de la perméabilité avec l'augmentation de la résolution de maillage et élargi leur enquête. Nous avons montré tha pratique courante où une image voxel est modélisé par un maille peut induire des écarts importants par les résultats en utilisant des maillages avec discrétisation plus élevé de la même structure. Il a été démontré dans le cas de haute résolution Berea images de grès comme ceux utilisés ici; résolution optimale de maille est si chaque voxel est représenté par 27 mailles. Pour les autres médias ce facteur peut varier considérablement en raison de la résolution de l'image et des propriétés milieu poreux, mais en règle générale, il est conseillé d'utiliser impaire facteur de raffinement de maillage pour les médias poreux de gorges étroites pour atteindre approximations de champ d'écoulement plus réalistes.

Modélisation du transport à l'échelle du pore

Le chapitre 5 présente des simulations de transport effectuées sur les images XRMT focalisation sur la dispersion de traceur idéal. Sous-volumes sélectionnés (3003 voxels) ont été post traité après des simulations de flux (chapitre 4) et utilisé comme une entrée pour les simulations de transport. Le transport hydrodiffusive d'une trace passive est modélisé par marche aléatoire méthode de suivi de particule dans laquelle la concentration du soluté est représentée par la moyenne d'ensemble de particules. En réalité, ces particules sont marcheurs aléatoires, qui sont considérés être sans masse, infiniment petit et ils ne interagissent entre eux ou avec le milieu poreux. Dans ce travail, nous utilisons le domaine du temps de marche aléatoire (TDRW). TDRW avérée outil très efficace car il est basé sur les mouvements de particules avec une longueur constante, ce qui est très approprié à utiliser dans les médias discrétisé avec une géométrie complexe. En cas de TDRW stochasticité provient de la direction et pas de temps entre deux étapes consécutives.

Principaux résultats, la discussion et les conclusions sont présentées sous forme d'un article (voir rubrique 5.3) accepté dans Water Resources Research. Théorie et hypothèses élargi pris en compte lors du transport de modélisation dans le domaine microporeux sont présentés ci-après (section 5.2). Une fois de plus, la résolution de maillage avéré être un facteur important. Dans les simulations de transport insuffisante résolution de maillage conduit à surestimer le transport anormal et l'erreur dans les résultats semble augmenter avec la diminution de Peclet valeurs numériques. Comparaison entre simulations de transport, y compris l'hétérogénéité de champ seulement de flux et ceux dont l'hétérogénéité de champ d'écoulement et de transfert de masse mobile-immobile souligne leur contrôle concomitante dans le domaine intermédiaire du BTC queue tandis que, comme prévu, le contrôle de transfert de masse mobile-immobile le comportement de temps tardif qui est, comme on le verra dans la section 3.3.3, difficile à aborder expérimentalement.

Des images XRMT, nous ne pouvons pas extraire beaucoup d'informations concernant la microporosité (par exemple, la tortuosité, seuil de percolation). En fait seule chose qui peut être estimée est sa porosité intrinsèque: la qualité de cette estimation dépend de la qualité de la procédure de segmentation 3 phases. Par conséquent nous avons effectué une analyse paramétrique du seuil de percolation et la diffusion efficace de la forme BTC. Augmentation du seuil de percolation, les valeurs inférieures augmente le temps de séjour des particules dans le domaine immobile, tandis que des valeurs plus élevées, il diminue de manière significative la fraction de domaine immobile accessible aux particules qui se traduit par temps de séjour plus court et une diminution de traînée de la CTB. Inversement, la diminution de la diffusion efficace entraîne une augmentation dans le temps de séjour des particules dans le domaine de queue immobile augmentant la CTB.

Un point intéressant en évidence par l'analyse du résultat est que, si l'on suppose que les propriétés de la zone microporeuse sont en corrélation positive avec la porosité intrinsèque, la distribution hétérogène de la zone microporeuse peut être substituée par sa répartition homogène équivalente. Dans ce cas, le coefficient de diffusion unique pour la microporosité doit être égal à la moyenne harmonique de la microporosité distribué de façon hétérogène.

Enfin, nous avons proposé un modèle 1D rehaussée sur la base du domaine temporel continue approche de marche aléatoire en mesure de capturer le comportement causés par l'hétérogénéité de champ d'écoulement et de transfert de masse mobile-immobile. Ceci est réalisé en ayant deux distributions en loi de puissance différentes pour représenter les temps de transit dans le domaine mobile et immobile.

Simulations de flux à la fois dans la macroporosité et la microporosité: l'approche de Darcy-Brinkman

Dans le chapitre 6, nous nous concentrons sur les simulations d'écoulement pores échelle, qui comprennent à la fois dans le domaine flux micro et macroporosité. Comme indiqué précédemment approche «normalisée» de résoudre débit à pores échelle consiste à résoudre l'équation de Stokes dans macroporosité, tandis que les flux dans la microporosité est négligée. A partir de 3 phases segmenté images XRMT (voir section 4.2.2) nous avons effectué des simulations 3D des pores d'écoulement d'échelle. Le nouveau solveur développé par Cyprien Soulaïne de Stanford University dans le cadre de OpenFOAM est avérée appropriée pour résoudre simultanément le débit de la macroporosité et le domaine microporeux. L'approche est basée sur l'équation de Darcy-Brinkman, qui utilise une seule équation pour calculer la vitesse du fluide dans les deux Stokes (c.-à-macroporosité) et Darcy (c.-à-microporosité) domaine. Elle consiste à ajouter Darcy terme de résistance dans l'équation de Stokes, qui représente la friction entre le solide et non avenue dans le domaine macroporeux. Dans le domaine de la macroporosité le terme de résistance Darcy est nulle et nous résoudre Stokes standard. La partie la plus importante de définir le terme de résistance Darcy est dans la détermination de la perméabilité dans le domaine microporeux. Depuis que nous n'avons pas de données réelles sur les propriétés de microporosité (voir rubriques 4.2 et 5.2), la perméabilité est estimé par l'équation Kozeny-Carman.

Le but de ce travail était d'étudier l'importance de la circulation supplémentaire dans la microporosité, même dans les roches à faible teneur en microporosité tels que le grès de Berea (2%). L'augmentation de la perméabilité en raison de la microporosité est d'environ 5% (voir la comparaison dans le tableau 6.1) qui est relativement petite, mais toujours perceptible et nous pouvons anticiper que la contribution de l'écoulement dans la microporosité devrait devenir un processus majeur dans les roches avec une fraction élevée de microporosité comme le grès et les carbonates modifié.

Bien que, dans ce travail, nous n'avons pas réussi à établir un lien formel entre les données expérimentales sur le grès de Berea et les simulations de transport effectuées sur les images de XRMT de la même roche, mais nous avons fait quelques comparaisons qualitatives qui ont prouvé que la mise en œuvre dans les modèles de le transfert de masse dans la microporosité est obligatoire pour expliquer les observations. En outre, nous avons identifié les exigences méthodologiques et les améliorations nécessaires technologiques qui semblent être essentiels pour améliorer le dispositif expérimental. Plus précisément, les modifications doivent être faites 1) pour permettre à plus de débit Peclet afin de mieux enquêter sur l'hétérogénéité de la vitesse d'écoulement sur le transport anormal et 2) à même d'accroître la précision et la résolution de mesure de la concentration. Inversement, nous croyons que les développements futurs devraient se concentrer sur une meilleure caractérisation de la microporosité et de la distribution de vitesse afin de relier les paramètres du

modèle CTRW aux propriétés mesurables. Bien que les directions de recherche pour caractériser la microporosité peuvent être facilement établis (par exemple, la mesure du volume de la microporosité de cluster, zone d'interface, ...), l'amélioration de la caractérisation du champ d'écoulement avec l'objectif de paramétrage CTRW est plus difficile et nécessitera sans doute d'analyser les corrélations de vitesse dans un cadre de Lagrange.